UNIVERSITY OF MESSINA

DEPARTMENT OF BIOMORF

PhD. COURSE IN BIOENGINEERING APPLIED TO THE MEDICAL SCIENCES

XXXVII CYCLE

Coordinator of the PhD Course: ***Prof. Michele Gaeta***

Fatigue in bioengineering: a focus on Thermography and Finite Element Simulation for materials, components and biomechanical systems

Author:
Ing. Davide Crisafulli

Tutor:
Prof. Ing. Giacomo Risitano

Cotutor:
Prof. Ing. Dario Santonocito

SSD: ING/IND-14

Mechanical design and machine construction

2023/2024

SUMMARY

The present Ph.D. thesis represents a collection of research activities carried out over three years concerning the study of fatigue phenomena in the biomedical field using energy approaches and numerical simulations.

The energy release evaluation into the different applications were studied using experimental and simulation methods.

The experimental approach concerns to monitor the surface temperature of materials, component or biomechanical system using Infrared Thermography technique.

The Static Thermographic Method and the Risitano Thermographic Method were used for the rapid estimation of fatigue proprieties of plain and notched AISI 304L specimens, and AISI 316L specimens produced by traditional and additive manufacturing.

The use of an infrared camera is presented for the study of the effect of heat dissipated during drilling process of titanium dental implants into resin D3 bone-like blocks, and for an analysis of the temperature distribution in the knee area before and after performing an exercise in relation to the weight distribution on the legs.

Structural finite element simulations were performed on components, such as hip joint, to optimise the tribological and mechanical properties of the prosthesis, and, on notched specimen and welded details using the Strain Energy Density method, comparing results with codes or thermographic methods.

The experimental activities were conducted at the Mechanics Laboratory of the Engineering Department of the University of Messina. Analyses of the microstructure of AISI 316L were performed at the Institute of Physics of Materials in Brno, Czech Republic, during a three-month visit under the supervision of Prof. Ing. Stanislava Fintová.

These studies leave room for numerous lines of research that can be further explored in the future.

TABLE OF CONTENTS

INTRODUCTION

This PhD thesis aims to explore the phenomenon of fatigue in bioengineering by examining the properties of the materials used in biomechanical components, the design solutions adopted and common failure mechanisms. Through a review of the literature, analysis of case studies and experimental activities, the aim is to provide insights for a better understanding of the factors influencing the durability of materials in biomechanical devices or components, in order to improve the design and reliability of future developments in this field.

Most of the experimental work carried out in this thesis involved energy-based approaches, such as Thermographic Methods (TM) and Strain Energy Density (SED) method.

Risitano Thermographic Method (RTM) and Static Thermographic Method (STM) are used to estimate the fatigue properties of the studied materials.

The numerical approach through the use of finite element simulations with both 2D and 3D models enabled the optimisation of component design. A focus on the presence of notches or geometric imperfections affecting the fatigue life of the material is done through the application of the Strain Energy Density local approach.

Temperature measurement has been used not only as a parameter to study the fatigue life of materials used in bioengineering, but also to improve the study of the diagnosis of possible diseases in a rapid and non-invasive manner.

The thesis is divided into two parts:

Part I - deals in a simple manner with the theory behind the methods used and explores the literature and applications on the topic in the biomedical-bioengineering sector.

Part II - presents a number of experimental activities carried out during the PhD period.

PART I - Theoretical Background

In Chapter 1, *Fatigue in materials*, an overview of the phenomenon of fatigue is presented, briefly describing what it consists of and what effects it causes on the human body and biomedical devices.

Chapter 2, *Materials applied to bioengineering*, describes the characteristics and applications of some of the materials used in bioengineering that were studied in this thesis.

The additive manufacturing technique that has become widely used in the biomedical sector is also described.

Chapter 3, *Thermography*, presents the thermographic technique and some examples of its use in the bioengineering and biomedical fields. The use of the RTM and STM for estimating the fatigue mechanical properties of materials are also illustrated.

In Chapter 4, *Strain Energy Density method*, another energetic approach for estimating the fatigue properties of materials, is briefly presented. This method will be used to compare and verify the results of thermographic methods and to study the influence of geometric imperfections on the fatigue life of materials.

PART II – Experimental activities

In Chapter 5, *AISI 304L - Thick Notched specimens*, RTM and STM are used to estimate the mechanical fatigue properties of thick notched specimens made of AISI 304L steel. The application of the local SED approach is also shown, and the results are compared.

In Chapter 6, *AISI 304L - Solution annealing treatment*, AISI 304L specimens were analysed in two different microstructural states, one as received and one after solution annealing treatment. Using TM and microscopic analysis, their fatigue properties were correlated with the internal microstructure.

In Chapter 7, *AISI316L - Traditional and Printed*, analysis of the fatigue properties of AISI 316L steel specimens produced by additive manufacturing and compared with conventional specimens are shown. Static tensile tests and fatigue tests with TM applications accompanied by in-depth microstructural analysis allowed the mechanical properties of the materials to be estimated.

Chapter 8, *Effect of geometric imperfections on fatigue strength: SED*, shows the application of the SED method for studying the effect of geometric imperfections on fatigue life in welded joints. In bioengineering, this approach can similarly be used to study geometric imperfections in lattice or scaffold structures due to additive manufacturing techniques.

In Chapter 9, *A new approach for customised Hip Prosthesis*, machine learning, motion capture and numerical simulation techniques were used for the tribological study and topological optimisation of a hip prosthesis.

In Chapter 10, *Heat control during Dental Implant*, the temperature on a bone-like structure was monitored during drilling process for the installation of a dental implant.

In Chapter 11, *Temperature and weight distribution over the knee region*, a test campaign was carried out to monitor the temperature distribution on the knee area in participants before and after performing sit and stand cycles in relation to the load distribution on the legs.

PART I - THEORETICAL BACKGROUND

1. FATIGUE IN MATERIALS

Fatigue failure is one of the main causes of failure of common engineering materials; it has been estimated that 80-90% of failures are caused by fatigue [1]. The fatigue fracture occurs when a component is subjected to repeated stresses over time that can induce microscopic damage that accumulates and can lead to fracture even at stress values below the static tensile strength of the material.

While in the static case a single value can define the stress state of a component, which can be a uniaxial stress or an ideal stress, in the dynamic case at least two values are needed to describe the nominal stress that varies over time. The variation of stress over time can be figured as a sinusoid (Figure 1.1); all periodic phenomena can be decomposable, into a Fourier series, as a sum of sinusoids.

The characteristic parameters describing the fatigue load condition are defined below.

$$\sigma_m = \frac{\sigma_{max} + \sigma_{min}}{2} \tag{1.1}$$

$$\Delta\sigma = \frac{\sigma_{max} - \sigma_{min}}{2} \tag{1.2}$$

$$R = \frac{\sigma_{min}}{\sigma_{max}} \tag{1.3}$$

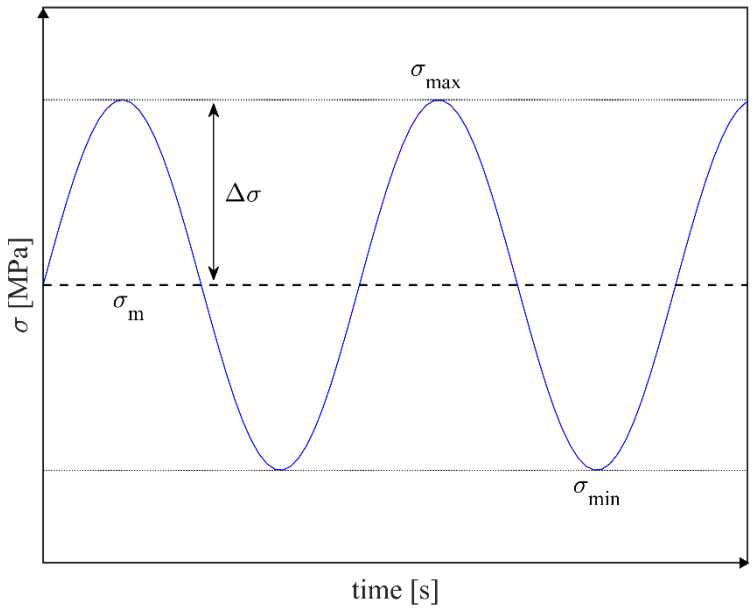

Figure 1.1: Cyclic fatigue load condition parameters

Studies to establish the relation between material strength and the number of cycles to failure were conducted by August Wohler in 1870 [2]. Figure 1.2 shows the S-N graph or Wöhler curve, which represent the number of cycles to failure of a mechanical component as a function of the maximum stress applied for a defined load ratio R (Eq.(1.3). When the applied stress is high, the number of cycles the material can withstand before breaking is relatively low. As the stress decreases, the number of load cycles to failure increases and the curve begins to level off, indicating a greater resistance of the material to fatigue.

The most widely adopted model for describing the S-N curve is the Basquin model, which uses a linear bi-log correlation between the stress amplitude σ and the number of cycles to failure N_f, where a and b are constants evaluated from experimental results.

$$\sigma = a \cdot (N_f)^b \tag{1.4}$$

Fatigue resistance is influenced by many factors, including the mechanical properties of the material and manufacturing processes, its surface roughness, microstructure, operating conditions, and the presence of cracks. Depending on the fracture mechanisms, a distinction can be made between fatigue regimes using the number of cycles range.

For a cycle range between 10^3 and 10^4, the mechanical behaviour of the component is characterised by high stress and large plastic deformation; this is the region called Low-Cycle Fatigue Regime (LCF) in which the strain-life analysis method is mainly used.

Above 10^6 cycles, High-Cycle Fatigue (HCF) occurs, in which the material is subjected to stresses much lower than its yield strength limit for a high number of cycles. In this case, the relatively low stress levels are often related to elastic deformation, so the stress-life method is more appropriate. Failure typically occurs with the propagation of microscopic crack over the time.

The boundary between LCF and HCF is not defined by a precise number of cycles because it depends on the type of material and other variables, but it possible to define an Intermediate Cycle Fatigue (ICF) regime between the two.

Other remarkable fatigue regimes in the S-N curve are the Very Low Cycle Fatigue (VLCF), below 10^3 cycles, and the Very High Cycle Fatigue (VHCF) over 10^8 cycles.

For some materials, especially metals, there is a point called the “fatigue limit” or “endurance limit”, below which the material can theoretically survive an infinite number of

cycles without breaking. Typically for steels, this limit is reached around $1x10^6$ or $2x10^6$ cycles. This phenomenon is not true for all materials; for example, for non-metallic materials such as plastics, the S-N curve may continue to decrease even at low stress levels.

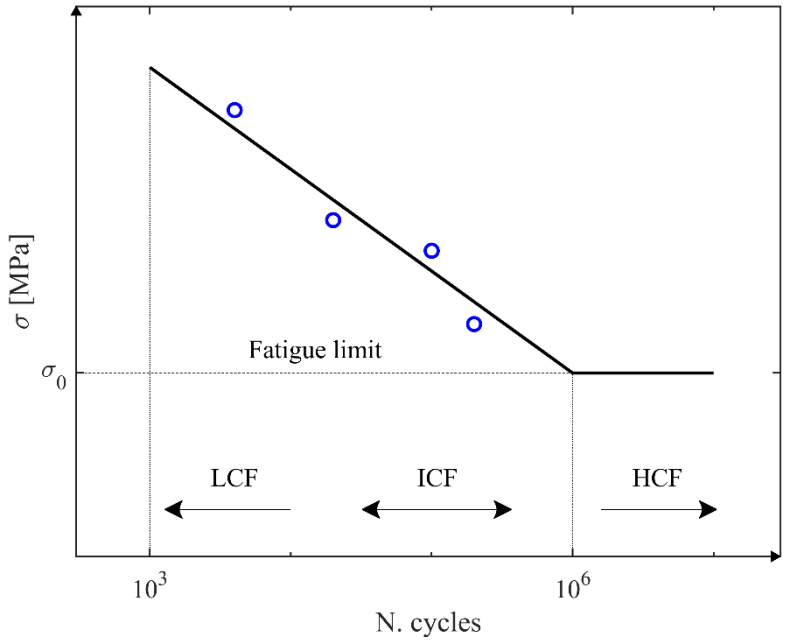

Figure 1.2: Wöhler curve with fatigue limit and regimes.

1.1 Fatigue on Bioengineering field

Mechanical fatigue in the human body is a phenomenon that occurs when tissues such as bones, tendons, muscles and ligaments are subjected to repeated or prolonged loads, causing them to degenerate or become damaged over time. This phenomenon is similar to what occurs in materials such as metals, where continuous exposure to cyclic loading conditions can cause degradation of its mechanical properties, generate cracks and/or fractures.

Bones are subjected to mechanical stress during physical activities such as walking, running, or jumping and their integrity are fundamental to protect the organs and support the movement.

In 2018 E.F. Morgan et all., present a review of the bone mechanical properties in healthy and diseased states [3]. The authors evidence the importance structural function of the bones and how they have unique mechanical properties with permit resistance and flexibility.

Classifying the bone tissue into two types: cortical bone (the compact bone fraction), and the trabecular bone (spongy fraction) a description of their peculiarities based on density, tension or compression behaviour, damage mechanism and crack propagations analyses was provided. The estimation of the mechanical behaviour of the whole bones becomes more complicated than studying only one part, also because there are a lot of different variables to consider such as thickness distribution, change with disease and age with affect their structural integrity.

Regarding ligaments several investigations show attention to the risks of repetitive load injuries and fatigue, particularly with regard to knee ligaments. By comparing the effect of fatigue and creep (slow deformation) on ligaments, it is shown that fatigue has a greater impact on the reduction of elastic modulus and residual ligament strength [4]. Anterior cruciate ligament failure can be caused by accumulated tissue fatigue damage; repetitive strenuous submaximal knee loading can lead to its fatigue failure especially at the femoral enthesis, with represent the insertion of muscles, tendons on bones, as confirmed also from in vitro studies [5,6]. Research on golf athletes explore the risk of fatigue injuries in the anterior cruciate ligament during the golf swing movement [7]. The study uses biomechanical models to analyse the stresses acting on the knee of the supporting leg, suggesting that the repetitive and asymmetrical motion of golf may increase the risk of anterior cruciate ligament injury.

For engineering application on the biomedical field, fatigue phenomena represent one of the principal challenges, where durability and reliability of materials, component and biomechanical systems are crucial.

This phenomenon occurs especially on implantable biomedical devices, such as articular prothesis [8–10], dental implants [11–13], implantable Cardioverter-Defibrillator lead [14,15], as well as biomechanical system like exoskeleton and auxiliar robotic devices, where the security and efficiency on long term period are essential.

For example, fatigue failure is the prevalent reason for hip prosthesis replacement, as these implants are continuously subjected to cyclic stresses from everyday activities such as walking, jogging, running, and movements associated with bearing body weight. Over time, these repetitive mechanical loads can weaken the prosthesis, leading to failure and the need for replacement [8].

Figure 1.3 (a,b) shows the fractured hip implant images of a recent study about the failure analysis of titanium hip prosthesis [16].The fracture occurred in the middle of the implant neck zone, placed between the head and the stem of the device.

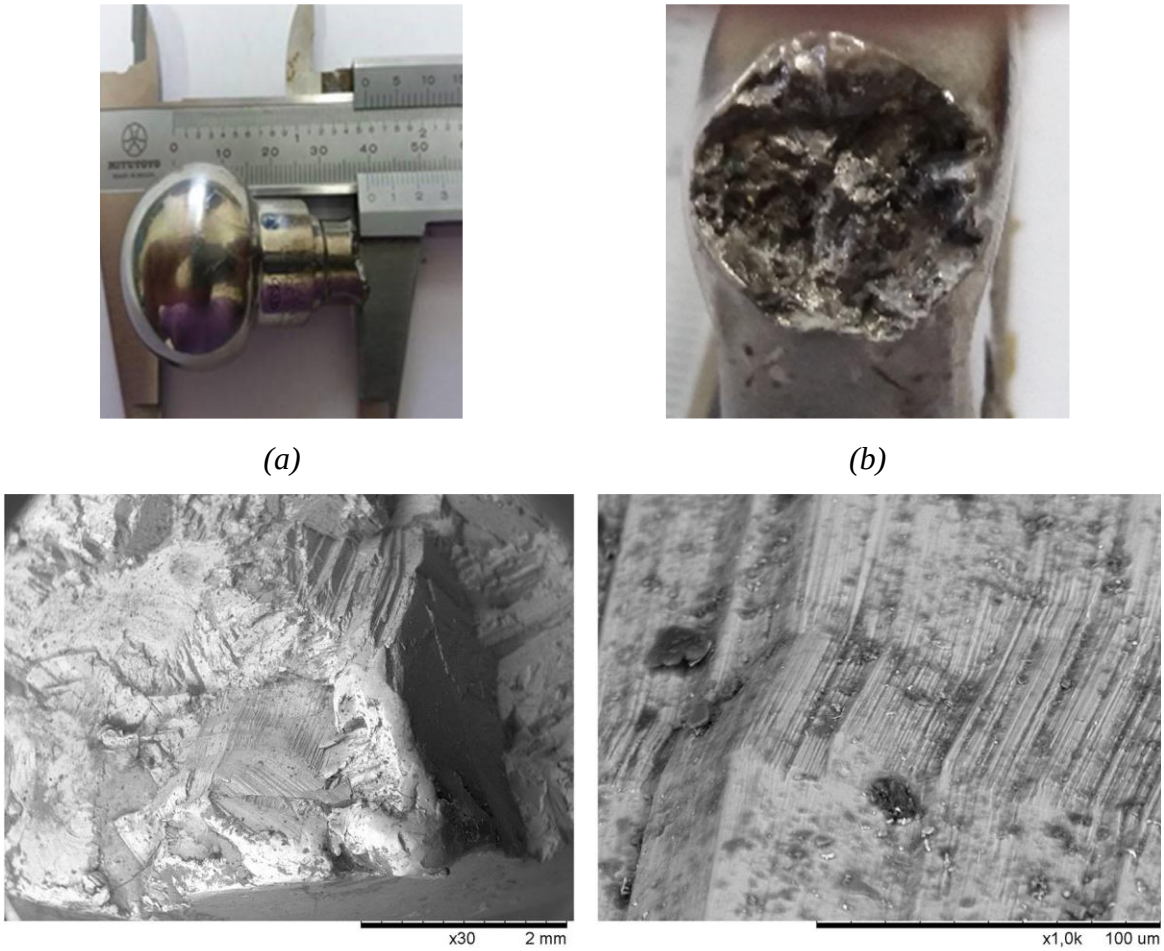

(a) *(b)*

(c) *(d)*

Figure 1.3: Fractured hip implant. (a) Femoral head; (b) fracture surface SEM images of the THR implant. (c, d) fracture surface with fatigue striation marks. Figure adapted from [16].

The images of fracture surface on scanning electron microscope (SEM), Figure 1.3 (c-d) exhibit the striation marks typically indicative of the fatigue failure mechanism.

2. MATERIALS APPLIED TO BIOENGINEERING

The introduction of advanced materials, such as metal alloys, biocompatible polymers and composite materials, has expanded the possibilities of design and application in bioengineering field. However, each material presents specific characteristics in terms of fatigue resistance, which must be carefully evaluated during the design and development phase of the new devices. In addition to materials, component design and integration into biomechanical systems also play a key role in determining fatigue resistance. For example, component geometry, processing techniques and surface quality can significantly influence fatigue behaviour. Materials used in bioengineering are selected for their biocompatible, mechanical, and functional proprieties.

Biocompatibility is one of the most important requirements for biomaterials. It is the ability of a material to interact with biological tissues without causing adverse reactions, such as inflammation or rejection, while maintaining its functionality. A biocompatible material must be safe and non-toxic so that it can be used in medical devices, such as implants or prostheses, without harming the body or altering its physiological functions [17].

The biomaterial used for an implant must also be biomechanically compatible, i.e. it must not fail due to inadequate mechanical strength or a mismatch of mechanical properties between the bone and the implant. The difference in young modulus between the bone and the implant leads to the phenomenon of stress shielding. It well knows that bone adapts to the repeated loads it is subjected to, according to the Wolff's law [18], whereby bone is deposited and reinforced at areas of increased stress and vice versa. At the contrary, the presence of the implant causes less stress on the bone, resulting in a reduction of bone mass and instability of the prosthesis. Therefore, a material with an excellent combination of high strength and low modulus closest to the bone must be used for the implant [19].

Below is an overview of the state of the art regarding the main metallic materials used in bioengineering and adopted on the research activities of these thesis.

2.1 Metallic materials

Metallic materials play an important role on bioengineering, especially for their application on orthopaedical, dental implant and in other medical device that require a combination of mechanical strength, biocompatibility and corrosion resistance [20].

Biomechanics finds its main use in orthopaedic prostheses. The current metals used in orthopaedics application such as knee and hip implants (Figure 2.1) can be manufactured from stainless steel, CoCr, Ti and Ti alloys.

There are three parts to a knee prosthesis: the femoral component, the tibial component (which includes the tibial plateau and tibial insert "spacer"), and the kneecap. The tibial insert and patellar component are often made of plastic materials, such as ultra-high molecular weight polyethylene (UHMWPE) or cross-linked polyethylene, to ensure durability and strength. Femoral components and the tibial plateau are metallic and are commonly manufactured using titanium alloys, stainless steel or cobalt-chromium-molybdenum alloys (Co-Cr-Mo), due to their high resistance to wear and corrosion [17].

In hip prostheses, the femoral stem is made of titanium alloy coupled with a femoral head, which may be made of metal or ceramic, with an acetabular cup on the outside, typically made of UHMWPE [17].

Concerning the hip prosthesis, material coupling in the femoral head and topological optimisation of the stem structure will be explored in more detail in the work in Chapter 9.

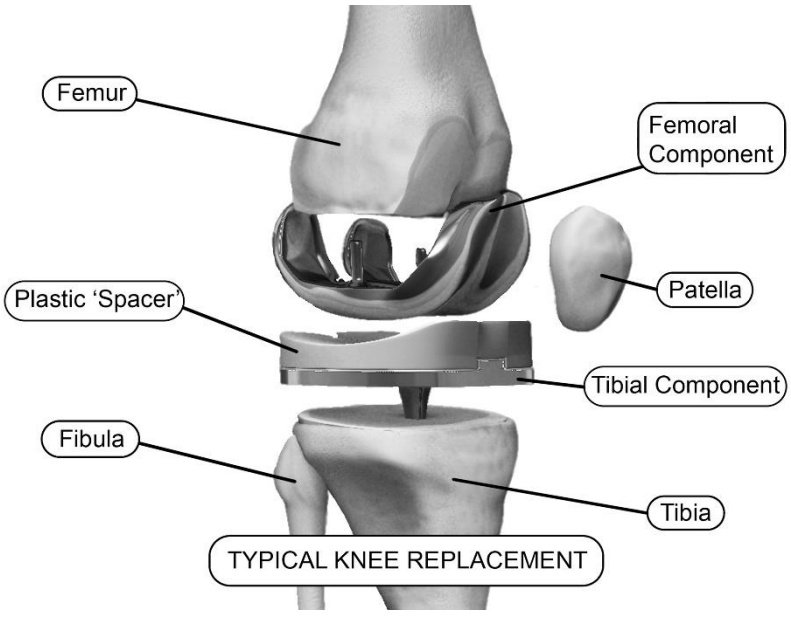

(a)

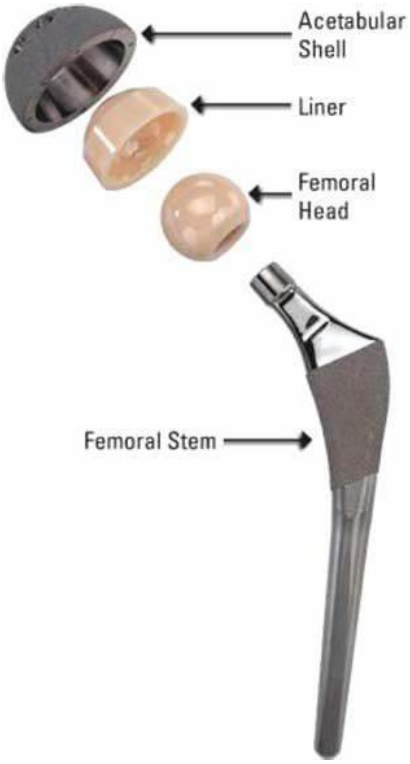

(b)

Figure 2.1: Components of (a) total knee [21] and (b) hip implants [17]

2.1.1 Titanium and alloys

Titanium has an excellent combination of light weight and mechanical strength, making it ideal for implants that must withstand high loads.

It is known for its excellent biocompatibility, which is the ability to integrate without adverse reaction with body tissue, a process known as osseointegration, which is essential for the long-term stability of implants. This property results mainly from the spontaneous formation of a titanium oxide (TiO2) layer, typically 3-7 nm thick on the surface, which is inert and resists corrosion [22] .

The most common field of application is orthopaedical, for realizing screws, plates, nails, and articular replacements (e.g. hip and knee) which use titanium and its alloys, such as Ti-6Al-4V (an alloy with aluminium and vanadium), because of their excellent mechanical properties and biocompatibility.

In 2020, Campanelli published a review [23] regarding the fatigue performance of the titanium alloys, focusing on the orthopaedic applications. The author discusses the importance of factor such as crystalline grain, the effect of heat treatments and additive

manufacturing technique, and how these affects overall performance, remarking how complex is to study his fatigue behaviour especially for medical device applications.

Regarding hip joints, one of the primary causes of the setbacks is the stress shielding phenomena [24] caused by the difference between the modulus of elasticity of the bone, 10-30Gpa [25] and that of the prosthesis material such as 316L (190Gpa) – CoCrMo (210-220Gpa) – Ti and its alloy (100-110Gpa)[19].

For this reason, the strategy is reducing the Young's modulus of titanium by changing the porosity to lead the value equal to that of the cortical bone, but on the other hand that compromise the strength of the prothesis.

The use of biocompatible polymer into the titanium porous could be a solution. One example is the realisation of a hybrid structure implant using the ultra-high molecular weight polyethylene (UHMWPE) which showed that their mechanical properties in tension and compression were similar to those of natural bone [26]. Another method to resolve the reduction of mechanical property with the increase of porosity consist of filling the porous architecture of titanium with biomedical polymethyl methacrylate (PMMA) increasing is mechanical properties [27]. Further investigations to improve these issues are ongoing with a growing number of studies available in the recent literature.

Titanium dental implants are widely used because of their ability to integrate with the maxillary and mandibular bone. Dental implants can be classified as subperiosteal, transosteal and endosseous based on their position and shape [22]. Subperiosteal implants are actual titanium alloy grids that are custom-made according to the different needs and physical conformations of each patient. This type of implant is designed to be placed under the periosteum, which is the connective tissue lining the maxillary or mandibular bone. Unlike endosseous implants, subperiosteal implants are not inserted directly into the bone, but are placed on top.

Transosseous implants, also known as zygomatic implants, are adopted only in the frontal lower jaw in cases of severe jawbone loss. These implants are anchored not to the jawbone, but directly to the cheekbones.

Endosseous are the most used implants, can be placed in either the upper or lower jaw through a mucoperiosteal incision. They consist of a titanium screw or cylinder that is inserted directly into the maxillary or mandibular bone. To produce the latter kind of implant are used CP Ti (commercial purity Ti) and ($\alpha + \beta$) Ti alloys (Ti6Al4V) [28]. This kind of implant are commonly produced from bar stock and then surface finished. Additional

treatments on external surface are done to improve the osseointegration process, such as grit blasting, laser ablation, plasma spray coating, acid etching or addition of metal powder sintered surface layers [13].

Nichel Titanium, also called nitinol, must be cited though the biomedical material, it is used for wires for orthodontic arches, podiatric orthotics, flexible surgical instruments, intravascular stents, catheter guide wire, bone fracture fixtures, staples for healing small bone fractures etc [29]. It is nickel titanium alloy of the class of the shape memory materials, characterised by super elasticity, good ductility, and corrosion resistance proprieties. The super elasticity characteristics of Nitinol is preferred in orthodontic wires compared to stainless steel wires that are too stiff and hard for the tooth [30], because they allow large strain recovery capacity and to generate stresses that are useful for the alignment of teeth during teeth alignment [29].

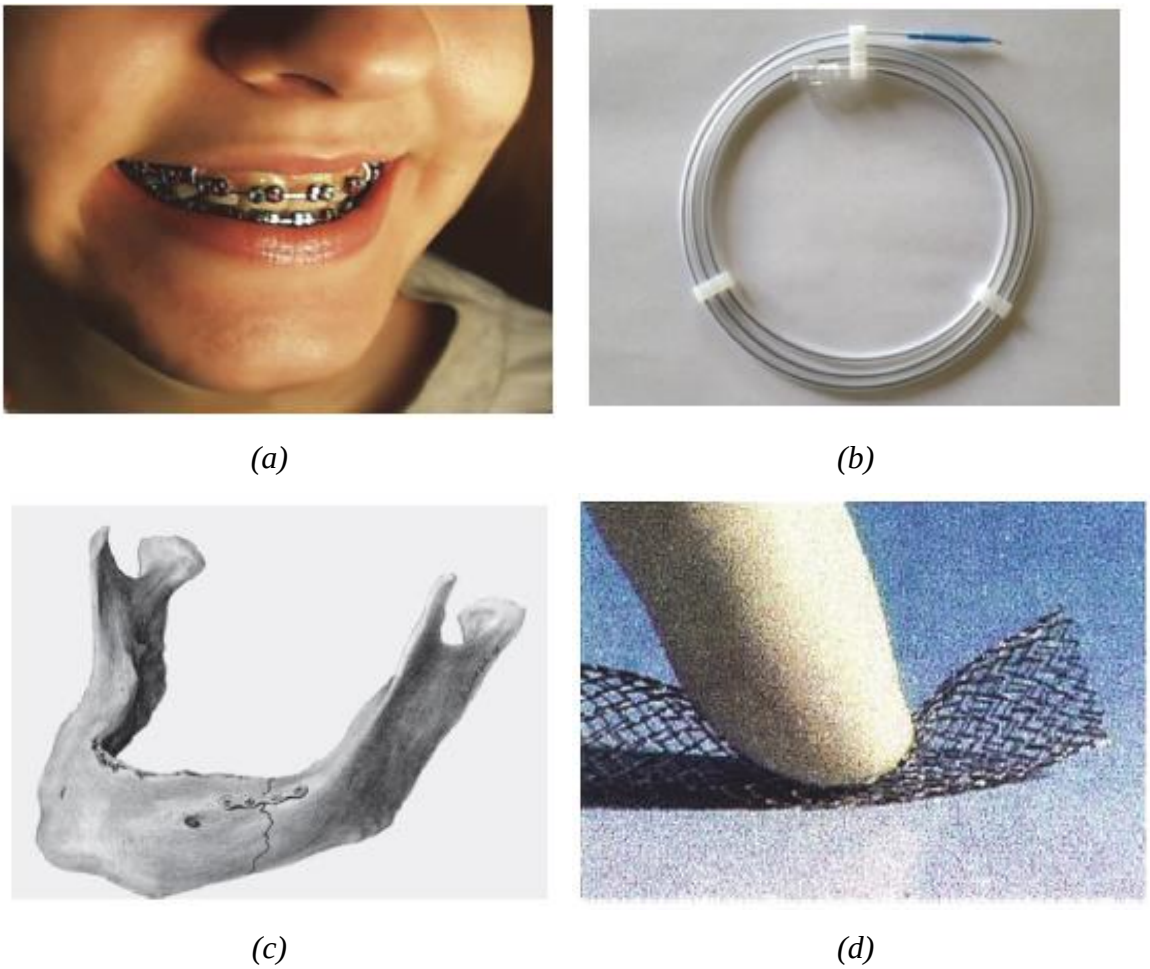

(a) *(b)*

(c) *(d)*

Figure 2.2: Biomedical application of nitinol: (a) Orthodontic arch wire; (b) Guided wire; (c) Bone fixation; (d) Stent. [29]

2.1.2 Stainless Steel

Stainless Steels are iron-based alloy that contain a chromium percentage from 11-30 wt% and undefined amounts of nickel [31].

These alloys are classified mainly according to their crystalline structure, which determines their properties and applications on medical field (Table 2.1).

Steels with martensitic structure (BCT-hardest crystalline structure) contain a small amount of carbon and they can be tempered, hardened and sharpened. They are known for their high hardness and wear resistance, but they have a lower corrosion resistance than austenitics and ferritics. Ferritic crystalline structures (BCC structure) are magnetic, less ductile than austenitics, have lower corrosion resistance and cannot be hardened by heat. Austenitics (FCC structure) have high ductility, toughness and corrosion resistance. They are not magnetic and are easily welded and machined. Every group of stainless steels is used in medical devices, with the exception of the duplex type.

Martensitic stainless steels are mainly used for dental and surgical instruments due to their high hardness. Ferritic stainless steels find few applications other than for surgical instruments. Austenitic stainless steels are the most commonly used in the medical field because they have good corrosion resistance and moderate strength, they are in fact the only ones used in implants.

Table 2.1: Four categories of stainless steels and typical medical applications [31]

Material type	**Application grade**	**Examples**
Martensitic	Dental and surgical instruments	Bone curettes, chisels and gouges, dental burs, dental chisels, curettes, explorers, root elevators and scalers, forceps, hemostats, retractors, orthodontic pliers, and scalpels.
Ferritic	Very limited surgical instruments	Solid handles for instruments, guide pins, and fasteners

Austenitic	A large number of non-implantable medical devices Many short-term implants Total hip replacements	Canulae, dental impression trays, guide pins, hollowware, hypodermic needles, steam sterilizers, storage cabinets and work surfaces, and thoracic retractors. See Table …
Duplex	Not yet applied in the biomedical field	

The development of Type 304 stainless steel in the 1920s marked a significant advance in improving the corrosion resistance and strength of metal implants. This steel has helped extend the life of implants and reduce the incidence of post-operative complications, such as metallosis (the medical condition involving deposition and build-up of metal debris in the soft tissues of the body). The presence of 18% chromium (Cr) allows passivation of the alloy, i.e. the rapid formation of a protective layer of chromium oxide, which regenerates itself and prevents oxygen from penetrating the underlying material. In parallel, the 8% of nickel (Ni) promotes the formation of an austenitic crystalline microstructure with a face-centred cubic lattice (FCC), increasing the steel's density, hardness and abrasion resistance. However, while being more resistant to uniform corrosion than carbon steels, grade 304 can be vulnerable to pitting corrosion when exposed to fluids rich in chloride ions and dissolved oxygen, typical conditions of the environments in which the implants operate [32].

The 316L austenitic stainless steel provides superior corrosion resistance due to a reduced carbon content, limited to 0.03%, and an increased nickel content of between 10% and 12%. In addition, the inclusion of 2-3% of molybdenum (Mo) is particularly important to decrease the susceptibility of the alloy to pitting corrosion. For this reason, the American Society for Testing and Materials (ASTM) have recommended 316L steel as a principal alloy for implant fabrication in comparison to other stainless-steel grades.

In orthopaedic surgery, stainless steel is preferred when rigidity is the main requirement. Due to its greater ductility compared to CP Ti, stainless steel is easier to shape, making it easier to shape plates than titanium plates [33].

However, due to the risk of corrosion of 316L stainless steel inside the body under certain conditions, such as in high-stress and low-oxygen areas, surface modification methods are widely used to improve the corrosion, wear and fatigue resistance of the material. Among these methods, anodising, passivation and nitrogen implantation by glow discharge are particularly effective [34].

It should be noted that the high nickel content (10-14%) in stainless steel implants has been associated with allergic reactions in tissues and dermatitis [35]. This issue has prompted the development of new nickel-free austenitic stainless steels, which offer excellent mechanical and technological properties [36].

Despite these limitations, these materials continue to be widely used in the medical field (Table 2.2), mainly due to their easy availability, excellent manufacturing properties, acceptable biocompatibility, high strength and significantly lower costs than titanium or cobalt-chromium alloys. Stainless steels are particularly popular in short-term applications, such as temporary devices in traumatology (e.g. fracture plates, hip screws and nails) and in environments where corrosion is not rapid, such as in vascular stents [32].

Table 2.2: Biomedical applications and devices of stainless steel [31]

Materials	**Devices**	**Applications**
Type 316L stainless steel	Bone screws and pins	Internal fixation of diaphyseal fractures of cortical bone, metaphyseal and epiphyseal fractures of cancellous bone; screws comprised of hexagonal or Phillips recess driving head, threaded shaft, and self-tapping or non-self-tapping tip
Type 316L stainless steel	Onlay bone plates	Internal fixation of shaft and mandibular fractures: thin, narrow plate with slots or holes for retaining screws
Type 316L stainless steel	Blade and nail bone plates	Internal fixation of fracture near the ends of weight-bearing bones: plate and nail, either single unit or multicomponent
Type 316L stainless steel	Intramedullar bone nails	Internal fixation of long bones: tube or solid nail

Materials	**Devices**	**Applications**
Orthinox stainless steel	Total joint prostheses	Replacement of total joints with metal and plastic components (shoulder, hip, knee, ankle, and great toe): humeral, femoral (hip and knee), talus, and metatarsal components
Type 316L stainless steel	Wires	Internal tension band wiring of bone fragments or circumferential cerclage for comminuted or unstable shaft fractures
Type 316L stainless steel	Harrington spine instrumentation	Treatment of scoliosis by application of correction forces and stabilization of treated segments: rod and hooks
Types 316 and 316L stainless steel	Mandibular wire mesh prostheses	Primary reconstruction of partially resected mandible
Types 304, 316, and 316L stainless steel	Sutures	Wound closure, repair of cleft lip and palate, securing of wire mesh in cranioplasty, mandibular and hernia repair and realignment, tendon and nerve repair
Types 316 and 316L stainless steel	Stapedial prostheses for middle ear repair	Replacement of nonfunctioning stapes: various types comprised of wire and piston or wire and cup piston (synthetic fluorine-containing resin/stainless steel piston, platinum and stainless steel cup piston, and all stainless steel prostheses)
17-7PH, 17-7PH (Nb), PH-15-7Mo, and types 301, 304, 316, 316L, 420, and 431 stainless steel	Neurosurgical aneurysm and microvascular clips	Temporary or permanent occlusion of intracranial blood vessels; tension clips of various configurations, approximately 2 cm (0.8 in.) or less in length and constructed of one piece or jaw, pivot, and spring components (similar and dissimilar compositions)
Stainless steel wire formed in a zigzag configuration of 5–10 bends	Self-expanding stent	Treatment of tracheobronchial stenosis, tracheomalacia, and air collapse following tracheal reconstruction: 0.457 mm (0.018 in.)
Stainless steel	Balloon-expandable stent	Dilation and postdilation support of complicated vascular stenosis (experimental)

Materials	**Devices**	**Applications**
Type 316 stainless steel	Hydrocephalus drainage valve	Control of intercranial pressure: one-way valve
Type 304 stainless steel	Trachea tube	Breathing tube following tracheotomy and laryngectomy: tube-within-a-tube construction
Type 316 stainless steel, with spring steel diaphragm	Electronic laryngeal prosthesis system	Electromagnetic voicing source following total laryngectomy: implanted unit comprised of subdermal transformer, rectifier pack, and transducer encased in type 316 stainless steel, with spring steel diaphragm
Types 304, 316, and 316L stainless steel	Electrodes and lead wires	Anodic, cathodic, and sensing electrodes and lead wires: intramuscular stimulation, bone growth stimulation, cardiac pacemaker (cathode), electromyography (EMG), electroencephalogram (EEG), and lead wires in a large number of devices
Stainless steel	Arzbaecher pill electrode	Atrial electrocardiograms: swallowed sensing electrode of short metal tubing segments forced over plastic tubing
Type 316L stainless steel	Cardiac pacemaker housing	Hermetic packaging of electronics and power source: welded capsule
Types 316 and 316L stainless steel	Wire mesh	Inguinal hernia repair, cranioplasty (with acrylic), orthopedic bone cement restrictor
Types 304 and 316 stainless steel	Retention pins for dental amalgam	Retention of large dental amalgam restorations: cemented, friction lock, and self-threading pins, placed approximately 2 mm (0.08 in.) within dentin with approximately 2 mm (0.08 in.) exposed
Types 304 and 316 stainless steel	Preformed endodontic post and core	Restoration of endodontically treated teeth: post fixed within root canal preparation, with exposed core providing a crown foundation
Type 304 stainless steel	Preformed dental crowns	Restoration for extensive loss of tooth structure in primary and young permanent teeth: preformed shell

Materials	**Devices**	**Applications**
Types 302, 303, 304, and 305 stainless steel	Fixed orthodontic appliances	Correction of malocclusion by movement of teeth: components include bands, brackets, archwires, and springs
Stainless steel	Percutaneous pin bone fixation	External clamp fixation for fusion of joints and open fractures of infected nonunions: external frame supporting transfixing pins
Stainless steel	Variable capacitance transducer	Measurement of pressure on sound: metal diaphragm, mounted in tension
Stainless steel	Variable resistance transducer	Measurement of respiratory flow: metal arms supporting wire strain gage
Stainless steel	Intrauterine device (IUD)	Contraception: stainless steel (Majzlin spring, M-316, M device), stainless steel and silicone rubber (Comet, M-213, Ypsilon device), stainless steel and natural rubber (K S Wing IUD), stainless steel and polyether urethane (Web device)
Stainless steel	Intrauterine pressure-sensor case	Protective shroud for transducer
Stainless steel	Osmotic mini-pump	Continuous delivery of biologically active agents: implanted unit comprising elastomeric reservoir, osmotic agent, rate-controlling membrane, and stainless steel flow moderator and filling tube
Stainless steel	Radiographic marker	Facilitation of postoperative angiography of bypass graft: open circle configuration of 25 gage suture wires
Stainless steel	Butterfly cannula	Intravenous infusion
Stainless steel	Cannula	Coronary perfusion: silicone rubber reinforced with an internal wire spiral
Stainless steel	Acupuncture needle	Acupuncture: 0.26 mm (0.01 in.) diameter × 5–10 cm (2–4 in.) length needles

Materials	Devices	Applications
Steel and stainless steel	Limb prostheses, orthoses, and adaptive devices	Substitution, correction, support, or aided function of movable parts of the body, and technical aids not worn by the patient: components such as braces, struts, joints, and bearings of many items

2.1.3 Cobalt-Chrome alloys

Co alloys are more advantageous than other alloys for the manufacture of wear parts of medical devices. Moreover, these alloys are highly resistant to corrosion even in a chloride environment, due to the spontaneous formation of a passive oxide layer in the body environment [19]. Co alloys for biomedical applications are grouped into two categories: Co-Cr-Mo alloys, which are usually used for product casting, and Co-Ni-Cr-Mo alloys, which are usually processed by hot forging [13].

The most common example of Co-Cr-Mo casts are the heads of artificial joints, such as those of hip prostheses, which exhibit high strength and ductility.

Compared to cast Co-Cr alloys, wrought Co-Ni-Cr-Mo alloys can be used for implant devices with high strength requirements which require long service life without any fracture or stress fatigue, for example, in case of stems of the hip joint prostheses [19].

The presence of considerable amount of Ni improves the castability and workability of the material[13]. However, the Ni content in forged Co-Cr alloys can causes cause allergic or inflammatory reactions in some patients [37].

A maximal Ni content of 1 wt% and a maximal C content of 0.35 wt% are simultaneously allowed in order to improve the wear resistance [38,39].

Currently, biomedical applications of Co-Cr alloys mainly concern the fabrication of orthopaedic prostheses for knee, shoulder and hip replacement, as well as their use as fixation devices for fractured bones [40]

In dentistry, cobalt-chromium alloys are commonly used for the fabrication of metal frameworks of removable partial dentures (RPDs) and have recently been employed as metal substructures for the fabrication of porcelain-fused-to-metal restorations and implant structures [41].

2.2 Additive manufacturing

Additive manufacturing (AM), also known as 3D printing, is a production process that allows three-dimensional objects to be created by adding material layer by layer until the desired shape is achieved. Unlike traditional subtractive manufacturing methods, such as milling or turning, additive manufacturing builds objects by adding material instead of removing it.

This innovative manufacturing approach offers new opportunities for the design and production of complex structures with high precision and customisation grade in a short time and with reduced waste production.

Compared to conventional production, AM significantly reduces material waste, shortens the production period and eliminates the need for most manual operations [42].

The potential applications of this technology also involve the field of bioengineering with the realisation, for example, of customised medical device, prostheses, surgical and dental implants, highly porous scaffolds, organ and tissue manufacturing, anatomical models and pharmaceutical products [43].

Figure 2.3 shows some examples of the wide range of applications of additively manufactured biomedical prostheses.

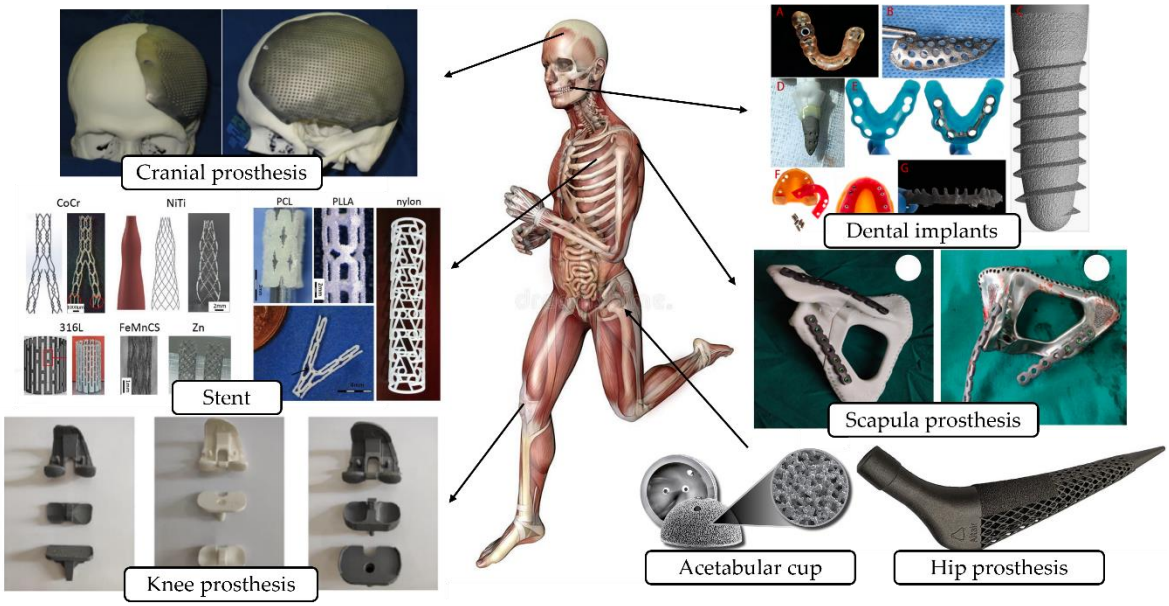

Figure 2.3: Additively manufactured different biomedical prosthesis [44–50]

Additive manufacturing comprises a wide variety of techniques that can be classified according to different characteristics. A distinction based on the physical state of the raw material is given in the review by Jayanth et all. [51] which categorized liquid-based, solid-based, and powder-based approaches. The advantages and disadvantages of the AM techniques with the relatively material used and applications are shown in the Table 2.3 [51].

Among powder-based techniques (laser-assisted printing), the most popular are selective laser sintering (SLS), electron beam melting (EBM), selective laser melting (SLM) and laser powder forming. These processes are particularly used for the fabrication of complex and intricate structures [52]. Metals such as stainless steel, cobalt-chromium alloys and titanium but also ceramic materials such as aluminium oxide, hydroxyapatite and calcium phosphate are normally suitable with these technique [43].

In solid-based 3D printing, ultrasonic AM and laminated object production are mentioned, which are able to produce objects with a high degree of precision and detail [53]. The liquid-based category, on the other hand, comprises two main techniques: the extrusion process, exemplified by Fused Deposition Modelling (FDM), and the vat polymerisation technique, further subdivided into Stereolithography (SLA) and Digital Light Processing (DLP) [54]. In these technique models are generated by the solidification of liquid resins, so thermoset photopolymers are normally used. These techniques find wide application in the field of 3D-printed ceramic biomedical devices [55] for the production of dental implants and cardiovascular treatments [56]. The printing procedure between DLP and SLA is similar, the difference is only in the light source used, in addition, DLP production is mainly applied to the development of conductive objects for the electrical industry[43]. These methods are distinguished by their ability to achieve exceptional accuracy and surface resolution, making them suitable for applications requiring high-fidelity reproductions [51].

The process of bioprinting of biopolymers such as chitosan, alginate, cellulose, collagen, gelatin, etc. has been increasing day by day due to more refined and efficient treatments, and they have numerous applications including bone, cardiac and liver regeneration, wound healing and drug delivery systems [57].

Table 2.3: Categorized AM Techniques along with Advantages and Disadvantages[51].

Classification based on the state of material	AM Technique	Materials Used	Resolution	Advantage	Disadvantage	Application
Powder Based (Laser-Assisted Printing)	Selective Laser Sintering (SLS)	Polyamide (PA12), Polyether ether ketone (PEEK)	50 – 100 µm	Lesser anisotropy with better mechanical properties	Rough surfaces & poor reusability of unsintered powder	Tissue Engineering, Implantable Devices
	Selective Laser Melting (SLM)	Stainless steel, β-tri-calcium phosphate, NiTi	20 – 100 µm	Components with structured porosity & high cyclic stability	Allows production of single material parts only	Load-Bearing Bone & Biodegradable Implants
	Electron Beam Melting (EBM)	Low alloy Steel, Nickel and Titanium Alloys	5 – 15 µm	Eliminates impurities such as oxides & nitrides and gives high strength	Vacuum is required which adds the cost due to maintenance	Dental Tissues, Bones and Joints
	Laser Powder Forming	Stainless Steel, Aluminium, and Titanium Alloys	50 – 100 µm	Reduced material waste and faster printing	Higher costs and higher energy consumption	Dental Fields, Joint Replacements, Implants, Orthodontic Parts, Surgical Instruments
Solid Based	Ultrasonic AM	Aluminium Alloys, Nickel Alloys, Brass, And Steel	20 – 40 µm	Produce metal parts with complex internal geometry and able to bond multiple metals	Inferior bonds at surfaces and increased surface roughness	Implants, Tools, and Supportive Guides
	Laminated Object Manufacturing	PVC, Paper	200 – 300 µm	High Surface Finish, Low cost, No support structure required	Debuting issue & Slow Delamination	Bones, Jaw, and Mandibles
Liquid Based	Stereo Lithography (SLA)	Acrylate-based resins, ceramics, thermoplastics, biomaterials, hydrogels	50 – 100 µm	Faster fabrication process & precision	Low build volumes for ceramic structures & high cost of raw materials	Casting, Prototyping, Tissue scaffolds
	Digital Light Processing (DLP)	Photopolymers, metals, ceramics	50 – 120 µm	Better resolution & ability to print at lower temperatures	A lower number of photocrosslinkable polymers	Microfluidics, Dentistry
	Fused Deposition Modeling	ABS, PLA, PC, HIPS	100 – 150 µm	Inexpensive machines & materials	Rough Surfaces & High-Temperature Process	Bone Implants & Dentistry

In tissue engineering, scaffold fabrication by additive manufacturing techniques seems to be very dominant. Bone is a naturally regenerative tissue, but due to significant trauma, bone defects such as fractures can be generated which hinder the normal regeneration process [57]. Since the introduction of 3D printing techniques, numerous researchers have pursued the development of scaffolds to facilitate bone tissue regeneration. Scaffold design can provide structural support for newly formed tissues and allows the transport of cells to a specific area. They are suitable to repair damaged nerves and other body parts effectively [43]. Usually in the case temporary implants, the scaffolds are made of metals defined as biodegradable, which are specifically designed to naturally degrade within the organism after serving their intended purpose without causing adverse effects on the host. Biodegradable metals are generally divided into three main families: Mg, Fe, and Zn.
Figure 2.4 reports some example of scaffold structures obtained by laser powder bed fusion (L-PBF) technique realised with biodegradable materials [58].

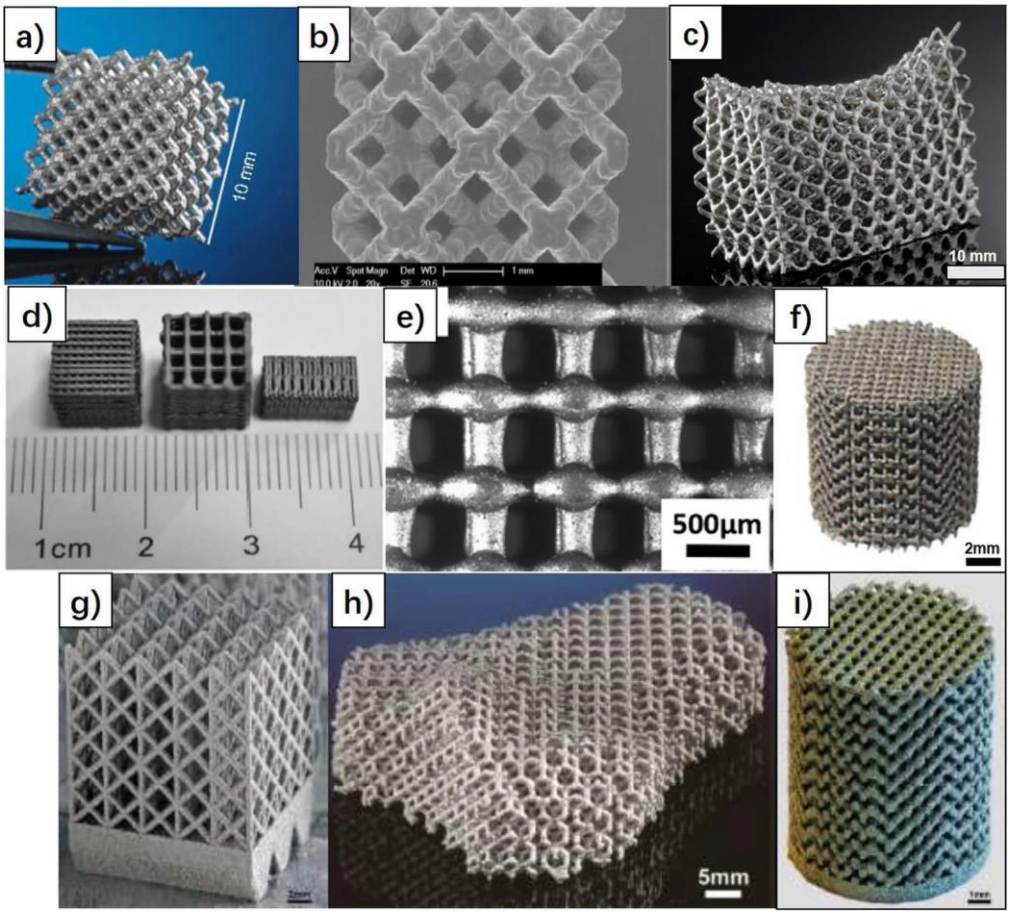

Figure 2.4: Biodegradable metal scaffolds made by L-PBF [58]: (a–c) WE 43 [59–61], (d–f) pure Fe [62,63], (g–i) pure Zn [64].

In another example, Dienel et al. [65] employed the SLA technique to fabricate biodegradable implants for bone generation. Figure 2.5 shows the use of a 3D-printed porous scaffold incorporated into the human maxilla.

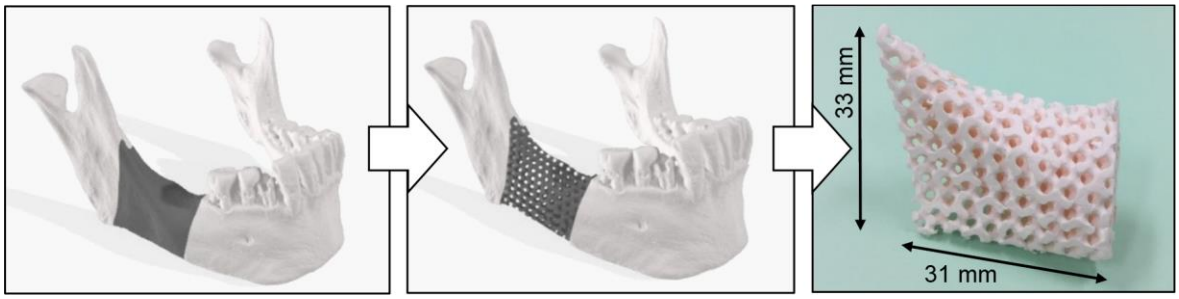

Figure 2.5: Implantation of 3D-printed PMTC-based (Poly trimethylene carbonate) scaffolds into the human jawbone manufactured through SLA strategy[65].

Among the many advantages of additive manufacturing is the ability to design components with a desirable strength-to-weight ratio. This finds application in the prosthetic industry where various difficulties such as stress shielding, tissue integration, and bone degradations over time are tried to be solved. Various implicit lattice-based models have been introduced to overcome these problems [66,67]. The choice of lattice structure for additive manufactured implant reduces the implant mass and, due to higher stress distribution and deformations as compared to the rigid implants, it brings down the stress shielding issues.
In 2022 Izri et al. [68], propose a prosthesis composed by a rigid shell with an infill lattice design (Figure 2.6). In this study, sixteen beam-type lattice structures were investigated numerically to optimize the mechanical properties of the implant (Figure 2.7). The mechanical behaviour of the prosthesis is influenced by several parameters such as the beam thickness, the unit cell size and the different materials adopted.

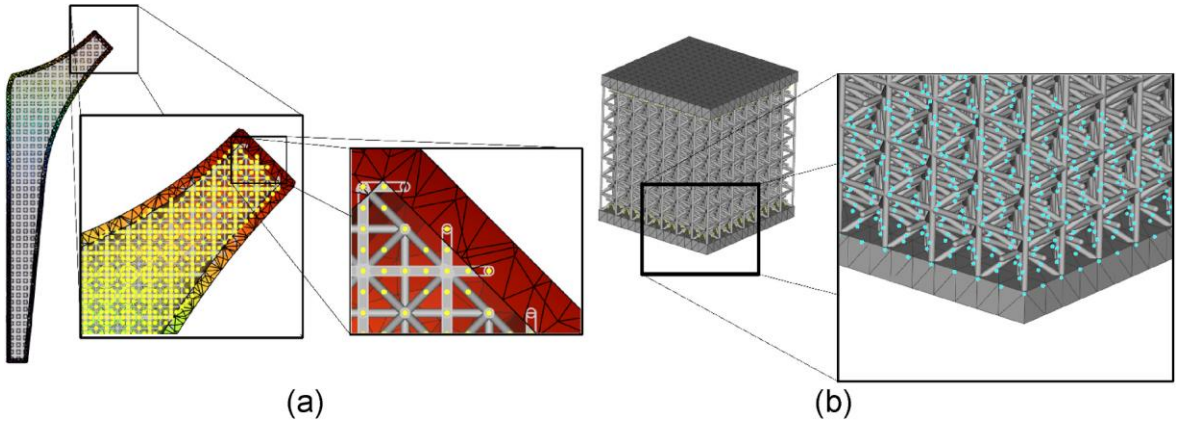

Figure 2.6: Rigid shell and infill lattice design. a) Hip implant b) Cube [68].

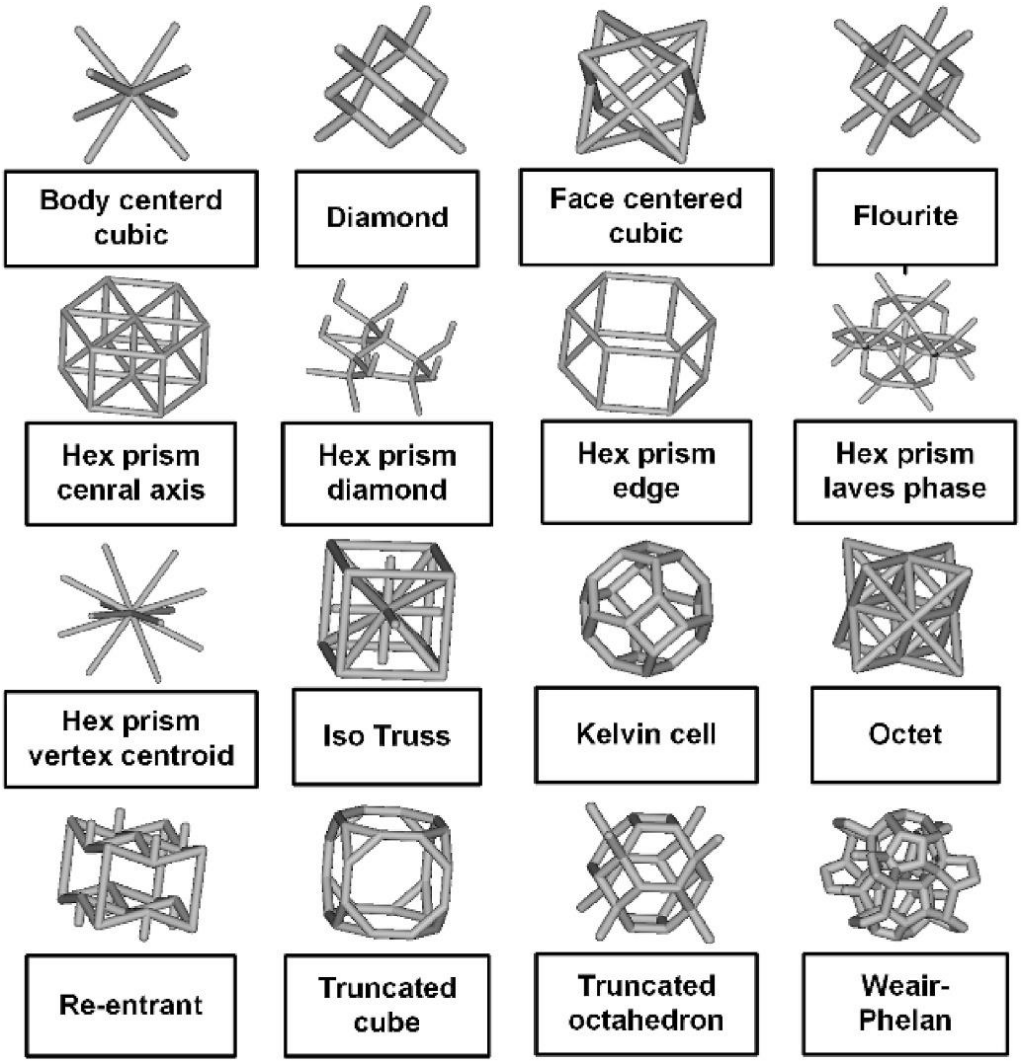

Figure 2.71: Various beam-based lattices [68].

The maximum stress distribution and strain were evaluated after a static force of 2300 N was applied to the hip implant specimen.

Among the lattices, the Weaire-Phelan structure showed the best performance at different thicknesses and unit cell sizes. In fact, the greater number of beam elements per unit volume decomposed the applied axial force with a consequent reduction in the stresses acting on each beam element. In addition, iso, octet, truncated octahedron, and Re-entrant lattice structures presented better characteristics than other types. Concerning the materials tested, the Ti-6Al-4V structure experienced the least stress on its elements, while the CoCr28-Mo6 structure exhibited the lowest deformation due to its higher modulus of elasticity.

However, no consideration is given to the fatigue life of the prosthesis in relation to the material or the type of geometric structure used. It is well known in mechanical engineering how the presence of geometric discontinuities and notches considerably affects the life of components, in fact most failures in metals that occur due to the phenomenon of fatigue, as seen in Chapter 1. In addition, additive manufactured parts present several intrinsic discontinuities, such as lack of fusion and gas porosities [69,70].

As confirmed by Campanelli in 2021 in a review about the fatigue life of titanium alloys prosthesis for orthopaedic applications [71], surface roughness and porosity are essential factors for fatigue performance. The introduction of surface discontinuities is dangerous because the fatigue property involves local phenomena, and therefore, is sensitive to any lack of continuity.

These issues are generally addressed in this thesis, but in particular, some experimental activities will be presented that involved studying the microstructure of specimens also made with the additive manufacturing technique (Chapter 6-7), and a methodology for studying the effect of geometric imperfections on the fatigue life of components (Chapter 8) will be shown.

3. THERMOGRAPHY

Thermography is a non-contact, full-field technique by which the energy in the infrared range, emitted by bodies at temperatures other than absolute zero, is measured by appropriate sensors and correlated with the temperature of the body itself. It is based on the link that exists between the temperature of an object and the electromagnetic radiation emitted by it in the infrared range, in which all wavelengths ranging from 0.7 μm to nearly 1 mm are included.

Each body radiates energy provided its temperature is above absolute zero (>0 K). This emitted energy in form of electromagnetic radiation is proportional to the temperature of the emitting body and can be captured by a thermal imaging camera to create a thermal image or thermogram.

The main feature that makes thermography an increasingly popular technique is that it allows the temperature of any body to be analysed contactless, non-invasively, safely, allowing measurements to be repeated over time, and that the fields of application are varied and numerous, from industrial to medical. The main difficulties are related to the inaccuracy of the measurement due to thermal losses for unavoidable convection and heat radiation from the environment, and the possibility of performing a thermal analysis of a body only for a limited thickness of material below the surface, which is influenced by the thermal properties of the body [72]. The cost of the equipment is mainly related to the accuracy of the IR camera required and the presence of post-processing software.

In the industrial field, the technique is widely used for non-destructive controls, a class of methods for identifying the integrity or compliance of a structure without damaging or destroying the material in any way.

Considerable use of thermography is made in research and development sector, in fact, it is used in scientific research in various fields, from industrial to medical, from diagnostic purpose to mechanical characterization and optimization of materials and production processes.

3.1 Thermography on bioengineering

Several articles present in literature describe the different application of the thermography on biomedical field.

In 2001 Tracy A. Turner [73], analyses several clinical cases to demonstrate the effectiveness of thermography in diagnosing musculoskeletal problems in horses. Turner discusses the use of thermography to detect tendon injuries, which are often difficult to diagnose early by traditional methods and thermographic images can show areas of increased temperature that indicate inflammation or damage. The same application for identify abnormalities in joints, such as arthritis or other inflammatory conditions, through the detection of areas of abnormal heat around it. The difference of temperature can help locate points of muscle stress or pain that may not be evident during a normal physical examination.

Another example of applications in biology and medicine is offered by the review article of Glenn J. Tattersall into 2016 [74], highlighting how this technique is useful for studying thermal physiology noninvasively. The author reported several case studies about the study of thermoregulatory behaviour in animal, for example reptiles use behaviours such as basking (warming in the sun) to regulate their internal temperature by the regulation of blood flow [74,75], or birds, in which thermography can detect how heat loss through beaks and legs varies in relation to environmental temperature and metabolic heat production [76].

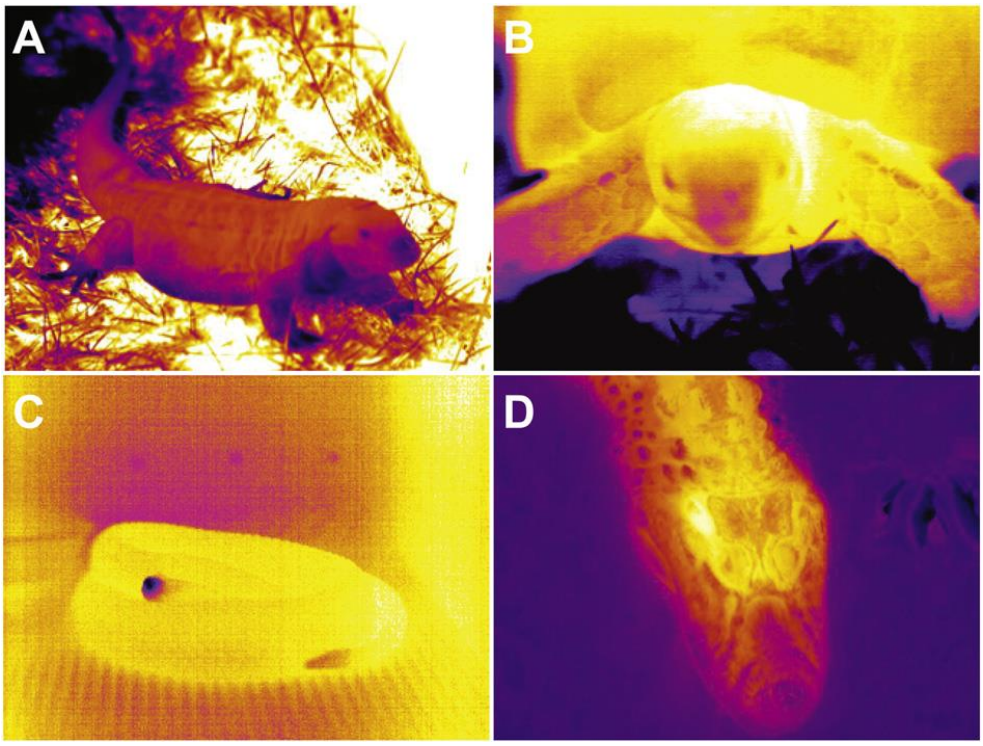

Figure 3.1: Respiratory and evaporative cooling in various reptilies: a. Argentine black andwhite tegu lizard; b. South American tortoise; c. South American rattlesnake; d. broad-nosed Caiman [74,75]

The use of thermography as a method of diagnosing cancer was explored without any significance results. Changes in temperature can be indicative of pathological processes, such as tumours, because cancer cells tend to have a higher metabolism and thus produce more heat than surrounding healthy tissues. An applied study on small animals [77] found that there is no evidence to support the use of thermography as the sole diagnostic method for cancer detection, because there are many different parameters that can influence the results of thermal imaging and that need to be investigated in depth, such as the physical properties of the surface being studied in relation to its position on the body, the stage of the cancer, the preparation of the patient and the environment for the examination, the quality of the equipment used etc. However, research confirms that IR can be used as a complementary diagnostic tool in oncology.

Thermography can be used to map biomechanical stress in biological tissues, such as bones, muscles and joints. The ability to detect micro changes in temperature can help identify areas under high loads or at risk of injury. Some examples of applications of thermography for stress analysis, from qualitative and quantitative point of view, have been described on [78]. A static or dynamic loading test is used to generate temperature variations on the specimen. For dynamic cyclic loads the most used frequencies used goes from 1 to 20 Hz to cover the human physiological activities, such as walking and running [79], but also to ensure adiabatic condition and reduced the influence of external heat source that can affect the results. The correlation between the thermographic data and strain gages or stress state data in axial compression tests is demonstrated on different application related on cortices of bovine femurs [80], human femurs [81], artificial human femurs [82–84], canine femur [85,86], fracture implants such as bone fracture plate [87], bovine tendons [88].

The validation methods of data adopted in the cited articles regards the use of the thermoelastic equation, explained in the next chapter, the use of the correlation coefficient R between the thermographic stresses and strain gages, or the use of a conversion factor between temperature and a known stress state.

Quantitative results about the stress field and fracture criteria are not always possible to understand with temperature maps but they are useful also simply for identify zones of low and high stress or monitor state of component and/or process on various biomechanical applications such as during drilling bone operations [89–91], drilling on dental implant surgery [92–94], on foot sole after walking [95], on prosthetic foot-ankle during simulated walking load cycles [96].

3.2 Thermographic Method

The previous chapters have highlighted various applications of thermography in the biomedical and biomechanical fields. Most of these are aimed at the use of thermography for diagnostic purposes and for understanding the damage mechanisms of biomechanical components and systems to predicting their fatigue life.
Estimating the fatigue life of the materials used is crucial to ensure the reliability and safety over time of the components that are used, and thermographic method allows to do it in rapid way than the conventional fatigue tests.

Fatigue is a dissipative phenomenon that leads to the propagation of a large amount of energy. Part of the energy is dissipated within the material and causes transformations first on a microscopic scale and then on a macroscopic scale until failure occurs.

During cyclic load condition, most of the energy is dissipated in the form of heat to the external environment; this accounts for about 90 per cent of the plastic deformation energy generated during dynamic loading at different strain rates [97,98]. From the measurement of the dissipated energy, it is possible to extract information on the fatigue life of the material. The measurement of this dissipated energy can be carried out by applying thermocouples or, more commonly, using the full field technique of Infrared Thermography (IR).

As observed by La Rosa and Risitano [99], by monitoring the surface temperature of a specimen under a constant amplitude fatigue test using an infrared camera, three phases can be distinguished (Figure 3.2).

In the first phase the surface's specimen temperature start to increase until reaching a constant value called stabilization temperature ΔT_{st}. The plateau region where the temperature is almost constant define the second phase. The third phase is characterized by a very rapid increase of temperature until the specimen failure.

These three phases appear only if the material is loaded with a stress value over is fatigue limit, otherwise the change in temperature ΔT, defined as the difference between the instantaneous and the initial temperature value, can be considered zero or as noise, hence negligible.

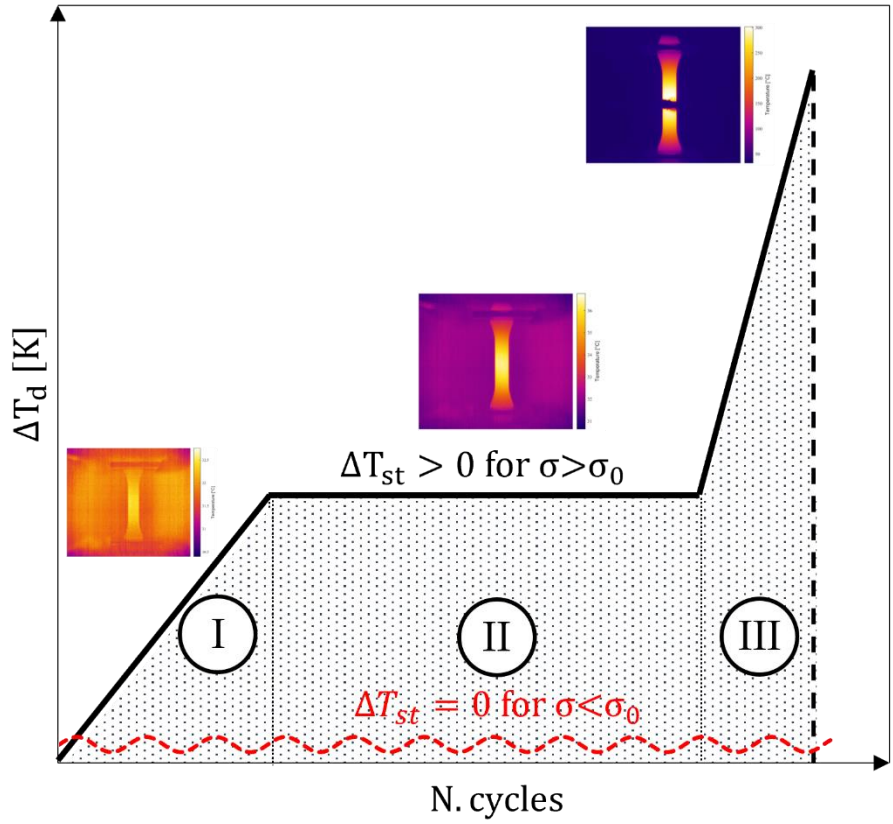

Figure 3.2: Temperature evolution during a fatigue test.

The temperature gradient in terms of number of cycles of the first phase ΔT/ ΔN, and the stabilization temperature depends on the intensity and frequency of the applied stress. Over the fatigue limit, the higher the applied stress and the higher the temperature gradient and stabilization temperature, the same is valid for the frequency.

The Thermographic Method (TM) or the Risitano Thermographic Method (RTM) is a rapid procedure that allow the estimate the fatigue limit defined macroscopically as the stress value for which the temperature of the material increases. From this consideration, reporting in a graph the stabilization temperatures against the square of the applied stress, the fatigue limit can be assessed by the intersection of the linear regression of the data with the stress axis.

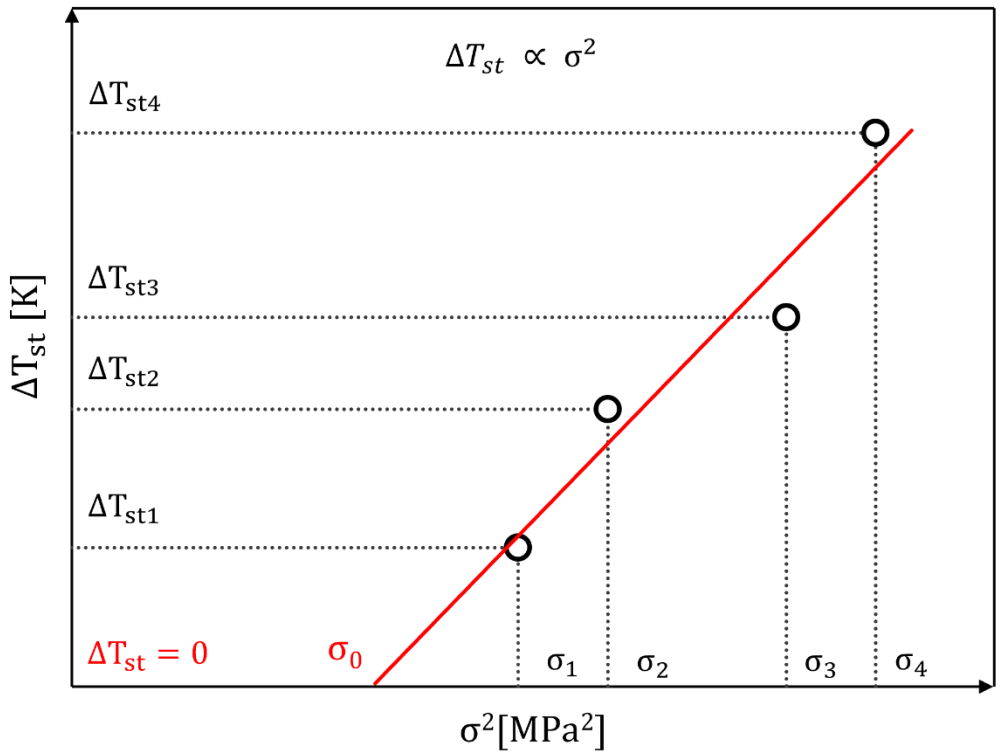

Figure 3.3: Fatigue limit estimation by RTM.

In case of limited number of specimens, even one, the RTM can be applied as proposed by Fargione et al. [100]. From an energetic point of view, considering E_p the plastic energy per unit volume each cycle, it possible to define the cumulative damage on the specimen during the first N_0 cycles as:

$$\int_0^{N_0} E_P \, dN \tag{3.1}$$

During the test, the plastic energy will increase until reaches a critical value E_c and the residual lifetime E_r of the specimen can be defined as:

$$E_r = E_c - \int_0^{N_0} E_P \, dN \tag{3.2}$$

Since that the energy stored in the specimen is less than the heat dissipated into the environmental Q, there is a proportion between the critical energy of the material E_c and the heat loss ($Q \propto E_c$).

From experimental test, the subtended area of the temperature trend versus the number of cycles is defined as the Energy Parameter Φ, and, as well as the energy loss Q, is proportional to the limit energy E_c ($\Phi \propto E_c$) (Eq.(3.3)).

$$\Phi = \int_0^{N_0} \Delta T \cdot dN \propto \mathrm{Ec} \tag{3.3}$$

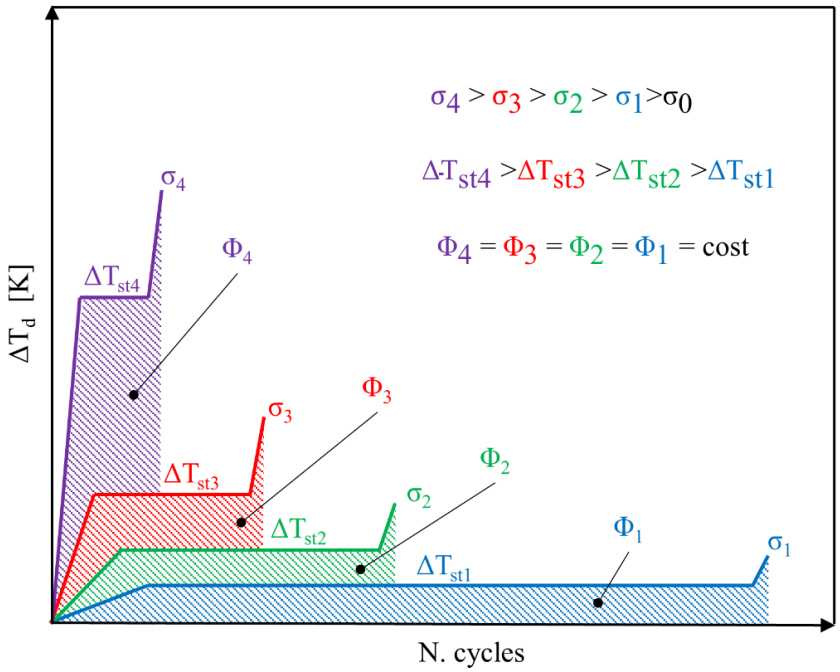

Figure 3.4: Temperature trend during constant amplitude fatigue test with different stress level.

The energy parameter Φ is characteristic only of the material, i.e. if the applied stress increases also the stabilization temperature increases but the energy parameter can be assumed as constant. From this observation, it is possible to evaluate the entire fatigue curve of the material with a limited number of specimens performing a stepwise fatigue test. Stepwise fatigue test consists into a fatigue test using increasing stress levels until the failure of the specimen. For each stress level, the stabilization temperature is recorded, assuming that the second phase of the thermographic method usually appears in short number of cycles.

Moreover, the duration in terms of cycles of the first and third phase are negligible compared to the second, so the parameter Φ can be evaluated as:

$$\Phi \approx \Delta T_{st} \cdot N_f \tag{3.4}$$

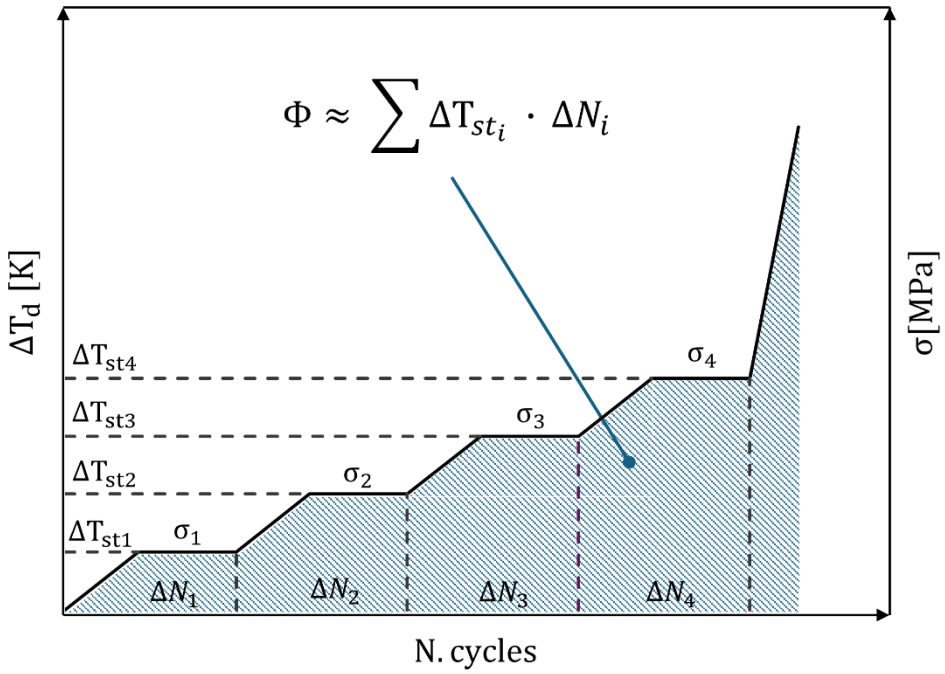

Figure 3.5: Temperature trend during a stepwise fatigue test.

From Equation (3.4, knowing the parameter Φ and stabilisation temperatures, it is possible to estimate the number of cycles to failure N_f for each applied stress level. Therefore, with just one specimen and in a short time it is possible to obtain the slope of the SN curve of the material.

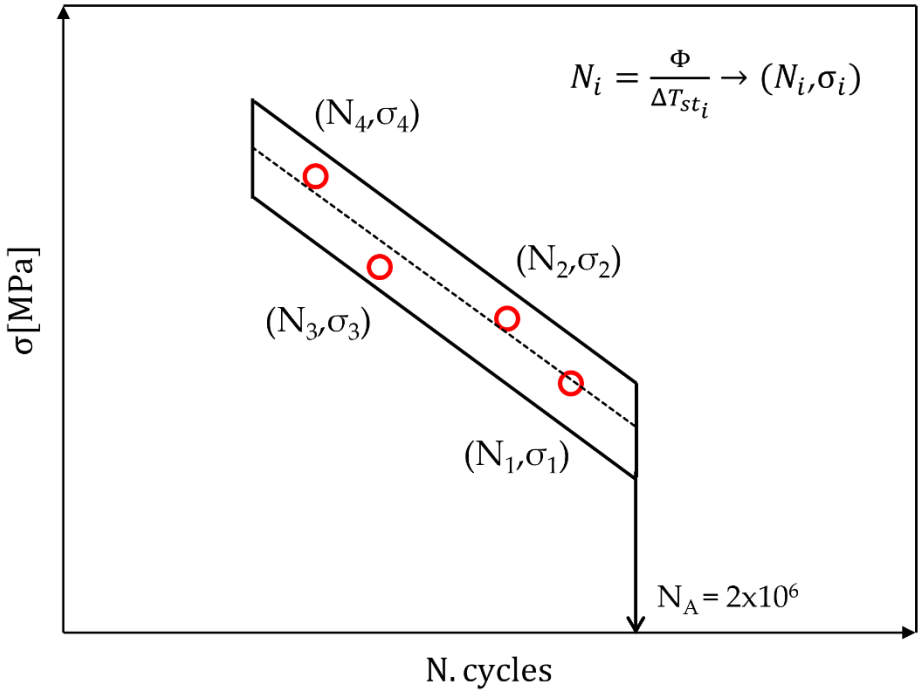

Figure 3.6: S-N curve evaluation from stepwise fatigue tests.

3.3 Static Thermographic Method

The analysis of the temperature trend in static tensile test can provide useful information also on the fatigue behaviour of the material.

During a static tensile test, a material with crystalline structure, such as metals, is characterised by an initial elastic zone, where the relationship between stress and strain is linear, followed by a plastic zone where the deformation became irreversible and lead to the final failure of the material.

The macroscopic phenomenon of heat dissipation during a static test was studied also from a microscopic point of view by several expert [101–103]**.**

Into the elastic field if the stress is removed the material return to his previous deformation because the energy is not enough to cause a permanently interatomic separation. Vice versa, when the microplasticity deformation begin, below the macroscopic yielding stress, the movement of the dislocations, which are inclined to move from one minimal energy level to another, causes a redistribution of the stress field and temperature variation.

The Static Thermographic Method (STM) was proposed in 2013 [104], as a result of other studies powered by the same research group[105,106], for the estimation of the fatigue limit of a material under static traction test.

The method allows to find the "limit stress", that correspond to the first macroscopic level of stress that if is it applied on the material under fatigue test conditions (stress ratio R= -1), lead to the specimen failure. This stress value is able to create the first irreversible plastic deformation, localized on the micro defects within the material that act as stress intensification sites.

Temperature trend during a static tensile test can be divided into three phases (Figure 3.7).

During the first phase (I) all crystals in the material are elastically stressed and the temperature behaviour decrease according to the thermoelastic law.

Under the hypothesis of adiabatic conditions, for an elastic homogeneous isotropic material the temperature variation follows the Lord Kelvin's law:

$$\Delta T = \frac{\alpha}{\rho c} \cdot T_0 \sigma_{nom} = -K_m \cdot T_0 \cdot \sigma_{nom} \tag{3.5}$$

Where α is the thermal expansion coefficient, ρ the density, c the specific heat, Km the thermoelastic constant, T_0 the initial temperature and σ_{nom} the nominal applied stress.

The second phase (II), the crystals are not only elastically stressed but some begin to deform plastically, and the temperature trend changes slope, losing the linear behaviour. The deviation from the linear trend is a consequence of the onset of heat release from the crystals due to plastic deformation. Therefore, in the last phase (III), the crystals are totally plastically deformed, and the temperature increases very rapidly until the specimen fails.

The transition point between phase I and phase II, corresponding with the change in slope from the linear trend, can related to the stress level that causes the first irreversible plastic damage on the material and can be used as an indicator for the fatigue limit estimation of the material.

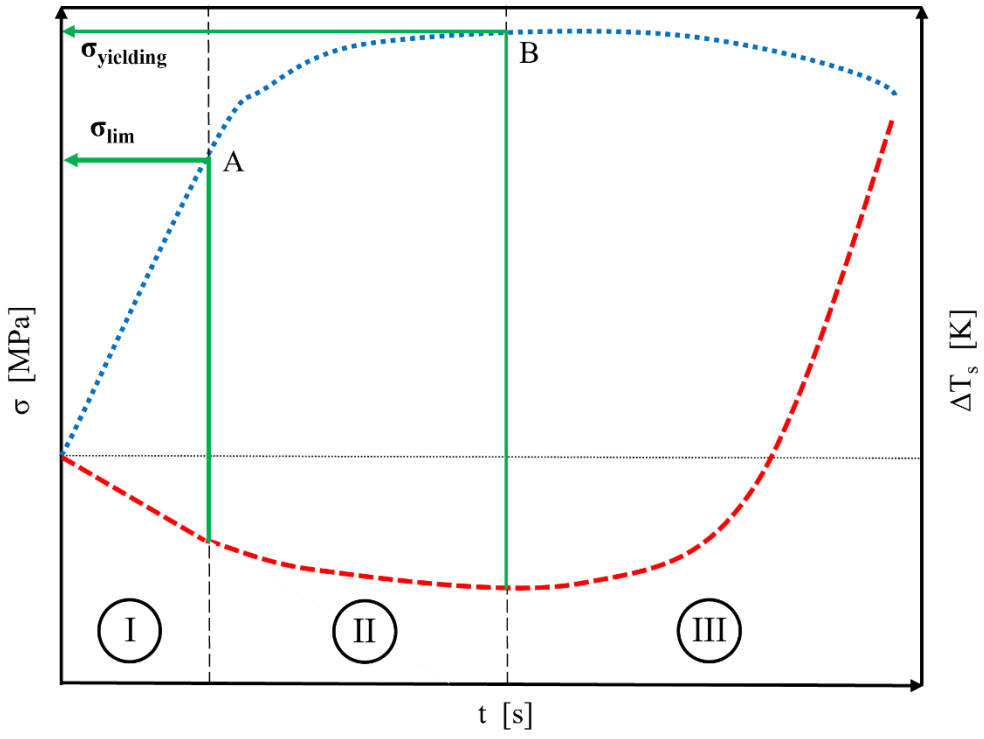

Figure 3.7: Temperature trend during a static tensile test.

4. STRAIN ENERGY DENSITY METHOD

In this paragraph the Strain Energy Density (SED) local approach is briefly presented. This energy method is adopted for the evaluation of the fatigue life of notched components, and it was used by the author as a validation or alternative approach to verify the results obtained with the thermographic method.

Due to the variability of parameters that can differs in a component, i.e. welded joints, such as geometries configurations and loading modes, the fatigue life estimation can require several fatigue tests and time.

Using the local approaches, the fatigue life of a notched component can be referred to the study of a local phenomenon on the notched detail using the theory of fracture mechanics.

The main advantage of this method is that this variability related to geometries configurations and loading modes doesn't affect the results, and the obtained equivalent S-N curve is related only to material properties.

The SED method, proposed by Lazzarin and coworkers [107–109], is based on the concept that the fatigue fracture appears on the linear elastic filed with a brittle behaviour. In detail, the fracture occurs when the strain energy density parameter W reaches a critical value W_{crit}. The SED value is averaged in a properly defined volume of material, called control volume, around the notch tip.

The critical cyclic averaged SED for a smooth specimen under linear elastic condition can be estimated with the following equation:

$$\Delta\overline{W}_N = \frac{\Delta\sigma_{N,0}^2}{2\mathrm{E}} \tag{4.1}$$

Where $\Delta\sigma_{N,0}$ is the fatigue strength at a given number of cycles, N, and at a load ratio R= 0 and E is the modulus of elasticity derived from standard tensile test.

The critical SED value will correspond to a critical control volume defined by the critical control radius R_0, which is a characteristic length of each material. Usually, the more brittle is the material and the smaller is the control radius R_0. In case of plane condition, the control volume degenerates to a circular sector.

The definition of the control volume depends on the shape of the local geometry and the loading conditions. Figure 4.1 shows representations of control volumes for V- and U-notches, either sharp or blunt, and for loading modes I and II.

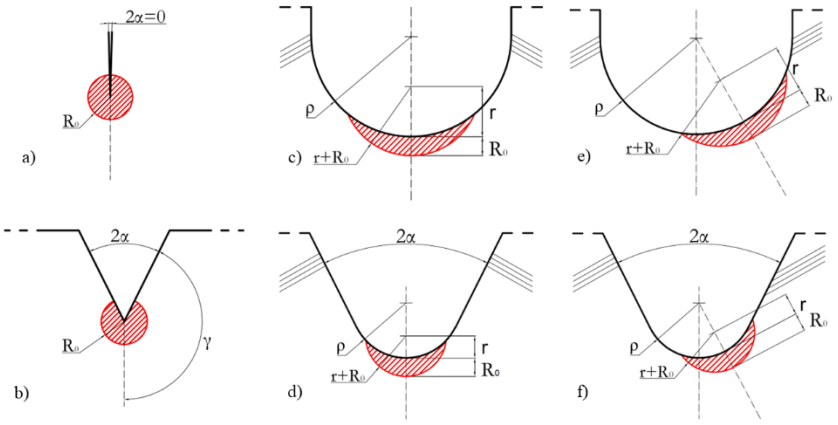

Figure 4.1: Control volume under different geometries and loading conditions: a-b-c-d) Mode I loading condition; e-f) Mode II loading condition; a) crack and b) sharp V-notch; c) U-notch and d) blunt V-notch; e) U-notch and f) blunt V-notch. Figure adapted from [110].

In the case of blunt notches, the center of the R_0 is shifted by a distance r_0 which takes into account geometric factors, in particular the fillet radius ρ and the opening angle 2α.

$$r_0 = \rho \cdot \frac{(\pi - 2\alpha)}{(2\pi - 2\alpha)} \tag{4.2}$$

Considering that the method assumes that the cyclic averaged SED value is the one leading to fatigue failures, it also allows for a direct consideration of the load ratio effect. To properly estimate the value of the cyclic evaluated SED under different load ratios, taking advantage of the benefits introduced by this method, the following equation can be applied to directly evaluate it starting from the stress range values [111]:

$$\Delta W_c = \frac{(1-R^2)}{(1-R)^2}\frac{\Delta\sigma^2}{2E} = c_w \frac{\Delta\sigma^2}{2E} \qquad 0 \le R < 1 \tag{4.3}$$

$$\Delta W_c = \frac{(1+R^2)}{(1-R)^2}\frac{\Delta\sigma^2}{2E} = c_w \frac{\Delta\sigma^2}{2E} \qquad -\infty < R < 0 \tag{4.4}$$

Applications of the SED method are shown in the research activities on chapters 5, for blunt V-notch specimen and in chapter 8 for cruciform welded joints.

PART II - EXPERIMENTAL ACTIVITIES

5. AISI 304L - THICK NOTCHED SPECIMENS

Crisafulli D., Foti P., Berto F., Risitano G., Santonocito D. An innovative and sustainable methodology for fatigue characterization and design. Under submission.

Highlights

This study concerns the application of energetic methodologies for the fatigue assessment of stainless steel AISI 304L thick specimens. The combination of Risitano Thermographic Method, Static Thermographic Method and Strain Energy Density approach produced reliable results for the prediction of material fatigue life. The results obtained with only a few specimens and with considerable time savings compared to traditional fatigue life estimation procedures were in good agreement with the data in the scientific literature for this material.

Abstract

Most failures in engineering components and structures are determined by the fatigue phenomenon, known for being lengthy to be experimentally investigated and challenging to be properly accounted in design. These aspects can represent a barrier for companies working on the edge of new technologies due to the duty and need to ensure reliability for their products. This work aims to propose a methodology to couple the economic and sustainability advantages of Thermographic Methods in investigating the fatigue behaviour of materials with those of local approaches to provide a simple, yet reliable, fatigue design tool. To pursue this aim we intentionally conducted in the present work the minimum required experimental campaign needed by Thermographic Methods to achieve the basic information to calibrate a local approach, the Strain Energy Density one. The proposed methodology has been satisfactorily validated by applying the calibrated local approach to foresee the fatigue behaviour of a vast experimental database, characterized by a variety of notched geometries, retrieved from literature.

5.1 Introduction

Stainless steel 304L is a low carbon variant of stainless steel 304. This material is widely used in a range of applications due to its excellent mechanical properties, corrosion resistance, and ease of fabrication.

The application of AISI 304L spans multiple industrial sectors. In the chemical and petrochemical industries, it is used for manufacturing tanks, pipes, and heat exchangers due to its resistance to corrosion from acids and chemical agents [112]. In the food industry, AISI 304L is employed for processing equipment, tanks, and surfaces in contact with food because of its chemical inertness and ease of cleaning [113]. In the biomedical field, it is used for surgical instruments, implants, and medical devices thanks to its biocompatibility [114]. In the marine industry, this steel is used for parts exposed to seawater due to its resistance to chloride-induced corrosion [115]. In the automotive industry, AISI 304L is utilized for various components, such as exhaust systems, engine parts, and tanks, due to its corrosion resistance, ease of fabrication, and robust mechanical properties [116].

Given the extensive use of AISI 304L in industrial applications, universities and research centres frequently receive requests from companies for the mechanical fatigue characterization of this material, which is crucial for designing machine components. The challenge lies in balancing the lengthy testing processes with the need for rapid and comprehensive results demanded by the industry.

Moreover, this material is often used to create components with complex geometries, such as tanks. These components may have large thicknesses and include notches (rivets, bolts, etc.) due to the necessity of joining. Under these conditions, in addition to the extended times required for the fatigue characterization of the base material, uncertainties arise from the presence of notches in thick sections where theoretical plane conditions are no longer applicable [117,118]. Another common issue is the insufficient number of samples available or obtainable by the company, which is inadequate for thorough fatigue characterization according to traditional guidelines. From an analytic point of view, the evaluation of the energetic field around the notch tip is used as a parameter for the estimation of the fatigue properties of a material by local approach such as the Strain Energy Method (SED) [107,108,119–123].

Over the years, researchers have improved the SED approach, providing advice and recommendations on its applicability[119], including the case of localized and generalised plasticity[108]. As noted by Foti et al.[122,123] for estimating the fatigue life of welded joints, the SED method has been proved to be consistent with the codes and, taking advantage of its low sensitivity to mesh refinement, it is possible to apply it through a free-

mesh procedure[121] that reduces time and computational resources also in case of complex models.

On experimental mechanics, the Thermographic Methods are strongly established approaches based on monitoring the temperature trend on the surface of a specimen during a mechanical test by using an infrared camera [70,99,100,104,106,124]. The advantage of these methods is the rapid fatigue characterisation of materials through uniaxial tensile and fatigue tests[124]. The field of application ranges from the most common engineering to the most innovative materials obtained through additive manufacturing[70,125].

This work, leveraging the authors' expertise in the Risitano's Thermographic Method and SED (Strain Energy Density), aims to provide designers with quick insights into the fatigue characteristics of AISI 304L in the presence of notches with thick sections and a very limited number of samples.

5.2 Experimental campaign and numerical simulations

5.2.1 Material properties and specimen's geometry

Experiments were conducted on AISI 304L specimens of two different geometries showed in Figure 5.1. A plain geometry (Figure 5.1a) was adopted to estimate the mechanical properties and the stress-strain curve of the material. A double -edge blunt V-notch geometry was adopted to estimate the fatigue life of a thick notched detail (Figure 5.1b). The opening angle for notch specimen was fixed to $2\alpha = 135°$, with a fillet radius $\rho = 2$ mm. The thickness of the plain and V-notch specimens was chosen equal to 10 mm to obtain a thick notched detail and the width is equal to 24 mm; hence, the nominal cross section was equal to 24x10 mm^2. The choice for an equal nominal cross section between plain and notched geometries was made to highlight only the influence of notch effect on the fatigue strength.

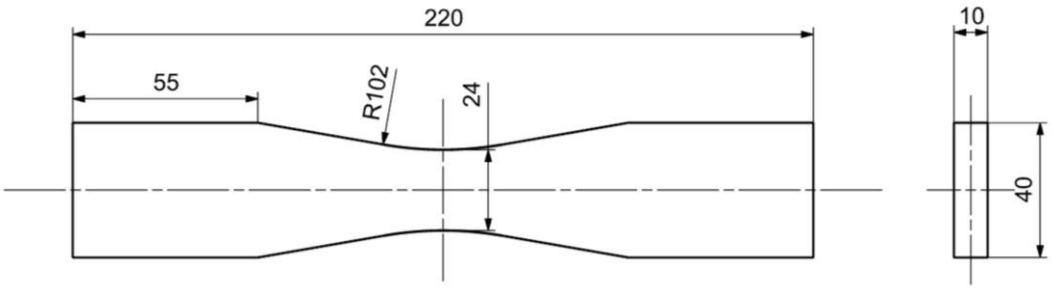

(a)

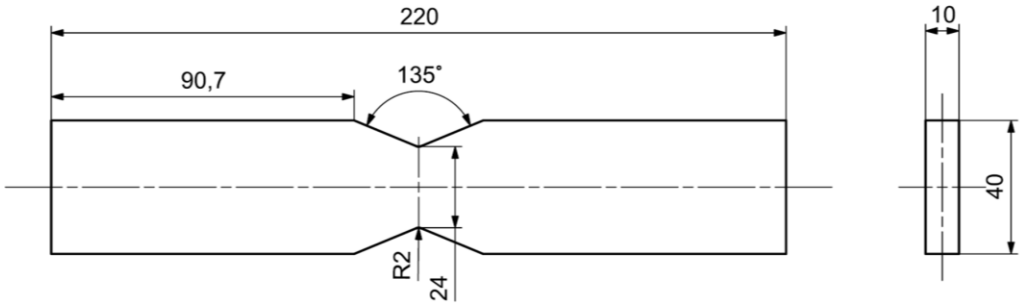

(b)

Figure 5.1: Geometry of the AISI 304L specimen: a) Plain b) V-notch (measures in mm).

Table 5.1 reports the average chemical composition of AISI 304L stainless steel obtained with the X-Ray Fluorescence (XRF) analysis with a SPECTRO instrument (AMETEK, Germany).

Table 5.1: Chemical composition of AISI 304L material (in wt. %)

Si	**Mn**	**Cr**	**Mo**	**Ni**	**Cu**	**Fe**
0.53	1.92	18.64	0.29	8.04	0.41	69.8

5.2.2 Mechanical tests

Static and fatigue tests were performed with a servo-hydraulic testing machine MTS 810, with a maximum load capacity of 250 kN, at the University of Messina. During the tests the specimen surface temperature was monitored by using the infrared camera FLIR, model A40, with a thermal sensitivity of 0.08 °C at 30 °C. Before each test, the surface of the specimen was painted with a thin layer of matte black paint, to increase its thermal emissivity (up to 0.98) and improve the quality of the emitted thermal signal. The image acquisition frequency of the infrared camera was set at 5 Hz for static tensile tests, while an image every 10 cycles was acquired during fatigue tests. All data results from the tests were processed using Matlab® software (MathWorks). Static tensile tests were conducted adopting stress rates within the range 2-6MPa/s to ensure adiabatic testing conditions; in this way, the specimen, due to its very small temperature gradient respect the environment, has not time to exchange energy. From the static tensile tests, the engineering stress, considering the nominal section of the specimen, and temperature trends over time were evaluated.

Fatigue tests were carried out using a sinusoidal stress wave with a zero-mean value (stress ratio R=-1) and a frequency of 5 Hz. The specimens were stressed in two different ways: one using a constant amplitude (CA) stress level and the other using a stepwise increase of the stress level every 10.000 cycles. These two approaches allow to estimate the S-N curve of the material in the traditional way and in a rapid way applying the RTM.

5.2.3 Literature data on AISI 304L

To compare the findings of this work with other results, the fatigue dataset has been extended with 100 fatigue tests carried out on AISI 304L in various literature works [126–129]. It is worth underling that the criterion chosen to select the fatigue data in literature relied solely on the declared nominal material. On the other hand, it must be considered that, although these tests are carried out on the same nominal material, i.e. AISI 304L, there could still be a variability on the materials themselves; such a variability can indeed be seen through the various Young's Modulus reported in these works for the same nominal material.

Fatigue data, together with the main geometrical features of the specimens retrieved from literature are reported in Figure 5.2. This set of specimens is composed by dogbone-shaped specimens and notched plates (V and U-notches and hole) with a thickness equal to 6 mm, and hourglass shaped specimen with a diameter of 3 mm.

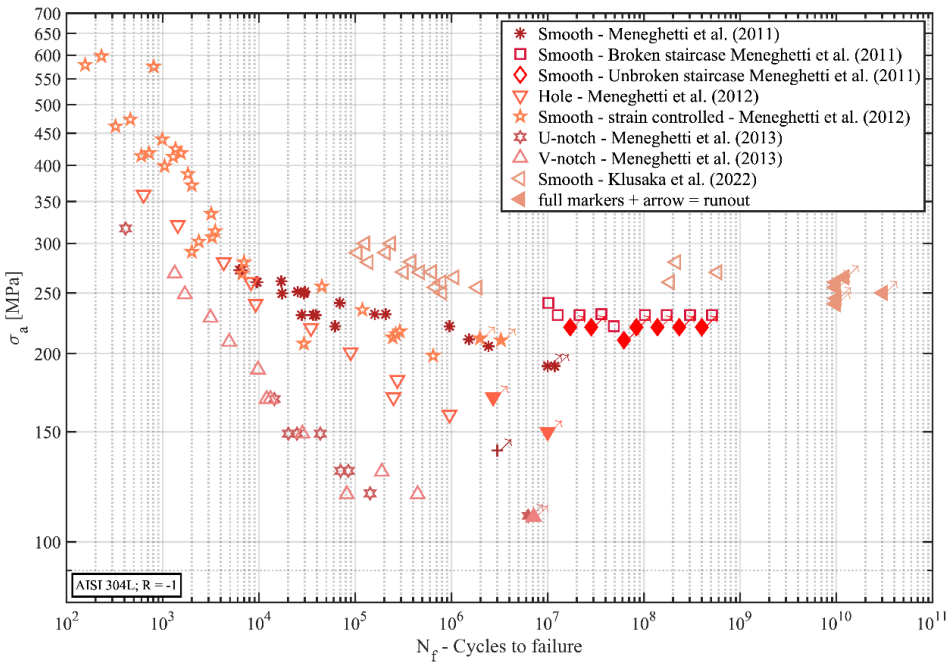

(a)

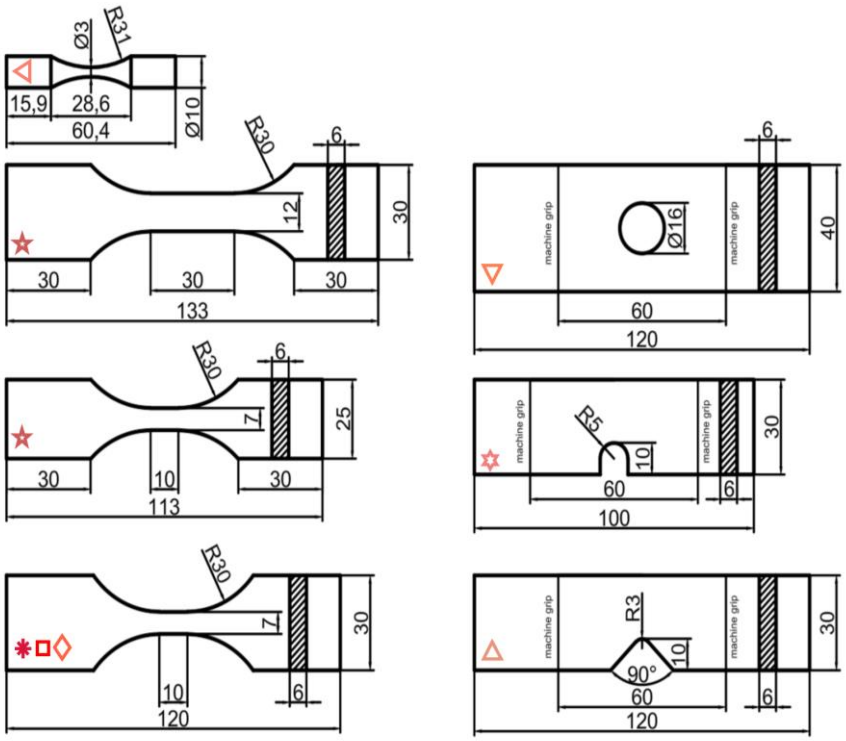

(b)

Figure 5.2: a) Fatigue dataset considered; b) geometry of the specimens with indication of the markers adopted in the graphs (measures in mm).

5.2.4 Numerical simulations

The presence of thick specimens with a quite ductile material required special attention in the estimation of the acting stresses, so it is worth noting a few considerations.

Performing 2D simulations for a thin plate, the influence of the thickness can be neglected, and the plane stress hypothesis is valid. For a thick plate the stress state changes also along the plate thickness and the third component of the stress must be considered, so the plain strain condition became dominant.

When considering a notched element, it is known that the effect of the stress intensification is proportional to the K_t factor, defined as the ratio between the elastic stress at the notch tip and the nominal stress, i.e. the average stress applied on the resistance section. Under fatigue condition, the mitigation of the effect lead by the stress gradients at notches is quantified by the fatigue notch factor K_f, lower than K_t, and usually evaluated between 10^6 and 10^7cycles. This factor varies according to the life of the material and is influenced by several effects such as the dimension of the notch radius and the reversed yielding effect.

For this reason, the authors performed preliminary 3D simulations campaign not to neglect the influence of thickness and to evaluate the fatigue notch factor, K_f^*, in case of completely reversed loading.

The simulations were realized using Ansys APDL finite element software, adopting a mapped volume mesh with 20-node hexahedra SOLID186 elements. Only one-eighth of geometry specimen was modelled, taking advantage of his symmetry planes. The mesh size varies from a minimum of 0.2 mm near the notch (Figure 5.3b) to a maximum of 6 mm at the furthest point. The mesh strategy was inspired by the study by Cichański [130]. The material behaviour was defined using an isotropic multilinear plasticity model through the data obtained from a static tensile test (cap. 5.3.1). From each simulation the average plastic stress was evaluated for the different nominal stress applied.

A second simulation campaign was performed to evaluate the averaged SED near the notch tip adopting a 2D elastic model for the various notch geometries considered (see Figure 5.1b and Figure 5.3).Whenever possible, the symmetry of the geometry have been exploited to reduce the computational and time effort.

A mapped mesh with 8-nodes quad and 6-nodes tria PLANE183 elements was adopted under the hypothesis of plane strain condition. As an example, the adopted mesh with the symmetric boundary condition and the applied tensile load on a quarter of V-notched specimen is showed in Figure 5.3a. The concentration key point technique was applied to achieve a proper mesh near the notch tip, where the element size reaches 0.025 mm and gradually becomes larger up to the distance of 3 mm. It must be highlighted that, although the low mesh sensitivity of the method being the SED parameter evaluated directly from the displacement field [131], the mesh size at the notch tip had to be fine enough to meet the conditions defined in [132,133]. Indeed, having to carry out a parametric study to calibrate the method, i.e. determining the value of R_0, for the analysed material, the averaged SED had to be firstly evaluated for different values of the control volume characteristic length. Under the linear elastic regime hypothesis, the averaged SED value has been calculated applying a traction load in the grip section resulting in a nominal stress at the net cross section of 1 MPa for R_0 ranging from 0.1mm up to 3mm with a step of 0.01mm. Therefore, the mesh size near the notch tip must be equal to at least ¼ of the minimum control volume radius considered according to [133]. To estimate the SED value at any other stress value, under the linear elastic hypothesis, the following equation was adopted:

$$\Delta W = W_{1MPa,R_0} \cdot \Delta\sigma^2 \cdot c_w \quad (5.1)$$

Where W_{1MPa,R_0} is the value of SED with the application of the nominal stress of 1 MPa at a given R_0, $\Delta\sigma$ is the value of the applied stress to be referred to, and the term c_W depends on the stress ratio adopted.

Figure 5.3c shows a detail of the mesh around the notch tip with the mesh inflation caused from the adoption of the concentration key point technique. For area of the specimen far away from the notch tip, an element dimension of 0.5 mm was used with a free mesh method.

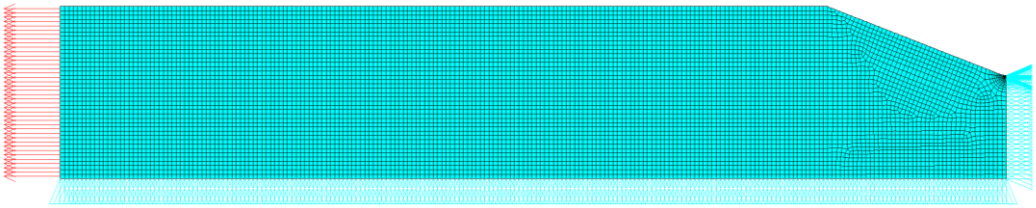

(a)

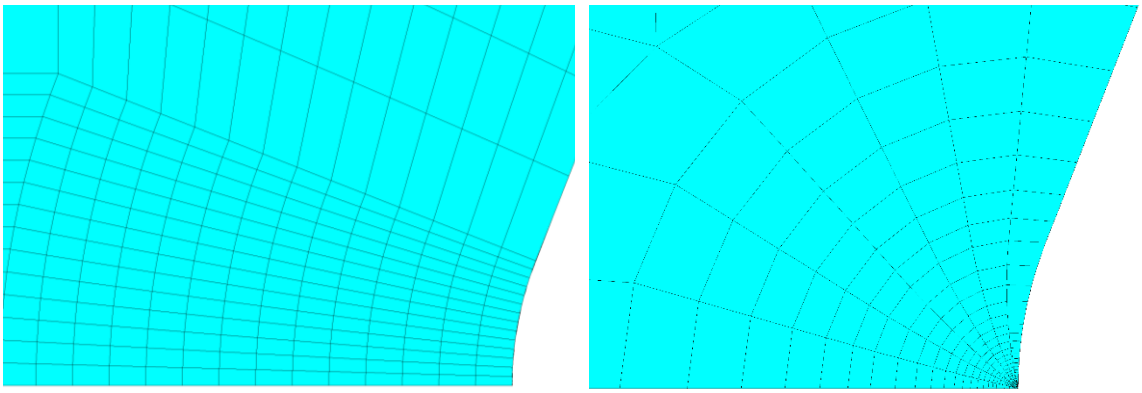

(b) *(c)*

Figure 5.3: 2D FEM model with symmetric boundary conditions and tensile load: a) Quarter of the V-notch specimen b) Detail of the mesh near the notch tip for elasto-plastic simulations; c) Detail of the mesh near the notch tip for SED simulations.

5.3 Results and discussion

The experimental test campaign has been performed on AISI 304L. Static tensile tests have been carried out monitoring the temperature evolution of the specimen to find the first

damage within the material applying the STM. A series of stepwise fatigue tests have been performed to find the fatigue limit and the fatigue life of the material with few specimens and in short amount of time, applying the RTM. Finite element simulations have been performed to investigate the notch effect on thick specimen and, finally, the SED method was applied to summarize the fatigue life of the AISI 304L with several plain and notched configurations. It is worth noting that, in this phase, the Thermographic Methods allow a rapid estimation of the control volume radius, instead of making a long test campaign.

5.3.1 Mechanical characterization of AISI 304L

A preliminary tensile test campaign has been performed on two plain specimens, to retrieve the mechanical properties of the AISI 304L under study. The tensile tests have been performed under displacement control with a velocity of 5 mm/min and during the test an extensometer with an initial gauge length of L_0= 25 mm has been adopted to estimate the stress-strain curve of the steel. The yielding stress has been estimated considering a residual plastic deformation of 0.2%; the ultimate stress as the maximum stress achieved by the specimen and, finally, the Young's Modulus with a linear regression according to ASTM E111.

Table 5.2: Mechanical properties of AISI 304L under study.

No. Specimen	**σ_y [MPa]**	**σ_U [MPa]**	**E [MPa]**
S-PL-01	395	612	257240
S-PL-02	439	622	243890
Avg.	417	617	250565
Std.Dev.	31	7	9440

The stress-strain curve of the second specimen has been reported in Figure 5.4.

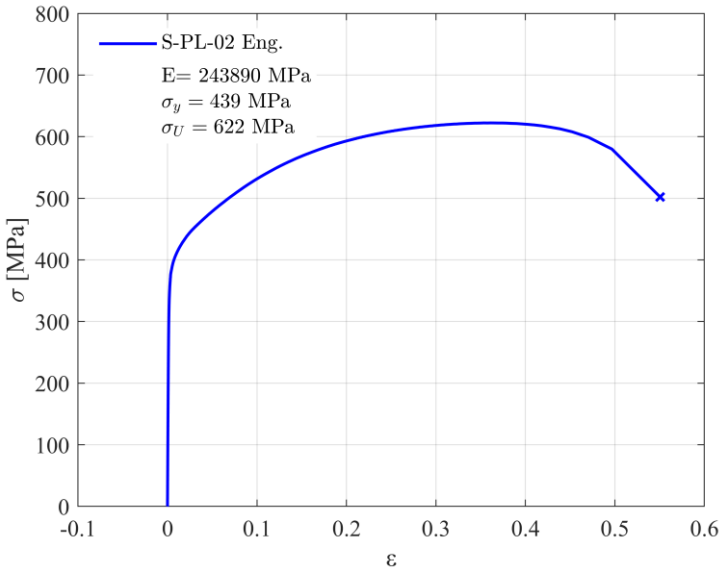

Figure 5.4: Stress-Strain curve of AISI 304L under study (specimen S-PL-02).

5.3.2 Estimation of the limit stress during static tensile test.

Tensile test can be adopted to obtain information regarding the damage state within the material. The adoption of the temperature as a third parameter, in adjunction to stress and strain, can indicate the transition from a stress state without any plasticity toward a stress state where some crystals of the material experience irreversible plastic deformation, with a consequent release of heat. It is possible to assess a corresponding macroscopic stress level where this happens, i.e. the limit stress σ_{lim}, and, according to Risitano [134], if that stress level is applied to the material in a cyclic way, it will experience fatigue failure.

Static tensile tests have been conducted on thick AISI 304L specimen in the plain and V-notched configuration. The maximum temperature of a rectangular spot has been measured in the gauge length for the plain geometry; while near the notch tip for the V-notch geometry (Figure 5.5a). The thermal data used is for the region of interest (ROI) with the highest temperature over time, corresponding to the notch where the crack originates and propagates. To observe the limit stress, a proper stress rate must be adopted. This is necessary because, if it is too slow, the specimen can exchange heat with the surrounding environment; while, if it is too fast, the cooling phase of the specimen is very short, and it is followed by a sudden increase of the temperature starting at the yielding stress of the material. For the three tensile tests on the plain specimens, stress rates of 2 MPa/s and 4 MPa/s have been adopted.

The raw temperature signal for the plain specimens S-PLAIN-03, referred to the temperature of the specimen at the beginning of the test, has been reported in Figure 5.5b versus the

applied stress and testing time. It is possible to observe a first cooling phase with an initial slope, followed by a second cooling phase with a flatter slope compared to the first one. When the yielding stress of the material is reached, the temperature signal begins to rise, up to the failure of the specimen. To assess the limit stress, the temperature signal from the beginning of the test up to the yielding stress has been modelled with a bilinear model composed by n temperature points (see the schematic representation reported in Figure 5.5c). Linear regressions of the experimental temperature points (ΔT_j) vs. time from the beginning of the test up to the i-th intersection point ($\Delta T_{1,i}$ data set, $t \leq t_{int\,i}$) and from the i-th up to the yielding point ($\Delta T_{2,i}$ data set, $t > t_{int\,i}$) have been performed obtaining the predicted j-th temperature ($\widehat{\Delta T_{j,i}}$) for the i-th iteration (Equation (5.2), with $t_{int\,i}$ the i-th intersection time, m the angular coefficient and q the intercept). An iterative approach evaluates the limit stress (Equation (5.3)) by maximizing the coefficient of determination R^2 for the bilinear model (Equation (5.4)) of the temperature signal considering the predicted j-th temperature ($\widehat{\Delta T_{j,i}}$) for the i-th iteration and the average temperature value of the whole temperature set ($\overline{\Delta T} = \frac{1}{n}\sum_{j=1}^{n} \Delta T_j$).

$$\widehat{\Delta T}_{j,i} = \begin{cases} \Delta T_{1,i} = m_{1,i}t + q_{1,i}, & t \leq t_{int_i} \\ \Delta T_{2,i} = m_{2,i}t + q_{2,i}, & t > t_{int_i} \end{cases} \tag{5.2}$$

$$\sigma_{lim} = \sigma_{lim,i}\ with\ i:\ R^2 = \max(R_i^2) \tag{5.3}$$

$$R_i^2 = 1 - \frac{\sum_{j=1}^{n}\left(\Delta T_j - \widehat{\Delta T}_{j,i}\right)^2}{\sum_{j=1}^{n}\left(\Delta T_j - \overline{\Delta T}\right)^2} \tag{5.4}$$

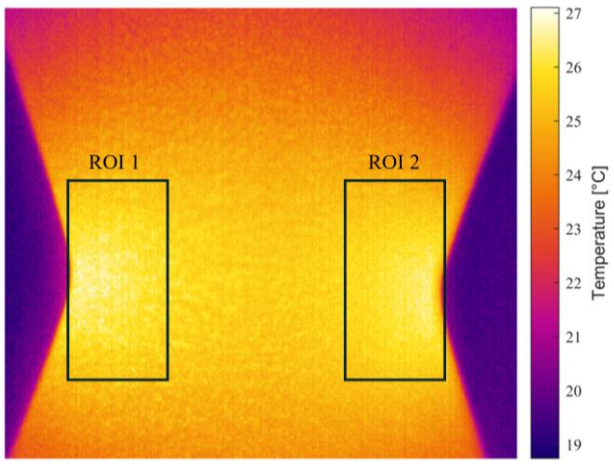

(a)

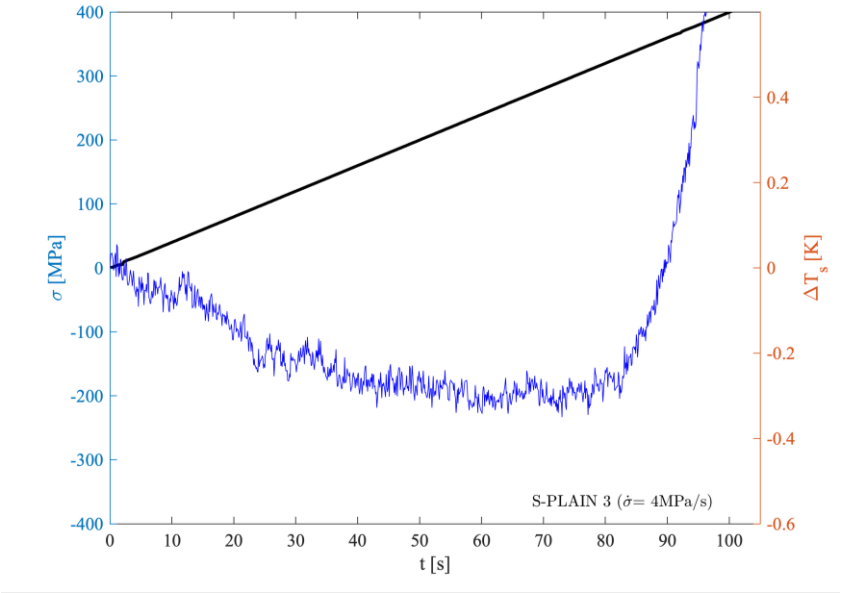

(b)

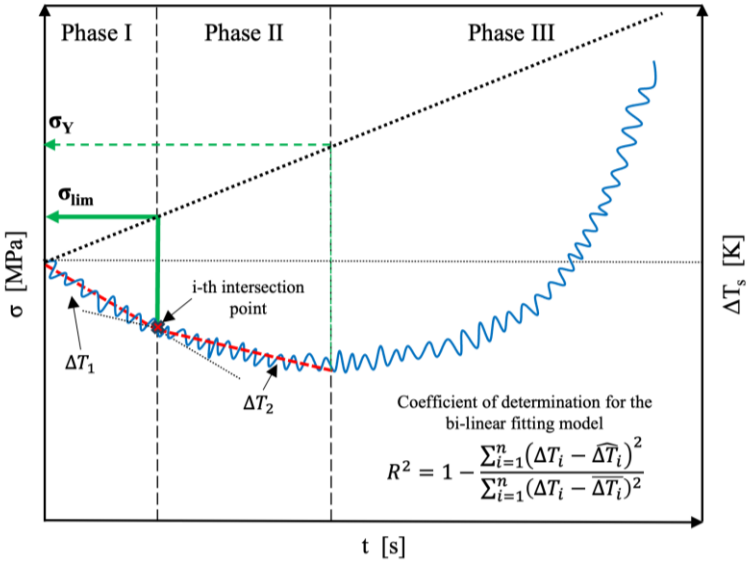

(c)

Figure 5.5: a) Measure spot on plain and V-notch specimens. The maximum temperature value has been recorded; b) Temperature evolution during a static tensile test on plain AISI 304L specimen. c) Bilinear mathematical model for raw temperature data fitting. The maximization of the R^2 leads to the limit stress evaluation.

In Figure 5.6, the temperature trends of all the three tested plain specimens have been reported, focusing just on Phase I and II of the temperature signals. For the S-PLAIN-01 specimen (Figure 5.6a), the stress rate of 2 MPa/s leads to a noisier temperature signal compared to the other two tests performed at 4 MPa/s; however, it is possible to assess the

limit stress. The iterative algorithm allows to assess the limit stress, i.e. the change in the slope of the temperature signal, at a macroscopic stress level equal to 190.5 MPa. The different adopted stress rates lead to different values of the maximum coefficient of determination, as can be noted in Table 5.3. The lower the stress rate, the worst the coefficient of determination and the noisier the temperature signal. The minimum temperature decrement is within the range of 0.2-0.5 K. For the plain material, the average limit stress is equal to $\sigma_{lim\ Plain}$= 197.5±6.1 MPa.

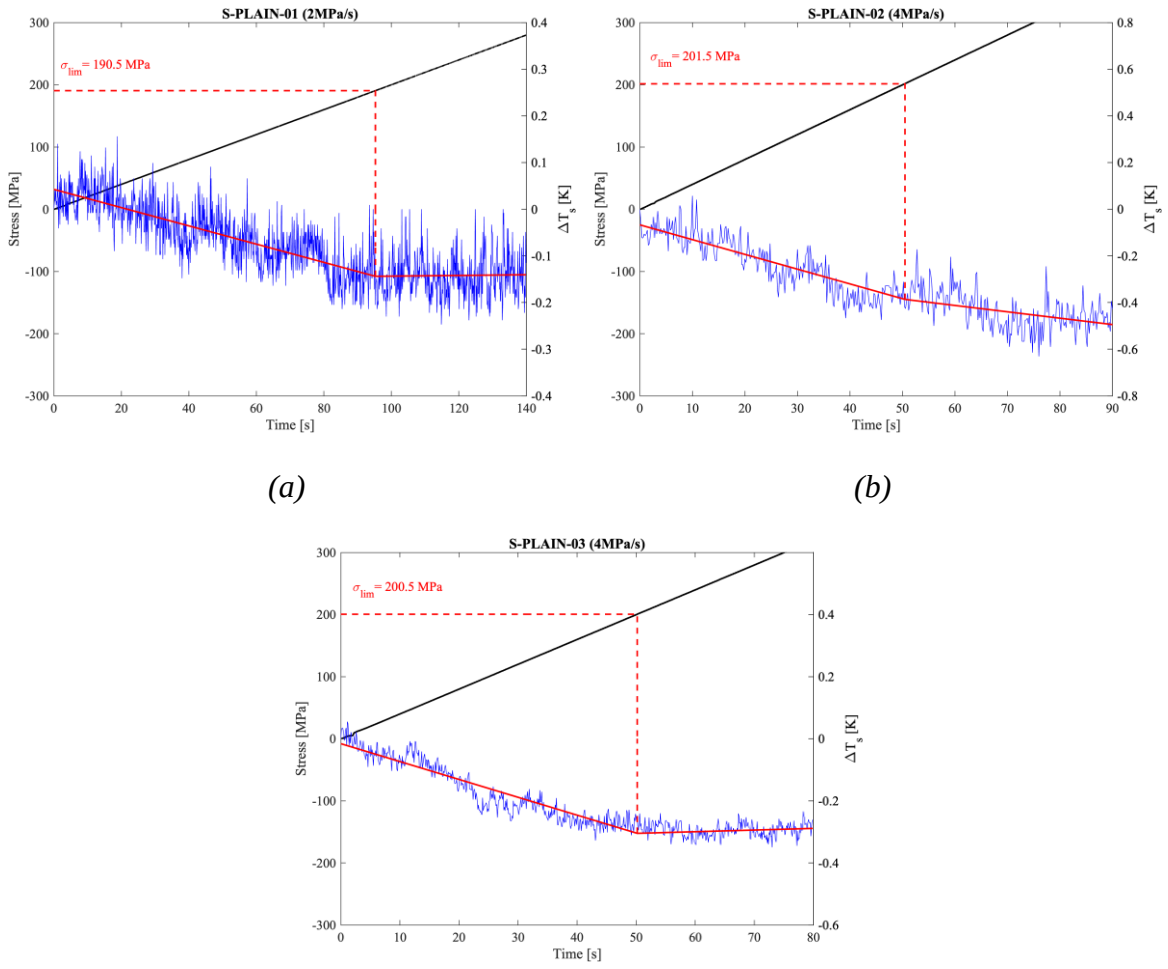

Figure 5.6: Temperature trend vs. applied stress level and time for plain AISI 304L specimens. Bilinear trend fitted on raw temperature data. The limit stress is evaluated as the knee of the two regression lines.

Table 5.3: Limit stress and maximum coefficient of determination (R^2) for the static tensile tests on plain AISI 304L specimens. The R^2 has been obtained by iterative estimation on the bilinear model.

	$\dot{\sigma}$ [MPa/s]	σ_{lim} [MPa]	R^2_{max}
S-Plain-01	2	190.5	0.6705
S-Plain-02	4	201.5	0.8041
S-Plain-03	4	200.5	0.9143
Avg.		197.5	
Std. Dev.		6.1	

By monitoring the superficial temperature near the notch tip for blunt V-notched specimens, it is possible to assess a limit stress. For this geometry, after some trials, a stress rate of 6 MPa/s has been adopted to highlight the bilinear trend of the temperature signal. The temperature trends for the V-notch specimens have been reported in Figure 5.7. Bilinear model has been applied to the raw temperature data and the coefficient of determination has been estimated iteratively, leading to the best estimation of the limit stress. For the first specimen it is difficult to observe clearly the bilinear trend, because the difference in the slopes between phase I and II is not so pronounced. However, the iterative algorithm allows to estimate the limit stress at σ_{lim}= 158.4 MPa. The other two tests have a more marked bilinear trend. The estimation of the limit stress, in these two cases in equal to 149.4 and 147.5 MPa. The minimum temperature decrement is within the range of 0.2-0.4 K, with a coefficient of determination higher than 0.82. For the V-notch specimens the average limit stress is equal to $\sigma_{lim\ V\text{-}notch}$= 151.8±5.8 MPa.

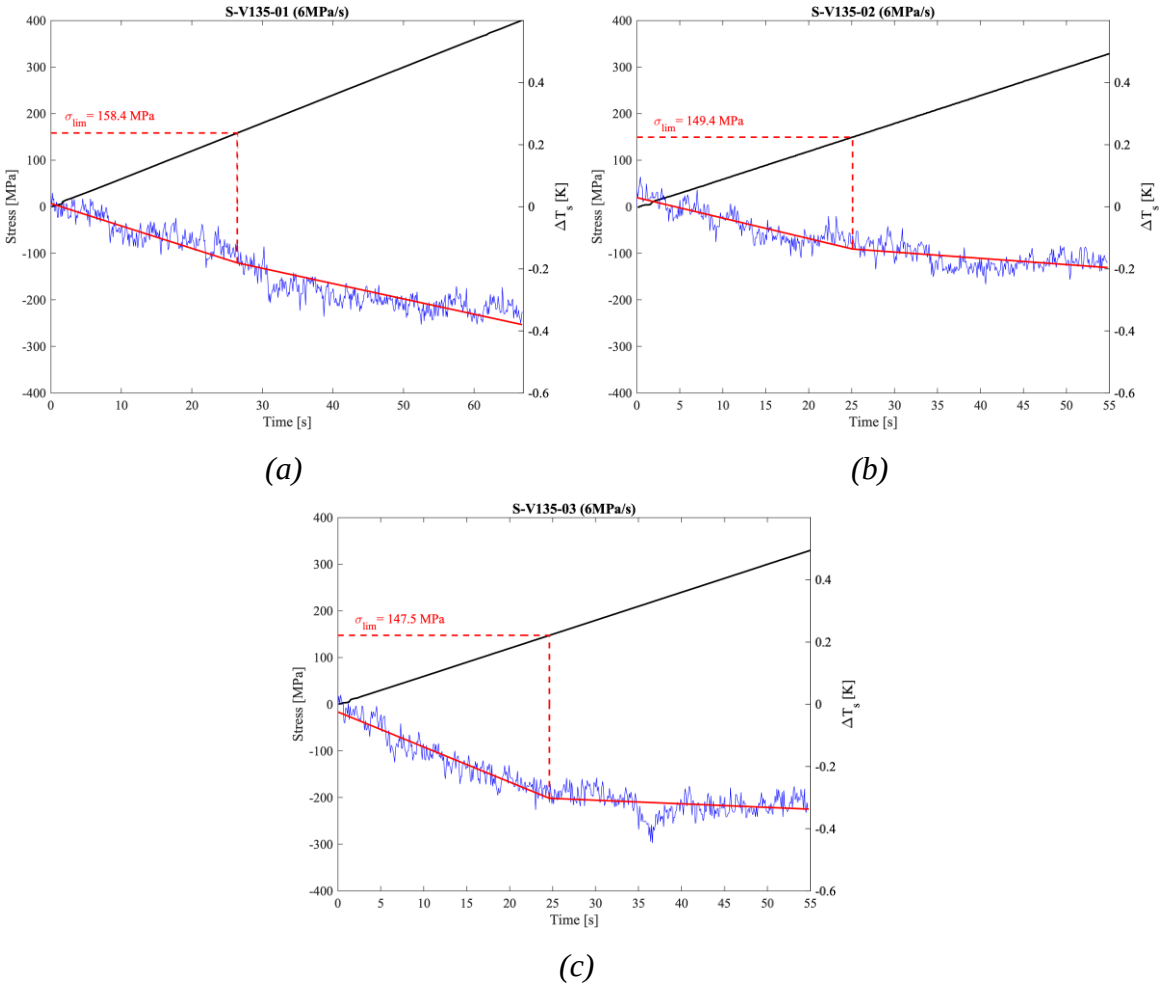

Figure 5.7: Temperature trend vs. applied stress level and time for V-notch AISI 304L specimens. Bilinear trend fitted on raw temperature data. The limit stress is evaluated as the knee of the two regression lines.

Table 5.4: Limit stress and maximum coefficient of determination (R^2) for the static tensile tests on V-notch AISI 304L specimens. The R^2 has been obtained by iterative estimation on the bilinear model.

	$\dot{\sigma}$ [MPa/s]	σ_{lim} [MPa]	R^2
S-V135-01	6	158.4	0.9073
S-V135-02	6	149.5	0.8298
S-V135-03	6	147.5	0.8939
Avg.		151.8	
Std. Dev.		5.8	

5.3.3 Fatigue strength estimation with RTM

For the estimation of the fatigue life, two stepwise stress-controlled fatigue tests were performed for each type of geometry. The temperature variation of the specimen's surface during the test was monitored with an infrared camera on area where fatigue failure happens.

The plain specimens were tested at the frequency of 5 Hz with a fully reversed load (R= -1) starting from a stress level of σ_a= 100 MPa, increasing the stress step of 10 MPa every $10x10^3$ cycles for one test and every $20x10^3$ cycles for the other, up to the specimen failure.

In Figure 5.8 are reported the stabilization temperature versus the number of cycles and the applied stress level for the plain AISI 304L specimens. The stabilization temperatures are evaluated respect the initial temperature assumed by the specimen, i.e. at a number of cycles equal to zero, and they are evaluated for each stress level considering temperature data between 30% and 90% of the temperature signal in the stress level. The average values of the stabilization temperature with one standard deviation are reported in the Figure 5.8.

Comparing the two graphs, the Energy Parameter Φ, evaluated as the subtended area of the temperature curve respect the number of cycles, has the same value; hence, there is a very good match in terms of dissipated energy during the fatigue test of both specimens. Stress levels from 100 MPa to 160MPa have shown noisy signal or no relevant increase of the temperature (below 2.5 K). Significative increments of the temperature signal can be observed for stress levels of about 170-180 MPa (above 3 K); then temperature continues to increase until the specimen failure. The maximum temperature reached by the specimens is 464.45 K and 455.54 K, respectively for test 1 and test 2.

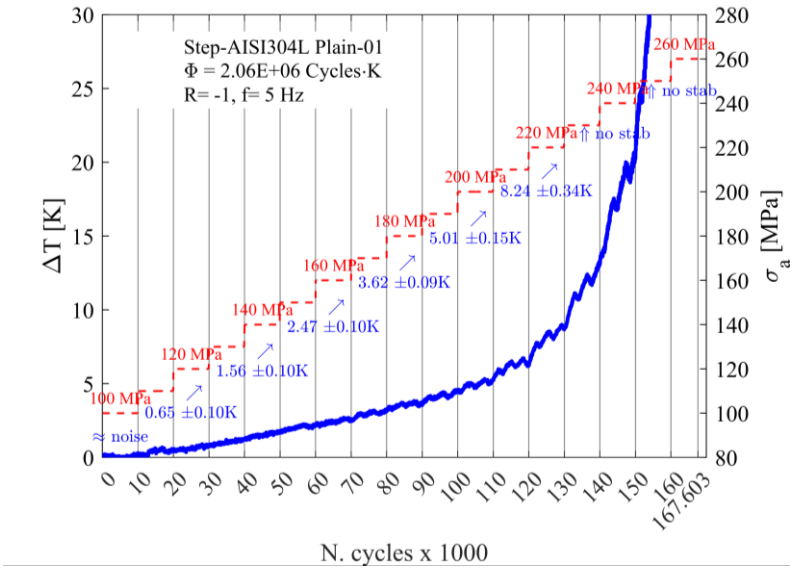

(a)

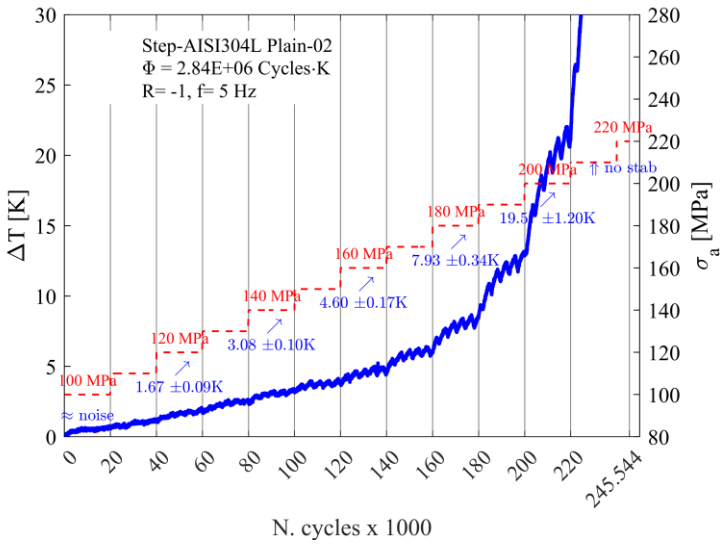

(b)

Figure 5.8: Stepwise fatigue tests on plain AISI 304L specimen a) Test 01; b) Test 02.

To assess the fatigue strength, the stabilization temperatures have been reported vs. the applied stress levels in Figure 5.9. As is possible to observe, when the applied stress increases, the stabilization temperature also increases, as expected; however, at a certain stress level, there is a knee, and the temperature increments become more marked. By fitting the data with two regression lines, the first below the knee region (ΔT_1, from 120 to 190 MPa), the latter after the knee region (ΔT_2, from 200 to 220 MPa), the fatigue limit, $\sigma_{0\,RTM}$, can be estimated from the intersection of the two regression lines. The results show an average fatigue limit value of $\sigma_{0\,RTM\,Plain}$= 193.2 ± 4.4 MPa for the plain specimens (Figure 5.9).

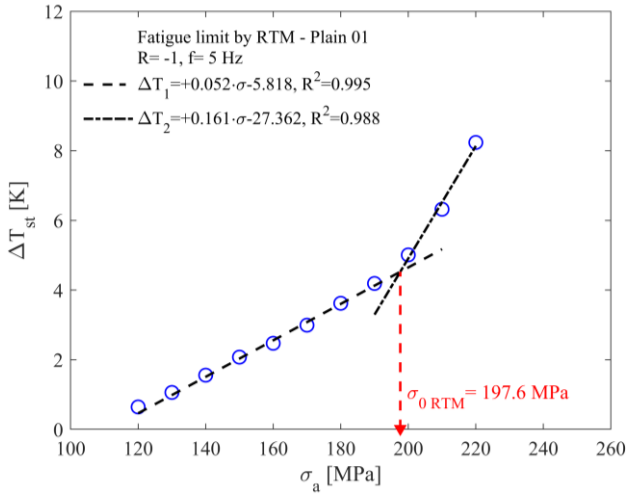

(a)

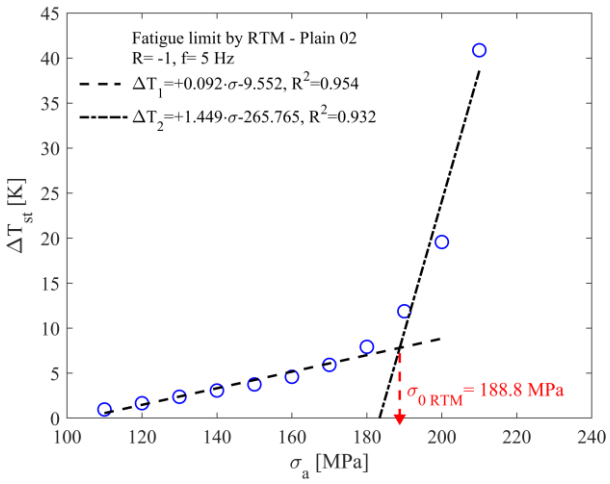

(b)

Figure 5.9: Fatigue limit estimation by RTM on AISI 304L plain specimen a) Test 01; b) Test 01.

The same testing procedure has been adopted for V-notched specimens at the same load frequency of 5 Hz and stress ratio (R= -1), increasing the load step of 10 MPa every $10x10^3$ cycles.

The temperature behaviour for the notched specimen is very similar to that of the plain specimens. The two stepwise tests for notched specimens were reported in Figure 5.10. The Energy Parameter from the two tests is similar; however, it is one order of magnitude lower than the plain specimen, even if the cross section is the same. The shorter fatigue life and the lower Energy Parameter can be addressed to the presence of notch. Figure 5.11 shows the result of the fatigue limit estimation by RTM. Even in this case there is a knee region, and it is possible to make two linear regressions below (ΔT_1, from 120 to 170 MPa) and above (ΔT_2, from 180 to 210 MPa) the knee. An average value of $\sigma_{0\ RTM\ Vnotch}$= 164.8 ± 2 MPa turns out to be lower, as expected, due to the presence of the V-notch which is known to affect the fatigue life of the component.

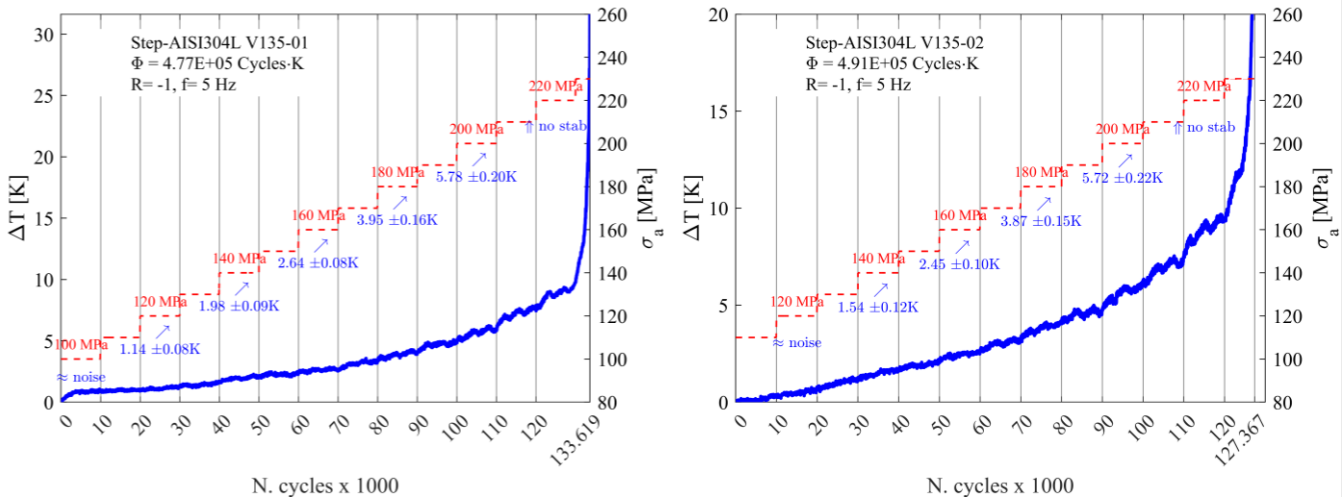

(a) *(b)*

Figure 5.10: Stepwise fatigue tests on V-notch AISI 304L specimen a) Test 01; b) Test 02.

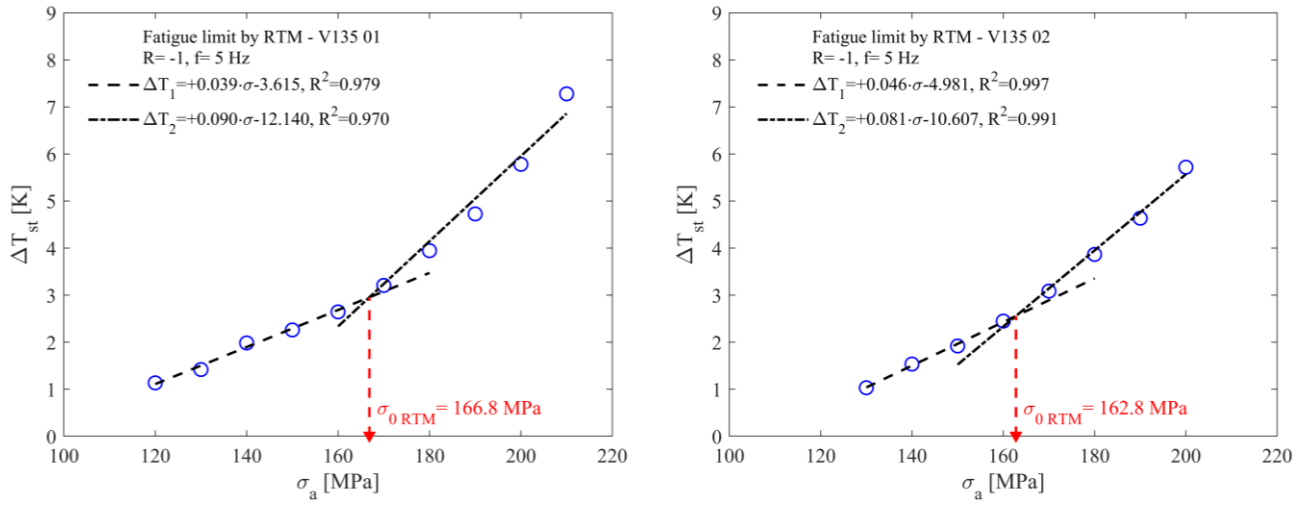

(a) *(b)*

Figure 5.11: Fatigue limit estimation by RTM on AISI 304L V-notched specimen a) Test 01; b) Test 02.

To validate the fatigue limit estimations by RTM, a series of constant amplitude stress-controlled fatigue tests were performed at stress levels near the estimated fatigue limit, imposing the run out, i.e. no fatigue failure occurs, at a number of cycles equal to $2x10^6$ cycles.

For the plain specimens, run-outs have been reached at stress levels below 180 MPa ($N \geq 2.14 \times 10^6$), which is in agreement with the prediction of the STM and RTM (Table 5.5). For V-notched specimens, run-outs have been reached up to 140MPa ($N \geq 2.99 \times 10^6$) and have shown failure at 160 MPa ($N_f = 5.30 \times 10^5$) and 180 MPa ($N_f = 2.16 \times 10^5$), confirming the prediction of the STM and RTM. It is to point out that the required time to obtain information regarding the fatigue limit of AISI 304L is dramatically reduced adopting the Thermographic Methods; indeed, just few minutes are necessary to retrieve the limit stress (≈5 min) with STM and few hours to retrieve the fatigue limit with the RTM (≈8 h). These values allow engineers to proceed with an early design of the mechanical component against fatigue failure. On the other hand, the required time per test to obtain information on the fatigue limit throughout constant amplitude fatigue tests and staircase procedure are very long and with a difficult evaluation of the real standard deviation[135–137], which can lead to an excessive overestimation of the fatigue strength, hence an overestimation of the reliability of the component[138].

Table 5.5: Fatigue limit estimation comparison between STM, RTM and constant amplitude fatigue tests.

	Plain	V-notch	Avg Test duration
σ_{lim} [MPa]	197.5±6.1	151.8±5.8	~5 min
$\sigma_{0\,RTM}$ [MPa]	193.2±4.4	164.8±2.0	~8 h
CA at run-out	≤180	≤140	~111 h

From the stepwise fatigue tests performed on AISI 304L specimens it is possible to predict the fatigue life in terms of applied stress (σ_a) vs. number of cycles exploiting the constancy of the Energy Parameter. Indeed, this parameter is almost constant for plain and V-notch specimens, once that stress ratio and test frequency are fixed. According to equation (3.4), by dividing the Energy Parameter for the i-th stabilization temperature recorded during the stepwise fatigue test, it is possible to predict the number of cycles to failure for the specimen. Having known the applied stress level, it is possible to obtain the S-N curve of the material (for plain specimens) or for the component (notched specimen).

In Figure 5.12, are reported the predicted fatigue life for AISI 304L by RTM (blue markers) with the prediction of other researchers (red markers) and CA fatigue test (full blue markers with arrow). The points predicted by RTM fall near other literature data; in particular, plain specimens are consistent with the value of strain-controlled tests [127] and smooth specimen [128]. This last dataset shows runout at a stress level equal to 190 MPa, which is consistent with the findings of STM and RTM.

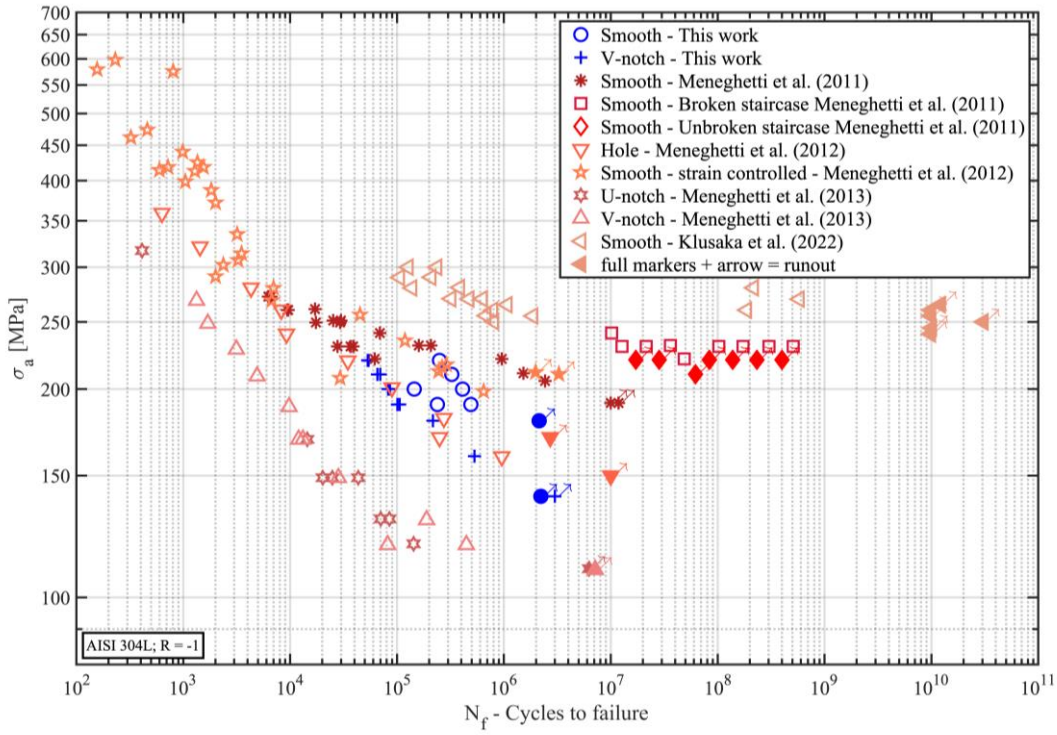

Figure 5.12: S-N curve for AISI 304L predicted by RTM and comparison with literature data.

On the other hand, V-notch specimens show early failures compared to plain specimens and their trend follows the one of hole specimen [128].

5.3.4 Summarize fatigue life with Strain Energy Density

The averaged Strain Energy Density method has been chosen in this work as design approach for the fatigue assessment of notched components; hence, in the following, we report the comparison between the calibration of the method, for the material AISI 304L, both starting from the experimental values evaluated through the Thermographic Methods and through a much more larger fatigue database retrieved from data available in literature.

The novelty of the present work is the adoption of the Thermographic Methods to retrieve all the necessary parameters that allow the SED method calibration.

Two different ways have been adopted to calibrate the SED method through the fatigue data presented in this work and retrieved from literature.

The first methodology, shown in Figure 5.13, has been proposed by Milone et al [139], and consists in evaluating the averaged SED curve vs the number of cycle for different values of the stress ratio R; the calibrated value of the control volume radius R_0 is the one that minimize the scatter index of the fatigue curve in terms of SED, $T_{\Delta W}$. The fatigue dataset collected in the present paper resulted in a control volume radius of R_0= 2.32 mm considering the fatigue data having failure between 10^4 and $2x10^6$ cycles. The determined fatigue scatter band is characterized by a stress-equivalent scatter index of $T_{\Delta\sigma_{eq}} = 1.63$ considering the fatigue curve having a probability of survival (P.S.) of 2.3% and 97.7%.

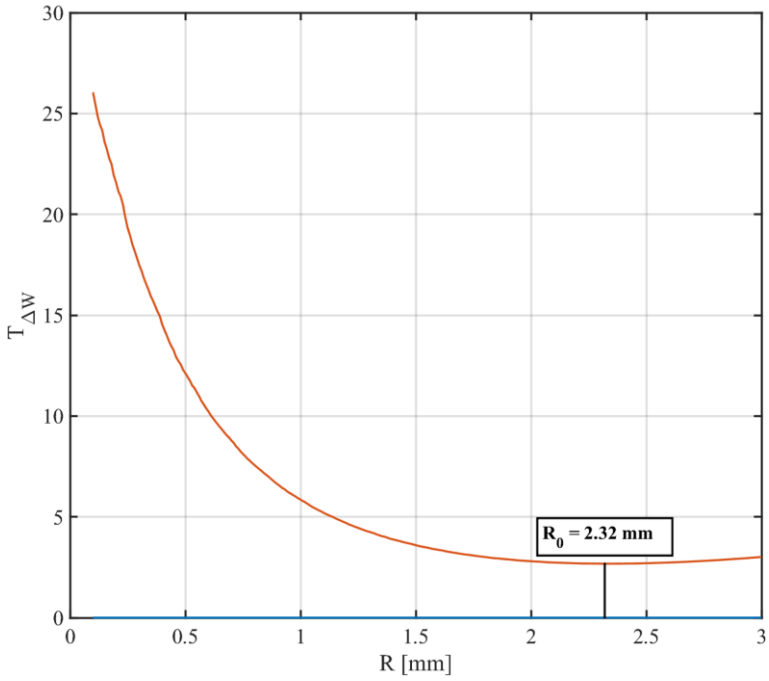

(a)

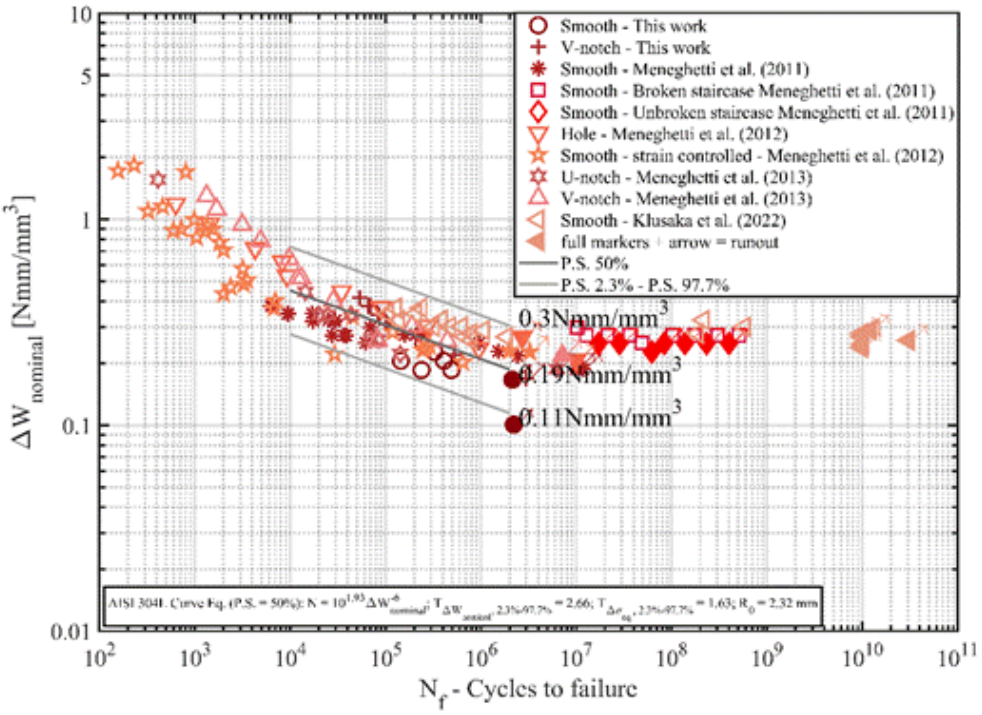

(b)

Figure 5.13: a) Scatter index vs control volume radius curve with R0 evaluated as the one minimizing the scatter index b) Nominal averaged SED vs. number of cycles to failure.

The second methodology adopted in the present paper consist in a procedure similar to the conventional one of the SED method that equates the averaged SED of two different geometries at $2x10^6$ cycles; however, in such a case, the limit stress derived through the STM method for the two different geometries have been considered to impose the equivalence of the averaged SED value of the two different geometries considered.

The calibrated value is equal to $R_0 = 2.28\ mm$, as shown in Figure 5.14a. The employment of these R_0 value to summarise the fatigue data in an averaged SED vs number of cycles data, shown in Figure 5.14b, resulted in a fatigue scatter band very similar to the one obtained through the other procedure; this is due to the fact that the R_0 value, determined through the limit stress achieved applying the STM method, is very close to the one achieved considering the procedure presented by Milone et al[139] . On the other hand, regardless of the slightly different R_0 value, the limited difference between the SED vs number of cycle curve determined according to the different procedure could be also evident through Figure 5.13a in which it can be noticed that the scatter index is not changing abruptly around $R_0 =$

$2.32mm$, the value minimizing the scatter index according to Milone et al [139] methodology.

It must be noted, on the other hand, that the variability in the limit stress determined by the STM method may result in an R_0 value ranging from about 1.9 mm to 2.9 mm depending on the smooth and V-notch tests considered. However, it is worth noting that, through the STM method, the R_0 calibration is possible with an already high accuracy considering only six static tests, three for each geometry, while the other methodology available in literature would need at the least two fatigue curves, one for a notched geometry and one for a smooth geometry, with almost thirty fatigue tests to ensure the statistical validity of the determined fatigue curves (15 specimens for each condition) and as a consequence of the R_0 value.

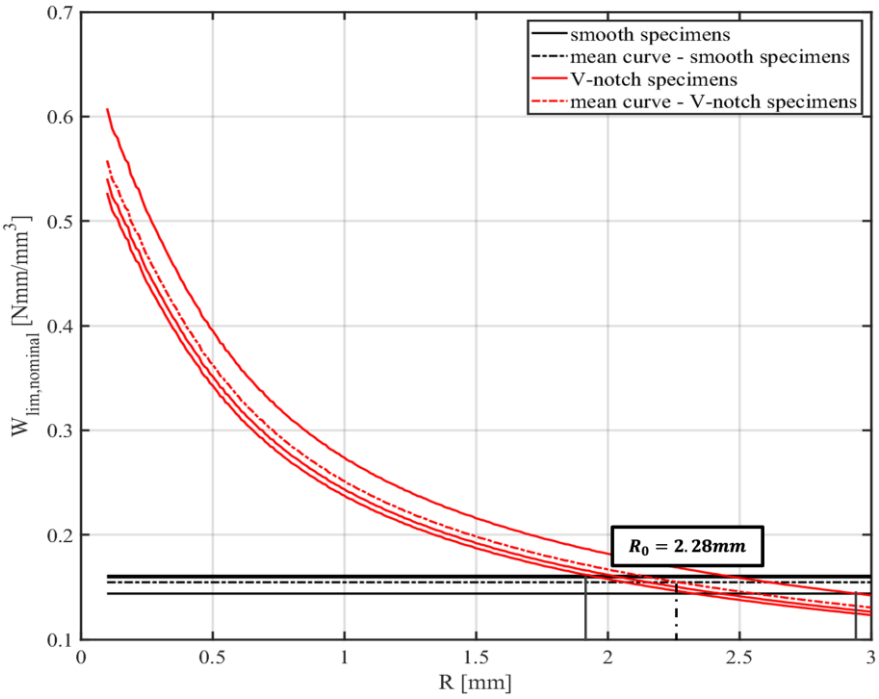

(a)

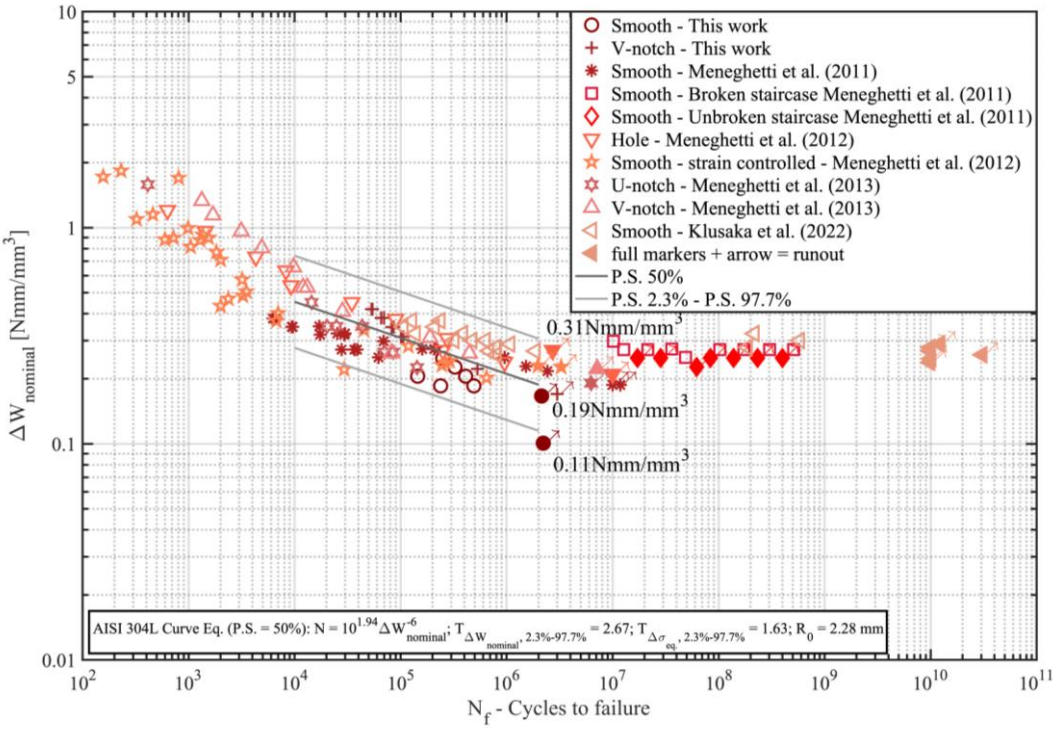

(b)

Figure 5.14: a) R_0 evaluation considering the limit stress determined through the STM method; b) SED data summary considering the R_0 value determined through the STM method.

It is worth highlighting that the high value of the control volume radius achieved, compared to other materials [140], can be justified by the high plasticity at the notch tip and reduced notch effect for AISI 304L, thus, the SED method has been applied in an unconventional way being the conditions for linear elastic fracture mechanics not accomplished; nevertheless, the achieved results, considering also the numerosity of the experimental fatigue data considered, lead to satisfying results.

5.3.5 Notch effect in fatigue life

For ductile steels, the reversed yielding effect and possible presence of plasticity near the notch tip become more predominant at higher stress and short fatigue life; indeed, it can happen that the ratio between the plain and notched fatigue strengths assumes value below K_f, defined as the ratio between the fatigue limit of the plain specimen and the notched one. It is possible to define an effective fatigue notch factor K_f^* that varies according to the life

of the specimens, due to the plasticity at higher stress levels. It is defined as the ratio between the peak plastic stress at notch over the nominal stress ($\sigma_{peak\ plastic}/\sigma_{nom}$)

Numerical 3D FE simulation results of one-eighth of the V-notched specimen under tensile loading conditions have been reported in Figure 5.15. When the applied nominal stress for the V-notch specimen is below σ_{linear}/K_t (A zone, Figure 5.15), with σ_{linear} the proportional stress value (i.e. last value of stress where the behaviour of the material is linear =280 MPa); no plasticity occurs at the notch tip and the effective fatigue notch factor is equal to the stress concentration factor ($K_f^*= K_t$, with $K_t= 2.49$); this behaviour can happen at low stress levels.

By increasing the applied nominal stress, the plastic stress will also increase considering a strain hardening model, as well as the plastic volume involved around the notch tip (B zone, Figure 5.15.); as a result, the effective fatigue notch factor value gradually decreases and it possible to define a region of local yielding around the notch tip.

If the applied stress is over the proportional stress value of the material (C zone, Figure 5.15), the extreme phenomenon of full yielding occurs, and the stress level become uniform over the entire net section of the specimen, equalling the nominal tension ($K_f^*= 1$).

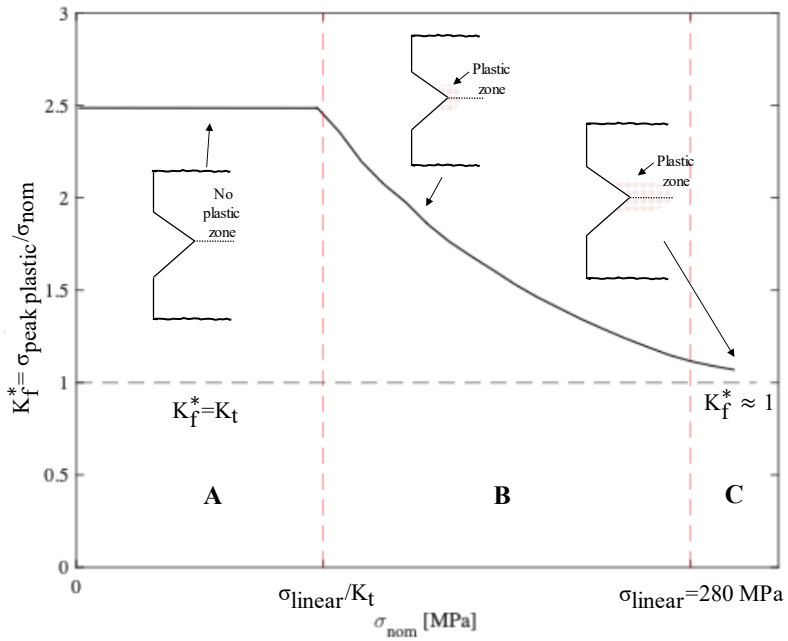

Figure 5.15: Change of the fatigue notch factor K_f^* during cyclic yield for V notched AISI 304L specimen

Nagaishi et al. [141] performed fatigue test campaign on circular notched hot-rolled AISI 304 steel and observed a dependency of the fatigue limit from the stress ratio R; indeed,

when R has negative value, the alternating tension-compression promotes the motion of dislocation [142] resulting in martensitic transformation inside the notch volume leading to a rise in local hardening. The increase of hardness at the notch tip can suppress fatigue crack initiation.

The presence of high plasticity at the notch tip for AISI 304L can be a justification for the SED high control volume radius obtained; anyway, SED approach can be applied for the design of notched components.

5.4 Conclusions

A rapid methodology has been proposed for the fatigue design of notched details. Indeed, it is not easy for companies to usually perform a complete fatigue test campaign according to standard due to the lack of material and time. Moreover, for a proper design of notches, it is necessary to evaluate the energy field around the notch tip and adopt a design curve. The material under study was an austenitic AISI 304L steel, where plain and V-notched specimens were retrieved.

Static tensile tests were performed to obtain the mechanical properties; meanwhile, the evolution of the specimen temperature was monitored with an infrared camera to apply the Static Thermographic Method (STM). The stress level of transition between the first linear cooling phase, in accordance with thermoelastic law, and the second linear cooling phase, having different slopes, was identified as the limit stress, σlim, where damage within the material arises. For plain material it was found a limit stress of σlim= 197.5±6.1 MPa, while for V-notched specimen it was equal to σlim V-notch= 151.8±5.8 MPa.

To obtain the fatigue limit of the material and compare it with the limit stress from STM, a series of stress-controlled stepwise fatigue tests were performed applying the Risitano's Thermographic Method (RTM). A fatigue limit of σ0 RTM Plain= 193.2±4.4 MPa was obtained for plain specimens, while σ0 RTM Vnotch= 164.8±2 MPa for V-notch specimens in well agreement with the estimated of the STM; thus, both methods provide a first indication for the design of the mechanical component. With the RTM it was also possible to obtain, adopting few specimens, the S-N curve of the material.

The design of notched details can be performed adopting the Strain Energy Density (SED) method calibrated based on the values obtained by the Thermographic Methods; such procedure has been validated by summarizing in a unique SED-based master curve (ΔW-N) the fatigue data obtained by RTM and other fatigue data from literature.

The novelty of the proposed approach is the estimation of the control volume radius, R0, needed to apply the SED method by means of the STM: a time saving procedure compared to the traditional estimation of this parameter via S-N curve. Even if the value of the control volume radius is higher compared to other material, this can be addressed to the high ductility of the steel under study and the presence of a large plastic area around the notch tip.
The proposed rapid methodology allows an easy design of mechanical components adopting few specimens and a short testing time.

6. AISI 304L - SOLUTION ANNEALING TREATMENT

Crisafulli D., Jambor M., Šmídb M., Santonocito D., Risitano G. Fatigue life analysis of traditional and annealed AISI 304L specimens by Thermographic Methods. Under submission.

Highlights

Another application of the thermographic method on stainless steel AISI 304L has been developed to investigate the effect of a heat treatment on the specimens.

In this work, fatigue properties were evaluated on AISI304L specimens having two different microstructural states, one in as-received condition and the other one after solution annealing.

Abstract

AISI 304L is a low carbon austenitic stainless steel widely used in common engineering application, according to his good mechanical properties such as high ductility, corrosion resistance and easy weldability.

This material is adopted in various environmental conditions, such as pressure vessels or in pipelines where fluid temperature variations occur and affect his mechanical behaviour.

Nowadays, the application of advanced investigation methodologies, such as infrared thermography, are widely adopted for the rapid investigation of the fatigue properties of common materials, especially metals.

In this work, fatigue properties were evaluated on AISI304L specimens having two different microstructural states, one in as-received condition and the other one after solution annealing. Static and fatigue test campaigns were performed with the application of the Thermographic Methods.

Due to deformation, both material states exhibit martensitic transformation resulting in cyclic hardening. However, the results in terms of estimated fatigue life differ. Thermographic Methods have proven to be a valid approach for the rapid investigation of these different characteristics, confirming that the annealing process led to an improvement in the mechanical resistance of the material.

6.1 Materials and method

The material used for the study is AISI 304L stainless steel in the form of hot-rolled and annealed sheet 20mm thick. The same material was used on the previous works by some of the authors [143,144] so the microstructures characteristics were reported. The chemical composition of the material is shown in the Table 6.1; it is possible to see the typical low carbon content indicated by the L in the steel name.

Table 6.1: Chemical composition of AISI 304L (in wt.%) [143]

AISI 304L	C	Mn	Cr	Ni	N	S	P	Si	Fe
	0.023	1.79	18.12	8.18	0.086	0.003	0.04	0.17	balance

Raw material specimens defined “as received” (AR) and specimens after solution annealing heat treatment (SA) were studied. The solution annealing process took place at 1050°C for 30 min in a nitrogen-protected atmosphere with subsequent cooling in a nitrogen flow.

Dog-bone test specimens whose geometry is shown in Figure 6.1 were used for fatigue tests using the servo-hydraulic testing machine MTS810 with load cell of 250kN.

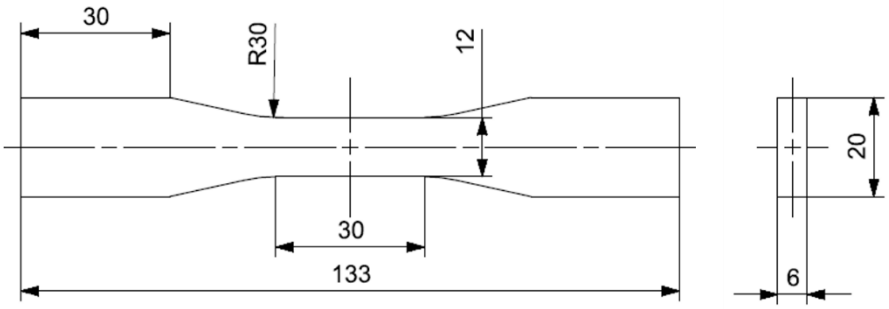

Figure 6.1: Geometry of AISI 304L dog bone specimens.

The surface temperature trend was monitored with an infrared camera, model Flir A40, and the thermal signal was extracted with a rectangular spot in the middle of the specimen, which correspond to the area where the fracture occurs. The thermal signal was then processed using Matlab software. Three specimens for each material state were tested for the fatigue tests.

The fatigue tests with the application of the thermographic method were carried out at the laboratories of the Engineering Department of the University of Messina.

6.1.1 Microstructure

The microstructure of this material was widely investigated by the coauthor of this work in other studies with the same steel sheet [143,144].

Colour images through the optical microscope of the metallographic surfaces (Figure 6.2) provide better evidence of the significant decrease in the volume fraction of delta ferrite present in the blue strings in the Figure 6.3. The different colour shades on the bands of the surface showed a chemical heterogeneity.

Analyses by means of magnetic induction with the feritscope allowed us to estimate a reduction in δ-ferrite from 1.24% in the AR state to 0.54% in the SA state.

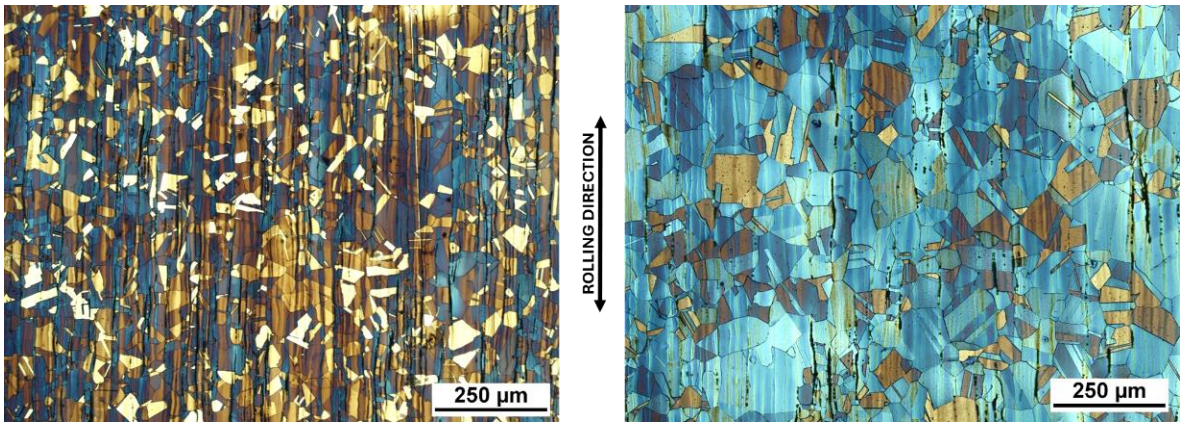

Figure 6.2: Optical light microscopes images of the microstructure of AR (left) and SA (right) 304L specimens. The δ–ferrite is represented as the black stringers aligned with the bands parallel to the rolling direction [143].

The results of the electron backscattered diffraction (EBSD) analysis of the two material states are shown in Figure 6.3.

Both material state present equiaxed austenite grains with numerous annealing twins and δ-ferrite stringers aligned along the rolling direction.

From the Figure 6.3a, it can be seen that after the solution annealing process, the regions near the δ-ferrite retain their original grain size, while in the other areas there is an increase in grain size. The δ–ferrite zones are better shown in Figure 6.3b and the dimension of grain size is reported in Figure 6.3c. Excluding the twin boundaries, the average grain size of AR

specimen was 32 µm ± 11 µm while a greater dimension grain size of 48 µm ± 32 µm was achieved after the heat treatment. Appear clear that the solution annealing process transformed the homogeneous microstructure of AR specimens into a heterogeneous microstructure characterised by regions with little grains or coarse grains.

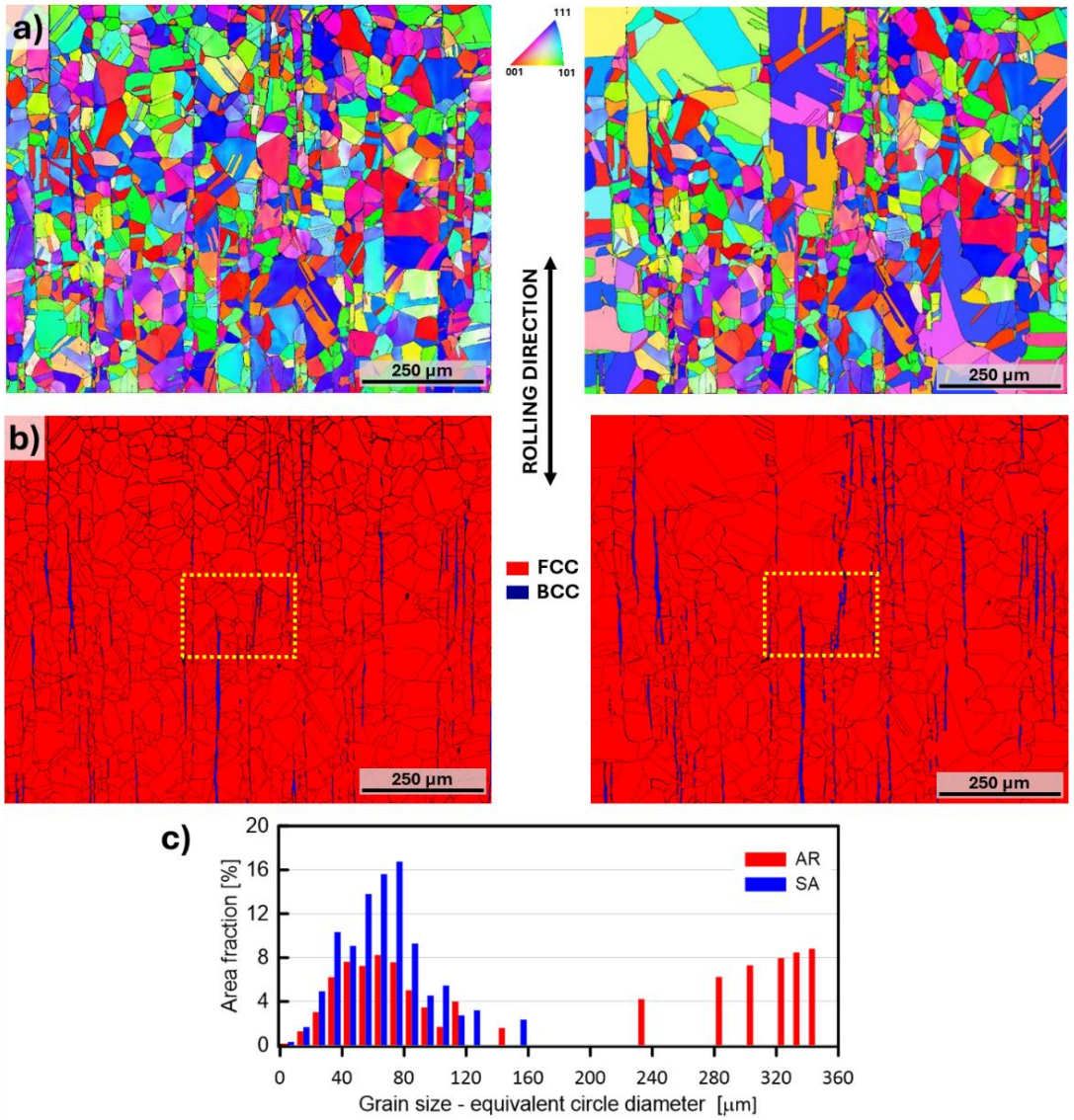

Figure 6.3: Microstructure of AR specimen (left side) and SA specimen (right side): a) Inverse pole figure maps of AR and SA states; b) phase maps evidence the presence of delta ferrite on stringers; c) grain size distribution on AR and SA states. The yellow rectangles indicate the regions used for the EDS analysis [143].

Figure 6.4 shows the results of the EDS analysis conducted on the same sample used for the EBSD analysis presented in *Figure 6.3*. The maps of Cr and Ni in both states are shown and

the yellow lines indicate the positions of the linescan analysis (Figure 6.4e). The microstructure consists of an apparent alternation of Cr and Ni bands, with the Cr bands containing δ-ferrite strings. It can be observed that the chemical segregation between states is reduced, in fact in the austenite between the δ-ferrite strings, fluctuations in Cr content are suppressed and Ni content is also partially reduced.

There is a noticeable difference in the two states in the morphology and volume of δ-ferrite, a Cr-rich phase. The fine strings partially or completely dissolved, while the thicker ones became slightly larger. The dissolution of the δ-ferrite probably led to an increase in the content of Cr, which is a stabilising element of ferrite, within the adjacent austenite matrix. This would explain the reduced fluctuations in austenite after solution annealing.

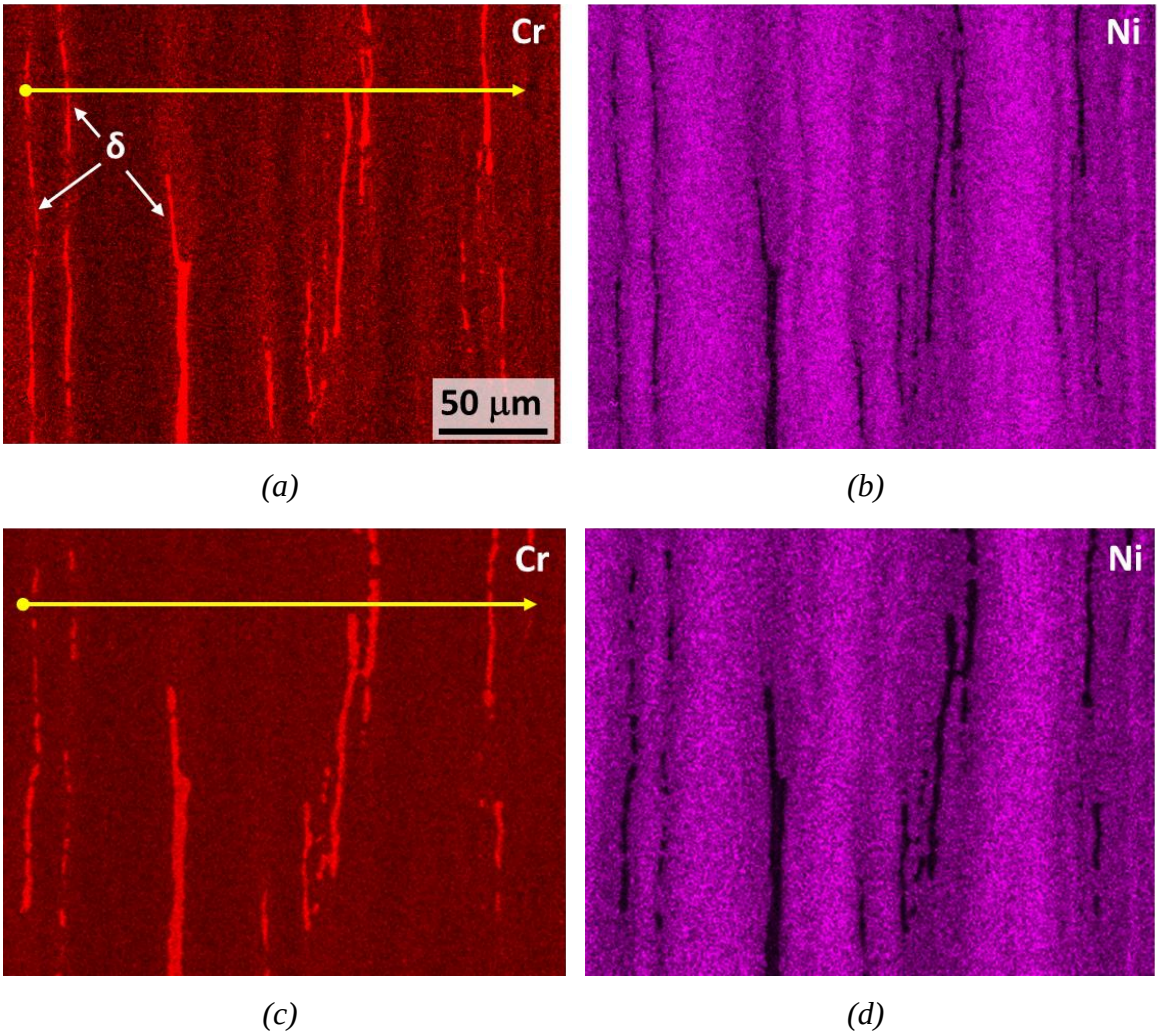

(a) *(b)*

(c) *(d)*

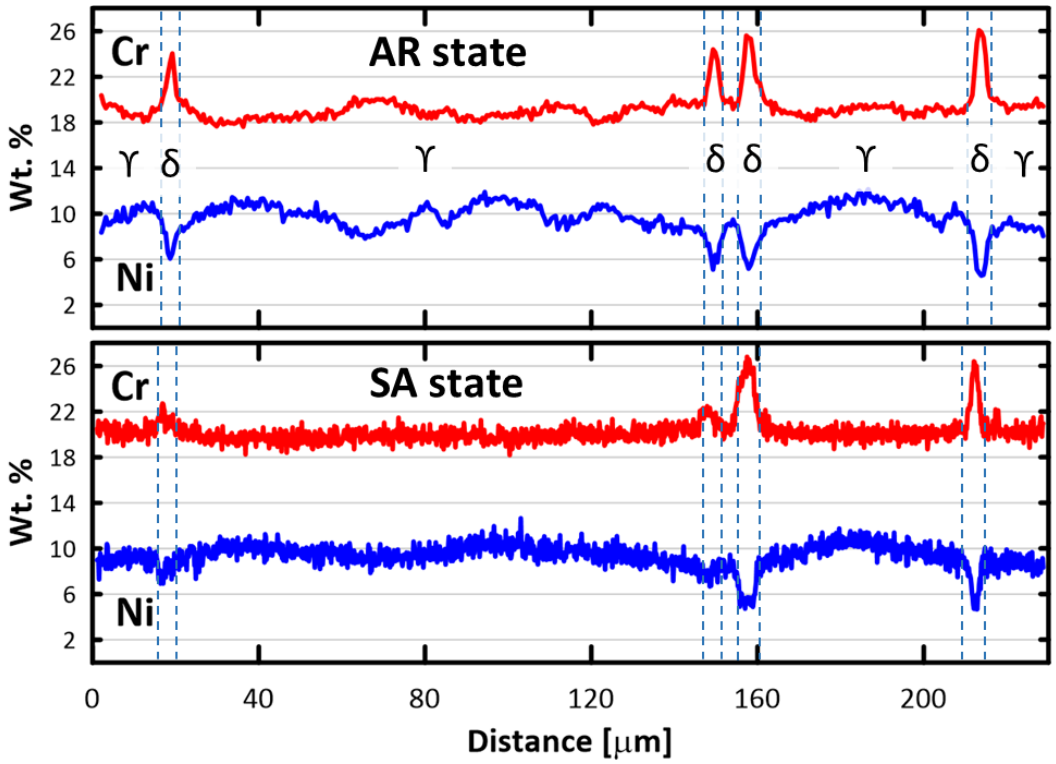

(e)

Figure 6.4: EDS analysis of the yellow area highlighted in Figure 6.3b: a-b) Cr and Ni maps distribution on AR specimen; c-d) Cr and Ni maps distribution on SA specimen; e) Linescan analysis along the yellow line showed in (a) and (c)[143].

6.2 Results and discussion

Stepwise tests were performed increasing of 10MPa the load levels from 120MPa to 200MPa every 10k cycles at the frequency of 10 Hz. Three tests were performed for each type of specimen. Figure 6.5 shows two examples of stabilisation temperature as a function of the number of cycles and the applied stress level for AR and SA AISI 304L specimens. It can be seen that the thermal behaviour between the two material states is quite different.

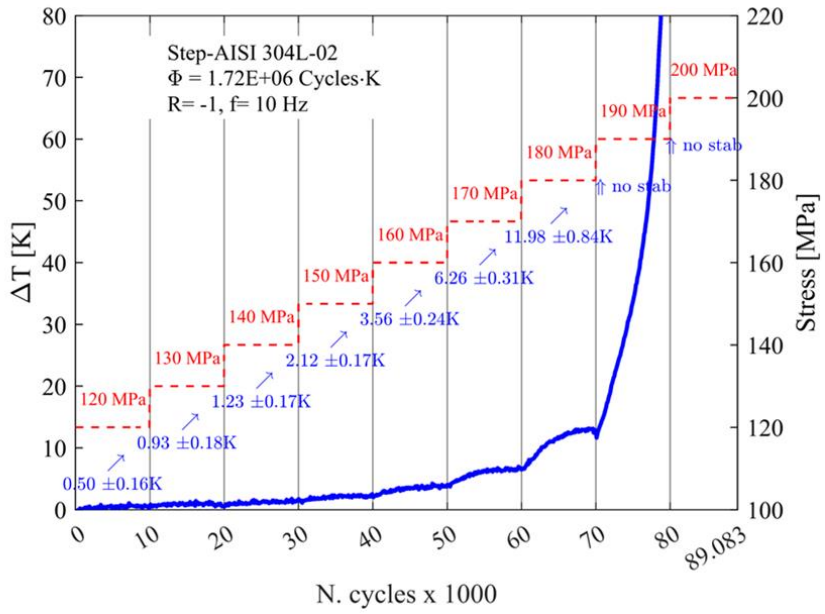

(a)

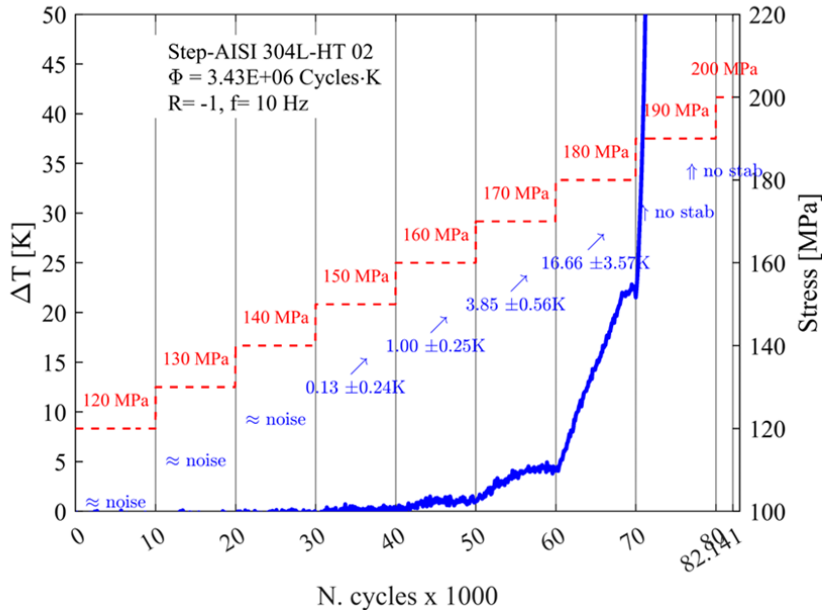

(b)

Figure 6.5: Stepwise fatigue test on AISI 304L specimen at frequency of 10Hz a) AR; b) SA.

For the AR specimens, the surface temperature increases more slowly than for the SA specimens, reaching a temperature of 10°C after 70k cycles at a stress of 180MPa, and then increasing rapidly until failure at about 89k cycles. In the SA specimens, on the other hand, the specimen surface temperature appears to remain unchanged for about 40k cycles but as

soon as it reaches 60k cycles it suddenly increases until failure at 82k cycles. With the same loading history, the SA specimen seems to have a more unpredictable thermal trend and failure occurs on average 10k cycles earlier.

The energy parameter Φ, evaluated as the area subtended by the curve in the graph indicating temperature variation and number of cycles, remains fairly similar in the tests.

Given the temperature trend, especially in the SA material, in order to avert any influence of the excessive test frequency used (10Hz) on the material, it was decided to repeat the three tests for each material state at a frequency of 5Hz and to change the loading history for the SA material.

The new temperature trends obtained for both specimen types with stepwise fatigue tests at a frequency of 5Hz are shown in Figure 6.6.

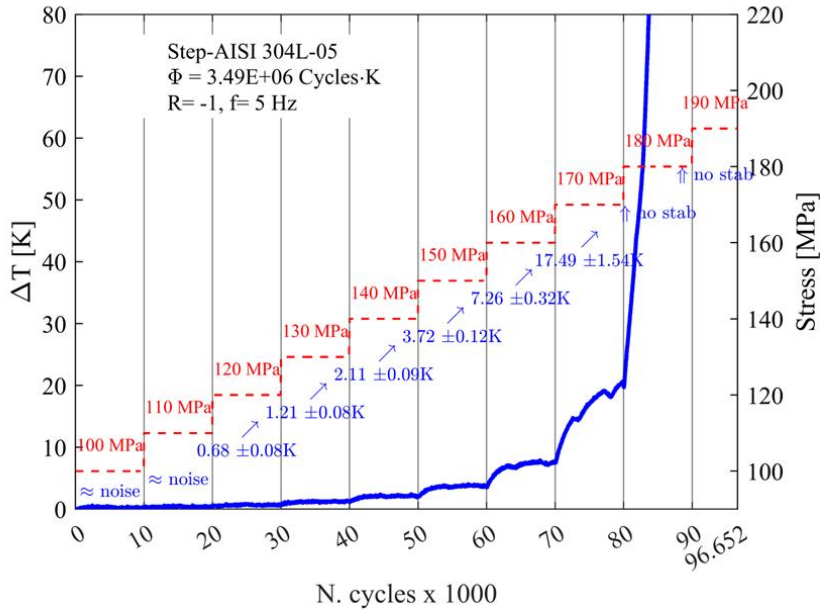

(a)

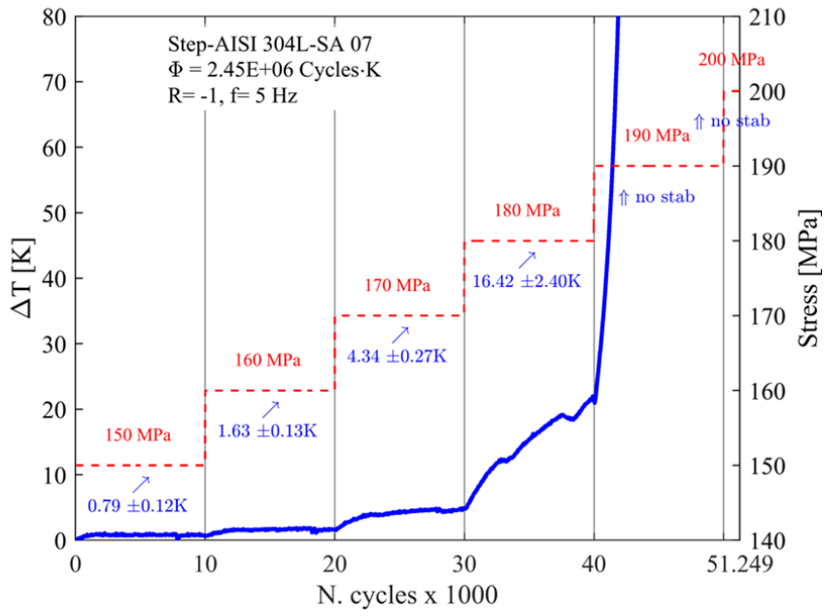

(b)

Figure 6.6: Stepwise fatigue test on AISI 304L specimen at frequency of 5Hz a) AR; b) SA.

Modifying the load histories did not show any significant change in the thermal trends for both states of the materials, so the same considerations made above for the thermal trends of the tests conducted at 10Hz are valid.

By plotting the stabilisation temperatures for each load level respectively, it was possible to estimate the fatigue limit of the materials. Figure 6.7 shows the fatigue limit estimations performed using the Risitano Thermographic Method for the stepwise tests shown previously.

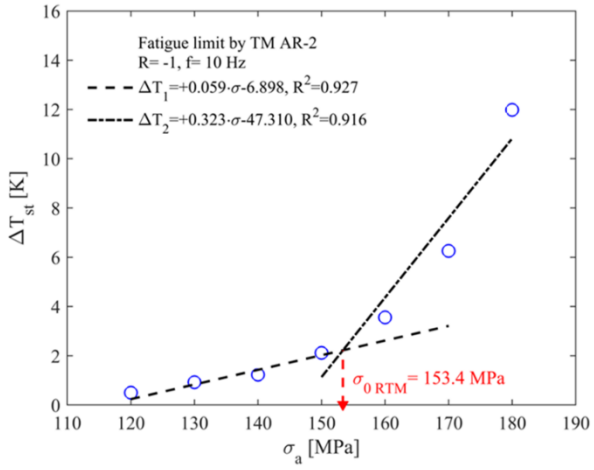

(a)

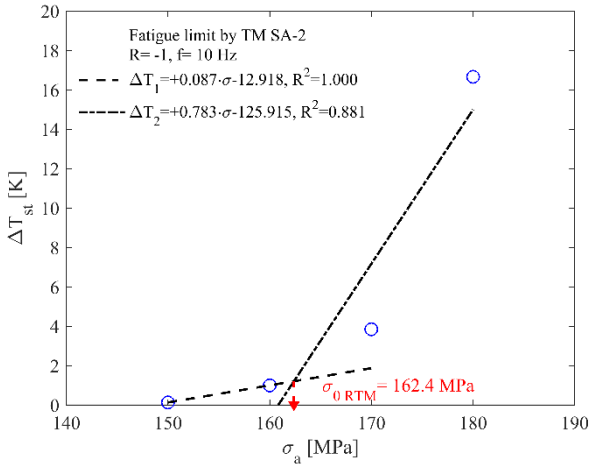

(b)

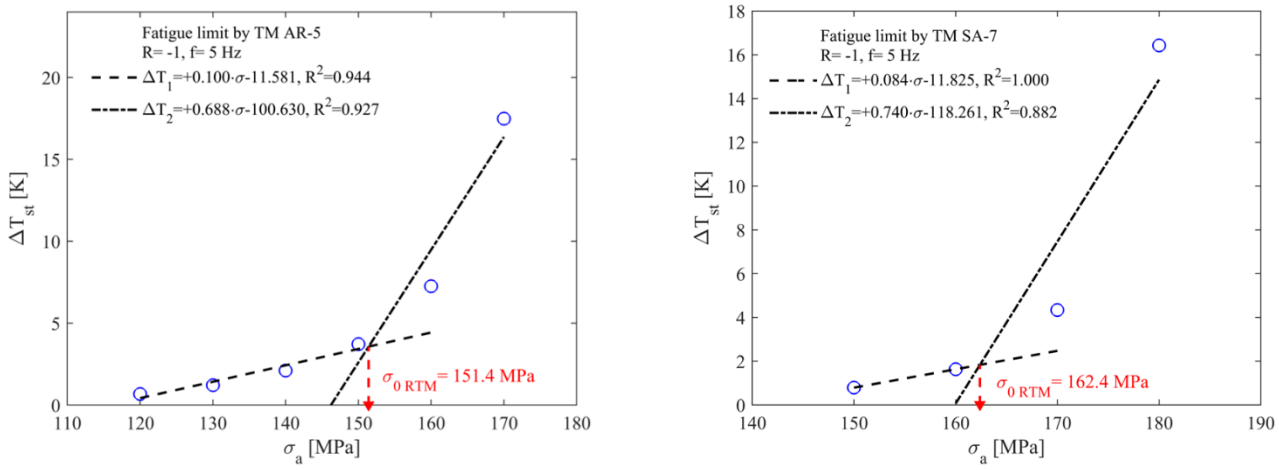

(c) *(d)*

Figure 6.7: Fatigue limit estimation according to RTM for AISI304L specimens: a) AR 10Hz; b) AR 5HZ; c) SA 10 Hz; d) SA 5 Hz;

The legends of the graphs show the R^2 coefficient, which estimates how closely the data, and the straight lines used are correlated. Due to the presence of few points for the SA specimens, a minimum value of 0.88 is reached, which is nevertheless acceptable.

The fatigue limit for the AR specimens was $\sigma_{0\ R\text{-}1}$=151.56 ± 1 MPa**,** while for the SA specimens was $\sigma_{0\ R0,1}$=163 ± 6 MPa. The higher standard deviation in the fatigue limit estimation for the SA specimens is due to the lack of points present for the linear regressions and thus resulting in more inaccurate estimation of the value.

6.3 Conclusion

The evaluation of the energetic release of two microstructural states of AISI 304L stainless steel has been evaluate during fatigue tests. No influence of loading history or frequency was found on the results. The application of RTM for the rapid estimation of the fatigue limit showed an improvement in fatigue life with solution annealing treatment.

From a microstructural point of view, the solution annealing contributed to the dissolution of δ-ferrite and grain coarsening. The heterogeneity of the SA material, due to the grain growth impeding effect of the retained δ-ferrite strings, seems to allow for a better tolerance to fatigue damage and increased HCF life.

7. AISI316L - TRADITIONAL AND PRINTED

Crisafulli D., Fintová S., Santonocito D., D'Andrea D. Microstructural characterization and mechanical behaviour of Laser Powder Bed Fusion stainless steel 316L. Theoretical and Applied Fracture Mechanics, 131 (2024). https://doi.org/10.1016/j.tafmec.2024.104343.

Highlights

Laser Powder Bed Fusion (L-PBF) is a highly precise and customizable additive manufacturing (AM) technique that uses a high-energy laser to selectively melt and fuse powdered material into a three-dimensional object. However, depending on the process parameters, the final components may have potential flaws that can affect their quality and mechanical properties, due to porosity, melting and incomplete fusion of powder particles; and because the process involves local heating and sometimes uneven heat transfer, the processed components may warp or crack due to residual stresses or thermal gradients. The manufacturing process itself reflects in the final component structure having a detrimental effect on the strength, durability, fatigue resistance, and corrosion. In this work, static tensile and fatigue tests were performed on traditional and L-PBF manufactured AISI 316L stainless steel specimens. The energetic release has been evaluated with an infrared camera during the static and fatigue tests aiming to identify material thermal response to the loading and to predict the failure in rapid way adopting Thermographic Methods. Differences were observed comparing the fatigue data of the L-PBF processed specimens with the traditional material. However, analysis of internal structure, porosity, and surface characteristics of the AM material in combination with fractographic analysis helped to explain the differences in the fatigue life. The observed energy release, different for both material types, was discussed based on the structural characteristics. The results show that the crack originates from a defect on the surface or just below the surface, with a transgranular propagation.

Nomenclature

c	specific heat capacity of the material [J/kg.K]
$D_{average}$, Dl, Dt, Dp	average grain dimension, in longitudinal, transverse and parallel direction
f	test frequency [Hz]
I_σ	first invariant of the stress tensor [MPa]
k	inverse slope of the S-N curve

K_m thermoelastic coefficient [MPa^{-1}]

N, N_f, N_i number of cycles, number of cycles to failure, number of cycles of failure of i-th stress level

R stress ratio

R_a average roughness [μm]

t test time [s]

T, T_i instantaneous value of temperature [K]

T_0 initial value of temperature estimated at time zero [K]

α thermal diffusivity of the material [m^2/s]

ΔN_i number of cycle block length

ΔT surface absolute temperature variation during a fatigue test [K]

ΔT_s surface absolute temperature variation during a static tensile test [K]

ΔT_{st} stabilization temperature for fatigue tests [K]

Φ Energy Parameter [Cycles·K]

Φ_{ave} average value of the Energy Parameter [Cycles·K]

ρ density of the material [kg/m^3]

σ stress level [MPa]

σ_{lim} limit stress according to STM [MPa]

$\sigma_{yielding}$ yield stress [MPa]

σ_{sup} maximum applied stress [MPa]

σ_U ultimate tensile strength [MPa]

$\sigma_{0,\,RTM}$ fatigue limit (R= -1) estimated with the RTM [MPa]

$\dot{\sigma}$ stress rate [MPa/min]

7.1 Introduction

In the recent years, Additive Manufacturing (AM) of metal powder materials has gained great industrial and scientific interest offering a high geometrical design freedom and the possibility to produce light-weight components [145–147]. AM utilizes a variety of techniques, such as Selective Laser Melting (SLM) or Laser Power Bed Fusion (L-PBF) [148–150], Electron Beam Melting (EBM) [151,152], Binder Jetting (BJ) [153–155], and it is used to create customized parts with complex shapes and geometries for a variety of industries, such as aerospace [156], medical [157,158], and automotive [159,160], using variety of metal alloys. The interest in the investigation of the microstructure of final AM components is rapidly increasing in the recent years. Bedmar et al [161] have studied different AM technologies to produce AISI 316L stainless steel samples. It has been demonstrated that the mechanical properties and microstructure depends on printing parameters and technology used to obtain the specimen. However, AM of metal powder has some drawbacks, such as the potential for warping and distortion due to rapid cooling rate [162], as well as the presence of residual stress induced by the uneven heating and cooling of the layers [163]. Surface finish can be considered even an issue due to the AM technique, as the layer-by-layer nature of the process can lead to a rough surface finish [164]. Also, the raster angle orientation influences the mechanical behaviour of the components obtained by AM process [165]. The main problem is related to the microstructure which is often characterized by the presence of voids, porosity, unmelted powders, and excessive growth of grains, which cause a deterioration of the mechanical properties of the materials [166–168].

The presence of flaws and defects has a detrimental effect on the fatigue strength of final AM components and can represent an issue for the adoption of AM in industrial context. The effect of layer orientation and surface roughness was investigated in Shrestha et al. [169], where static tensile and fatigue tests of several samples of L-PBF AISI316L, fabricated in different directions, have been performed. Anisotropy was noticed due to the layer orientation which affect the defects' directionality with respect to the loading direction. Stern et al. [170] highlighted the presence of porosity due to L-PBF printing process, hence the fatigue behaviour is strictly related to the building orientation, with a severe reduction of the fatigue life, in particular due to defects and pores in contact with the surface. Liang et al [171] performed a numerical study to the effect of individual and competitive effects of surface defects and microstructural components in L-PBF AISI 316L. They considered the

effects of grain morphology with their preferential crystallographic orientation, roughness and surface defects. Based on the presented results, lack of fusion is responsible of high cycle fatigue (HCF) failures, and it is predominant compared to roughness and grain size.

The aim of this work is to assess the fatigue properties of a L-PBF AISI 316L stainless steel, using conventional stress-controlled constant amplitude (CA) tests and energy methods, such the Risitano's Thermographic Method (RTM) [172] and the Static Thermographic Method (STM) [134]. Moreover, the fatigue behaviour is analysed considering the microstructure features of the specimens prepared by L-PBF technique.

To obtain the S‑N curve of the material with conventional fatigue tests, it is necessary to test a relevant number of specimens, consuming a lot of time; particularly with AM production where by changing printing parameters different mechanical properties can be achieved, leading to high cost for the industry. On the other hand, by applying Energy Methods it is possible to assess the fatigue limit with good accuracy, saving time and material. The adoption of the RTM allows the assessment of the fatigue limit of the material and the S‑N curve. More recently, the STM has been proposed to assess the first damage initiation, that is, the first irreversible energetic release, within the material by monitoring the superficial temperature evolution during a static tensile test.

In this work, the fatigue limits obtained with conventional fatigue tests and through RTM and STM methods were compared for two different types of AM specimens obtained by changing the printing parameters. The mechanical properties were then correlated with the microstructural characteristics. The results show that the energetic methods allow to determine the fatigue damage and S-N curve of AM steel in a short amount of time and with less material consumption compared to traditional CA tests. The applicability in the case of printed materials is influenced by the microstructure of the alloy impaired by the printing process.

7.2 Materials and Methods

7.2.1 Specimen and raw material properties

The same specimen geometry was used for the static tensile and fatigue tests. AM specimens were printed along the Z direction using a 3D4Steel® (3D4Mec, Italy) L-PBF printer by setting proper printing parameters (Figure 7.1a). The printing process consist in the distribution of the metal powder necessary to process a layer of the part, then the laser source is activated to melt the powder, with laser spots within 30-50 μm, adopting a proper laser

scanning speed. A laser power of 210 W and a laser scanning speed of 800 mm/s were adopted to produce the AISI 316L specimens (Figure 7.1b). According to the manufacturer, these printing parameters allow to obtain a relative density of 99.7% of the produced parts. The height of each layer was 50 μm with a hatch spacing of 0.14 mm. The printing process was performed in nitrogen atmosphere, with a printing volume of 210×210×230 mm^3, to avoid interaction between the metal and oxygen. The loading axis was the same of the printing direction in the case of the AM material, and of the rolling direction in the case of the traditionally produced steel used for comparison. The hourglass geometry of the specimens meets the ASTM E466 standard with the smallest diameter of 10 mm (Figure 7.1c).

The composition of the AM AISI 316L stainless steel was obtained with an X-Ray Fluorescence (XRF) (SPECTRO, AMETEK, Germany) analysis, as shown in Table 7.1.

Table 7.1: Chemical composition of traditional and AM AISI 316L material (in wt. %)

AISI 316L	Mn	Cr	Mo	Ni	Cu	Fe
AM	1.81	16.99	2.57	12.83	0.037	balance
Traditional	1.73	16.68	1.98	10.22	0.37	balance

7.2.2 Mechanical tests

Static tensile tests were performed on traditional and AM specimens adopting a stress rate of 3 MPa/s with a servo-hydraulic testing machine MTS 810 (maximum force of 250 kN). The value of the stress rate was chosen in order to perform the tests under adiabatic conditions, which are necessary to highlight the temperature trend evolution as exposed in Section 3.2-3.3. During the static tensile tests, the specimen must not have the time to exchange heat with the environment or with the testing machine. From the static tensile tests, the stress vs. time curve was obtained, evaluating the stress as the ratio between the instantaneous applied force and the nominal cross section of the specimen. During the test the temperature evolution has been monitored adopting a micro bolometric infrared camera FLIR A40, with a thermal sensitivity of 0.08° C at 30° C, and the image acquisition frequency was set to 5 Hz. The specimens' surface, both traditional and AM specimens, was cleaned with absorbent paper by hand to remove the oil and dust from it; in this way, the roughness conferred by the machining process, for traditional specimens, and by printing process, for AM specimens, was preserved. The AM specimens were tested in the "as-built"

conditions. To increase the thermal emissivity of the specimens, after the cleaning process, the surface was covered with a high-emissivity black paint (up to 98% coverage).

Constant amplitude (CA) fatigue tests were performed with the same testing machine, adopting a sinusoidal stress wave with several maximum stress levels and a frequency of 10 Hz. The stress ratio R was equal to -1. Another set of fatigue tests was performed with the same frequency and stress ratio but increasing the maximum stress level in a stepwise way. For this kind of test, the temperature evolution was monitored with the infrared camera with a sampling rate of one image every 10 cycles. The first kind of test was useful to obtain the S-N curve of the material with classical fatigue tests, while the second kind of test was adopted to obtain the S-N curve and the fatigue limit of the material in a rapid way, adopting the RTM.

7.2.3 Microstructural characterization

Investigation on the microstructure of the AM and traditional (conventionally rolled) AISI 316L specimens was performed to correlate the mechanical properties with the internal structure. Metallographic samples were prepared from parallel and perpendicular cut section to the specimens printing direction. Metallographic procedure to prepare the samples consisting of moulding into resin, grinding on SiC papers (P400, P800, P1200, P2500) and polishing on diamond pastes (3, 1 μm).

Electrolytic polishing was performed on the samples surface at 35 V and 5.3 A for 40 s at 8 °C using Electrolyte A3 (600 ml methanol, 360 ml ethylenglykolmonobutylether, 60 ml $HClO_4$), recommended for stainless steel by Struers Company. The preparation of the surface was necessary for the analysis of the possible preferential texture. After electro-polishing, the surface was etched with Beraha II etchant (800 ml distilled water, 400 ml HCl, 48 g NH_4HF_2, to 100 ml of this stock solution add 1-2 g $K_2S_2O_5$ for etching.) for 10 s at 28 °C to reveal the microstructure.

Digital optical microscope (OM), Olympus DSX1000, has been used to document the microstructure of both materials. The porosity images have been acquired with digital microscope and then they have been processed with the ImageJ software for the evaluation of the voids area on the sample surface.

Vickers microhardness (HV) measurements were carried out using DuraScan 70 G5 ZwickRoell hardness tester with a load of 5 N for 15 s. The microhardness tests were performed at different depths from the specimen surface. To check the grain size and the

presence of possible preferential texture, electron backscatter diffraction (EBSD) analysis was performed using Tescan LYRA 3 XMU FEG/SEMxFIB scanning electron microscope (SEM) with a FEG electron source (Tescan, Brno, Czech Republic). The external roughness was also analysed with a digital roughness tester Mitutoyo SURFTEST SJ201P. Tests were performed on the specimen external surface in the restricted section, near and on the grip sections of both specimens. For each measured area of the specimen, six detections were taken, each of the measurement was made twice by rotating the specimen of 90°. The average roughness parameter, R_a, was considered by adopting a header movement of 12.5 mm and the standard cut-off length of 2.5 mm. The average roughness was calculated by the instrument by adopting an averaging process, taking all detectable peaks and valleys on the surface evaluation line and neutralizing, thanks to the arithmetic averaging operation, the extreme values.

The SEM was used to analyse the fracture surfaces of AM specimens and to analyse their microstructure in detail. The analysis of the fracture surfaces (after the fatigue tests) was performed using the OM and SEM to investigate the failure phenomena at different stress level and to reveal the potential differences between the two materials.

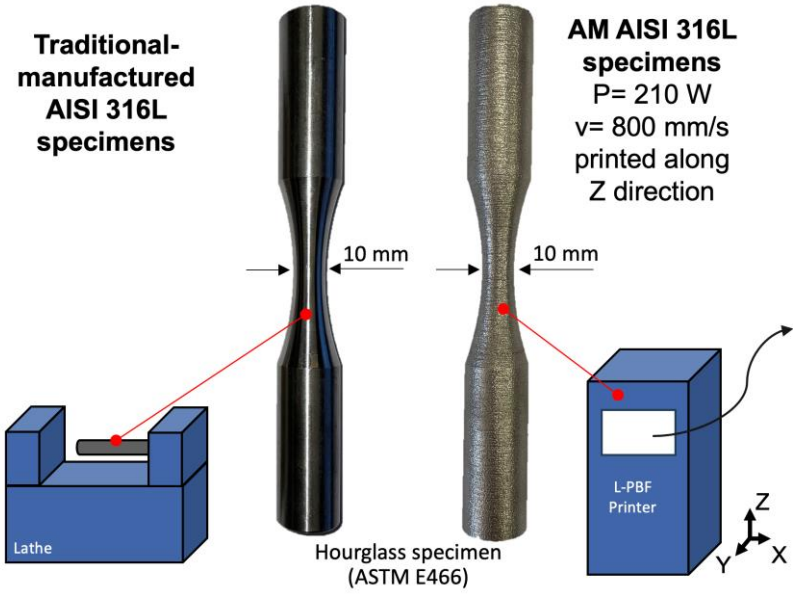

(a)

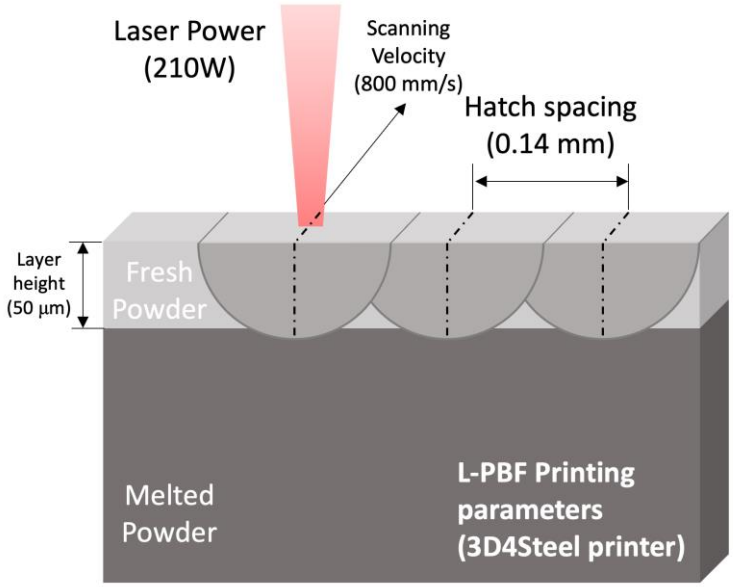

(b)

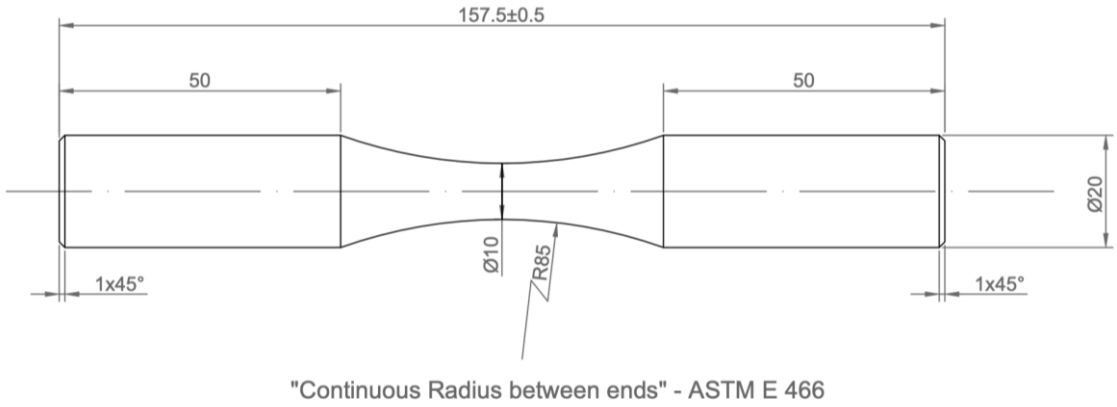

(c)

Figure 7.1: Test equipment for AISI 316L: a) Specimens adopted for the tests and tested in the machined and "as-built" conditions for the traditional and AM materials, respectively; b) L-PBF printing process; c) ASTM E 466 hourglass specimen geometry.

7.3 Results and Discussions

7.3.1 Structure

Microhardness

The microhardness tests have been performed on samples extracted from the specimens of traditional and AM AISI 316L. The specimens have been cut in the grip part with direction

parallel and perpendicular respect the specimen's axis. The polished surface with the micro-indents can be seen in Figure 7.2. By measuring the dimension of the signs leaved from the indenter it is possible to obtained measurements of the Vicker's micro-hardness.

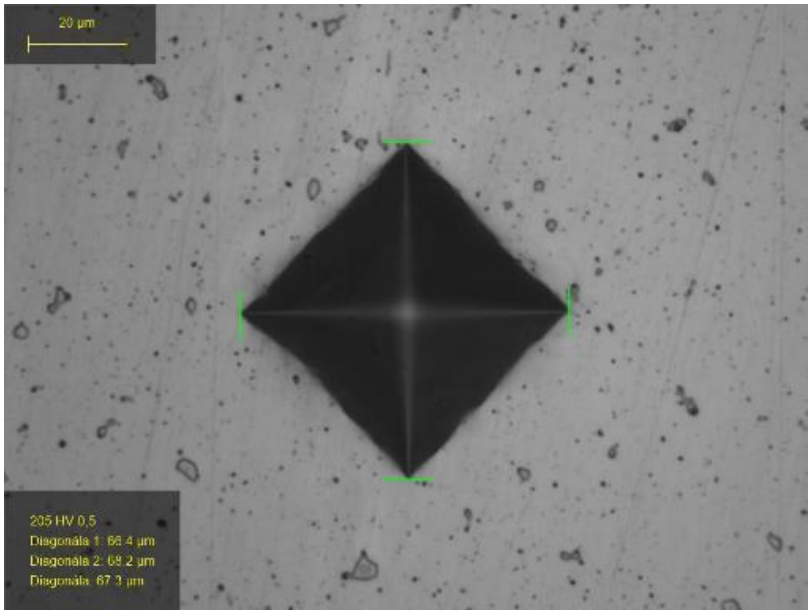

(a)

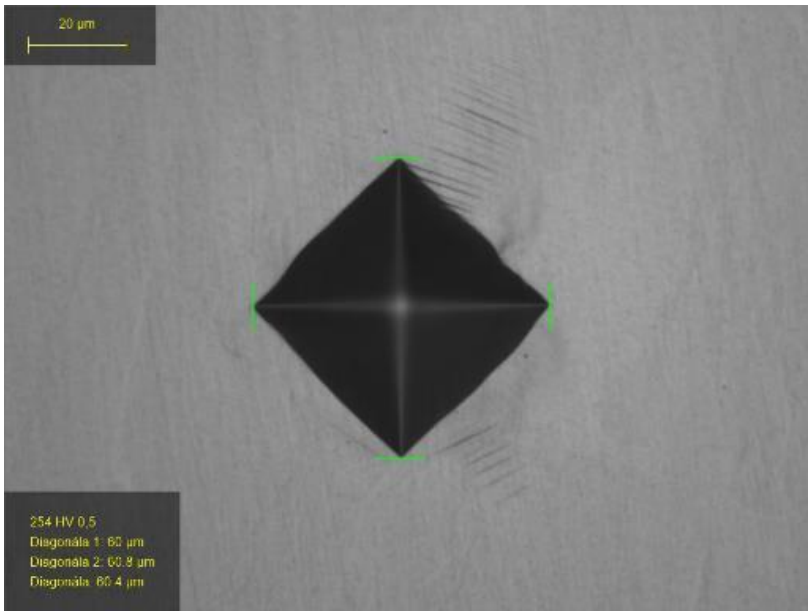

(b)

Figure 7.2: Indents in the polished surface of sample of AISI 316L:

a) Traditional; b) AM.

Micro-hardness has been evaluated considering its distance from the centre of the specimens (Figure 7.3a, diameter of 20 mm, where 0 mm is the position of the axis) for samples perpendicular to the specimen's axis, and in the axis of the specimens (Figure 7.3b) for

samples parallel to the specimens' axis. Twenty micro-hardness measurements have been taken along the diameter of the specimens.

For traditional AISI 316L steel, surface hardening occurred, as can be seen in Figure 7.3a near the edge of the specimens (292 HV at -10 mm and 303 HV at +10 mm); while, in the sub-surface region and in the middle region of the sample, an almost constant value of microhardness can be seen (202÷210 HV). In the case of AM material, there is no significant difference in the hardness along its diameter, moving from the surface; indeed, at the surface region we have a microhardness of 214 HV at -10 mm and 236 HV at +10 mm, and in the middle region the values are within a range of 220÷240 HV, with a maximum of 254 HV at -3.78 mm. The microhardness values reflects the characteristics of the manufacturing process. Indeed, for traditional steel the hardened surface is conferred by the rolling process; while for the AM steel there is no influence of the printing process on the surface.

The average microhardness value for the traditional steel is 205.5 ± 4.6 HV, while the value for the AM steel is 228.9 ± 7.0 HV, considering the measurement on samples parallel to the axis of the specimens. The value measured for the AM material is higher compared to the traditional one; however, also the standard deviation is higher, which can be connected to the internal structure and potential internal defects.

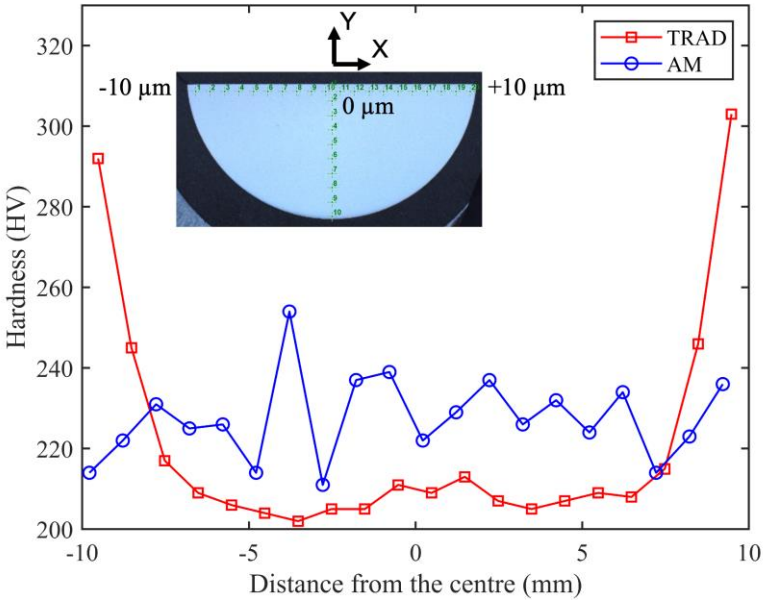

(a)

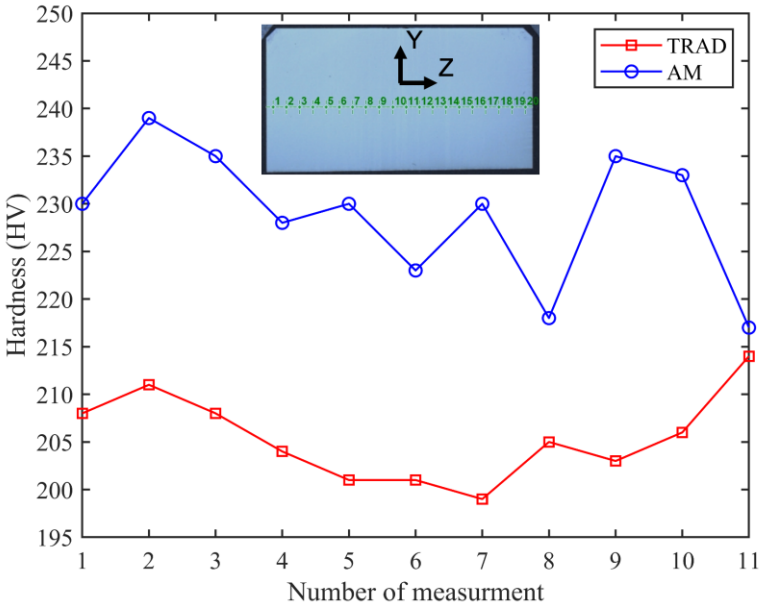

(b)

Figure 7.3: Microhardness (HV) trend (a) according to the distance from the centre for Traditional and AM samples and (b) in the centre of the samples.

Roughness and porosity

The measurement of surface roughness using the roughness tester have shown an average value of 0.86 ± 0.06 μm for traditional samples and 8.87 ± 1.35 μm for the AM samples. Performing the roughness measurement in different areas of each sample, the values of the average roughness do not change within the range of one standard deviation. Since comparable roughness was measured in the area below and above the minimum cross section of the hourglass specimen, the building direction does not seem to influence the specimen roughness. By observing at the same magnification scale with SEM both the surfaces of traditional and AM stainless steel, it is possible to highlight several features (Figure 7.4). Macroscopically, the traditional AISI 316L steel has an homogenous surface with a fine-morphology due to the turning process; on the other hand, slight waviness and large superficial defects can be seen for the AM sample due to the L-PBF printing process, as shown in the detail of Figure 7.4b.

In the case of the traditional AISI 316L, the scratches due to the tool tip adopted for the specimens machining can act as stress concentration and results in possible fatigue crack initiation sites. As the surface roughness is a key factor which influences the fatigue crack initiation, the higher roughness and the presence of superficial defects on the AM steel may

cause earlier crack initiation compared to traditional steel. As can be seen in the detail for AM steel (Figure 7.4b), the defects reach the size of several hundreds of micrometres in diameter.

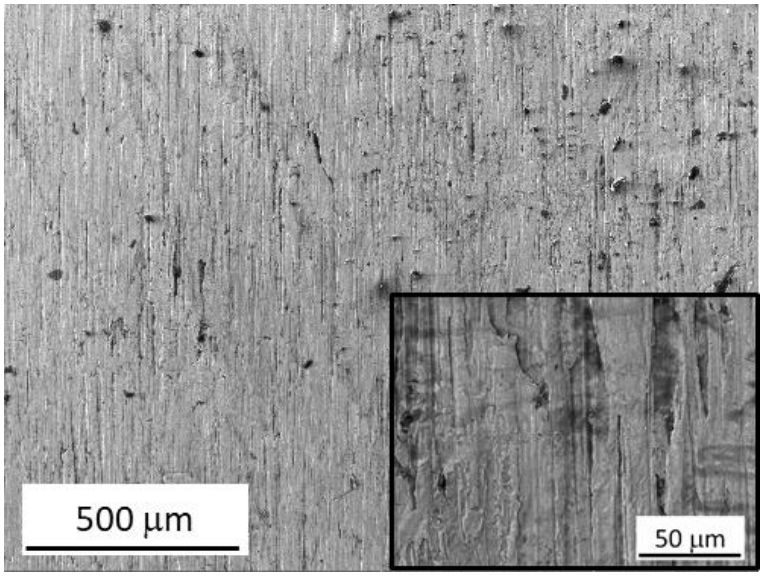

(a)

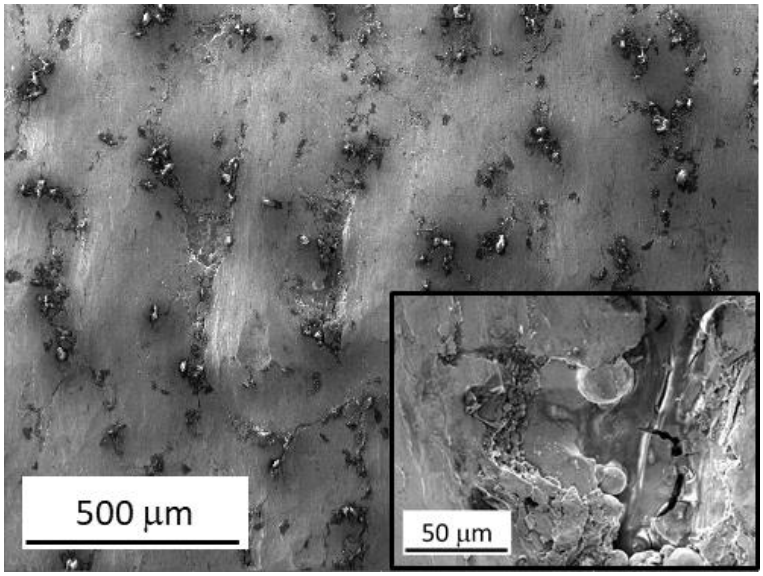

(b)

Figure 7.4: SEM observation of AISI 316L specimens surface morphology with details for: a) Traditional and b) AM samples (the load axis is in the horizontal plane).

Besides the surface defects, also internal defects were observed in the AM steel. Panoramic views of the porosity of the AM samples are shown in Figure 7.5. By calculating the area fractions occupied by the voids and the Feret diameters characterizing their size, a statistical analysis has been performed. The traditional AISI316L steel showed an average porosity of

less than 0.005%, so the presence of few pores was considered irrelevant for the purposes of evaluating the material's mechanical properties. Even though the porosity of AM steel varies from sample to sample, which is a consequence of the random selection of area for inspection and its orientation during 2D sample cutting, the fraction volume of defects was almost up to 0.45%, hence the average porosity of AM samples reached higher values respect the traditional steel. A value of porosity of 0.45% for AM steel is in quite good agreement with the 3D printer producer which declared a relative density of 99.7% for printed metal components. A random distribution of defects in the material volume can be considered with presence of pore clusters and large pores (Feret diameter from 3 μm to 77 μm) that has been detected along the printing direction. The defect size can be detrimental for the fatigue life; however, the pore clusters will be a bigger issue considering their combined effect. The clusters could be even more dangerous when present in a plane perpendicular to the printing axis, especially in the central part of the hourglass shaped specimens used for fatigue testing. However, due to the size of superficial defects, the internal defects should be more dangerous in the HCF region, characterized by low stress levels. Nevertheless, the porosity observed in the printing direction indicates an improper printing process, where there is a heat distribution issue; indeed, the defects are located in the same area in each layer along the printing direction (Figure 7.5d).

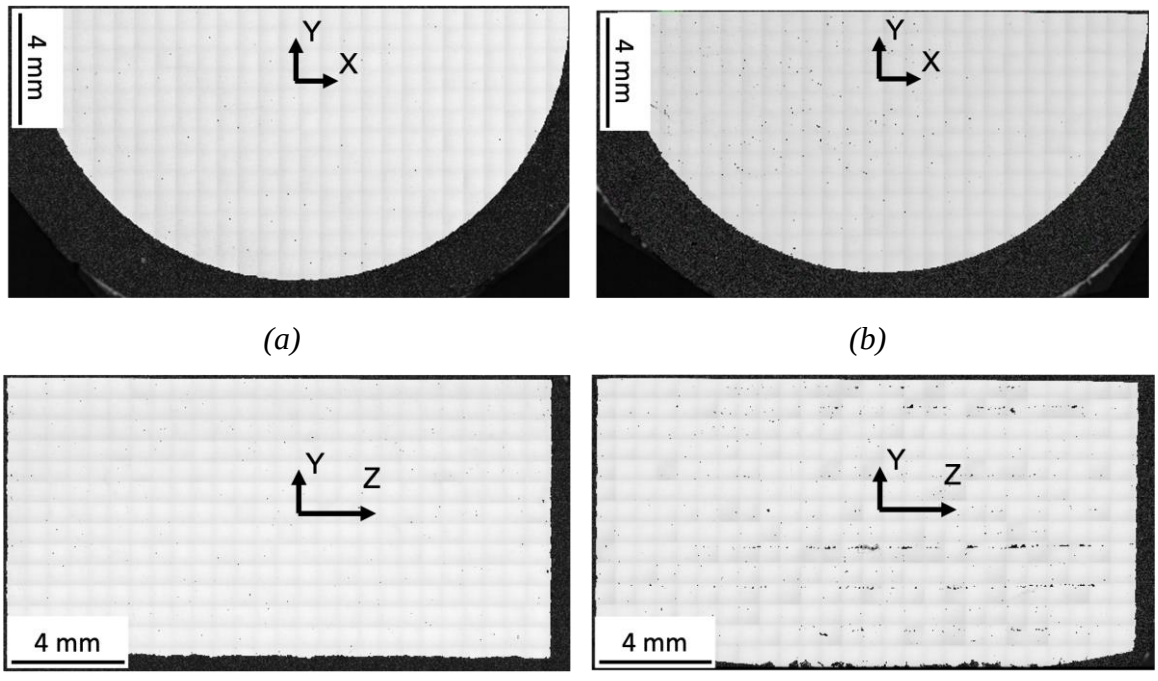

Figure 7.5: Optical microscope panoramic views of the porosity of AM material in direction a-b) perpendicular to the printing axis and c-d) parallel to the printing axis.

In Figure 7.6 it is shown the pore size distribution on the two different cross-sections for the AM sample affected by large porosity (Figure 7.5b-d). The samples perpendicular to the printing axis have the 37.16% of the total amount of pores with a Feret diameter under 5 µm and the 66.47 % of the total is under the diameter of 10 µm. The samples parallel to the printing axis reached the value of 58% of the pores under the size of 5 µm and the 77.87 % under 10 µm.

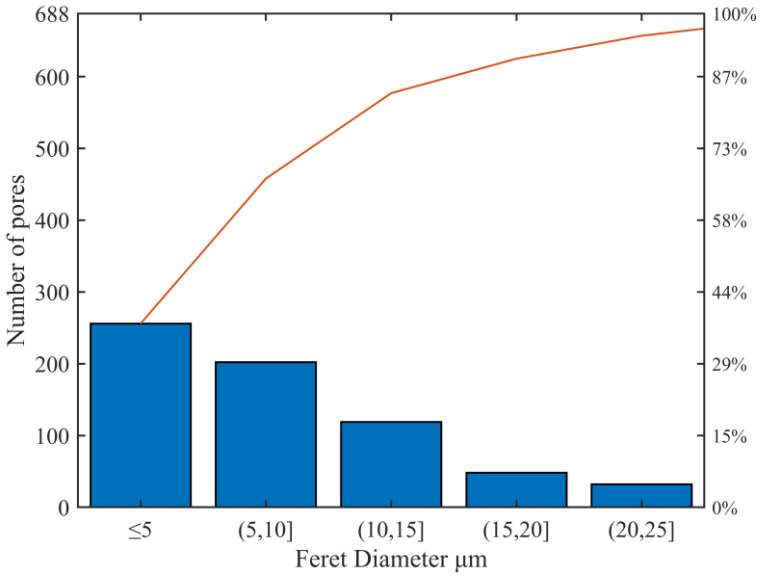

(a)

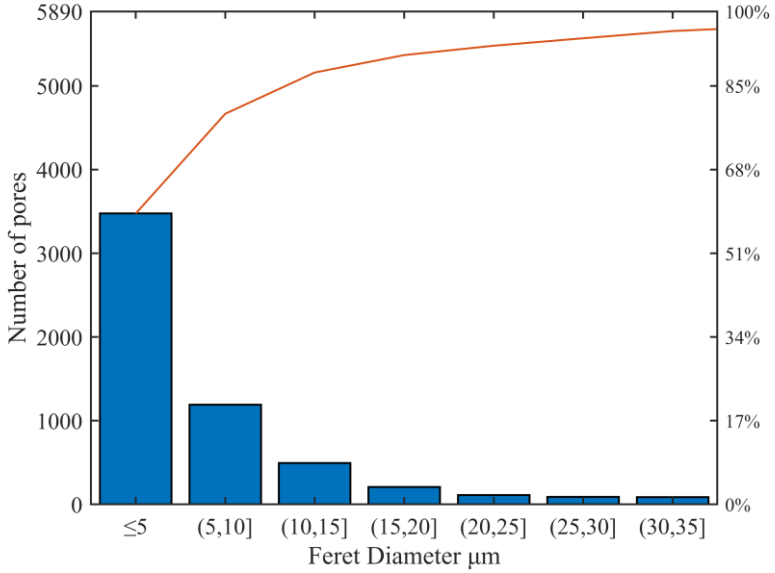

(b)

Figure 7.6: Pore size distribution in AM specimen a) Perpendicular to the printing axis and b) Parallel to the printing axis. Orange curves represent the cumulative pore distribution.

Microstructure

Traditional AISI 316L steel cross-sections are characterized by polyhedral grains of austenite containing delta ferrite (Figure 7.7a-b), where the delta ferrite stringers are aligned along the rolling direction. Deformation twins created due to the rolling can be seen in the austenite polyhedral grains.

On the other hand, the AM steel (Figure 7.7c-d) clearly reveals the printing strategy with the presence of several melt pools, whose dimensions are strictly related to the printing parameters. Between the melt pools it is possible to see the presence of grains growing through their boundaries following the heat flow. Larger defects on the melt pools boundaries and smaller defects within the pools can be seen for both the crosscuts through the AM structure.

From the macroscopic point of view, both the materials appeared homogeneous; however, the grain size of the traditional material is finer than the AM one.

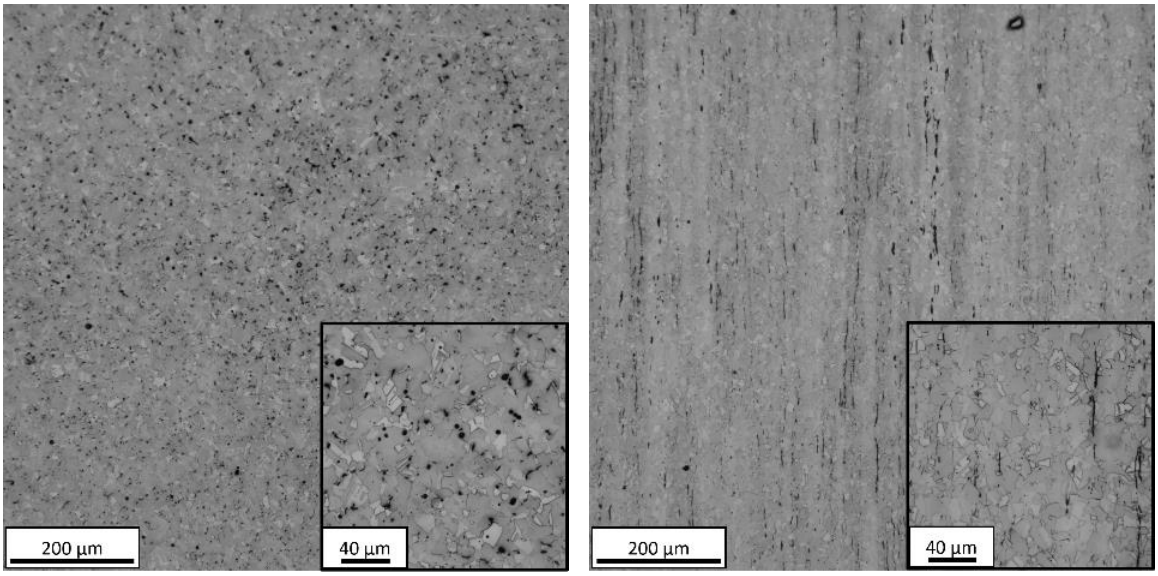

(a) *(b)*

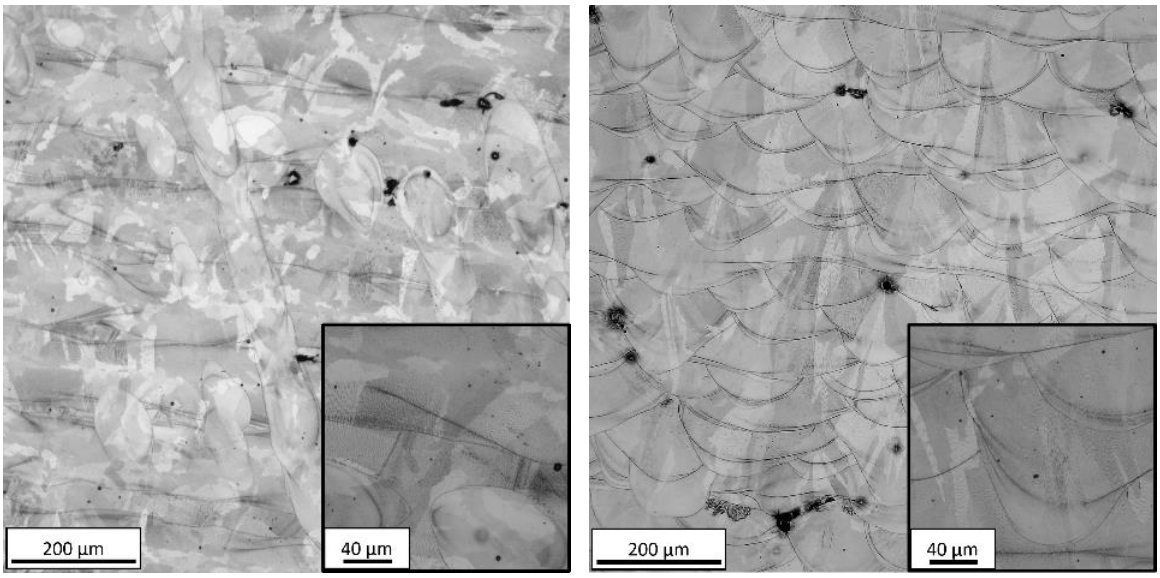

(c) *(d)*

Figure 7.7: Microstructure of AISI 316L specimens with details obtained by OM: a) Traditional - Perpendicular to the printing axis; b) Traditional - Parallel to the printing axis; c) AM - Perpendicular to the printing axis, d) AM - Parallel to the printing axis.

Information about grain size and their orientation have been obtained with the EBSD analysis for both steels. The acquired data have been processed with the AZtecCrystal software package and the results are shown in Figure 7.8. The average grain size was determined using the equivalent circle diameter function. The misorientation angle of 10° was used to determine the high angle grain boundaries and the border grains were excluded from the measurement.

For AISI 316L traditional stainless steel, the average grain size determined in the direction parallel to the printing axis is 3.4 ± 2.6 µm, including 954 grains, and in the direction perpendicular to the printing axis is 4.1 ± 3.0 µm, including 596 grains. The average grain size for the AM AISI316L in the direction parallel to the printing axis is 4.9 ± 6.8 µm, considering 1530 grains, while the direction perpendicular to the printing axis is 11.0 ± 10.9 µm, considering 741 grains. No preferential grain orientation in terms of texture expressed by the multiples of unit distribution parameter (MUD) provided by the software was observed for both the materials. The MUD parameter did not exceed value of 2.0 and 2.9 for the traditional and AM materials, respectively.

Due to the elongated grain structure for the parallel direction sections shown in Figure 7.8d, the equivalent circle diameter function could not results properly accurate. By following the guidelines outlined in ASTM E-112, the average grain size ($D_{Average}$) for an elongated grain

morphology can be calculated by obtaining the average of grain sizes in three mutually perpendicular planes.

$$D_{Average} = \left(D_l \cdot D_t \cdot D_p\right)^{\frac{1}{3}} \tag{7.1}$$

Where D_l, D_t, D_p are the average grain size, respectively, in the longitudinal, transverse, and parallel sections.

It can be assumed that all planes parallel to the building direction exhibit similar microstructures; consequently, it is possible to adopt the parallel section to represent two of the three perpendicular planes for the grain size analysis, obtaining an average grain size for AM AISI 316L of 6.41 μm.

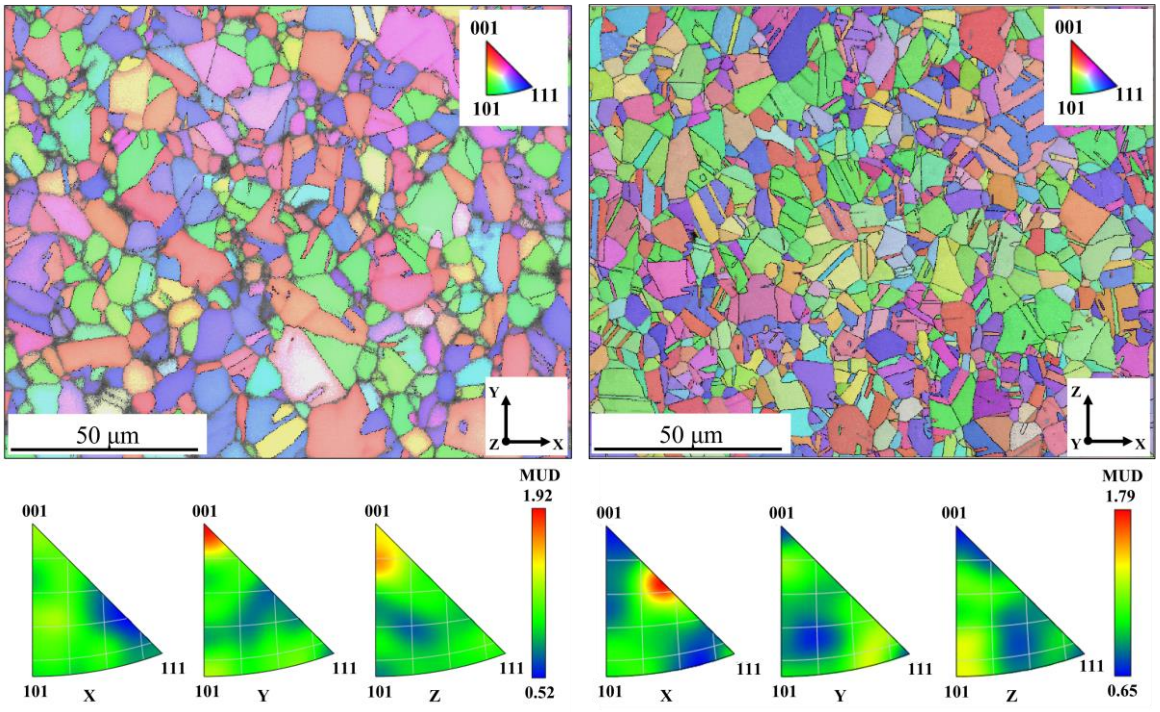

(a) *(b)*

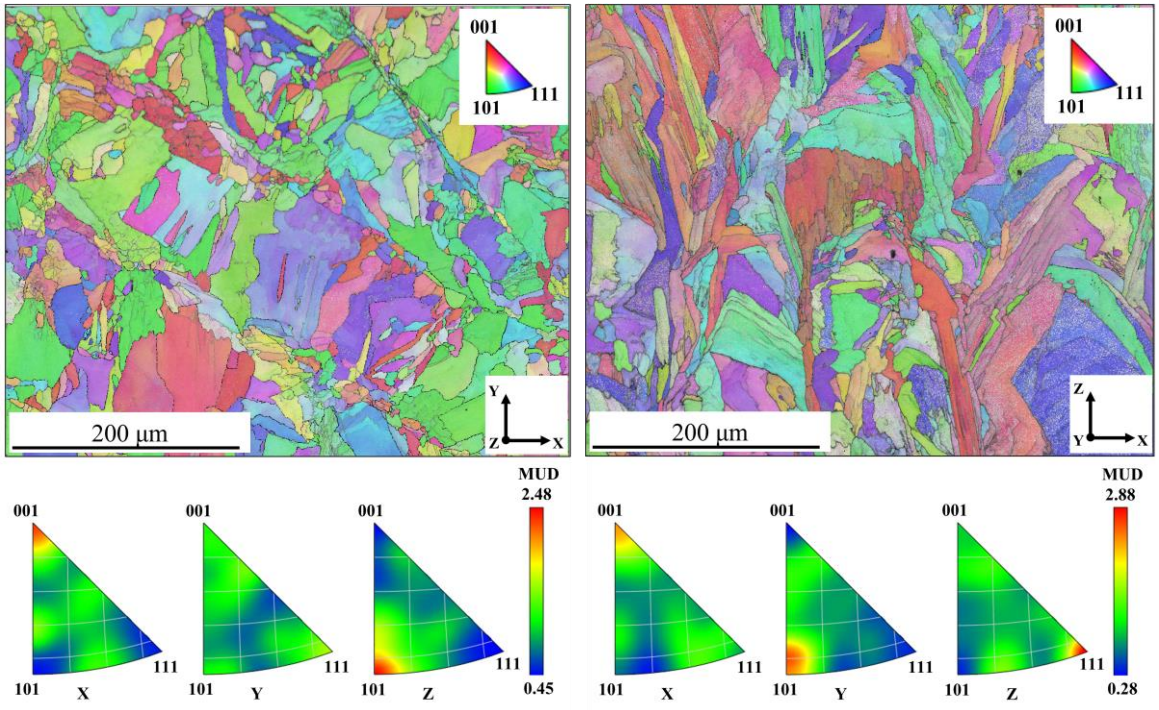

(c) *(d)*

Figure 7.8: EBSD maps of AISI 316L materials including IPFs showing no preferential grain orientation a) Traditional - Perpendicular to the printing axis; b) Traditional - Parallel to the printing axis; c) AM – Perpendicular to the printing axis; d) AM - Parallel to the printing axis.

7.3.2 Static tensile test

Static tensile tests have been performed on traditional and AM AISI 316L specimens to retrieve their mechanical properties. The applied stress level has been reported vs. time and temperature signals. The temperature has been estimated as the difference between the instantaneous maximum value retrieved from a rectangular area placed on the specimen gauge section and its initial temperature value at time zero (t= 0).

The ultimate tensile strength, σ_U, for traditional and AM AISI 316L steel has been estimated and compared. In Table 7.2 are reported the results coming from three static tensile tests performed on both the steel. The ultimate tensile strength of the traditional stainless steel is the highest one (714±11 MPa), followed by the AM steels: 640±8 MPa for 210W, 800 mm/s and 329±74 MPa for 230W, 1400 mm/s (just added here from [173] for comparison). The ultimate tensile strength of 230W AM steel shows a bigger scatter compared to the other two specimen types, and it also exhibits a higher porosity compared to 210W AM specimens. By

changing the printing parameters, different mechanical performance for AISI 316L steel can be achieved; particularly, the microstructure of the material can be severally influenced.

Table 7.2: Ultimate tensile strength for different kinds of AISI 316L steels.

AISI 316L specimen type	No. Specimen	σ_U [MPa]	$\sigma_{U\ ave}$[MPa]
Traditional	1	707	714 ± 11
	2	709	
	3	727	
AM (210W, 800 mm/s)	1	639	640 ± 8
	2	633	
	3	650	
AM (230W, 1400 mm/s) from [173]	1	370	329 ± 74
	2	373	
	3	244	

Indeed, the microstructure of the steel can severally affect the way how the heat is dissipated into the surrounding environment by the material. In Figure 7.9 are reported two static tensile tests performed on AM specimens obtained with a laser power of 210W and laser scanning speed of 800 mm/s. One test has been performed at 3 MPa/s (Figure 7.9a), while the other at 4 MPa/s (Figure 7.9b). As it is possible to observe, the temperature signal does not follow the typical trend illustrated in section 2; indeed, it is not possible to distinguish three marked different phases of the temperature. In [173], the tests performed on AM AISI 316L specimens clearly show the transition from phase I to phase II, so a limit stress can be assessed (191 MPa). In the same work, the static tensile tests performed on traditional AISI 316L specimens show the same behavior, but with a limit stress equal to 236 MPa. It is evident how the microstructure can affect the way in which the material dissipates the heat due to internal damage and microplasticity nucleation. This behavior can be addressed to porosities, melt pools and their boundaries and it requires further investigations.

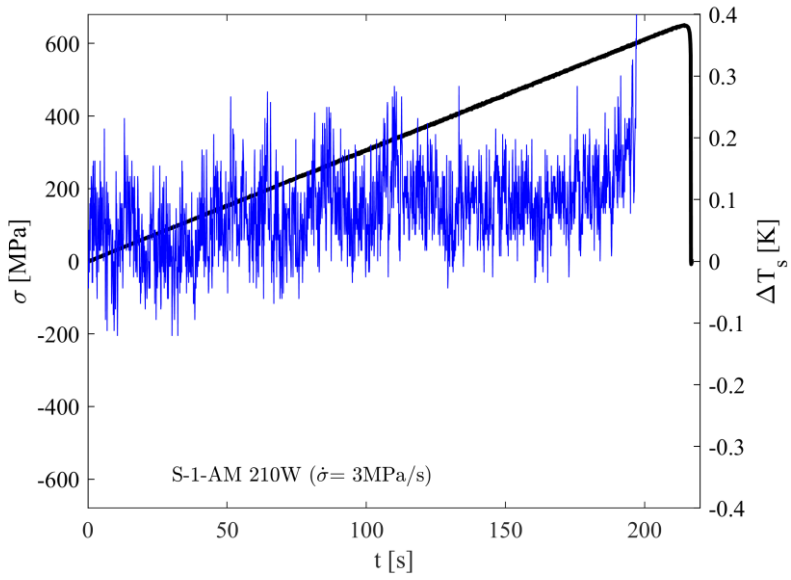

(a)

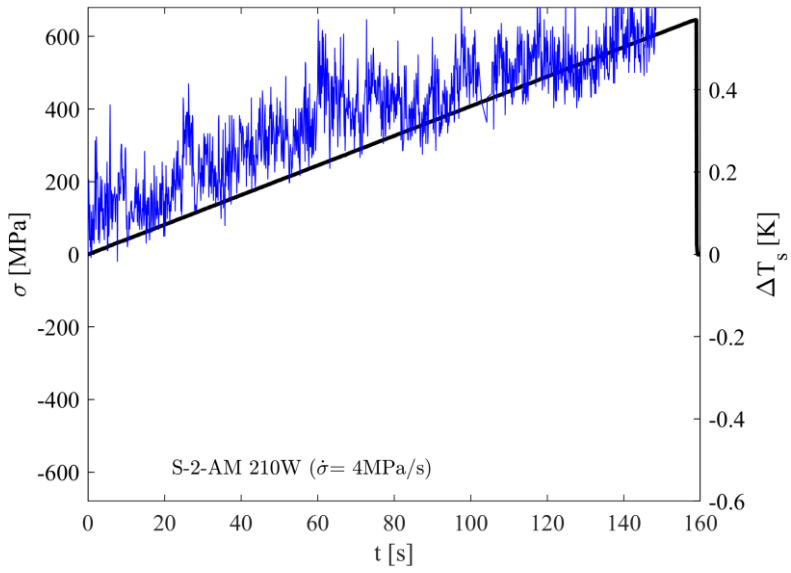

(b)

Figure 7.9: Static tensile test performed on AM AISI 316L (210W, 800 mm/s) at: a) 3 MPa/s; b) 4 MPa/s.

7.3.3 Fatigue tests

Two stepwise fatigue tests have been performed to apply the RTM and rapidly assess the fatigue life of the steel. The tests have been performed considering several stress levels with a stress ratio of R= -1 and a testing frequency of 10 Hz. The stress level was maintained for 10^4 cycles and then increased by 10 MPa up to the specimens' failure. During this kind of test the superficial temperature trend of the specimen has been monitored with the IR camera,

recording every 10 cycles the maximum temperature value of a rectangular area, placed on the specimen's gauge length, respect its initial value. In Figure 7.10, the temperature trend has been plotted vs. the applied stress level and the number of cycles. In the same figure, the stabilization temperature ΔT_{st} has been reported for each stress level, evaluated as the average value of temperature signal within the 10% and 80% of the number of cycles of the stress block. The first stress levels (200÷210 MPa) show a noisy temperature signal, with no evident temperature increment. Moving from 220 MPa to 290 MPa, the temperature signal increases in a clearer way, till the last stress level reached by the specimen (300 MPa) where the temperature signal does not stabilize, and the specimen fails (phase III of section 2). The same consideration can be applied to Figure 7.10b. It is possible to plot the stabilization temperatures respect its correspondent applied stress level (Figure 7.11). It is evident how the temperature trend looks bilinear, with a first set of data from 210 to 250 MPa and a second set of data from 260 to 290 MPa. By making the linear regression of these two sets of data and making their intersection, it is possible to assess the fatigue limit according to the RTM, $\sigma_{0\,RTM}$. The assessed value is equal to 262 MPa. In [173] the authors carried out stepwise fatigue tests on traditional AISI 316L specimens with the same procedure exposed above finding a fatigue limit, according to RTM, equal to 274 MPa.

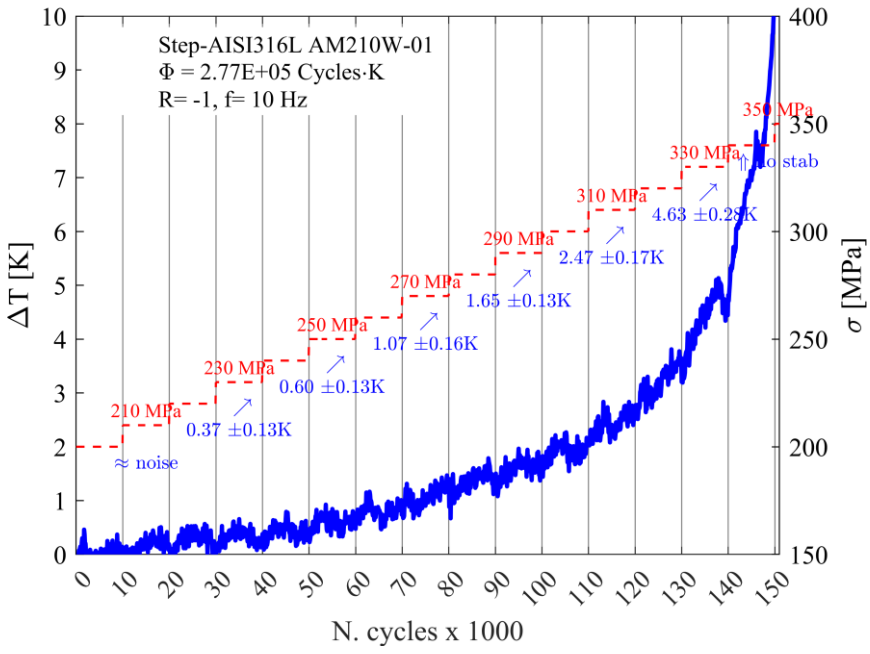

(a)

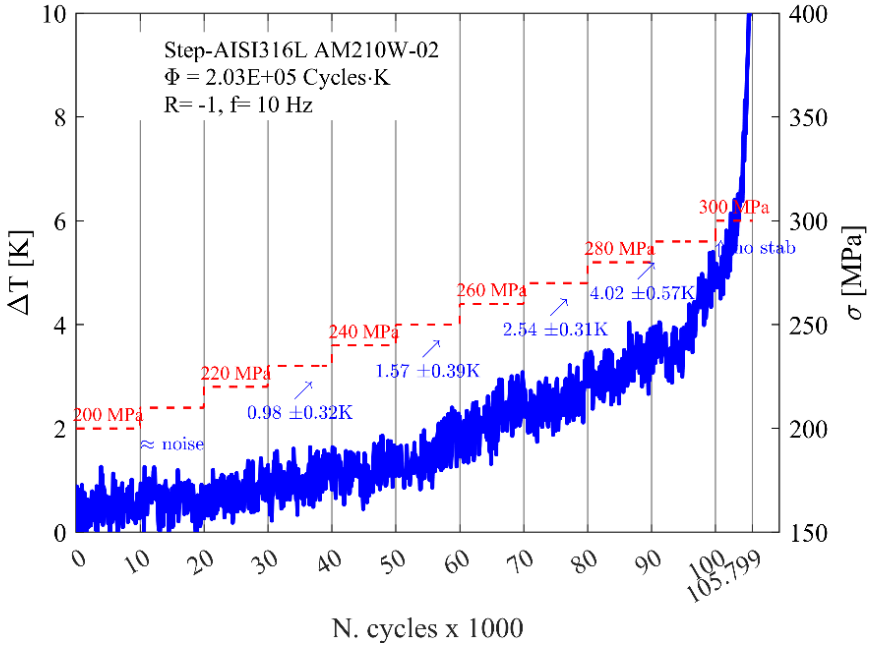

(b)

Figure 7.10: Stepwise fatigue tests on AM AISI 316L: a) Test 1; b) Test 2.

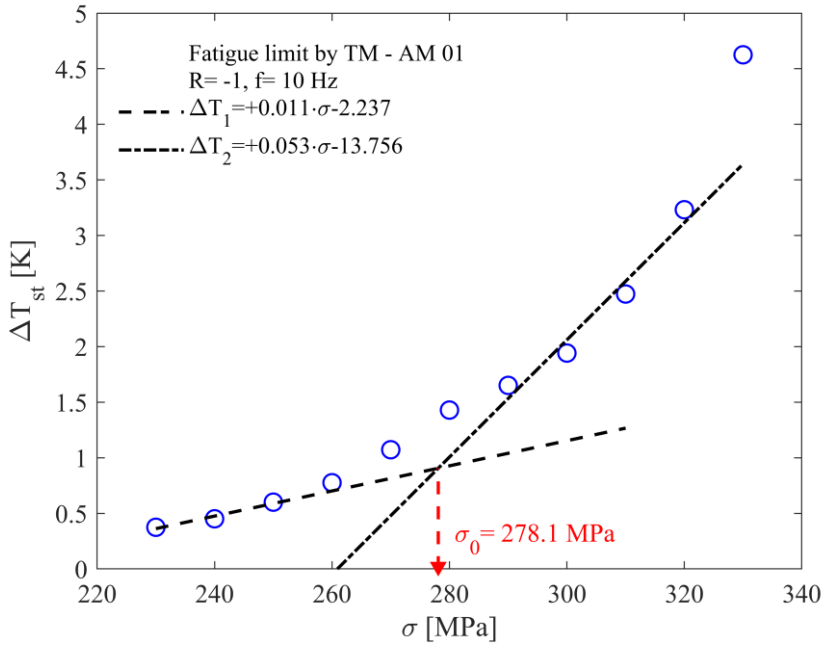

(a)

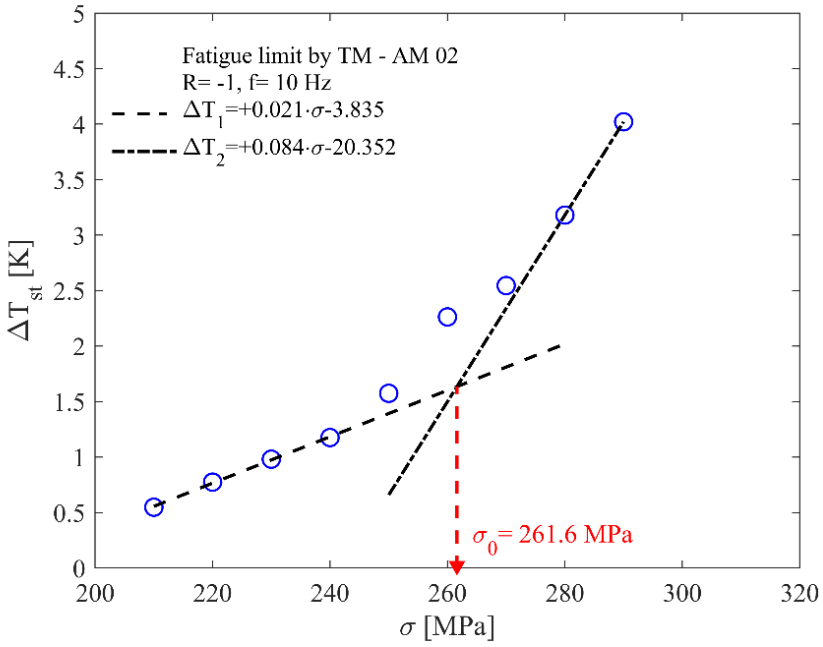

(b)

Figure 7.11: Assessment of the fatigue limit according to RTM for AM AISI 316L steel for: a) Test 1; b) Test 2.

Constant amplitude (CA) fatigue tests have been performed on AM specimens with fixed stress levels, stress ratio R= -1 and the testing frequency of 10 Hz. The temperature trend has been monitored with the IR camera and it is in good agreement with the one exposed in section 2. From each fatigue test (Figure 7.12), it has been possible to perform estimation of the Energy Parameter Φ as the subtended area of the temperature vs number of cycles curve. For CA tests the stabilization temperature and the Energy Parameter Φ have been reported in Table *7.3*, together with the applied stress level and the number of cycles to failure. It is evident that the higher the applied stress, the higher the stabilization temperature. The average value of the Energy Parameter for CA tests is equal to $\Phi_{ave\ AM\ CA}$= 2.05±0.94E+05 Cycles·K, which is in good agreement with the one from stepwise fatigue tests, $\Phi_{step\ AM}$= 2.03E+05 Cycles·K; while the Energy Parameter of traditional AISI 316L[33] steel [173] is one order of magnitude higher than the AM steel ($\Phi_{step\ Trad}$= 2.58E+06 Cycles·K).

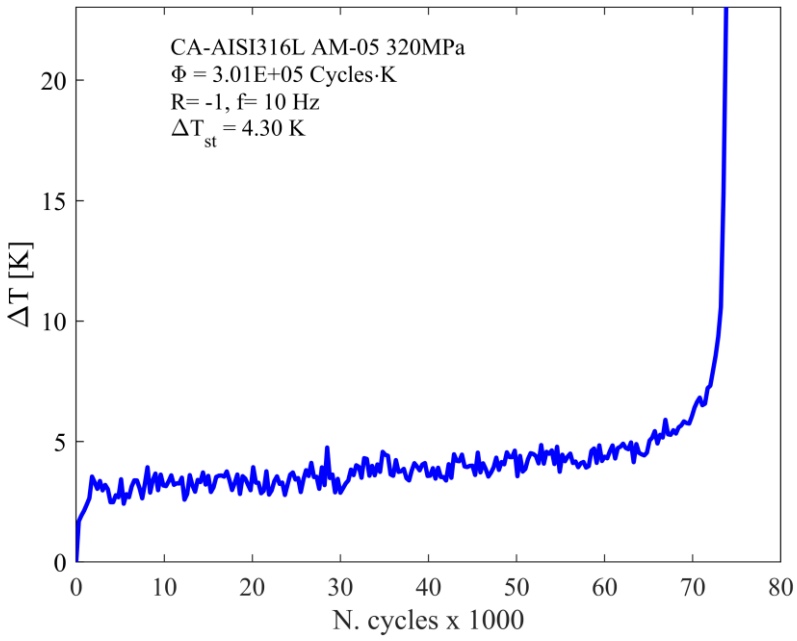

(a)

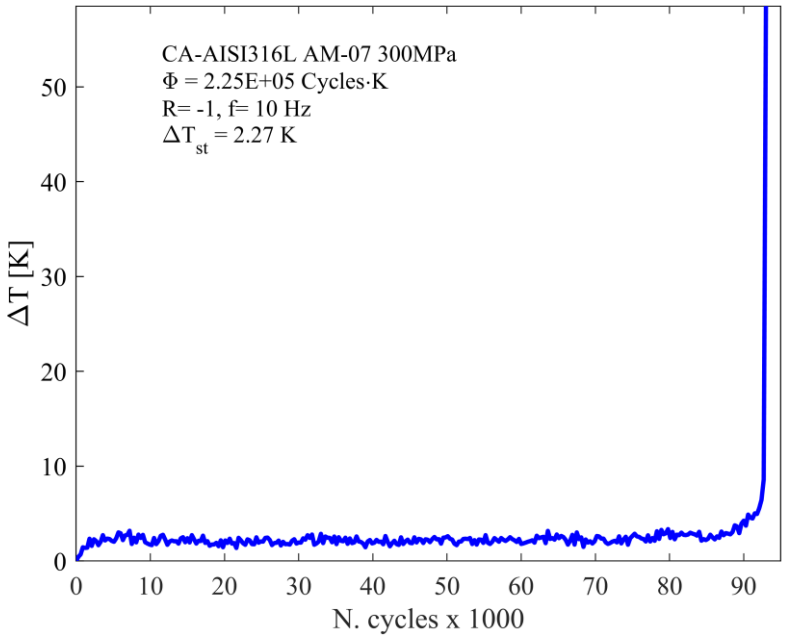

(b)

Figure 7.12: Temperature trend for CA fatigue tests performed on AM AISI 316L steel.

Table 7.3: AISI 316L AM (P = 210W; v= 800 mm/s, R=-1, f=10Hz) CA fatigue tests results.

No. Specimen	σ [MPa]	ΔT_{st} [K]	Φ [Cycles K]	N_f
1	340	9.62	3.98E+05	46.167
2	320	4.3	3.01E+05	73.955
3	300	2.52	2.39E+05	92.831
4	300	2.27	2.25E+05	93.298
5	280	1.94	1.42E+05	68.303
6	280	1.24	1.71E+05	119.788
7	260	0.85	1.37E+05	154.387
8	260	0.13	2.41E+04	93.747

The results of the CA fatigue tests have been reported in Figure 7.13, together with the CA fatigue tests performed on traditional AISI 316L specimens. The two materials show a different trend, indeed, AM steel (violet crosses) has a high slope compared to the traditional steel (black squares). In addition, the AM steel experiences failure for stress levels where the traditional steel has an infinite life, i.e. run-out at more than $2x10^6$ cycles. For AM AISI 316L, an inverse slope of k= 2.93 with a scatter index of T_σ= 2.05 and a fatigue limit of 100 MPa, extrapolated at N= $2x10^6$ cycles, has been obtained. The trend of the fatigue curve is in a good agreement with Braun et al. [174] where, for the same AM steel tested in the as-built condition at R= -1, they found an inverse slope of k= 2.87 with a scatter index of T_σ= 1.45, and a fatigue limit of 165 MPa evaluated at N= $2x10^6$ cycles. The steeper slope of the AM steel compared to the traditional one can be related to a fatigue life dominated by fatigue crack propagation, while higher values of the inverse slope are characteristic of long crack initiation phase [174]. As highlighted from the thermal observations (Figure 7.11), even small temperature increases are observed for stress levels below the knee region of the stabilization temperature-stress level curve; indeed, this phenomenon can be related to a more pronounced fatigue crack propagation regime.

Mechanical and thermal process can improve the fatigue strength of the AM steel, as observed by Wang et al. [175] that, for L-PBF AISI 316L specimens machined and annealed, found an inverse slope of k= 15.3 with a scatter index of T_σ= 1.147 and a fatigue limit of 249 MPa evaluated at N= $2x10^6$ cycles. These findings are congruent with the traditional steel in [174], with an inverse slope of k= 13.68 and scatter index of T_σ= 1.24, and with the

traditional AISI 316L of the present study which has a shallower slope of k= 30.94 with a scatter index of T_σ= 1.302.

The S-N points of the AM steel have been also obtained with the RTM, exploiting the constancy of the Energy Parameter Φ, from the two stepwise fatigue tests (red and blue circles). They follow the same trend of the CA fatigue points and they are in good agreement with the results coming from CA tests; indeed, some points are very close. The fatigue limits obtained with RTM (Figure 7.11) for AM and traditional steels have been also reported in the figure (red and blue line-dot contour), together with the limit stress for traditional AISI 316L obtained with STM (black line-line contour). For the traditional AISI 316L, the fatigue limit (extrapolated at $2x10^6$ cycles) and limit stress are in good agreement with the findings coming from CA tests. For the AM AISI 316L, there is a more marked dispersion ($\sigma_{0\ RTM\ AM}$= 261 and 278 MPa). Given the scatter between AM specimens lifetime, the fatigue limit values obtained via RTM are still consistent with the statistical scatter of conventional CA tests. It should be emphasized that useful information for fatigue design can be obtained in a short time and with less waste of material compared to conventional constant amplitude fatigue tests. The different fatigue behaviour of the AM steel respect the traditional one can be related to the microstructure, superficial roughness, subsurface defects and residual stresses impaired by the printing process that are not removed by machining [174], as analysed in section 4.4.

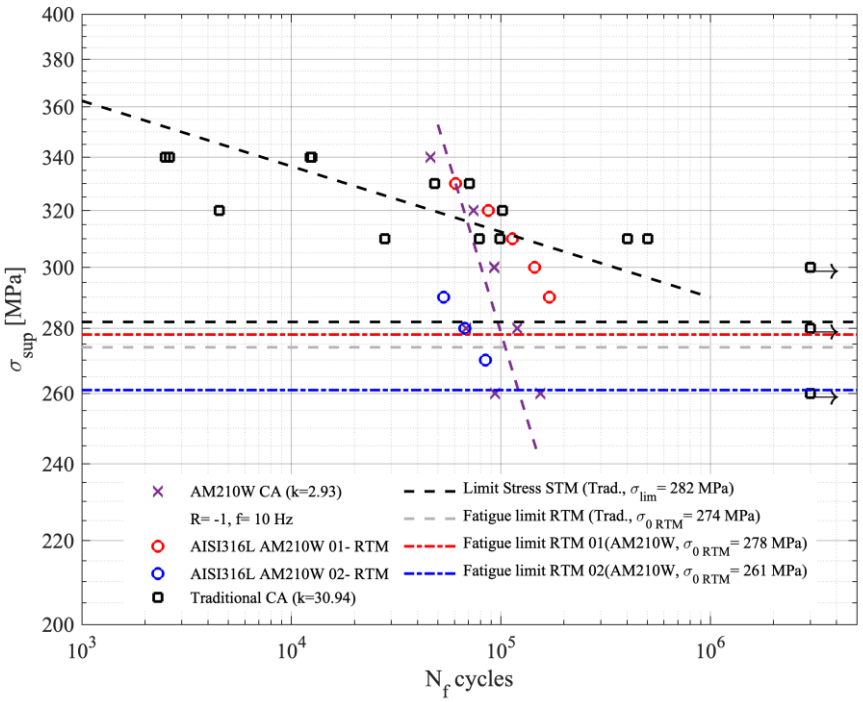

Figure 7.13: S-N curve for AM and traditional AISI 316L steel.

7.3.4 Fractographic analysis

The analysis of the fracture surface has been performed using OM and SEM after the failure of the specimens.

After static tensile tests, the fracture surface of the traditional AISI 316L material exhibits a ductile fracture. The plastic deformation generates irregularly shaped cavities and micro voids which lead to the failure of the specimen. Figure 7.14 shows this typical cup-cone fracture having dimple morphology, with the flat central zone formed by the coalescence of micro voids and the outer surface zone dominated by the sliding of grain planes. On the other hand, the surface of the AM steel with a dimple morphology shows a cup cone fracture less pronounced than traditional one; indeed, some defects and partially melted particles were present.

(a)

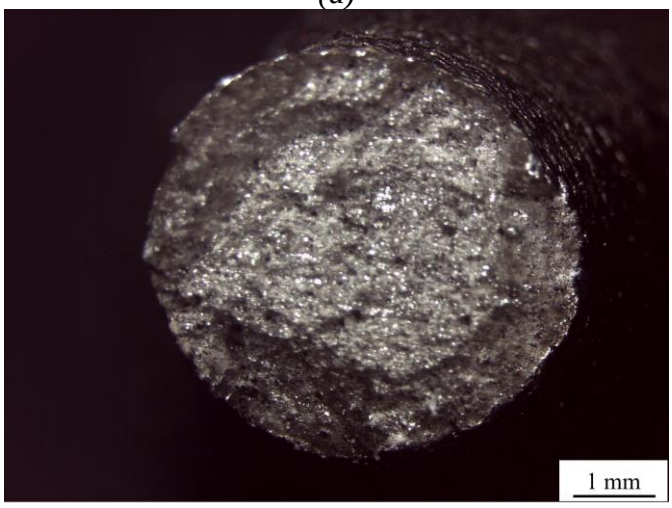

(b)

Figure 7.14: SEM Fracture surfaces images of AISI 316L specimens after tensile tests:

a) traditional; b) AM

In Figure 7.15, an overview of the fracture surface can be seen for fatigue tests on traditional and AM specimens.

For each specimen it is possible to clearly distinguish three main regions: the fatigue fracture region, the transition region, and the final ductile fracture region. The major crack growth direction is indicated by the arrows in Figure 7.15. Surface, or subsurface fatigue crack initiation can be estimated from the overviews.

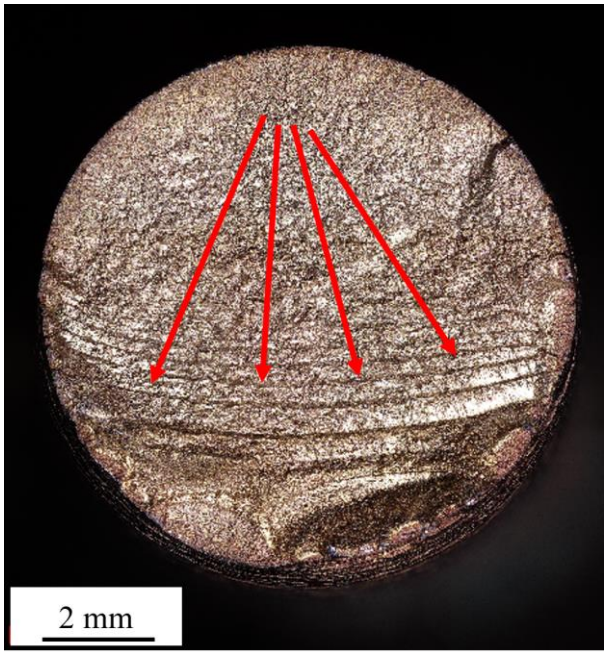

(a)

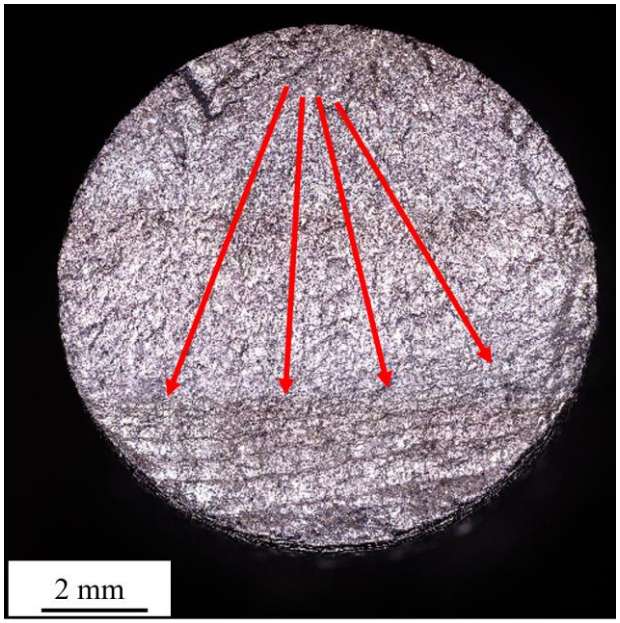

(b)

Figure 7.15: OM panoramic overview of the fracture surface after fatigue test of: a) Traditional and; b) AM material.

For the traditional material a typical cup-cone fracture surface occurred. The fracture surface morphology can be related to the surface hardening resulting from the material processing route – rolling. As a consequence of the processing route, softer core and harder surface is reached, exhibiting different response to the loading. This fact was supported also by the microhardness measurements. A multiple surface fatigue crack initiation has been a characteristic feature for this material while the major crack propagates via the transgranular mechanism (Figure 7.16). The number of fatigue crack initiation sites slightly decreased with decreasing stress level, however, the mechanism remained unchanged. Striations were observed in the fatigue fracture region close to the initiation place. A dimples morphology typical of a ductile fracture mechanism has been observed in the final fracture region.

Due to the lack of defects in the material (no internal/subsurface fatigue crack initiation observed), the surface roughness, impaired by the machining, plays a role in the fatigue crack initiation. In all the cases, the surface roughness act as stress concentrator and is responsible for the fatigue crack initiation. Delta ferrite stringers present in the structure seems to have neither an impact on the fatigue crack initiation, nor on the propagation.

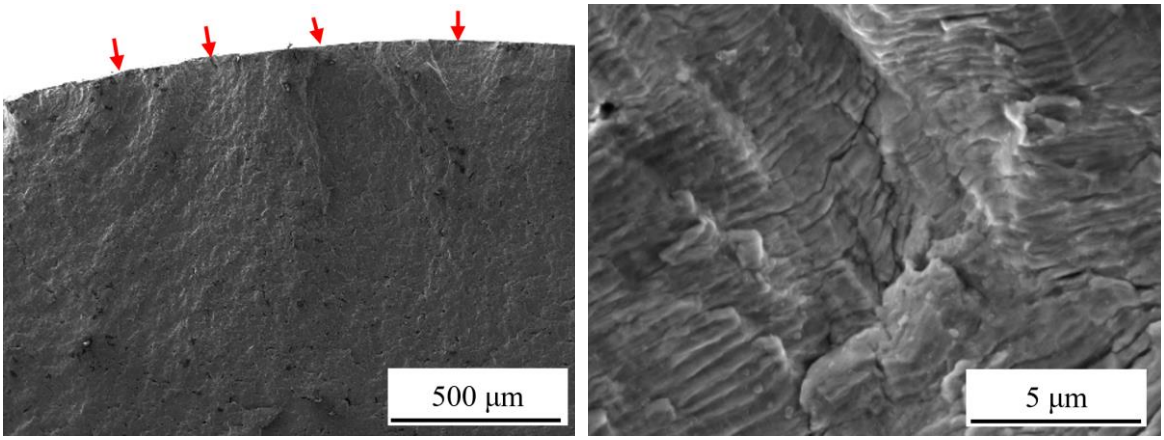

(a) *(b)*

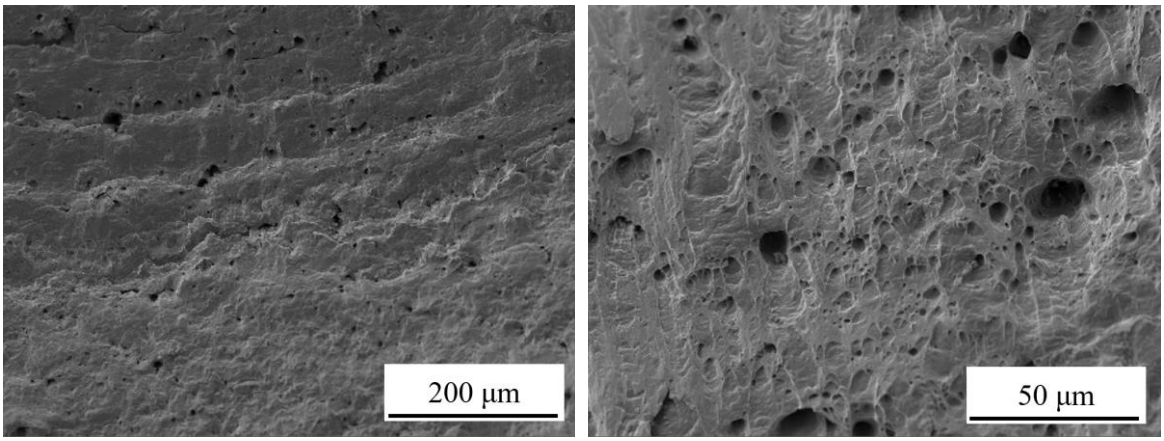

(c) *(d)*

Figure 7.16: SEM fracture surface images of the traditional specimen (σ=320MPa; N_f=4521) a) Fatigue fracture region with marked fatigue fracture initiation sites; b) Fatigue striations near the fatigue fracture initiation place; c) Transition region, mixed failure mechanisms; d) Dimple morphology in the final fracture region.

For the AM material (see Figure 7.17), the fatigue crack originated from a defect on the surface or more commonly from a defect just below the surface of the specimen. Only one initiation site is characteristic for the AM material. The fatigue fracture mechanism, also in this case, is transgranular. Then there is a well-developed transition region in which exist a combination of a transgranular and dimple morphology, followed by the final fracture region. For all the specimens a ductile fracture with a dimple morphology occurred in the final fracture region.

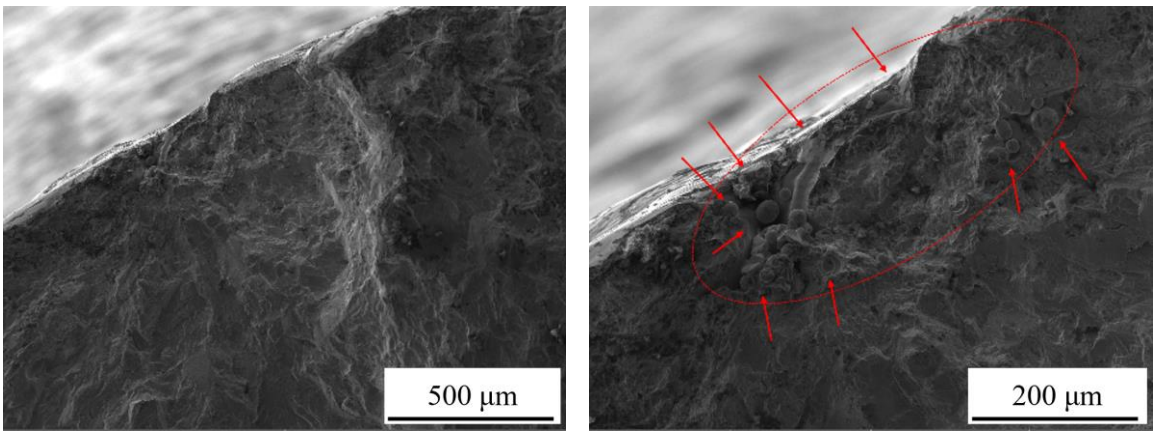

(a) *(b)*

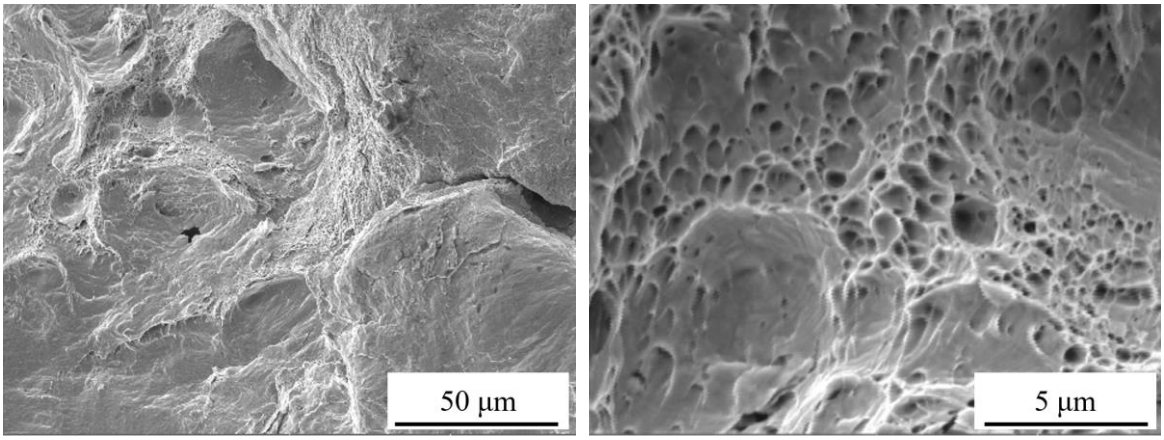

(c) *(d)*

Figure 7.17: SEM fracture surface AM specimen (σ=320MPa; N_f=73955): a) Fatigue fracture region with marked fatigue fracture initiation site; b) Defect, initiation site; c) Transition region, mixed failure mechanism; d) Dimple morphology in the final fracture region.

Several types of defects with different shapes have been identified to act as fatigue crack initiation sites. Some examples are shown in Figure 7.18. As mentioned, from the fatigue point of view, the defects localized on the surface or just below the surface played a role as stress concentrators responsible for the crack initiation. The size of defects observed in the crack initiation sites was even several millimetres (Figure 7.18c).

Most of the defects were formed due to the lack of fusion, creating voids with unmelted powder particles inside. Besides them, also gas pores were frequently observed on the fracture surface and the surface imperfections were also considered to be dangerous from the fatigue point of view. The defects observed on the fracture surface correspond to the porosity analysis (Figure 7.5). There were observed differences between individual printed specimens, which can explain the scatted of the fatigue data.

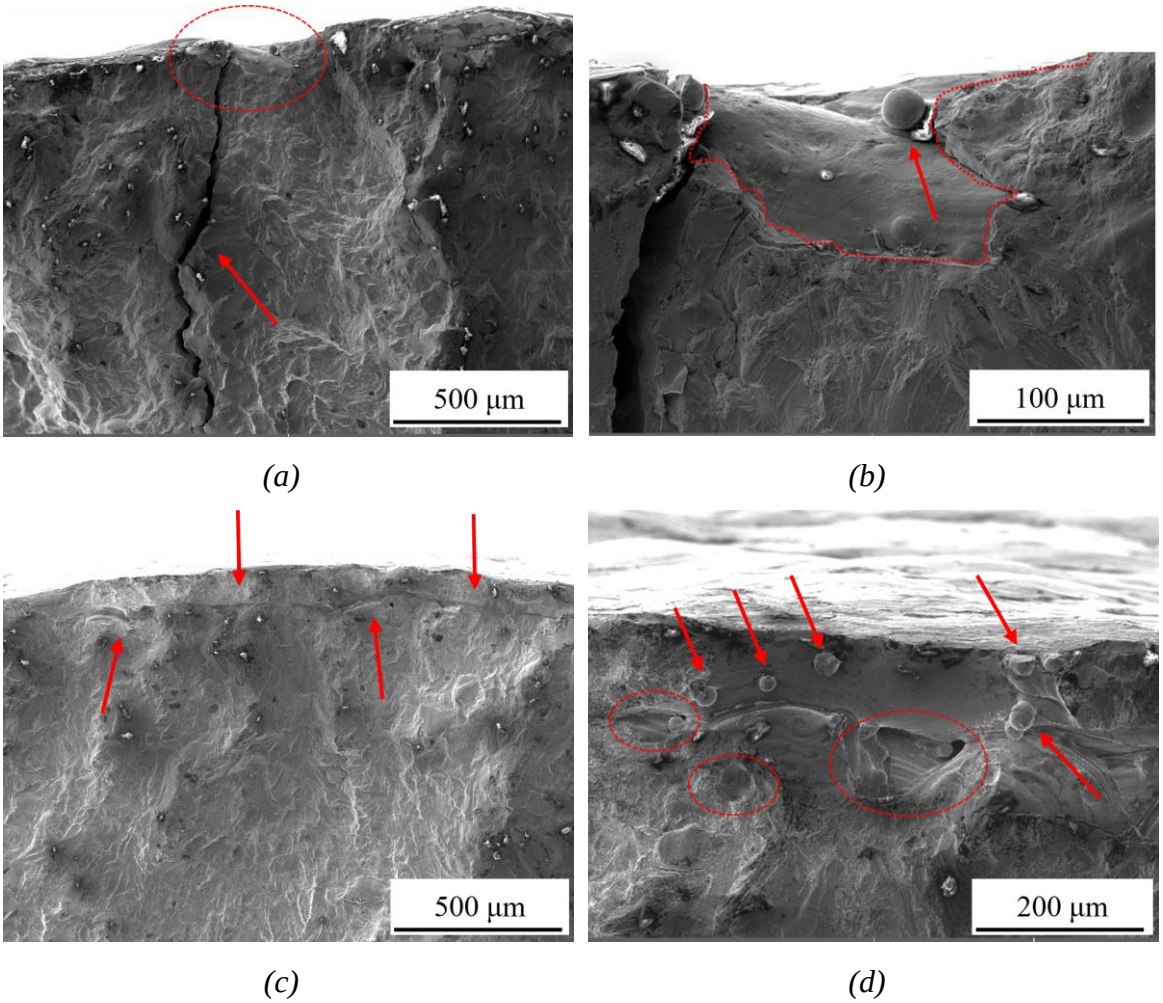

Figure 7.18: SEM view of different types of defects: a) Surface imperfection/notch with a crack along the fatigue fracture region; b) Surface imperfection/notch with an unmelted particle; c) Subsurface defect of more than 1mm in length; d) Unmelted particles and voids.

7.4 Conclusion

The mechanical behaviour and the microstructural characterization of L-PBF stainless steel 316L has been performed and compared to the same steel obtained by traditional machining process.

The microhardness of AM AISI 316L is higher (228.9 ± 7.0 HV) compared to the traditional steel (205.5 ± 4.6 HV); however, a lower ultimate tensile strength has been noticed for AM steel due to the presence of defects such as unfused particles and voids. A more marked difference between the two steels can be noticed in superficial roughness measurements (8.87 ± 1.35 µm for the AM specimens, 0.86 ± 0.06 µm for the traditional specimens). This difference can be addressed to the manufacturing process; indeed, turning process can impair

a better superficial roughness compared to the as-built 3D printed steel, where the presence of superficial defects can lead to an easy crack initiation process in AM AISI 316L steel.
Pore clusters and larger pores have been observed on AM specimens; however, the porosity remained below 0.45%. The internal microstructure of AM AISI 316L is characterized by the presence of several melt pools whose dimensions are strictly related to the printing parameters, while traditional material cross-sections are characterized by polyhedral grains of austenite containing delta ferrite.
Static tensile and stress-controlled fatigue tests have been performed on AM AISI 316L specimens to assess the mechanical properties. During the static tensile tests, the thermal release has been monitored with an infrared camera to assess the limit stress of the material through the Static Thermographic Method; however, due to the internal microstructure, the temperature signal was very noisy, without any significate change in the slope of the signal. Risitano's Thermographic Method has been adopted to assess the fatigue damage and S-N curve of AM steel and the results were compared with the fatigue limit estimated with constant amplitude stress-controlled fatigue tests, showing a reasonable agreement, also considering the amount of time and material required to obtain the result.
After that, fractographic analysis confirmed the failure mechanism and crack propagation under static tensile and fatigue loading conditions. The fatigue crack originated from a defect on the surface or more commonly from a defect just below the surface of the AM specimen; while for traditional AISI 316L steel a multiple surface fatigue crack initiation has been noticed and the major crack propagates via the transgranular mechanism for both the materials under study.

8. EFFECT OF GEOMETRIC IMPERFECTIONS ON FATIGUE STRENGTH: SED

Foti P, Crisafulli D, Santonocito D, Risitano G, Berto F. Effect of misalignments and welding penetration on the fatigue strength of a common welded detail: SED method predictions and comparisons with codes. Int J Fatigue. 2022;164.

Highlights

This work exploits the SED method to investigate the effects of the main geometrical parameters and geometrical imperfections - uncomplete penetration, axial and angular misalignment - on the fatigue strength of cruciform welded joints. The predictions by the SED method have been compared with those of the most known codes. The volume-free procedure for an easy application of the SED method has been used. The SED method has been proved to be consistent with the codes; however, the codes estimations result to be always more conservative than the SED method predictions. The SED method has been proved to be a valid tool to investigate different loading and boundary conditions and to provide useful information to evaluate the most critical point in the component.

Nomenclature

A_R	area of the control volume
$2a, 2a_{int}$	lack of penetration, critical lack of penetration
E	Young's modulus
e	axial misalignment
e_1, e_2, e_3	mode I, II and III functions of 2α in the SED expressions for sharp V-notches
F	remote applied force
FAT classes	the permissible values of the nominal stress ranges at 2 million of cycles
h	weld leg length
K^n_1, K^n_2	mode I and II notch stress intensity factors of a sharp V-notch.
k_m, $k_{m,c*}$,$k_{m,eff}$	fatigue reduction factor, already covered, effective

L_{E3}	transverse plate thickness
l_i	length of cruciform joint arms
N	number of cycles
R	stress ratio
R_0	characteristic length
r	radial coordinate
t, t_{ref}, t_{eff}	plate thickness, reference plate thickness, effective plate thickness (DNV-GL)
$\overline{W}$	averaged Strain Energy Density

Greek

2α	opening angle of V-notch
γ	supplementary angle of α
δ	angular misalignment
$\Delta\sigma_a$	fatigue strength of the butt ground welded joints
$\Delta\sigma_i$	nominal tensile stress
$\Delta\sigma_L$	fatigue limit of the component
$\Delta K_{1A}{}^N$	NSIF-based fatigue strength of welded joints
ΔW_i	critical value of the mean SED at working condition i
ΔW_L	critical value of the SED that corresponds to the fatigue limit
θ	angular coordinate
λ_1, λ_2	mode I and II Williams' eigenvalues for stress distribution at V-notches
λ_{axial}, $\lambda_{angular}$	parameter depending on boundary conditions for misalignment
ν	Poisson's ratio

8.1 Introduction

Welded joints represent one of the most used solutions to connect different members of a structure in several mechanical fields. The arrangement of the joint is usually chosen accordingly to the type of action, force or momentum, to be transferred and to the type of members to be connected. However, considerations about costs and time for the realization cannot be neglected as well [176]. Weld imperfections due to the welding process itself are not avoidable and should be properly accounted for to avoid unexpected failures and ensure the reliability of the entire structure. Typical imperfections that can affect a welded joint are of two main types. The first are flaws related to the welding process itself such as micro-cracks, inclusions, material modification due to the thermal history involved, undercuts and imperfect welding bead shape. The latter are imperfections related to the joint realization such as linear and angular misalignment or lack of penetration cracks, i.e., weld root, not accounted for during the design process. It is worth noting that, if properly considered, real applications could also allow for lack of penetration in the welding in order to decrease costs and time of realization.

The present paper is focused on the investigation of the former type of imperfections that can occur in welded joints. Unlike flaws related to the welding process itself, geometrical imperfections effects can be accounted for during the design of a welded structure.

Even if fatigue is a local phenomenon, the main approaches for the fatigue assessment of welded joints taken into account by most of the codes [177–182] are global design methods such as the nominal stress approach that considers modified nominal stresses in the critical cross section and compares them with the S-N curves related to a particular welded details, defined through its main geometrical parameters and loading conditions, through the so-called FAT class, the allowable stress at $2 \cdot 10^6$ cycles. The imperfections related to the welding process itself are considered by these methods only in a statistical way. On the other hand, dealing with geometrical imperfections, corrections factors are defined when misalignments exceed specific tolerance ranges. More conservative FAT classes are established through these correction factors dealing with both toe failures and root failures when joint with uncomplete penetration are considered. However, dealing with joints having uncomplete penetration, a direct comparison between the critical points in the component, i.e. weld toe and weld root, cannot be carried out. The fatigue assessment is carried out considering different FAT classes, i.e, different fatigue curves, and considering the modified

nominal stress in the attached plate, dealing with weld toe failures, and the modified nominal stress evaluated in the weld throat, dealing with weld root failures. This can represent a topic worth of investigation being failures from weld toe preferred over failures from weld root due to monitorning purposes. Besides, it is worth highlighting that the S-N curve obtained through the nominal stress approach are highly dependent on the geometrical parameters of the fatigue dataset on which they are based. Thus, the fatigue assessment of real industrial components lacks a direct experimental validation due to complex geometries and loading conditions that can differ significantly from laboratory specimens.

A valid alternative to global approaches is represented by local approaches that consider a local quantity as the parameter controlling the fatigue behaviour. This results in a fatigue design curve that does not depend on the global geometry and loading conditions with clear advantages on the fatigue assessment of real components. Several local approaches have been applied for the fatigue assessment of welded joints, such as the notch stress intensity factor (NSIF) method [183,184], the notch stress approach [185], the strain energy density (SED) method [186–190], the peak stress method (PSM) [191–193], and other fracture mechanics methods [194,195].

A characteristic that makes nominal stress approach widely appreciated lies in the fact that they can be also applied for the most common details through elementary theories of structural mechanics, under the assumption of linear-elastic behaviour [196]. On the other hand, local approaches require a certain expertise in their application, due to their peculiar methodology to be applied, and they are usually related to the adoption of finite elements (FE) software.

The main aim of the present work is to apply the SED method, a local approach, to investigate the effects of axial and angular misalignments in a common welded detail and to determine the geometrical conditions that allows to have uncomplete penetration with failure from weld toe. Numerical simulations have been performed adopting a free-mesh procedure, which make straightforward the application of the SED method on complex structures.

8.2 Strain Energy Density method theoretical background

The SED method is a local approach to investigate the fracture of materials both under static and fatigue loading conditions. As formalized by Lazzarin and co-workers [197–199], failure in mechanical components arises when the local SED reaches a critical value that is assumed

to be independent on the component geometry and on the loading conditions. The method is suitable to be applied both to smooth and notched components; dealing with smooth components the SED value can be simply evaluated through the nominal stress on the net section of the component while, dealing with notched components the SED value has to be averaged over a control volume near the notch tip. Recalling the concept of Neuber's elementary material volume [200], just the local stress state near the notch tip affects the fatigue life of the material [201]. Such approach has been applied on sharp and blunt V-notches and blunt U-notches under several loading conditions [202]. For more considerations about the analytic frame of the SED method, we remand to [202,203].

In the following subsections, an overview of the SED method applied to assess the fatigue life of welded details is given and the volume free mesh methodology for a simplified application of the SED method will be also presented.

8.2.1 Fatigue assessment by Strain Energy Density method

Dealing with high-cycle fatigue failure, the application of the SED method, in terms of the cyclic average SED $\Delta\bar{W}$ of the pointed weld notch [204–207], is allowed by two conditions characterising this kind of failure; indeed it usually happens under the linear elastic regime and shows a brittle nature.

According to above, considering a sharp V-notch at the weld toe having an opening angle constant and large enough ($2\alpha \geq 102.6°$) to ensure the non-singularity of mode II, the characteristic length of the control volume R_0 can be estimated by means of the following expression [208], using the fatigue strength of the butt ground welded joint and the N-SIF-based fatigue strength of welded joints ΔK_{1A}^{N}.

$$R_0 = \left(\frac{\sqrt{2e_1}\,\Delta K_{1A}^{N}}{\Delta \sigma_A} \right)^{\frac{1}{1-\lambda_i}} \tag{8.1}$$

Considering a simplified model of the weld toe regions as sharp V-notch, the first theoretical scatter band in terms of cyclic averaged SED [204,205] has been obtained analysing more than 300 fatigue strength data of welded joints characterised by weld toe failure, under different loading conditions. The geometry varied in a great range of the main plane thickness, transverse plate and bead flank (but large enough to ensure the non-singularity of mode II). The analysis was later applied in [204,205] to a larger bulk of experimental data,

with fatigue failures both from the weld toe and root, providing a final synthesis based on 900 experimental data, shown in Figure 8.1, where the number of cycles to failure is given as a function of $\Delta\bar{W}$.

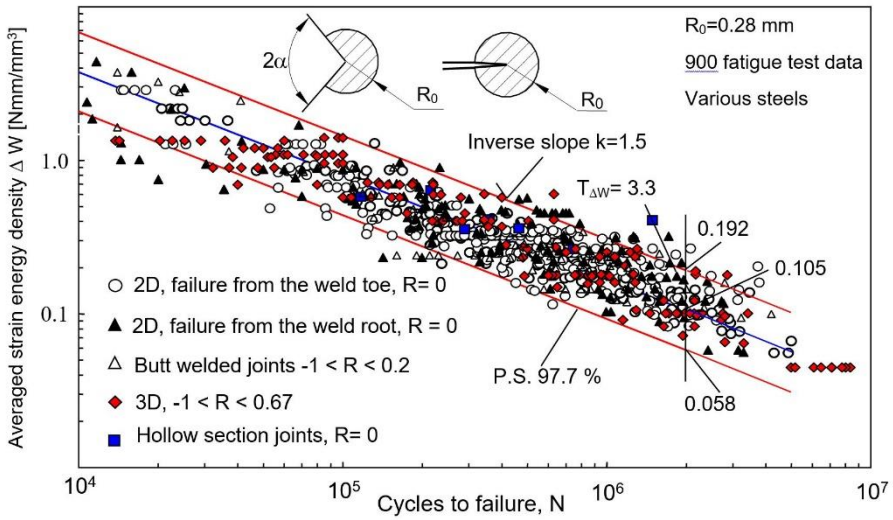

Figure 8.1: Fatigue strength of steel welded joints as a function of the averaged local Strain energy density. Figure from [209].

This provides a robust statistical validation for the SED method applied to high-cycle fatigue failure when the welded plate thickness is equal to or greater than 6 mm.

To evaluate the fatigue strength through the SED method, it is enough to calculate the mean-SED at the weld toe or root for a remote tensile load $\Delta\sigma_i$ through a linear static FE simulation. By means of Equation (8.2), valid only under the assumption of linear elastic behaviour, it is possible to evaluate the remote tensile load $\Delta\sigma_L$ that represents the fatigue strength of the component:

$$\Delta\sigma_L = \Delta\sigma_i \left(\frac{\Delta W_L}{\Delta W_i}\right)^{\frac{1}{2}} \tag{8.2}$$

Being ΔW_L the critical value of the mean SED that corresponds to the fatigue strength.

As regard steel welded joints, according to the above, this value is 0.058 Nmm/mm^3 with a probability of survival of PS= 97.7%.

For more considerations about the fatigue assessment with SED approach and current standards and recommendations, we remand to [210].

8.2.2 SED method application through the volume-free procedure

One of the main limitations for the application of the SED method on commercial FE codes is the need to model the control volume in the pre-processing phase. This sometimes also include to model the control volume in the CAD of the structure under analysis, resulting in a high time effort.

In some recent works, the SED has been evaluated on sharp V-notches under mode I [211,212] and mixed mode [213], blunt V-notches under mode I [214] and blunt U-notches under mixed mode I/II loading conditions [215] without considering the modelling of the control volume in the FE analysis.

To evaluate the average value of the SED in sharp notched components, it is adopted a cylindrical-shaped area centred at the notch tip, the so called "control volume", a circular sector having a radius equal to R_0, a characteristic length that depends only on the material. In general, the higher the brittleness, the lower the characteristic length value.

Useful expression to evaluate the characteristic length can be obtained for plane stress and plane strain conditions dealing with cracks ($2\alpha = 0°$) and sharp V-notches [216].

Dealing with sharp notches, the area of the control volume, being a circular sector of radius equal to the characteristic length R_0, is defined as Eq. (8.3).

$$A_R = \int_0^{R_0} \int_{-\gamma}^{+\gamma} r \cdot dr d\theta = \gamma R_0^2 \tag{8.3}$$

Recalling the average SED value in the control volume due to pure mode I, it can be seen that it is directly proportional to a power of the characteristic length R_0, and it can be given also as a function of the control volume area A_R (Eq. (8.4)):

$$\bar{W} = \left[\frac{e_1}{E} \cdot K_1^2\right] R_0^{2(\lambda_1 - 1)} = \left[\frac{e_1}{E} \cdot \frac{K_1^2}{\gamma^{\lambda_1 - 1}}\right] (\gamma R_0^2)^{\lambda_1 - 1} = \left[\frac{e_1}{E} \cdot \frac{K_1^2}{\gamma^{\lambda_1 - 1}}\right] A_R^{\lambda_1 - 1} \tag{8.4}$$

By applying the logarithm of the member of Eq. (8.4), it can be seen how the SED has a linear trend in a bi-logarithmic graph respect the area of the control volume. The slope of the straight line (λ_1-1) is negative for notch opening angle $2\alpha < 180°$, namely where mode I is singular (Eq. (8.5)).

$$\log \bar{W} = \log\left[\frac{e_1}{E} \cdot \frac{K_1^2}{\gamma^{\lambda_1 - 1}}\right] + (\lambda_1 - 1)\log A_R \tag{8.5}$$

The above equation suggests that the SED can be evaluated in a control volume different than the one with characteristic length R_0. Considering Eq. (8.5), it is possible to write the following equation by performing the ratio between the average SED ($W_{A'}$) evaluated at a generic control volume area A' and the average SED (W_{R0}) evaluated at a control volume with characteristic length R_0:

$$\bar{W}_{R0} = \bar{W}_{A'} \cdot \left(\frac{\gamma R_0^2}{A'}\right)^{\lambda_1 - 1} \tag{8.6}$$

It is to point out that the shape of the control volume, obtained through a selection of elements in the FE model, must be similar enough to a circular sector and that the control volume radius must be within a distance from the notch tip that ensure the prevalence of the notch tip local effect on the stress field. Polar selection (with coordinates r, θ) obtained with a characteristic length too big may result in an overestimation of the SED value.

Avoiding the use of the correction formula (Eq. (8.6)), it is also possible to obtain reliable SED values in a rapid way with an average mesh size (in the selection of elements representative of the control volume in a FE model) equal to 1/8 of the control volume radius [211].

The possibility to assess the SED in the post-processing phase, with a rapid polar selection centred at the notch tip and avoiding the model of the control volume in the pre-processing phase of a FE analysis, allows the adoption of this local approach in very large structures with complex shape and loading conditions.

8.3 Fatigue assessment of Cruciform joints by design Codes accounting for thickness effect and misalignments

All the codes consider the nominal stress approach as main fatigue assessment approach [178,196,217,218]. In codes, the welded joints are distinguished in several details according to their geometrical shape. A specific FAT class is defined for each detail considering a particular set of geometrical parameters while corrections factors are provided to obtain the FAT class for any other set of geometrical parameters according to simple rules. In general

the reference case, for which the FAT class is given, has a value of 25 mm for the principal geometrical parameter describing the joint. In the specific case of a cruciform welded joint, the classified detail has both the attached and the main plate with a thickness of 25 mm. It is worth reporting that, in order to keep the classification as simple as possible, the codes make also the assumption that the S-N curves have, for every welded detail, the same inverse slope. To evaluate the FAT class for a different set of geometrical parameters, a thickness correcting factor, $f(t_{eff})$, should be evaluated on the base of an effective geometrical parameters to be established according to the codes indications. The FAT class for the new set of geometrical parameters can be then evaluated according to the following equation:

$$\Delta\sigma_{(t_{eff})} = \Delta\sigma_{(t_{ref})} \cdot f_{(t_{eff})} \tag{8.7}$$

A detailed overview of the thickness correction factor $f(t_{eff})$, for the different codes considered in the present paper, is reported in Figure 8.4 where, dealing with cruciform welded joints, they are estimated considering the effective and reference thickness of the attached plate (t_{eff} and t_{ref}) and the FAT class ($\Delta\sigma_L$) reduction factor covered by the standards ($k_{m,c*}$). As regards cruciform joints having partial penetration, the codes generally require a double assessment; the weld toe must be assessed according to the FAT classes established for the full penetration joint while the weld root must be assessed considering the stress in the weld throat and considering a FAT class (depending on the codes this could be either 36 MPa or 40 MPa) different from that of the weld toe and not depending on the geometrical parameters of the cruciform joint.

It is important to highlight that, for a detail with a t_{eff} minor than the reference one, a higher fatigue strength should be expected according to the correction factor. On the other hand, such an increase in the fatigue performance should be proved by the designer himself through experimental tests; otherwise, the maximum allowable FAT class that can be used according to the codes is the one suggested for the reference geometrical parameters. Besides the joints must be inspected and found free from discontinuities and misalignments outside specific ranges of tolerance allowed by the codes.

Geometrical imperfections, such as axial and angular misalignments, result indeed in a stress increase in the welded joints as a consequence of secondary bending stresses [219,220]. Dealing with cruciform welded joint, codes already account for axial misalignment up to a certain range by decreasing the detail FAT class. IIW recommendations [196] consider axial misalignment, e, already covered up to $0.15 \cdot t$, being t the attached plate thickness, by

decreasing the FAT class value of a factor $k_{m,c*} = 1.45$, being k_m the fatigue reduction factor. The British Standard (BS:7910:2005) [178] considers axial misalignment, e, already covered up to $0.05 \cdot t$, by decreasing the FAT class value of a factor $k_{m,c*} = 1.15$. The Eurocode 3 standard (EC3) [217] and DNV-GL rules [218] consider axial misalignment, e, already covered up to $0.15 \cdot t$ that result in a factor $k_{m,c*} = 1.45$ considering the constrain condition (CC) shown in Figure 8.2b and an equal length for the attached plates ($l_1 = l_2$). Angular misalignment on the other hand should be always accounted for. When e exceeds the value listed in the above, a correction in the evaluated nominal stress should be considered. Most of the codes suggests equations for the evaluation of the effective fatigue reduction factor, $k_{m,eff}$, evaluable as:

$$k_{m,eff} = \frac{k_{m,calculated}}{k_{m,covered}} \tag{8.8}$$

Being $k_{m,covered}$ the value of k_m already considered in the FAT class and $k_{m,calculated}$ the value of k_m to be assessed through the following formulae, which consider both axial and angular misalignment, in the case of toe failure:

$$\begin{aligned} k_{m,calculated} &= 1 + \left(k_{m,axial} - 1\right) + \left(k_{m,angular} - 1\right) \\ &= 1 + \lambda_{axial} \frac{e}{t} \frac{l_1}{(l_1 + l_2)} + \lambda_{angular} \frac{\alpha}{t} \frac{l_1 \cdot l_2}{(l_1 + l_2)} \quad for\ weld\ toe;\ l_1 \\ &\leq l_2\ \ (EC3; IIW; BS) \end{aligned} \tag{8.9}$$

For root failure, the stress is referred to the weld throat and only the axial misalignment is considered:

$$\begin{aligned} k_{m,calculated} &= 1 + \left(k_{m,axial} - 1\right) \\ &= 1 + \frac{e}{t} \cdot \frac{1}{1 + h/t} \quad for\ weld\ root\ \ (EC3; IIW; BS) \end{aligned} \tag{8.10}$$

Being h the welding height, l_1 and l_2 the length of the attached plates while λ_{axial} and $\lambda_{angular}$ are parameters dependent on the boundaries conditions, listed in Figure 8.2 and reported from table D.2 of BS [221].

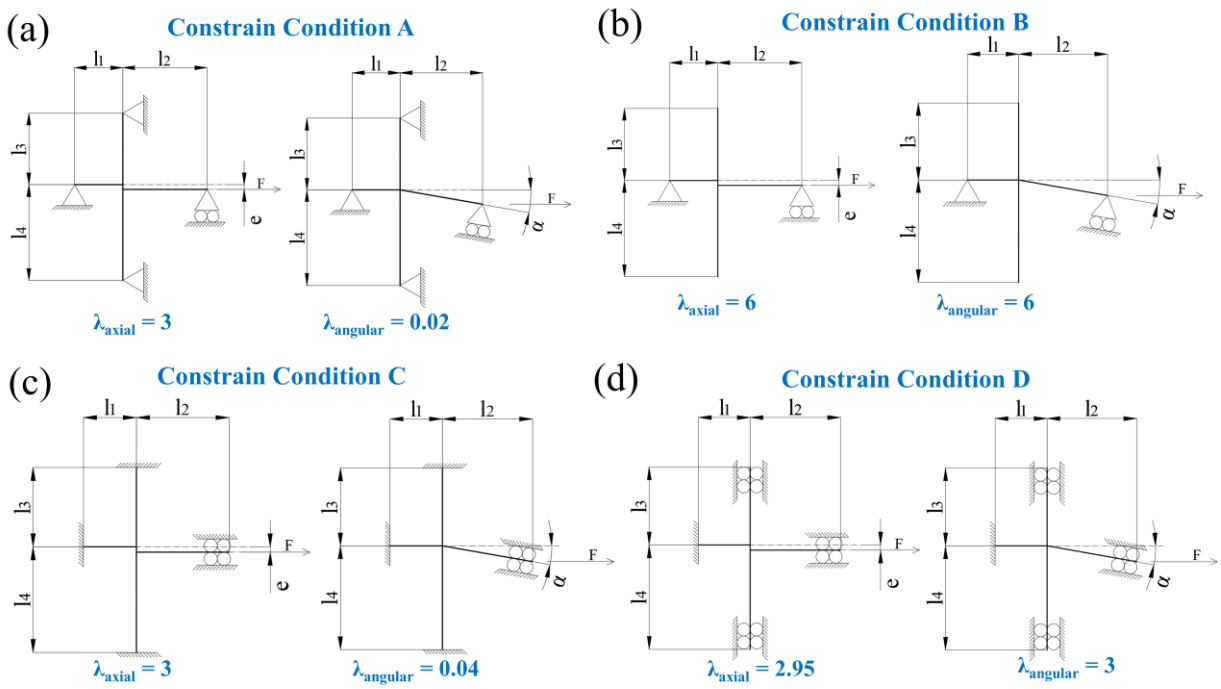

Figure 8.2: Values of the parameters λ_{axial} and $\lambda_{angular}$ for the four different constrain conditions (CC) considered by BS:7910:2005 [221].

It is worth noting that DNV-GL [218] rules report only the equation to assess k_m for axial misalignment and for boundaries conditions as in Figure 8.2a according to the following equation:

$$k_m = 1 + \frac{6 \cdot t^2 \cdot e}{l_i \cdot \sum_{i=1}^{4} \frac{t_i^3}{l_i}} \qquad for\ weld\ toe\ (DNV-GL) \tag{8.11}$$

being l_i the length of each plate and t_i the thickness of the i-th plate.

The value of k_m to be considered should then be the highest between the four values k_{m,l_i}. It is worth highlighting that the Eq. (8.11) results to be only a more general case of Eq. (8.9). Indeed, if we consider a unique value for the thickness of the four plates and assume that $l_1 \geq l_2$ as specified by IIW and BS, under the conditions that:

$$\frac{1}{l_1} + \frac{1}{l_2} = \frac{1}{l_3} + \frac{1}{l_4} \tag{8.12}$$

It is possible to obtain the fatigue reduction factor for this joint as:

$$k_m = 1 + 3 \cdot \frac{e}{t} \cdot \frac{l_1}{l_1 + l_2} \tag{8.13}$$

That is the Eq. (8.9) in case of just axial misalignment for the boundary conditions of Figure 8.2a.

In the present paper, due to different specifications between the codes considered, a comparison with the SED predictions will be done considering the same thickness and the same length for all the plates in the cruciform joint.

8.4 FE modelling

To assess the effect of axial and angular misalignment on a cruciform joint, several 2D finite element simulations were carried out under the plane strain conditions and with material properties typical of a structural steel (E= 206 GPa, ν= 0.3). Geometrical parameters of a cruciform joint were considered, such as the plate thickness t, the transverse plate thickness L_{E3} and the weld leg length h (Figure 8.3a). Some simplifying assumptions were made to properly model the cruciform joint geometry. The weld toe angle was modelled as a sharp V-notch with an opening angle of 2α= 135°; however, dealing with joints having angular misalignment the weld toe on the attached plate (T_3 and T_4 in Figure 8.3b) resulted in a notch opening angle $2\alpha = 135° \pm \delta$ being δ the angular misalignment. The weld leg length of the attached plate with angular misalignment was estimated from the interserction between the attached and transverse plates. To account for lack of penetration of the weld bead, a macrocrack of length 2a and weld root angle 2α= 0° was modelled between the attached plate and the transverse plate.

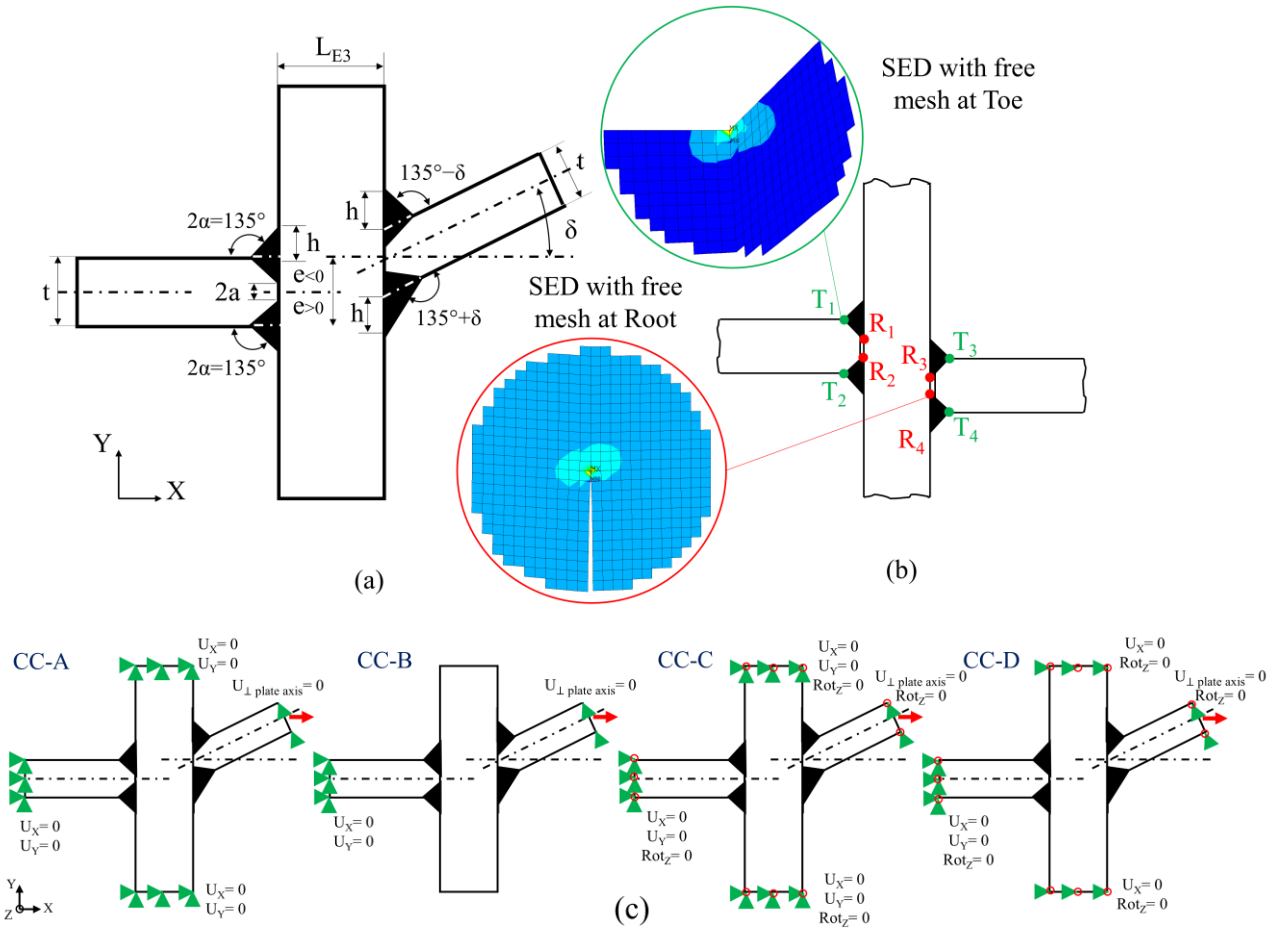

Figure 8.3. a) Parametric model of the cruciform joint with axial and angular misalignment; b) Critical points (Toe, T, and Root, R) where the SED is evaluated with a polar selection (r= 0.28mm); c) Constraint Conditions for the FE simulations.

The lengths of the joint arms (l_1 to l_2, Figure 8.2) were assumed all equal to 200 mm, while the weld leg length was assumed equal to 0.5t, with the attached plate thickness t= 25mm. Axial (e) and angular (δ) misalignment of the right attached plate were considered respect to the left one and the remote force F was applied on the right attached plate in X direction. The cruciform joint was analysed through a parametric model realized in Ansys® APDL. A free mesh procedure for the whole joint was adopted considering the 8-nodes element PLANE183. In order to decrease the computational time required, a mesh size of t/4 has been established at the end of the plate arms, while in the welded zone a mesh size of t/40 has been established and further refined at the weld toe and root to achieve a mesh size equal to $R_0/8$ (Figure 8.3b). The SED values at these regions were obtained with a polar selection from the notch tip with a radius $r=R_0= 0.28$ mm.

Four different constraint configurations (nominally A to D, Figure 8.3c), as observed in current standards and recommendations (Figure 8.2), were adopted.

A first group of simulations (I) was performed on cruciform joints without any kind of misalignment by varying the transverse plate thickness (L_{E3}=25÷300 mm) and the attached plate thickness (t= 20÷50 mm), adopting the CC-B of Figure 8.3c. A second group of simulations (II) was performed for a cruciform joint for each CC of Figure 8.3c, with L_{E3}= 25mm, that present at the same time axial and angular misalignment, therefore δ was ranged between 0° to 10°, while *e* was ranged from -12.5 mm to 12.5 mm. The condition of complete penetration (2a=0) was considered. A third group of simulations (III) was performed considering the variation of the weld leg length-plate thickness ratio (h/t) from 0.2 to 1, associated to an axial misalignment with the same range of variation of the previous simulations (e= -12.5÷12.5 mm). In this case, the condition of incomplete penetration (2a= t) was considered for each CC of Figure 8.3c. A fourth group of simulations (IV) was performed considering the variation of the transverse plate thickness (L_{E3}= 12÷150 mm) paired with an axial misalignment and a lack of penetration 2a up to 10 mm for each CC of Figure 8.3c.

8.5 Results and Discussions

From FE simulations performed under four different CC and varying the cruciform joint parameters (geometric configurations I to IV), the averaged SED over a control volume has been evaluated at toe and root regions. The modelling of the control volume has been avoided by adopting a free mesh procedure that consists in performing a polar selection of elements with a radius equal to 0.28mm at the notch tip representative of the control volume.

The SED of the cruciform joints with misalignments, axial or angular, has been estimated and compared with the one of the cruciform joints without any misalignment. To evaluate an equivalent fatigue reduction factor in terms of stresses, k_m, by the SED approach, the square root of the ratio between the averaged SED of the misaligned cruciform joint and the no-misalignment joint has been evaluated at toe or root regions according to Eq. (8.14):

$$k_{m,equivalent} = \sqrt{\frac{\overline{W}_{misalignment}}{\overline{W}_{no\ misalignment}}} \tag{8.14}$$

In the following sections, a comparison between the fatigue reduction factor as assessed by SED methos and by current standards and recommendations has been carried out.

8.5.1 Comparison between SED and Standards in cruciform joints without misalignment

The first series (I) of FE simulations investigates the effects of the main geometrical parameters of the cruciform joint, i.e., L_{E3} and t, considering boundary conditions as CC-B and the full penetration condition, that is, no macro-crack in the root region, and a constant value for the ratio between the welding leg length and the attached plate thickness ($h/t = 0.5$). The ranges chosen for the two main geometrical parameters of the joints have been established taking into account the ranges already considered by the EC3 which for this joint defines different FAT classes (Figure 8.4a). As it is possible to observe from Figure 8.4, the FAT classes, estimated through the SED method, are affected by the main geometrical parameters according to relationships different than those considered by the codes. However, the codes show a certain degree of inconsistency between themselves. In particular, the SED method predicts a higher sensitivity of the FAT class with changing the plate thickness t, while the transverse plate thickness L_{E3} shows a significant lower effect on the fatigue strength of the component. Regarding the absolute value of the predicted FAT, considering the SED fatigue curve for a P.S. of 97.7%, it is possible to see how the use of the SED method leads to more conservative estimations of the FAT class if compared to the ones suggested by the codes that has been increased in Figure 8.4 by a factor $k_{m,c*}$ to neglect the decrease in fatigue strength due to possible axial misalignments. This has been done because the SED estimations are carried out through FE models that consider a cruciform joint having the attached plates perfectly aligned.

The surface of the FAT classes predicted through the SED method can be approximated with a good degree of accuracy through the following equation:

$$\begin{aligned}\Delta\sigma_{L(t_{eff};L_{eff})} &= \left(\frac{L_{ref}}{L_{eff}}\right)^{0.0321} \cdot \left(\frac{t_{ref}}{t_{eff}}\right)^{1-\lambda_1} \cdot \Delta\sigma_{L(t_{ref};L_{ref})} \\ &= \left(\frac{20mm}{L_{eff}}\right)^{0.0321} \cdot \left(\frac{20mm}{t_{eff}}\right)^{0.3264} \cdot 69\ MPa\end{aligned} \tag{8.15}$$

In which λ_1 is William's mode I eigenvalue for a notch opening angle of 135°. The maximum error to estimate the FAT class with the proposed relation (Eq. (8.15)) is equal to

-5.5%, promoting a safe estimation of it respect the codes. Such equation is valid only for cruciform welded joints having $h/t = 0.5$.

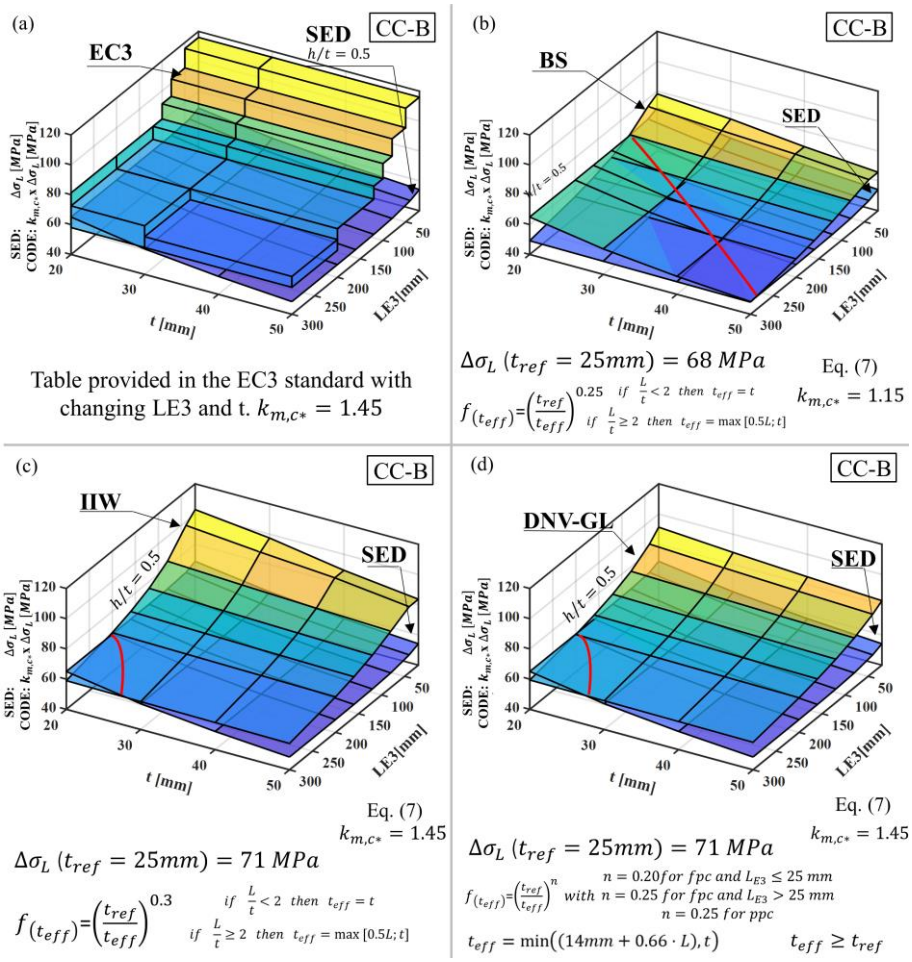

Figure 8.4: Comparison between standards and recommendations vs. SED

8.5.2 Full Penetration joint with misalignment (angular and axial)

Cruciform joints with a full penetration of the weld bead, and with axial and angular misalignment have been considered. From the analytical formulae reported in BS, the fatigue reduction factor k_m has been evaluated and compared with the one evaluated with the SED method (Eq. (8.14)). The results evaluated at the most critical toe regions, T_1 and T_3 (Figure 8.3b) have been reported, considering that these toe regions resulted in the highest value of SED and, as a consequence, more critical conditions for the component. The fatigue reduction factor has been reported respect the angular and axial misalignment normalized to the plate thickness (δ/t and e/t respectively).

As it is possible to observe from the diagrams reported in Figure 8.5, the SED predictions follow trends similar to those suggested by the codes for the different boundary conditions

considered; however, the codes resulted to be slightly more conservative with respect to the SED estimations. It is important to highlight that the estimations of the SED method could be slightly affected by the assumption done at the toe notch opening angle that result to be dependent on the angular misalignment, as explained in section 8.4, but the effect has been assumed to be negligible due to the range of angular misalignments chosen. As it is possible to observe from Figure 8.3, positive and negative values of axial misalignment have been considered, while the angular misalignment has been considered to be only positive. Indeed the results that could have been acquired considering also the negative values of the angular misalignment are already covered through the variation of the axial misalignment. As a matter of fact, the other combinations of axial misalignment and angular misalignment not considered would have been equal to the conditions studied with only a change in the toe that would result the most critical. Toe region T_1 at e/t<0 and δ/t<0 would follow the trend of T_2 at e/t>0 and δ/t>0; while T_3 at e/t<0 and δ/t<0 would follow the trend of T_4 at e/t>0 and δ/t>0 and vice versa. Similar consideration can be done comparing e/t<0 and δ/t>0 with e/t>0 and δ/t<0. It is worth highlighting that the codes result to be conservative also due to the consideration of the most critical combination of misalignments. Indeed, as it is possible to observe from Figure 8.5, the fatigue strength reduction found for e/t<0 and δ/t>0 are slightly less critical then those found for e/t>0 and δ/t>0; this result in conservative estimations when dealing with e/t<0 and δ/t>0. Finally, the most critical point in the component has been noticed to change from T_3 for e/t>0 and δ/t>0 to T_1 for e/t<0 and δ/t>0.

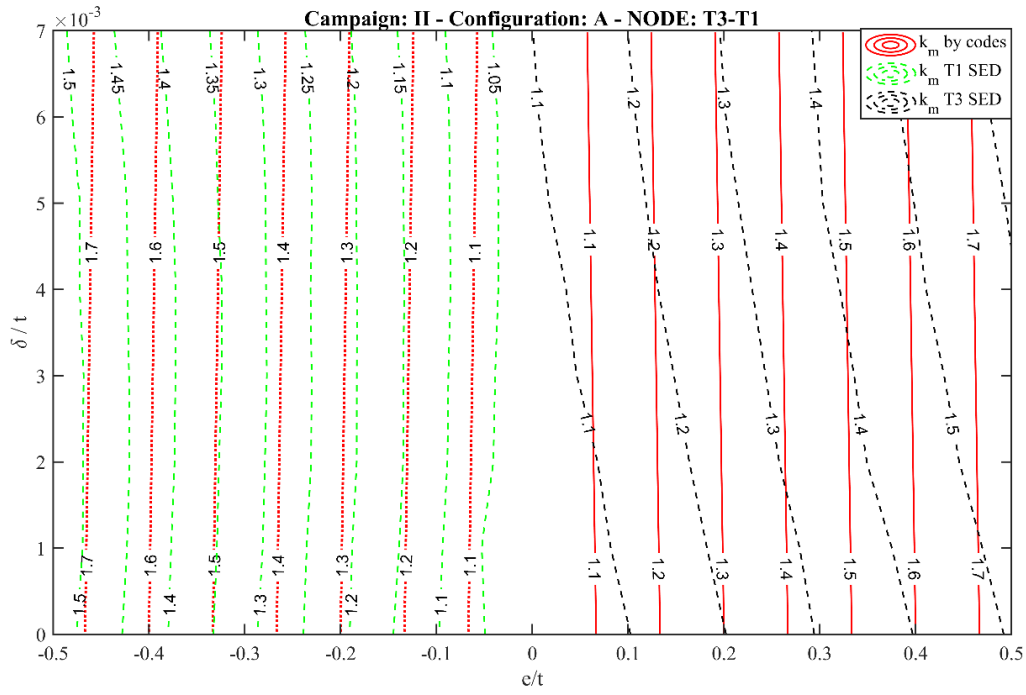
Campaign: II - Configuration: A - NODE: T3-T1
k_m by codes
k_m T1 SED
k_m T3 SED
×10^-3
1 / ρ
e/t

(a)

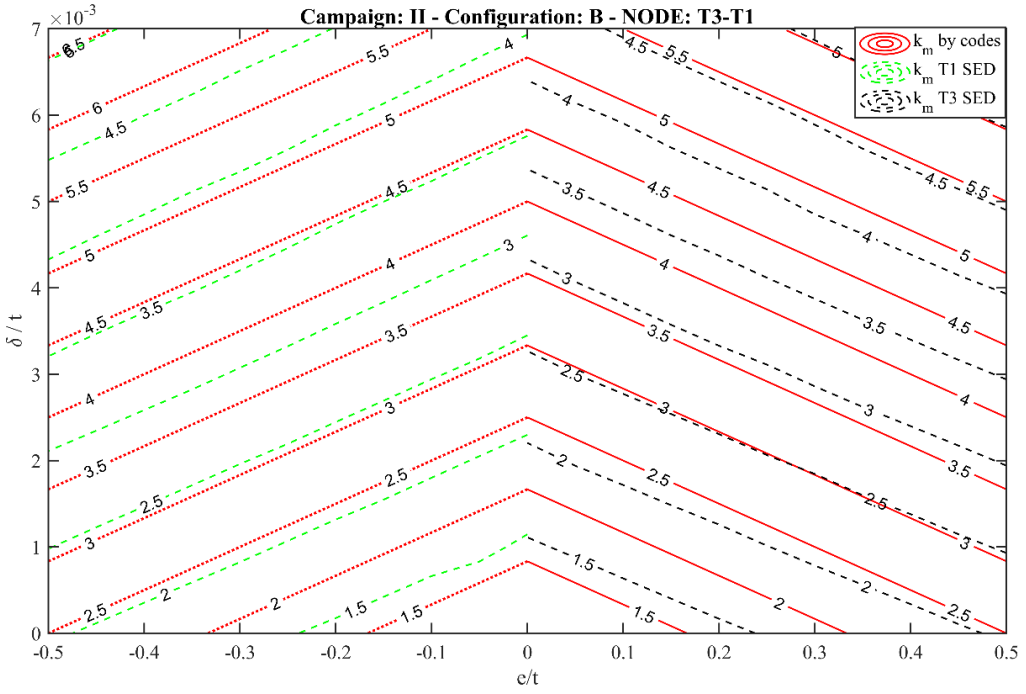
Campaign: II - Configuration: B - NODE: T3-T1
k_m by codes
k_m T1 SED
k_m T3 SED
×10^-3
1 / ρ
e/t

(b)

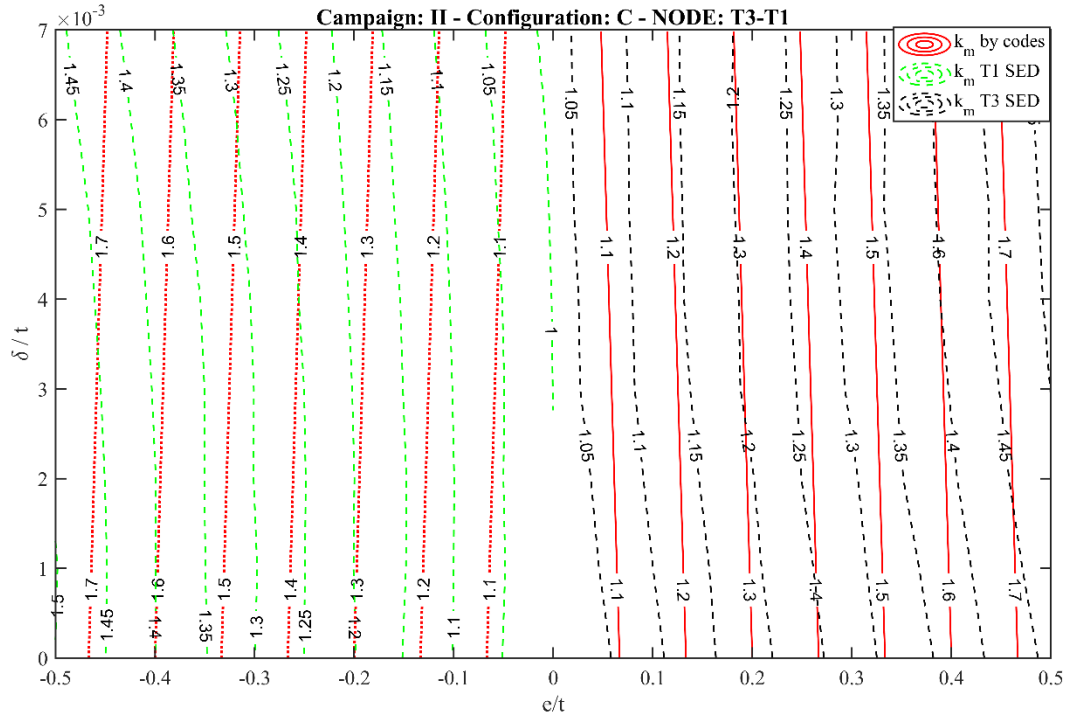

(c)

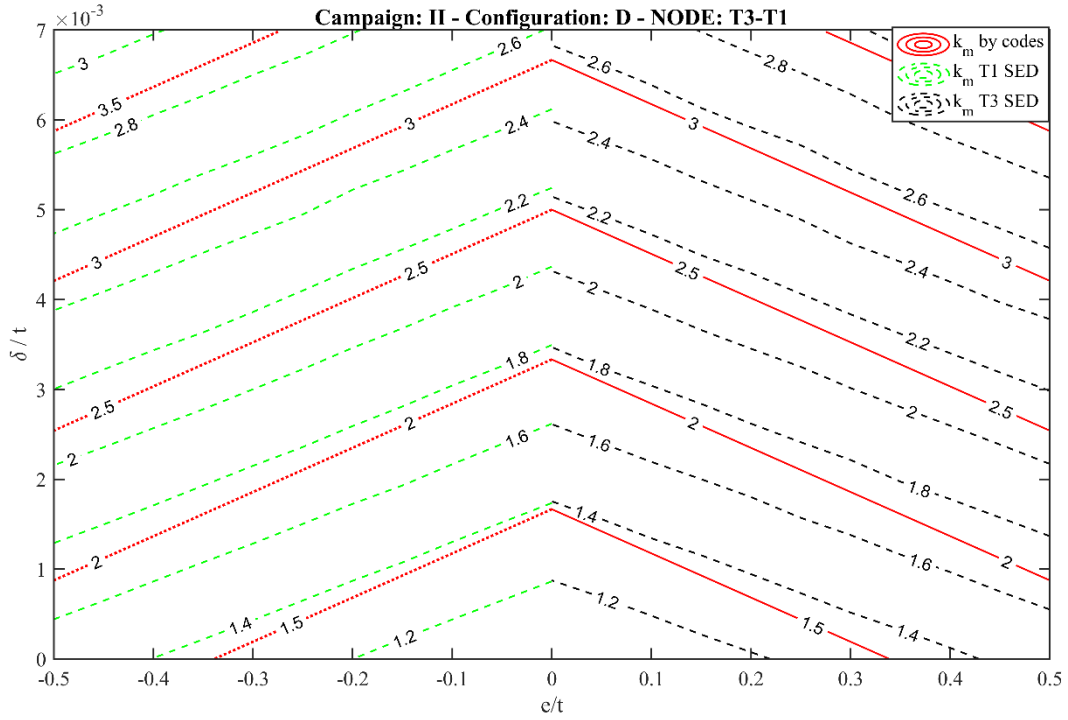

(d)

Figure 8.5: Fatigue reduction parameter km at toe region T1 and T3 for several constrain conditions of cruciform joint (t=LE3= 25mm) with axial and angular misalignment.

8.5.3 Incomplete penetration joint with axial misalignment

Cruciform joints having incomplete penetration, i.e. a macro-crack with length 2a=t, have been investigated with changing the axial misalignment. The results of the investigations through the SED method and the application of Eq. (8.14) have been compared with the fatigue reduction factor k_m suggested by BS. It is worth highlighting that, in this case, the value of $\bar{W}_{no\ misalignment}$ must change with changing the ratio h/t to properly account for the fatigue reduction. The fatigue reduction factors evaluated both with codes and SED approach have been reported versus the weld leg length and the axial misalignment normalized respect the plate thickness (Figure 8.6).

The most critical root in the component has been found to be the root R_3 (see Figure 8.3) regardless of the CC. Of course, having negative value for the misalignment, according to Figure 8.3, the most critical point is expected to be R_4 with the same values of fatigue reduction seen for R_3 and positive values of the misalignment. In general, the codes predictions, according to Eq. (8.7), for the fatigue reduction factor are more conservative than the SED predictions that show however similar trends to those of the codes.

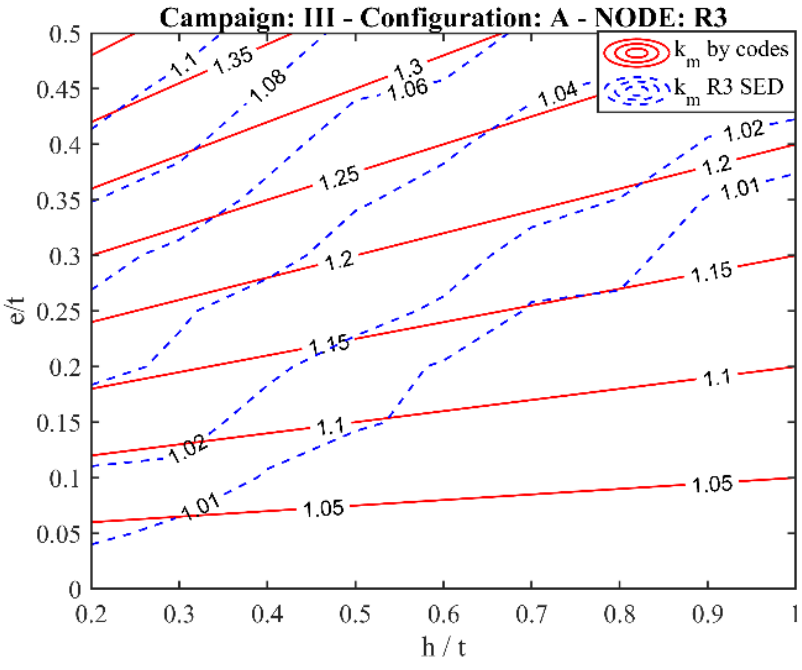

(a)

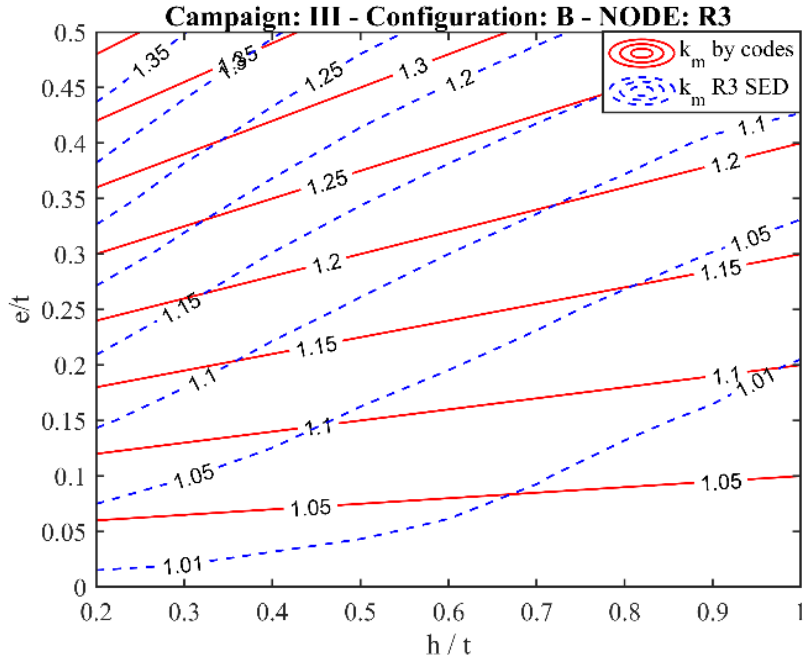
Campaign: III - Configuration: B - NODE: R3
k_m by codes
k_m R3 SED
e/t
h / t

(b)

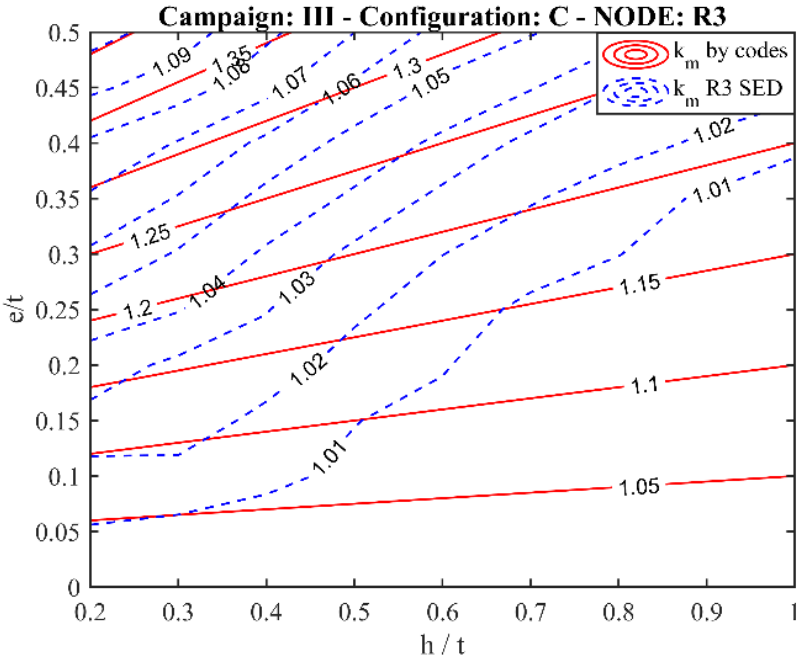
Campaign: III - Configuration: C - NODE: R3
k_m by codes
k_m R3 SED
e/t
h / t

(c)

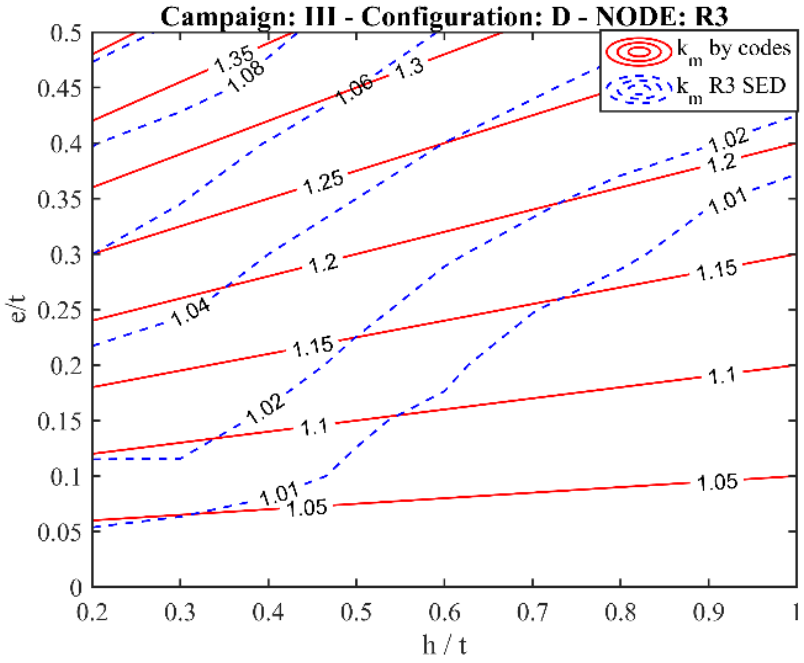

(d)

Figure 8.6: Fatigue reduction parameter km at root region R3 for several constrain conditions of cruciform joint with axial misalignment.

8.5.4 Equiprobability of failure without misalignment

According to the current standard and recommendations, the lack of penetration must be performed both at toe and root weld regions through different FAT classes depending to the critical point considered. On the other hand, the SED approach assesses the fatigue strength of both weld toe and root regions through a unique fatigue master curve ($\overline{W}$ vs. number of cycles to failure, Figure 8.1), allowing for a direct comparison between them to establish which is the most critical point in the component. The low computational resources, enhanced by the free mesh procedure, required by the SED method to obtain information about the level of criticality of weld toe and root regions allowed to perform numerical investigations to find the geometrical conditions that lead to an equiprobability of failure from both regions by varying the level of weld bead penetration (i.e. the lack of penetration 2a). Figure 8.7 reports the critical value of lack of penetration, where toe and root regions are equally critical respect the weld leg length and transverse plate thickness. Geometrical conditions that fall below the surface will have failure from the weld toe. Low values of the lack of penetration result in more critical value at the weld toe, a condition to be preferred for inspection purposes. As it is possible to see from Figure 8.7, considering different values

of the parameter h/t, a change in the trends of the curves describing the normalized crack length 2a/t that leads to equiprobability of failure from the weld toe and the weld root can be noticed. In particular, low values of h/t result in a crescent monotonic trend of 2a/t with increasing L_{E3}, while high values of h/t result in a first decrease of 2a/t followed by a crescent monotonic trend with increasing the value of L_{E3}. Such a change in the trend of the equiprobability surface with changing the parameter L_{E3} has to be related to the interaction of the two internal root cracks that, with decreasing L_{E3}, become closer. The effect has been seen to became more relevant when $L_{E3}/t<1$ and when the value of h/t increases, as it is possible to observe from the figures.

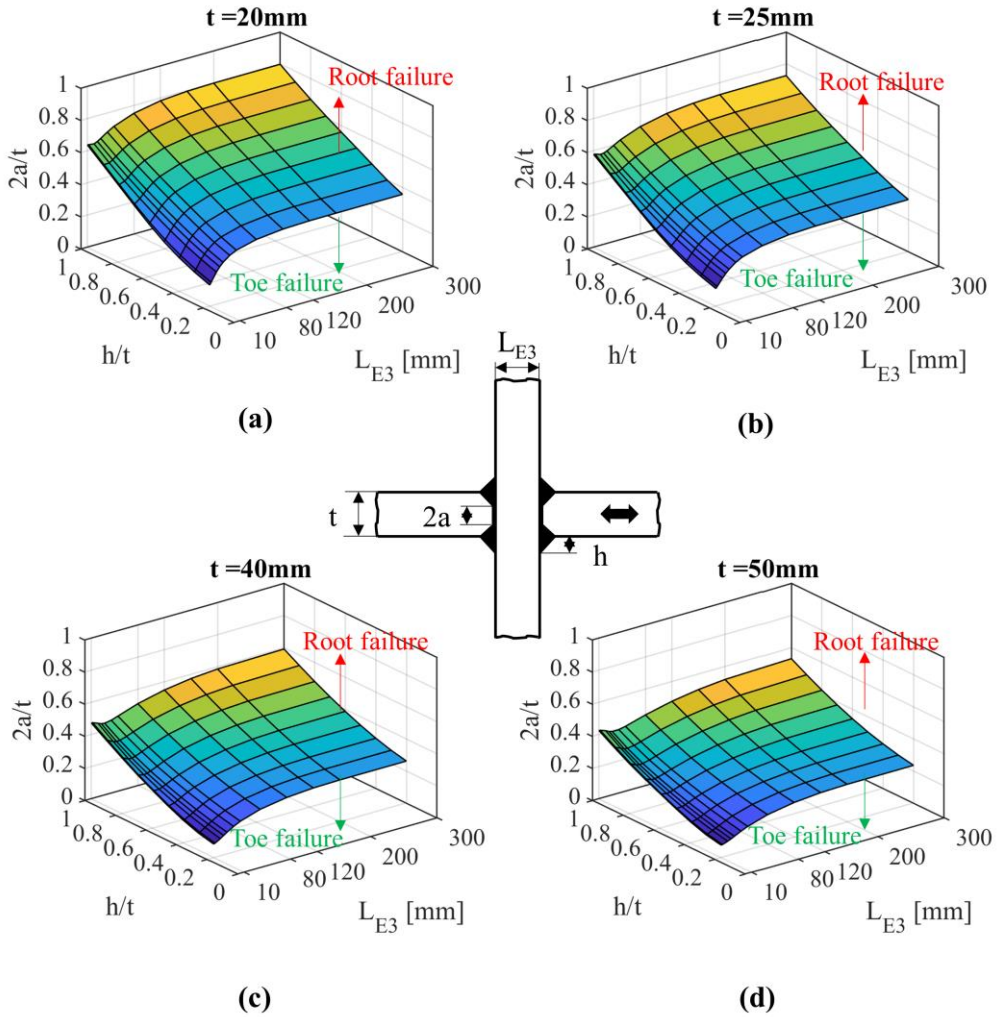

Figure 8.7: Equiprobability of failure from toe and root regions for different plate thickness.

8.5.5 Equiprobability of failure with axial misalignment

Finally, the IV series of simulations investigate the effects of the axial misalignment on the equiprobability of failure curves from the weld toe and the weld root. FE simulations have been carried out with changing the transverse plate thickness (L_{E3}), weld penetration (2a/t) and axial misalignment (e/t). By considering the SED *vs* 2a/t curves, as in Figure 8.8, the value of lack of penetration that leading to equally critical conditions at the weld toe and root have been established for different values of e/t and L_{E3}.

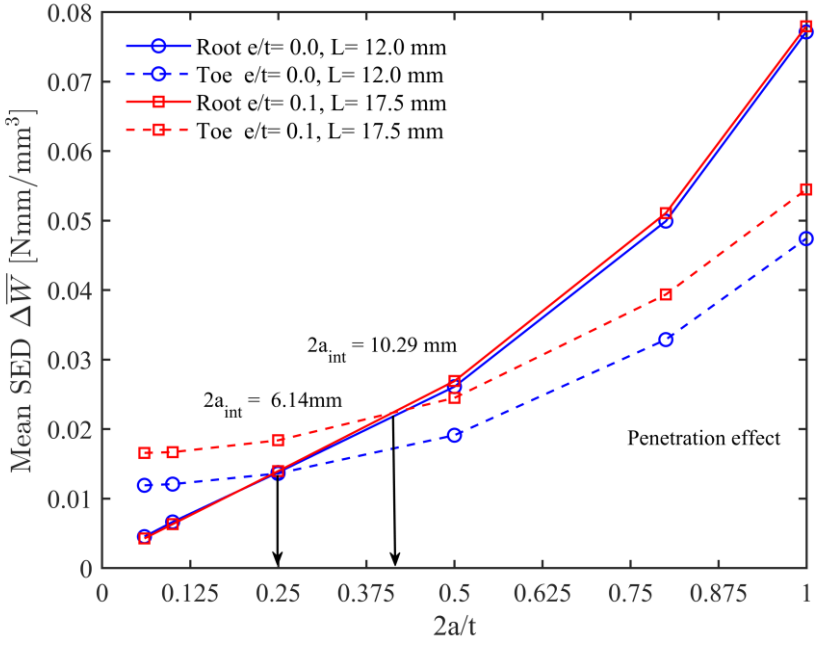

Figure 8.8: Effect of lack of penetration on the SED at toe and root region for constrain configuration C with different axial misalignment (t= 25mm, e/t= 0 and 0.1).

Figure 8.9 shows the equiprobability curves of failure from weld toe and root regions versus L_{E3} and 2a/t for different configuration of e/t. The axial misalignment affects the interaction between the two root cracks (R_1-R_2 and R_3-R_4), but no effect is detected on the equiprobability curves for large values of the transverse plate thickness when dealing with the configuration A, C and D. Indeed, it can be noticed from Figure 8.9a, that reports only the diagram of CC A due to similar trends for C and D, that the curves reach a convergence for large values of L_{E3} ($L_{E3}/t>3$). Large transverse plate thicknesses smooth the effect of the axial misalignment on the stress field of the cruciform joint. On the other hand, an effect of the axial misalignment has been found for CC B on all the range of L_{E3} considered.

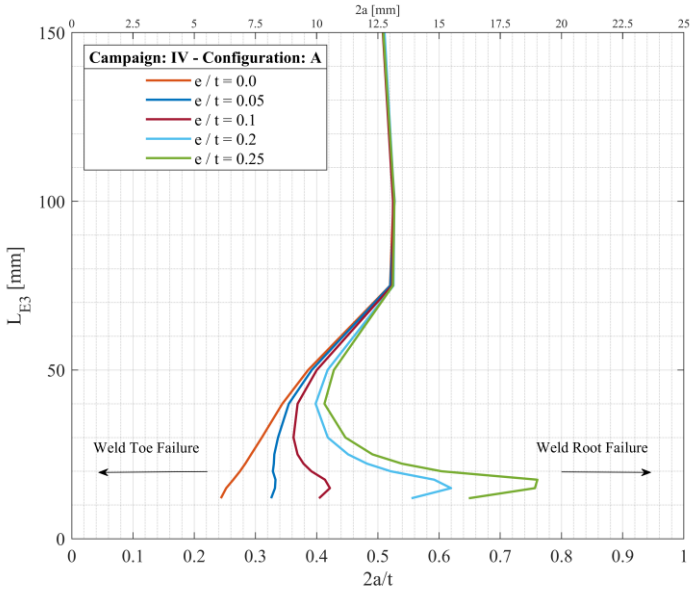

(a)

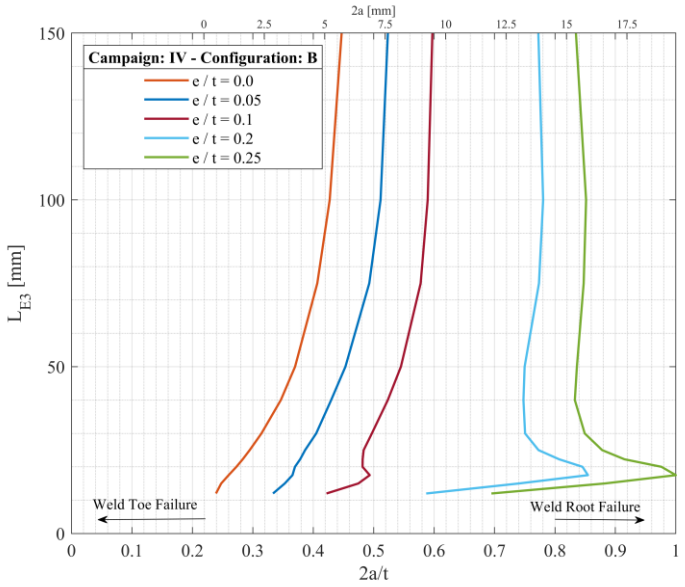

(b)

Figure 8.9: Equiprobability of failure from Toe-Root regions with plate thickness t= 25 mm and a) CC-A; b) CC-B.

8.6 Conclusions

In the present work, the SED method has been applied to investigate the effects of the main geometrical parameters and of geometrical imperfections -uncomplete penetration, axial and angular misalignment- on the fatigue strength of a cruciform welded joint. Comparisons between the SED predictions and several standards and recommendations -Eurocode 3

standard, British Standard, IIW recommendations and DNV-GL rules- are also provided. Four different numerical simulation campaigns have been performed exploiting the SED low sensitivity to mesh refinement and the volume-free procedure, which make straightforward the application of the SED on complex structures. The main outcomes of the work are as follow:

- The relationships suggested by the codes result in an overestimation of the effect of the intermediate plate thickness, L_{E3}, while the SED predictions show that it has a lower influence on the fatigue strength of the joint. If corrected for the axial misalignment already accounted for in the suggested FAT classes, all the codes overestimate the fatigue strength of the joint according to the SED predictions, while the BS suggested more comparable FAT classes.
- The relationships suggested by the codes to evaluate the fatigue strength reduction, k_m, due to misalignments in full penetration joints have been found to be more conservative than the SED estimations. The trends found through the SED method are consistent with those reported by the codes. This further proves the validity of the method to study the fatigue strength of these components when affected by geometrical imperfections also dealing with other boundary conditions that may be found in real applications and that are not considered by the codes.
- The most critical weld roots in the component have been found to be those on the externally loaded attached plate (R3 and R4 in Figure 8.3) regardless of the constraint conditions. The codes have been found to be conservative with respect to the SED predictions. The trends have not been found to be affected by the welding leg length and misalignment.
- While codes only suggest a different fatigue assessment at the weld toe and root when dealing with incomplete penetration cruciform joint, the SED method allows for a direct comparison of these two critical points of the component. The lack of penetration values, 2a, that leads to an equal probability of failure from the weld toe and weld root have been evaluated through the SED method with changing different geometrical parameters. It has been noticed that with changing the boundary condition, the axial misalignment could result in different effects on the equiprobability curves. The combination of geometrical parameters leading to weld toe failure, a preferred condition in real application due to monitoring purposes, can be chosen in clear way.

9. A NEW APPROACH FOR CUSTOMISED HIP PROSTHESIS

Milone D., Risitano G., Pistone A., Crisafulli D. and Alberti F. A New Approach for the Tribological and Mechanical Characterization of a Hip Prosthesis Trough a Numerical Model Based on Artificial Intelligence Algorithms and Humanoid Multibody Model. Lubricants 2022, 10, 160. https://doi.org/10.3390/lubricants10070160

Highlights

The aim of this work was to propose a new approach for the customised design of hip prosthesis. Based on the physical characteristics of the patient, a humanoid model is recreated using machine learning techniques, which simulates the movement cycles and estimates the acting forces to which the prosthesis is subjected. These forces will be used to optimise the design of the hip prosthesis from a tribological and mechanical point of view.

Abstract

In recent years, thanks to the development of additive manufacturing techniques, prosthetic surgery has reached increasingly cutting-edge levels, revolutionizing the clinical course of patients suffering from joint arthritis, rheumatoid arthritis, post-traumatic arthrosis, etc. This work aims to evaluate the best materials for prosthetic surgery in hip implant from a tribological and mechanical point of view by using a machine-learning algorithm coupling with multi-body modelling and Finite Element Method (FEM) simulations. The innovative aspect is represented by the use of machine learning for the creation of a humanoid model in multibody software environment aimed to evaluate the load and rotation condition at the hip joint. After the boundary conditions have been defined, a Finite Element (FE) model of the hip implant has been created. The materials properties and the information on the tribological behaviour of the material couplings under investigation have been obtained from literature studies. The wear process has been investigated through the implementation of the Archard's wear law in the FE model. The results of the FE simulation show that the best wear behaviour has been obtained by CoCr alloy/UHMWPE coupling with a volume loss due to wear of 0.004 μm^3 at the end of the simulation of ten sitting cycles. After the best pairs in terms of wear has been established, a topology optimization of the whole hip implant structure has been performed. The results show that, after the optimization process, it was

possible to reduce implant mass making the implant 28.12% more lightweight with respect to the original one.

9.1 Introduction

In recent years, thanks to the development of additive manufacturing techniques, prosthetic surgery has reached increasingly cutting-edge levels, revolutionizing the clinical course of patients suffering from joint arthritis, rheumatoid arthritis, post-traumatic arthrosis, congenital dysplasia etc. In fact, the use of 3D printing has made it possible to obtain prostheses optimized [222] on the needs of patients, using high-performance materials such as stainless steel 316L [69] or Ti-6Al-4V [223,224]. However, due to the kinematics and dynamic nature of implants, wear is primarily caused by regular gait activity such as walking, sitting, or running, leading to deterioration the material used in the joint [225,226]. The problems of friction and wear in hip prosthesis, as well as in other types of mechanical joint, have been studied by many authors [227,228] to quantify the effects on the quality, reliability, and durability of the prostheses. Shankar et al. [229] have investigated the tribological behavior of zirconia toughened alumina (ZTA) against titanium alloy (Ti-6Al-4V), using ball-on-disc tribometer with four loading conditions (15, 20, 25 and 30 N) and five different bio-lubricants to evaluate the friction and wear. They obtained results suggested that sesame oil could improve tribological behavior as a bio-lubricant for ZTA-Ti-6Al-4V combination. Mattei et al [230] have performed a preliminary experimental investigation on the evolution of the wear map of hip replacements during wear testing for ceramic-on-UHMWPE hip prosthesis. The results revealed important characteristics of the damaging process not highlighted by the standard gravimetric procedure such as worn area location and shape as well as the progress of local damages. As demonstrated by numerous studies, the use of traditional materials has been gradually replaced using more performing materials [231–233]. The attention has been focused on the wear resistance, corrosion resistance and biocompatibility, as well as the traditional techniques of production have been joined by Additive Manufacturing (AM) technique. Through the AM it was possible to obtain customized devices on the needs of patients and therefore more effective. Moreover, in order to guarantee a longer life cycle of the prosthesis and an appropriate lubrication, the application of nanostructured coatings and surface processing was studied [234–237], such as the surface laser texturing technique already widely used in other industrial sectors [238,239]. Numerical techniques have recently been adopted, such as the Finite Element

Method (FEM) to support experimental studies regarding the calculation of the useful life and the functionality optimization of the prostheses [240]**.** These techniques support the already developed algorithms based on the use of artificial intelligence and machine learning, which allowing to determine fundamental parameters such as the position of the centre of mass [241–243], permit to evaluate the exactly load distribution on the prosthesis. Fadela et al [244] have analysed the optimal stress distribution in the total hip prosthesis with the aim to the development of a redesigned prosthesis type in order to minimize stress concentration in the cement, using 3D-finite element analysis. Bhawe et al. [245] have analysed how the combination of UHMWPE, CoCrMo alloy, and Ti-6Al-4 V alloy affect the femoral head sizes from 24 mm to 48 mm to know the best size, using Finite Element Method (FEM). This work aims to evaluate the best materials for prosthetic surgery from a tribological and mechanical point of view by using a machine-learning [246] algorithm coupling with multi-body model of a human body and Finite Element Method (FEM) simulations. The innovative aspect is represented by the use of machine learning, which allows the identification of the marker motion of a humanoid model developed in a multibody software environment. This approach could be an alternative strategy for the simulation of the load and rotation condition on a hip prosthesis concerning the conventional ones, such as hip simulators. The information on the tribological behaviour of the materials obtained through a Pin on Disk FEM model, which allows the optimization of the prosthesis, suggesting the best geometry and the most performing materials. In particular, the attention has been focused on hip prosthetic implant and on the wear process between the femoral head and the acetabular cup. A humanoid model has been developed in MSC ADAMS™ environment aimed at evaluating the load and rotation conditions on the hip joint during sitting cycles. A FEM of a hip implant has been developed in Ansys workbench R2 2020™ environment in order to establish what of the following pairs have a better behaviour in terms of volume loss due to wear:

1. CoCr Alloy / UHWMPE
2. Ti6Al4V / Ti6Al4V
3. Si3N4 - TiN /Si3N4 - TiN

The choice of investigating these coupling is related to the fact that they are biocompatible materials largely used in commercial hip implant [247]. Moreover, metal-metal couplings such us CoCrMo and Ti6AlV are well investigated in literature from the stress distribution

point of view [248]. In this sense, this work represents an evolution because it gives additional information about the wear behaviour, which complete the general overview for this materials type. For what concern the ceramic-ceramic coupling (Si3N4-TiN), it was already investigated by the authors [240], but in this work, it has been adopted a different prosthesis geometry and the load and rotation conditions have been evaluated by a customizable humanoid model and not from gait cycles coming from literature studies[249], like in the previous work. The wear process has been investigated through the implementation of the Archard's law [240,250–252] in the FEM and whose characteristic coefficients have been obtained from literature studies [226,240,253–255]. At the end of the simulations, it has been observed that the best wear behaviour has been obtained for CoCr alloy/UHMWPE coupling, with a volume loss due to wear of 0.004 μm^3at the end of the sitting cycles. The results have been also compared with literature studied [225,226,229,230,240,249] showing a good agreement with them. After the best pairs in terms of wear has been established, a topology optimization of the whole hip implant structure has been performed. The results show that, after the optimization process, it was possible to reduce implant mass and minimize the compliance of the entire system, making the implant lightweight and more comfortable for the patients.

9.2 Materials and Methods

9.2.1 Numerical modeling

The development of human models increased with the necessity to understand the biomechanics of movements and their consequences on human comfort [245–248]. These models are always used to simulate prosthetic design's influence on the human system [249–251]. In recent years, particular importance has been given to modelling the jaw and its interactions with prostheses. The CT scan has characterized the bony structure. In the literature, various models allow extrapolating the mechanical characteristics, the constraints and the loads on certain bodies subjected to specific actions [255,256]. Researchers are increasingly focusing on creating models that simulate the whole body rather than limiting themselves to small specific sections [257]. Simulation techniques such as the multi-body study the whole-body motion since the body is considered a set of links connected by joints. Multibody [258] simulations find a great application in sports biomechanics [259]. On this basis, the definition of the dynamic equation of human movement and the acquisition of the dynamic parameters of human action are the critical steps in the theoretical analysis of the

biomechanics of movement. Another field of dynamic simulation is the analysis of the interaction between the human exoskeletons [260]. Finally, motion capture is often used to define the trajectories of body joints in multi-body simulations. With this technique, the movement of an object is recorded through various video acquisition devices arranged in space. From the recorded images, the coordinates (X, Y, Z) of a series of markers affixed to the subject are found; this allows to quantify the position, speed, acceleration of these points and consequently the movement produced by the subject during a given action. It will enable one to fully understand the mechanical characteristics underlying the human body's activities and the rules for controlling motor skills. The workflow adopted in this study is shown in Figure 9.1: Workflow adopted for the investigation of the wear process and the topology optimization of the implant structure.

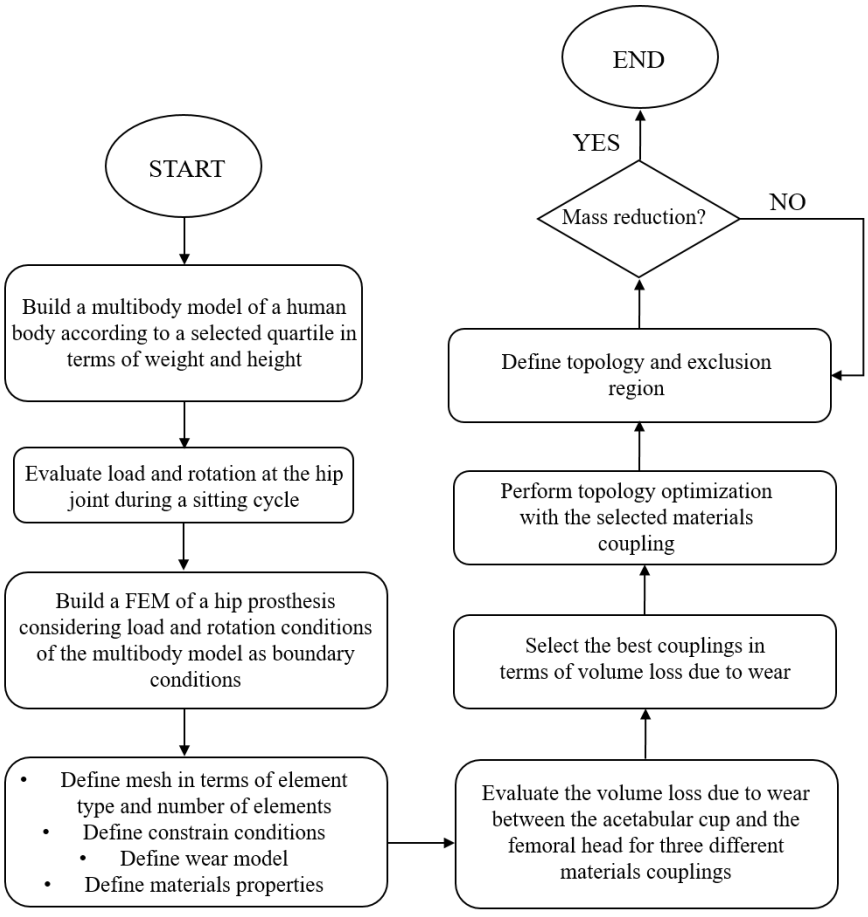

Figure 9.1: Workflow adopted for the investigation of the wear process and the topology optimization of the implant structure.

2.2 Parametric human model

As reported previously, this work aims to make a closing loop simulation, where the output is the optimization of a hip prosthesis. The first step was the building of the human model. Adams was used to build the multi-body model. as reported in [261–263] 31 dimensions were used to create the mannequin (Table 9.1).

Table 9.1: Body Dimensions

Reference Number	Dimension	Reference Number	Dimension
0	Weight	[236]	Hip Breadth, Standing
1	Standing Height	[237]	Shoulder to Elbow Length
2	Shoulder Height	[238]	Forearm-Hand Length
3	Armpit Height	[239]	Biceps Circumference
4	Waist Height	[240]	Elbow Circumference
5	Seated Height	[241]	Forearm Circumference
6	Head Length	[243]	Waist Circumference
7	Head Breadth	[242]	Knee Height, Seated
8	Head to Chin Height	[244]	Thigh Circumference
9	Neck Circumference	[245]	Upper Leg Circumference
10	Shoulder Breadth	[246]	Knee Circumference
11	Chest Depth	[247]	Calf Circumference
12	Chest Breadth	[248,249]	Ankle Circumference
13	Waist Depth	[249]	Ankle Height, Outside
14	Waist Breadth	[250]	Foot Breadth
15	Buttock Depth	[251]	Foot Length

The human model was divided into:

- Lower limbs: Left / Right Thigh, Left / Right Shank, Left / Right Foot.
- Upper limbs: Left / Right Upper arm, Left / Right Forearm, Left / Right Hand.
- Torso: Pelvis, Abdomen, Thorax.

Each part was connected to another by a spherical joint. Each human segment has 3 DOF. Two knee and elbow joint rotations were locked (Figure 9.2). Contact with the ground and left and right feet were created.

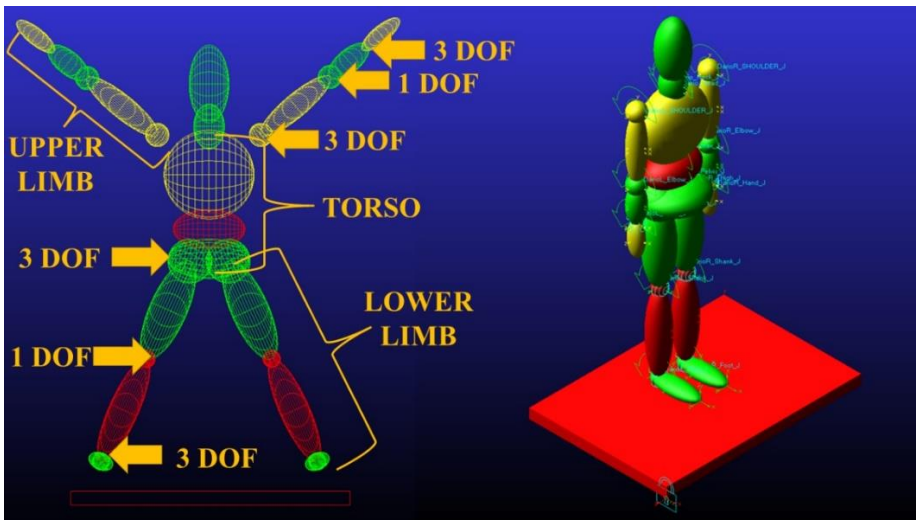

Figure 9.2: Dummy model

The mannequin has the following characteristics:

- Weight: 85 kg
- Standing Height: 1755 mm
- Seated Height: 918 mm

Inertial quantities and mass distribution were calculated as reported in [[264,265]. Finally, motion lows were applied to the knee and hip joint to reproduce the stand-to-sit movement.

9.2.2 Motion capture

Human pose estimation is the process of inferring human poses from a digital image. Pose estimation requires highly accurate detection and identification of human joints. Pose estimation algorithms follow a top-down or a bottom-up approach. As reported previously, after building the dummy, the motion lows were included in the model. For this reason, a

markerless motion capture analysis was performed. OpenPose was used to evaluate realtime body pose [266–269]. OpenPose is a bottom-up real-time multi-person human pose detection library that detects the human body, foot, hand, and facial keypoints on single images. It can detect 135 vital body points from a digital image. The innovative tense is that no markers are needed. A single CNN is used for both key-point detection and association. When key points are detected, a numerical score between 0 and 1 is assigned. It is a measure of the overall confidence in the key points estimated. OpenPose has been trained to produce three different pose models. The difference is represented by the number of points identified:

- MPI can estimate a total of 15 key-points.
- COCO can estimate a total of 18 points.
- BODY_25 can estimate a total of 25 points.

The most exhaustive pose model is the third. In addition to the key points estimated by MPI and COCO models, it contains descriptors for the feet and pelvic center. Exist also a new and experimental model of OpenPose that is named body_25b (Figure 9.3). As reported in [270,271], this model has the highest accuracy parameters, which is more accurate than the default body_25 and reduces the number of false positives. The keypoint definition differs from MPII for the evaluation of head and neck keypoints and removes the neck and middle hip keypoint of the body_25 model. As shown in Figure 9.2, BODY_25B was used for the analysis.

Figure 9.3: Human pose detection with OpenPose

9.3 Experimental tests

9.3.1 Sit-to-Stand Movement

The sit-to-stand test (STS) is movement done with great frequency in daily activities life. This test quantifies the type of movement to get up from a chair [272], and the loads acting on the locomotor system [273]. STS involves skills such as coordination, balance control and stability [274,275]. The number of repetitions completed provides quantitative information with which to assess functional fitness levels [276], and it was used in the rehabilitation field . Recently, several studies have highlighted the importance of kinematic parameters to provide qualitative information on how the movement is performed. This movement can be schematized as acting on the plane; for this reason, it is helpful for the calibration of the optimization algorithm.

Motion acquisition and multibody analysis

The subject was positioned in front of the camera in a standing position. The angle between hip/spine and knee/hip is 180 degrees in this situation. A video of its movement was recorded. The subject performed the sit-to-stand exercise sequentially. The handling of the points was extrapolated with the use of OpenPose. As in [277] The knee angle was calculated using the vector dot product.

$$\theta = \cos^{-1}\left(\frac{\vec{a} * \vec{b}}{|\vec{a}||\vec{b}|}\right) \tag{9.1}$$

Two vectors were constructed from the hip, knee, and ankle coordinates obtained from the pose data. The first vector was formed with the hip and knee joint, while the knee and ankle joint formed the second one. The same things were done to evaluate hip angle. The following equation gives the knee angle ($\boldsymbol{\theta}$) for the frame in Figure 9.4.

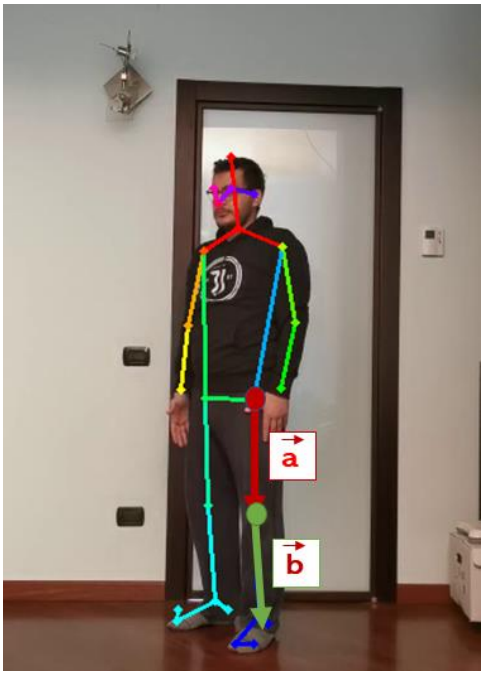

Figure 9.4: Angle measurements from video frame

Two vectors were constructed from the hip, knee, and ankle coordinates obtained from the pose data. The first vector was formed with the hip and knee joint, while the knee and ankle joint formed the second one. After the extrapolation of the angles from the frames, the laws of motion were created in Adams (Figure 9.5).

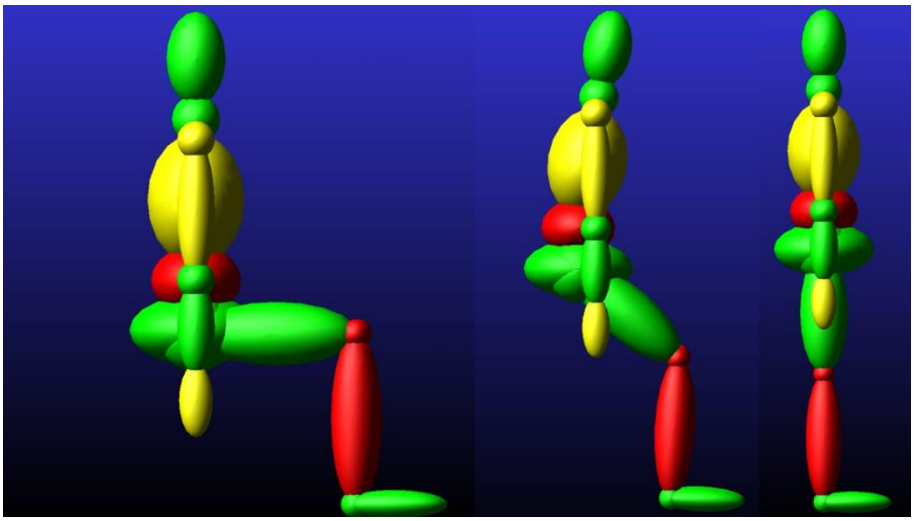

Figure 9.5: Simulation of motion in Adams

The movement of the humanoid was simulated; therefore, the loads acting on the hip were extrapolated over time.

9.3.2 Hip prosthesis Finite Element Model (FEM)

Geometry, mesh, and boundary condition definition

The prosthesis implant adopted in this work for the Finite Element Analysis (FEA) is a commercial hip implant. The main geometry parameters are shown in Figure 9.6.

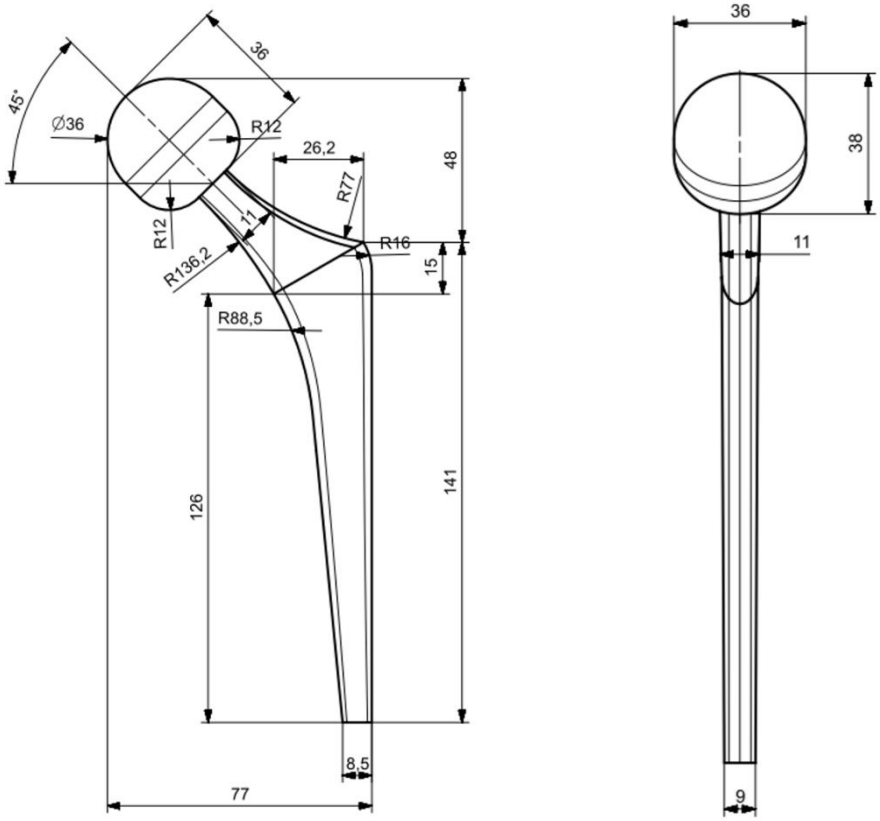

(a) (b)

Figure 9.6: Hip prosthesis implant adopted in this work (all the dimensions are in mm). (a) Side view (b) Front view

The FEM has been developed in Ansys workbench R2 2020™ environment. In order to establish the optimal mesh size, a convergence analysis has been performed at the first. This is made because the choose of the optimal mesh size allows to obtain accurate results without exceedingly too much with the simulation time. The convergence analysis has been carried out through a static simulation on the hip implant, choosing the maximum load components during a sitting cycle, evaluated from the human multibody model developed in MSC ADAMS™. The boundary condition adopted in the Finite Element Model consist of a fixed support applied to the prosthesis stem. The load condition has been applied to the femoral head and modeled as surface effect. Figure 7a show the load and constrain conditions while Figure 9.7b show the equivalent stress (Von Mises criterion) after the static simulation.

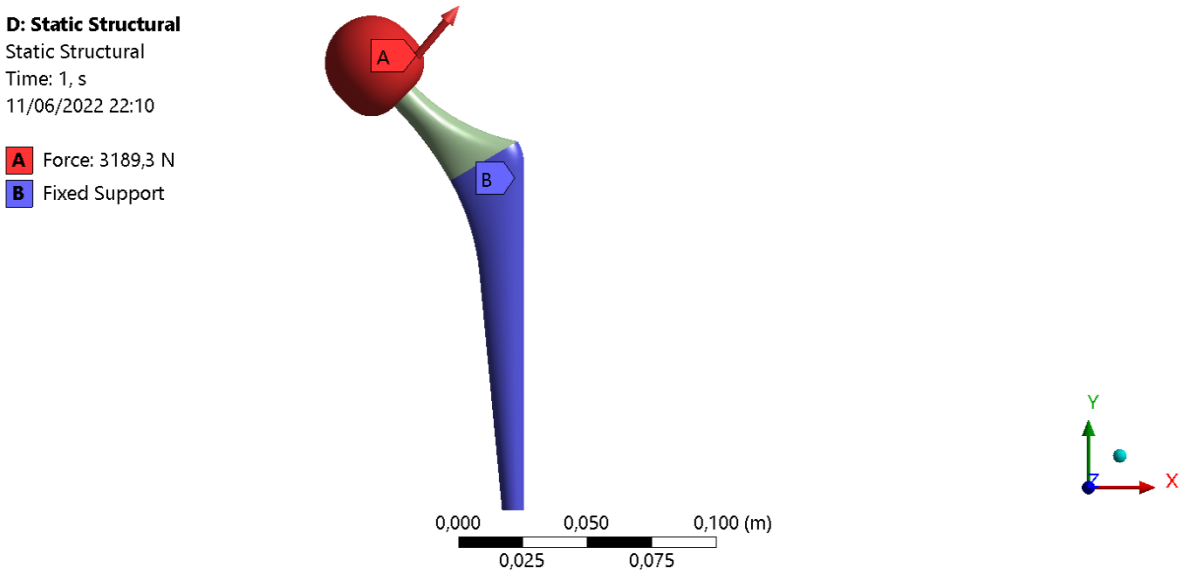

(a)

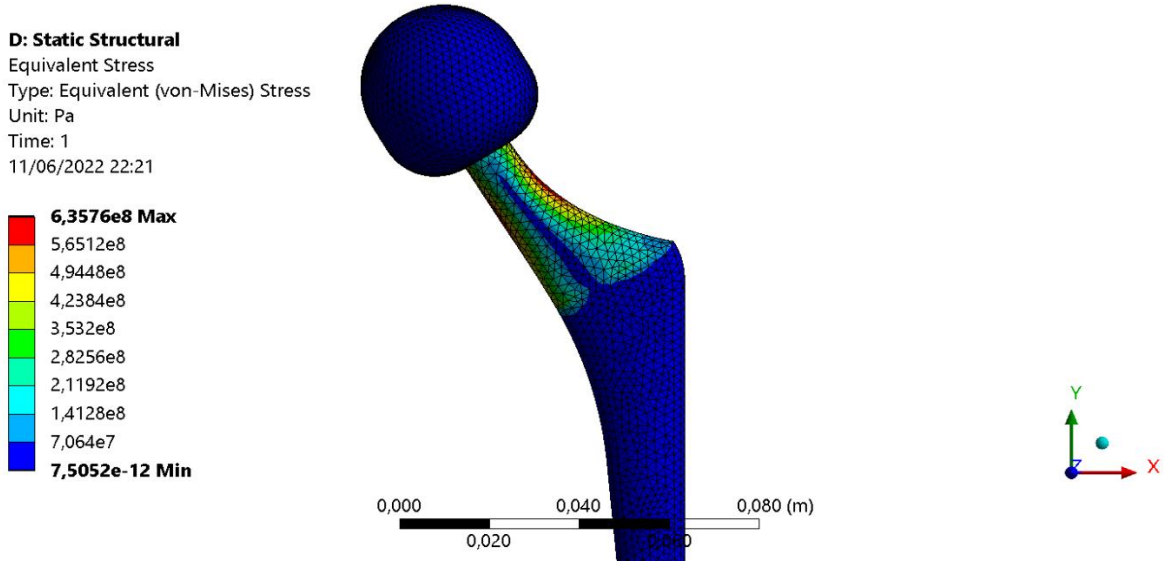

(b)

Figure 9.7: Static simulation carried out on the hip prosthesis for the mesh convergence evaluation. (a) Load and constrain condition: a fixed support has been applied to the prosthesis stem while the static load has been applied on the femoral head (b) Equivalent.

Starting from a coarser mesh, the convergence has been obtained increasing the number of element and at the same time reducing the element size. The results of the convergence analysis are shown in Figure 9.8 and Table 9.2 respectively.

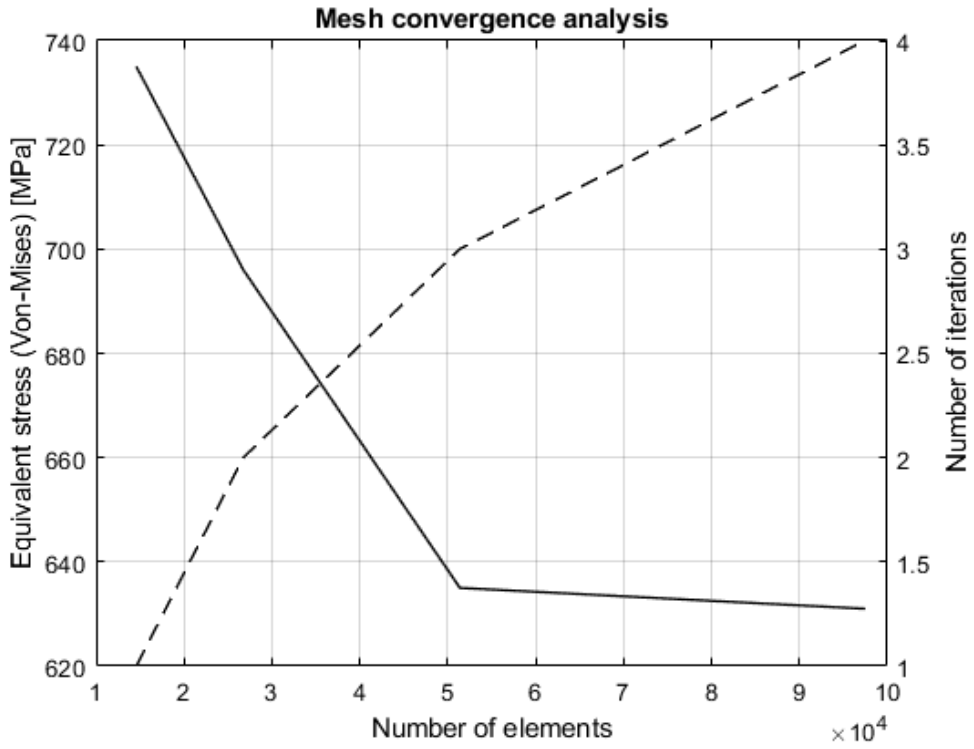

Figure 9.8: Mesh convergence analysis. It is possible to observe that with the increasing of number of iteration and number of elements the equivalent stress settled around 635 MPa.

Table 9.2: Mesh convergence analysis results

Number of iterations	Element size	Number of elements	Equivalent Stress
1	10 mm	14574	735 MPa
2	5 mm	26745	669 MPa
3	2 mm	51379	635 MPa
4	1 mm	97475	631 MPa

The selected mesh size for the simulations is 2 mm with 51379 elements, reached at the third iteration. In order to investigate the wear process between the acetabular cup and the femoral head and simulate the sitting cycles, a transient analysis has been carried out. In addition to the mesh size already defined, load, rotation and constrain condition have been considered into the model. A fixed support has been applied to the external and internal surface of the acetabular cup. The load condition has been applied to the femoral head and modeled as

surface effect. It means that the forces are applied to the selecting surface area through the definition of several nodes controlled by the software itself. Of course, the sum of the nodal forces is equal to the imposed transient force. This method is useful when rotations and area changes are expected during the simulation, like in this case. The mesh adopted in the simulation is shown in Figure 9.9a while the boundary conditions are shown Figure 9.9b.

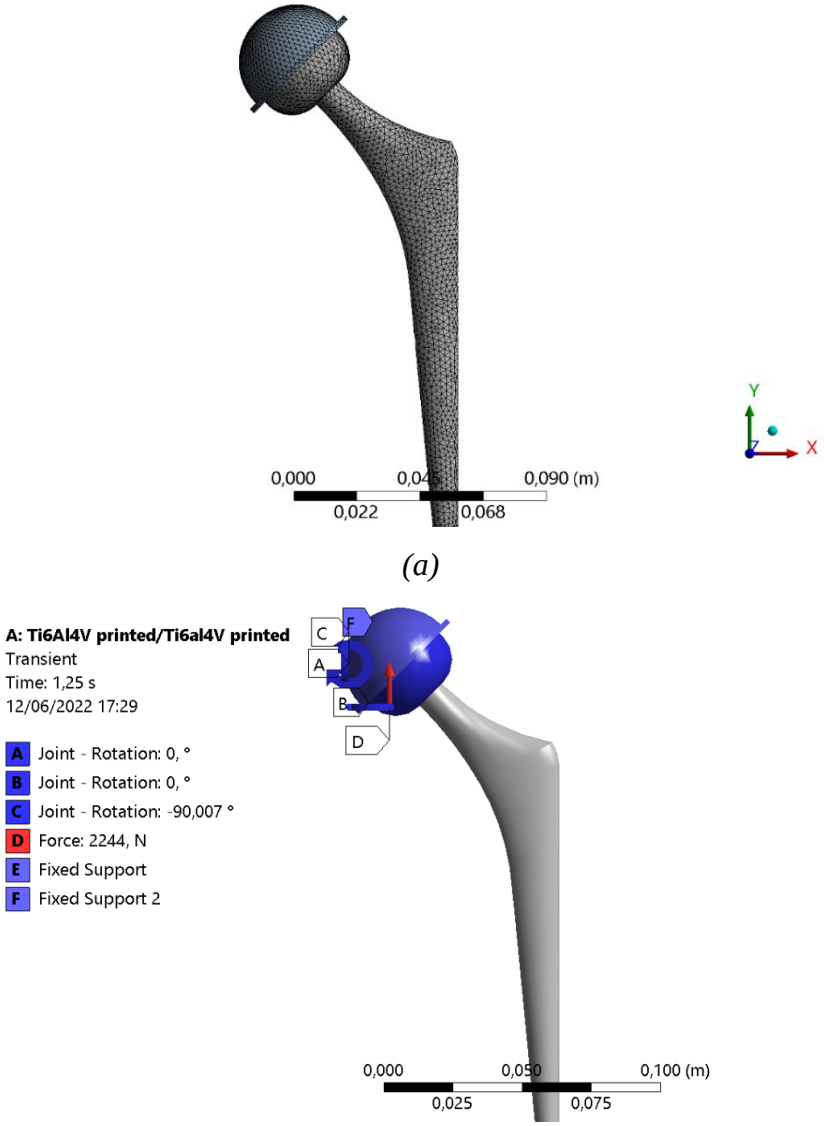

(a)

(b)

Figure 9.9: Transient analysis carried out on the hip prosthesis in order to investigate the wear process between the acetabular cup and the femoral head. (a) Adopted mesh (b) Boundary condition. A fixed support has been applied to the acetabular cup external and internal surface. The load and rotation condition has been applied to the femoral head according to the sitting cycles. As an example, in figure is shown the Ti6Al4V/Ti6Al4V pairs at 1.25 s simulation time.

The mesh element type used in the FEM is a Tetra 3D element which consist of a high order 20-node SOLID186 element. The element is defined by 20 nodes having three degrees of freedom per node i.e. translation in the nodal x, y and z direction. The element support also plasticity, large strain and large deflection. The solid mesh has been generated using "Automatic Method" workbench command. A frictional contact type has been implemented in the simulation considering the acetabular cup as target surface, modelled with TARGE170 element, and the femoral head as the contact surface, modelled with CONTA174 element.

Archard's wear law implementation

In order to investigate well the wear process between the acetabular cup and the femoral head, it is necessary to implement a wear model in the FEM. In this study, the Archard's law, defined in Equation (2), has been implemented in the transient simulation:

$$w = \frac{K}{H} p^m v^n \tag{9.2}$$

where w is the wear rate, K is the Archard's wear coefficient, H is the material hardness, p is the contact stress and v is the sliding velocity. The Archard's law described above makes no assumption about surface topography since the surface roughness effects are encompassed by the experimental wear coefficient K, calibrated through Pin On Disk experimental tests usually. In addition, it also make no assumption about variations with time. Although it is widely used, the Archard's law only provides for an order of magnitude estimate and is a true calculation of wear. Despite this, the Archard's law provides accurate information about the wear behavior of a material coupling, especially when the law is calibrated based on experimental tests [240]. Three different pairs have been compared in this work:

1. CoCr Alloy (femoral head) / UHWMPE (acetabular cup)
2. Ti6Al4V (femoral head) / Ti6Al4V (acetabular cup)
3. Si3N4 - TiN (femoral head) /Si3N4 - TiN (acetabular cup)

The materials pairs parameters [226,240,248,250,253–255,277] related to Equation (9.2) are shown in Table 9.3.

Table 9.3: Materials pairs parameters for the implementation of the Archard's wear model in the FEM analysis [226,240,248,250,253–255,277]. In this work, it was also adopted a linear model.

Pairs	Friction coeff.	Wear coeff.	Hardness	m, Pressure Exponent	n, Sliding Velocity Exponent	Poisson Ratio
CoCr alloy/UHMWPE	0.11	$1.0656e^{-6}$	1.22 GPa	1	1	0.3
Si3N4 - TiN/ Si3N4 - TiN	0.14	$2.03e^{-5}$	14.7 GPa	1	1	0.3
Ti-6Al-4V /Ti-6Al-4V	0.53	8e-5	1.09 GPa	1	1	0.3

The value of the friction coefficient, which is usually evaluated from experimental tests using a tribometer with Pin-On-Disk configuration, changes during the tribological test. This happens because the lubricant film adopted during the test, which simulate the synovial fluid, gets thinner away, increasing the value of the friction coefficient. Therefore, the final value assumed by the friction coefficient and adopted in the FEM, corresponds to that obtained in dry condition, neglecting the influence of the synovial fluid. This assumption is also in agreement with scientific studies [240,248].

9.3.3 Topology optimization

After establishing the best materials pairs in terms of volume loss due to wear, a topology optimization has been performed trough a static structural simulation, considering the maximum load components applied to the femoral head. This is made in order to reduce the prosthetic implant mass and at the same time minimize the implant compliance. Considering the boundary condition in Figure 9.7a and as consequence the stress distribution shown in Figure 9.7b, the attention has been focused on the implant stem, since this region is not affected by particularly high stress. Figure 9.10 show the decision region used for the topology optimization.

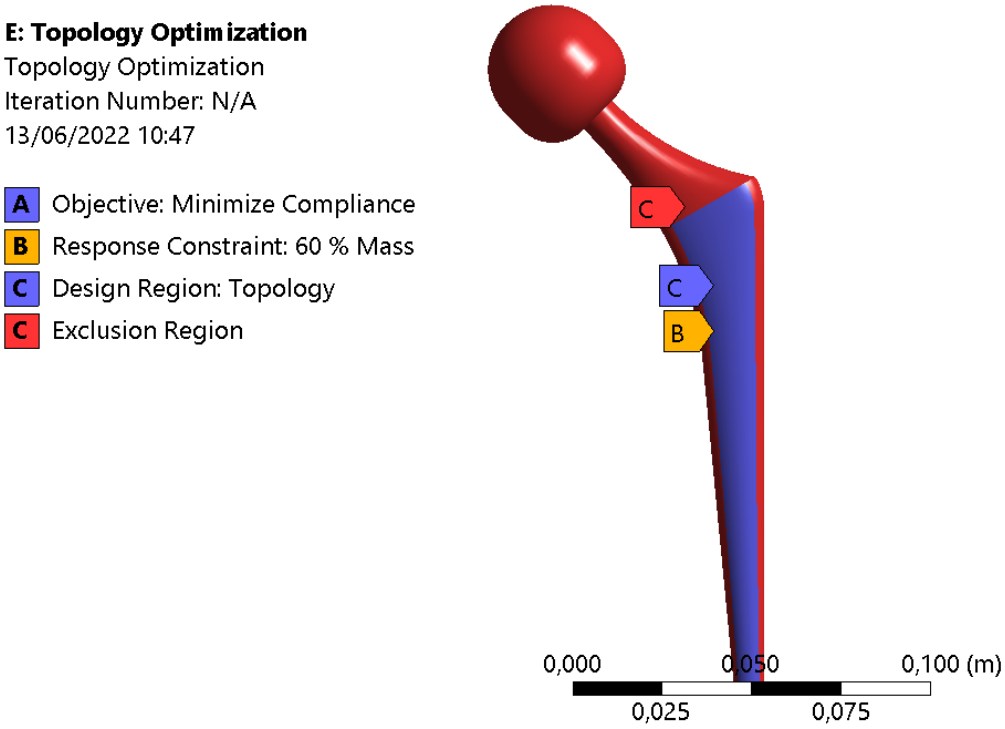

Figure 9.10: Topology optimization. The exclusion region is related to the femoral head and to the entire region interested by high stress level while the decision region is related to the implant stem. The topology optimization objective is to minimize the implant compliance and at the same time reducing the prosthesis mass. Moreover, it was also decided to save the 60% of the implant mass at least.

9.4 Results

The combined action of Artificial Intelligence and machine learning, together with a human model developed on a multibody environment, allow to evaluate the load and rotation conditions at the hip joint. In particular, ten sitting cycles have been considered for a simulation time of 10 s. Figure 9.11 show the load and the rotation conditions at the thigh joint evaluated from the multibody model.

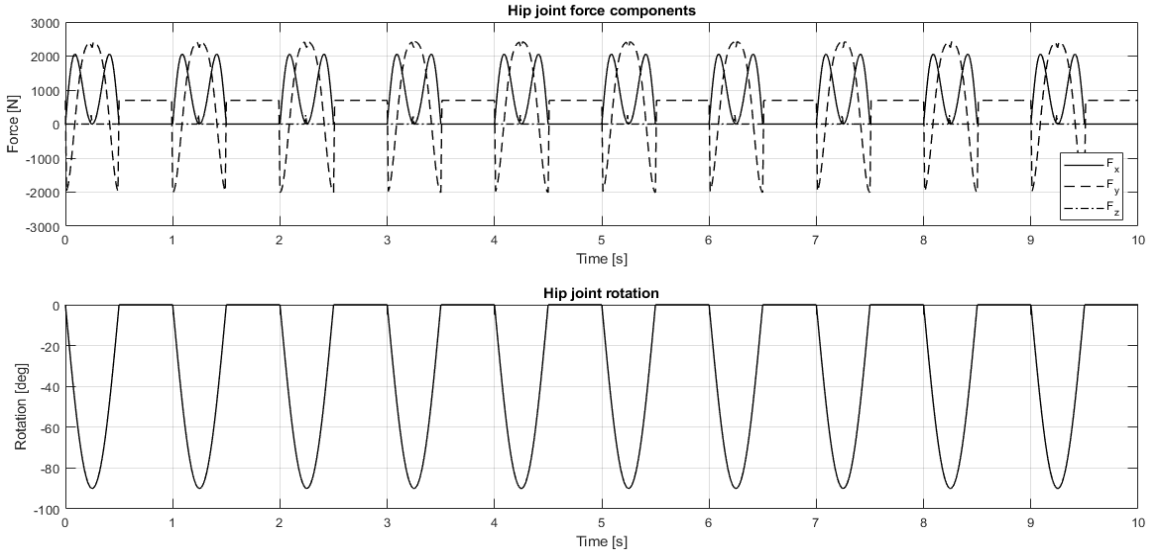

Figure 9.11: Force and rotation conditions evaluated at the hip joint through a multibody model of a human body. The force components follow the coordinate reference system defined in the FEM. The rotation condition presents only one component, perpendicular to x-axis.

The load and rotation conditions evaluated from the multibody model of a human body, represents the boundary condition for the study of the wear process between the femoral head and the acetabular cup, evaluated through a FEM. In particular, the attention has been focused on the volume loss due to wear of the femoral head, which behavior has been modeled through the Archard's law. Figure 9.12 and Table 9.4 respectively shows the comparison of the volume loss due to wear (related to the acetabular cup) for three different materials used in the prosthetic biomedical field.

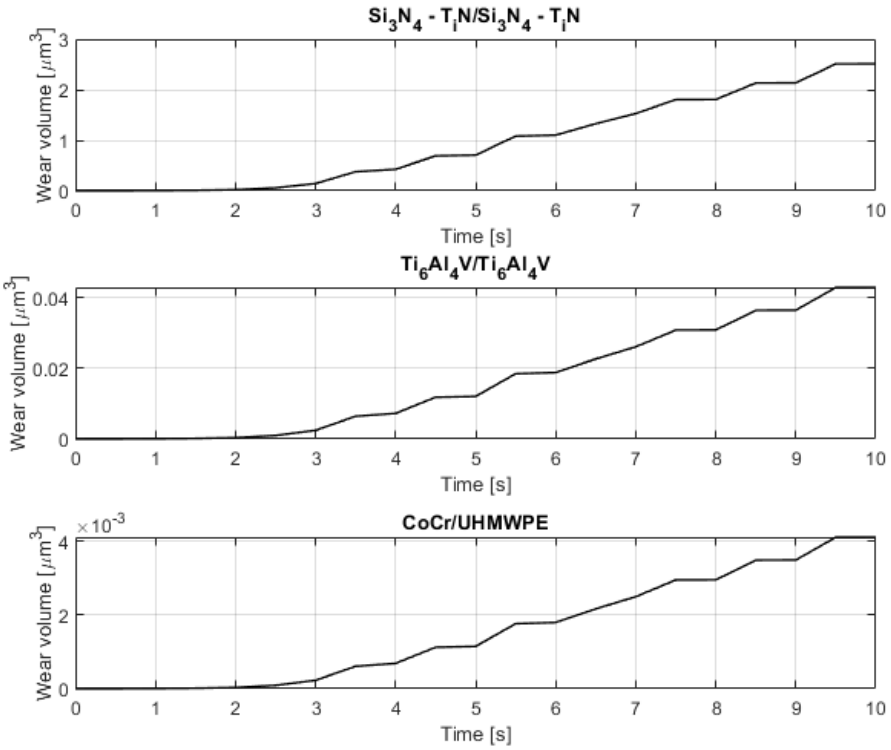

Figure 9.12: Volume loss due two wear during sitting cycles of 10 s simulation time for three different materials pairs.

Table 9.4: Comparison of the volume loss due to wear (related to the acetabular cup) for three different materials used in the prosthetic biomedical field.

Pairs	Volume loss due to wear
CoCr alloy/UHMWPE	0.004 μm^3
Si3N4 - TiN/ Si3N4 - TiN	0.04 μm^3
Ti-6Al-4V /Ti-6Al-4V	2.5 μm^3

According to the results exposed in Figure 9.12 and Table 9.4 respectively, the best materials pairs is CoCr alloy/UHMWPE, because presents the lower value of volume loss due to wear at the end of the sitting cycle. For this material pairs, it was also performed a topology optimization in order to minimize the compliance and at the same time reduce the prosthesis mass. Figure 9.13 shows the result of the topology optimization.

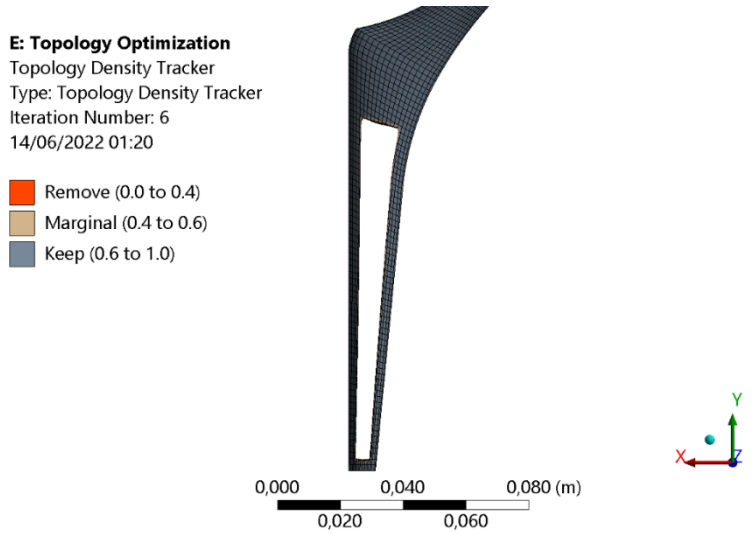

Figure 9.13: Topology optimization result. It is possible to see that the interested region of the optimization is the prosthesis stem and after six iterations, the optimizer is capable of removing material in order to lightweight the prosthesis.

Figure 9.14 shows the comparison between the original prosthesis design and the optimize one.

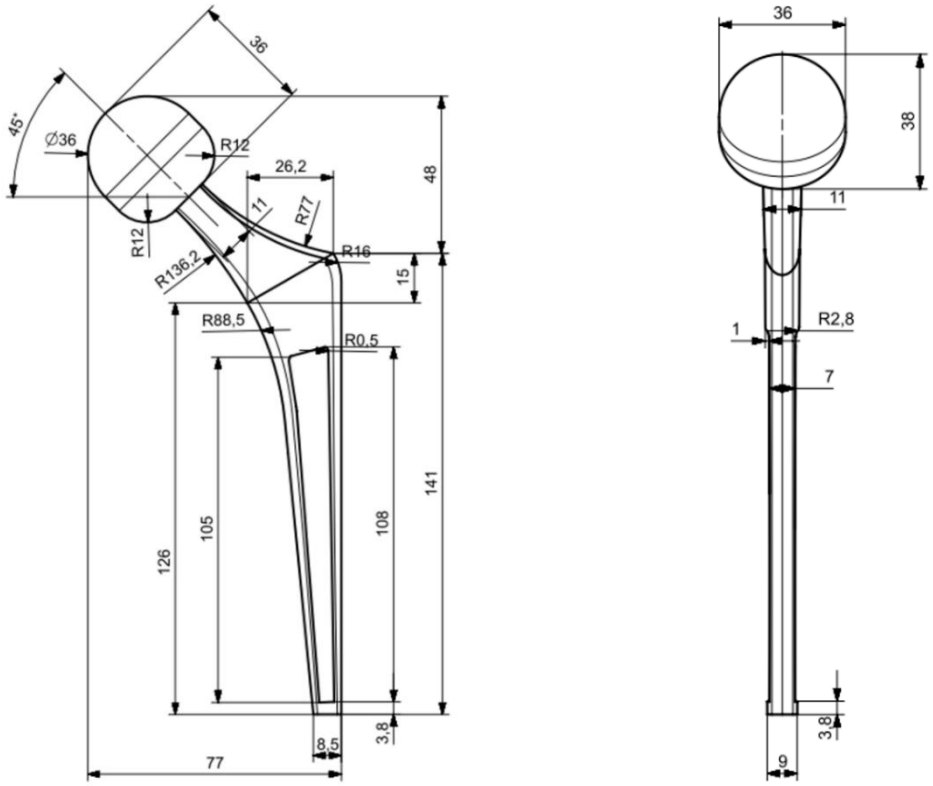

(a) (b)

Figure 9.14: Comparison between the original hip prosthesis design and the optimized one. (a) Side view of the original prosthesis (b) Side view of the optimized prosthesis.

The comparison between the original prosthesis mass and the optimized one is shown in Table 9.5.

Table 9.5: Comparison between the original prosthesis mass and the optimized prosthesis.

Original mass	Optimized mass	Mass reduction
0.41 kg	0.32 kg	-28.12%

9.5 Discussion

The results shown in Figure 9.3 and Figure 9.4 respectively, demonstrate that the implementation of an AI algorithm and the use of OpenPose software allows the identification of the main marker of a real human subject, including the hip joint position. Therefore, the multibody model of a human body developed in MSC ADAMS ™ has been validated based on a real human subject. Moreover, the multibody model is fully parametric and hence it is possible to select a specific quartile depending on weight and height of the human subject. In particular, the selected quartile adopted for the simulation is a male subject, 85 kg of weight and 1.75 m of height. Figure 9.10 shows that from the multibody model of a human body it was possible to evaluate the load and rotation conditions at the hip joint during ten sitting cycles. Figure 9.11 shows the sitting cycles that occurs in 10 s simulation time. The sitting cycles are composed by a dynamic part, related to the joint movement, and a static part related to the contribution of the human body mass, when it remains stationary. In addition, the joint rotation is a planar movement and, as consequence, has only the component perpendicular to the x-axis, from 0 to 90 degrees. From the FEM of a hip prosthesis developed in Ansys Workbench R2 2020™, it was possible to compare three different materials pairs used in biomedical fields, in terms of wear between the acetabular cup and the femoral head: CoCr Alloy/UHMWPE, Ti6Al4/Ti6Al4, Si3N4 -TiN/Si3N4 -TiN. The wear process has been studied trough the implementation of the Archard's wear law in the FEM. The materials properties have been obtained by previous literature study and the influence of the synovial fluid related to the coefficient of friction has been neglected. The results shown in Figure 9.12 and Table 9.4 respectively, demonstrate that the better behavior in terms of volume loss due to wear (related to the femoral head) was achieved by CoCr alloy/UHMWPE pairs, with a value of 0.004 μm^3 at the end of the sitting cycle. The obtained results are also in agreement with literature studies [225,226,229,230,240,249].

Investigating the trend of the volume loss due to wear shown in Figure 9.12 it is possible to assess that it is inherent with the imposed sitting cycle. In fact, during the movement of the hip joint, the volume loss due to wear increase, while it remains stationary during the stationary phase of the sitting cycle. Moreover, the increasing wear follows a linear trend, in agreement with the linear model (m and n equal to 1) adopted for the Archard's law defined in equation (9.2). After establishing the best materials pairs in terms of volume loss due to wear, a topology optimization of the implant structure has been performed. The attention for the topology optimization has been focused on the implant stem, since this part is not directly involved by the action of the applied load, but it is fixed to the bone. Its main contribution is related to the global implant stiffness. As shown in Figure 9.13, the optimization algorithm is able to remove material in the decision region, with the aim of minimize the implant compliance (and hence maximize the implant stiffness) and at the same time reduce the prosthesis mass. At the end of the optimization process, the new prosthesis design is 28.12% lightweight than the original one, as shown in Table 9.5.

9.6 Conclusions

The aim of this work was to perform a tribological characterization of three different materials pairs used in biomedical field, with the combined action of Machine Learning, Multi-Body modeling and Finite Element Analysis. The results show that the markerless approach represents an easy way to evaluate human motion without a sophisticated architecture. In particular, OpenPose is a machine learning algorithm that predicts well joints rotations A multibody model of a human body has been developed in MSC ADAMS™ environment and it is able to evaluate the load conditions at the hip joint during sitting cycles, together with the rotation condition evaluated from OpenPose. The human body model developed in multibody environment is fully parametric and, in this study, a male subject of 85 kg weight and 1.70 m height has been investigated. Through a FEM of a hip prosthesis developed in Ansys workbench R2 2020™, it was possible to investigate the wear process between the femoral head and the acetabular cup of, through the implementation of the Archard's wear law. The comparison between three material types largely used in the biomedical field, shows that the best behavior in terms of volume loss due to wear is achieved by CoCr alloy/UHMWPE pairs, with a final volume loss due to wear of $0.004\ \mu m^3$ after ten sitting cycles. All the results have been compared with literature studies showing a

good agreement with them. At the end, considering the best material coupling, a topology optimization of the whole prosthesis structure has been performed. The decision region has been focused on the implant stem, since this region is not characterized by particularly high stress. The results show that was possible to reduce by 28.12% the implant mass. At the end, it is possible to assert that the humanoid model developed in multibody environment could represents a valid alternative for the estimation of the load and rotation conditions acting on a hip implant, with respect to the conventional one, such as hip simulators. The future development regards the implementation of more complex movement, such as gait cycles, the calibration of the multibody model on a real clinical case, the calibration of the Archard's law with tribological experimental tests, avoiding the use of a linear wear model, and the study of the influence of coatings applied to femoral head and acetabular cup aimed to improving the wear behavior.

10. HEAT CONTROL DURING DENTAL IMPLANT POSITIONING

Fiorillo L., Santonocito D., Crisafulli D., Milone D. The Importance of Heat control during Dental Implant Positioning: an in vitro Thermal Analysis. Under submission.

Highlights

The application of thermal analysis in dental implant procedures represents a groundbreaking advancement, enabling the study of temperature changes during implant positioning. Studies have demonstrated the importance of thermal imaging in assessing the health of tissues and its potential in early damage detection and in assessing the biomechanical interactions during dental implant procedures.

Materials and Methods

The study conducted tests to evaluate heating produced by screwing titanium dental implants (Diagram®, Schutz-Dental GmbH, Rosbach, Germany) into resin D3 bone-like blocks, simulating the mechanical consistency of bone. Various screwing protocols were assessed based on the presence of lubricant or less, the instrument used for implant positioning (manual and micromotor screwing), and the number of revolutions. Temperature evolution on the screwed surface was monitored using a micro bolometric infrared camera FLIR A40.

Results

In the study, 24 dental implants were positioned using various protocols. Results showed that the highest temperature differences occurred during manual screwing without physiological solution, particularly in under-sized preparation sites due to increased friction. The presence of lubrication significantly reduced the surface temperature of the samples, though water accumulation affected the accuracy of temperature measurements. Overall, the study highlighted the impact of screwing speed, lubrication, and preparation size on the thermal dynamics during dental implant placement.

Conclusions

The study concludes that thermal analysis is crucial in dental implant procedure comprehension, with thermocameras offering a non-invasive method to evaluate thermal dynamics involved in dental implant insertion. This approach can lead to improved implant designs and techniques that minimize thermal damage to surrounding tissues, enhancing dental implant procedures' overall success and safety. The study underscores the need for

further in vivo research, innovative materials for drills and implants, and customized drilling protocols tailored to individual patient factors. Education and training in thermal analysis for dental professionals and addressing regulatory and ethical considerations in advancing these technologies are vital.

10.1 Introduction

Thermal analysis is a groundbreaking technique that allows us to study the temperature changes during dental implant positioning [278]. With this technique, we can ensure the implant is placed safely and efficiently, minimizing the risk of complications. By conducting thermal analysis, we can also determine the optimal implant placement to achieve the best results for our patients [279,280]. So, to experience a successful dental implant procedure, ensure that your dentist uses thermal analysis during implant positioning [281–283]. The use of thermographic cameras in bioengineering analysis presents a significant advancement in the field. These cameras, capturing infrared radiation, offer a non-invasive and detailed method for monitoring and analyzing various biological processes and structures. For instance, thermal imaging has been employed in assessing skin health, as seen in the study by Handley and Hessefort (2019)[284], where they analyzed the skin condition of healthcare workers' hands over a year. In dental bioengineering, Matos et al. (2022) [285] highlighted the application of thermographic cameras alongside other tools for in vitro and silico analyses, proving its importance in modern dentistry.

Moreover, Zhao et al. (2022) [286] demonstrated the effectiveness of thermographic cameras in detecting cracks in frozen soils, showcasing the camera's versatility beyond traditional bioengineering applications. Hoshino, Seo, and Yamazaki (2021) further explored its use in disaster response, using drones equipped with thermographic cameras for victim detection. In medical diagnostics, Vasconcellos et al. (2021) successfully utilized a thermographic camera for evaluating small fiber peripheral neuropathy in prediabetes, revealing its potential in early disease detection. These diverse applications underscore the significant role of thermographic cameras in bioengineering and related fields, offering innovative approaches to research and diagnostics. Applying thermographic or thermographic cameras to evaluate thermal changes during dental implant insertion is an innovative approach to dental bioengineering. These cameras offer a unique way to monitor and record temperature variations, providing valuable insights into the thermal effects associated with implant placement procedures. In an in vitro setting, a thermocamera can allow for a detailed analysis

of how different factors—such as implant material, design, insertion speed, and bone density—affect the thermal environment during implant placement. For instance, studies such as those by Demirbaş et al. (2021) [287] have explored the distributions of stress and damage during dental implant insertion, highlighting the importance of understanding the biomechanical interactions during such procedures. Similarly, Yang et al. (2022) [288] developed an analytical model for dental implant insertion torque, considering factors that could influence thermal changes during implant placement. Moreover, research by Klär et al. (2021) [289] combined strain gauge and histologic analysis to study bone damage during dental implant insertion, which can be complemented by thermographic analysis to understand the thermal impact on bone tissue. Varghai et al. (2020) [290] investigated the effect of drilling speed on dental implant insertion torque, which can significantly influence thermal generation and can be effectively monitored using thermocameras. These studies underscore the potential of thermocameras in providing a non-invasive and precise method to evaluate the thermal dynamics involved in dental implant insertion. This approach could improve implant designs and insertion techniques that minimize thermal damage to surrounding tissues, enhancing dental implant procedures' overall success and safety.

10.2 Materials and Methods

10.2.1 The test

The test aims to evaluate the heating produced by screwing dental implants onto resin blocks with D3 bone consistency used for exercises in implant surgery and simulating the mechanical consistency of the bone. The blocks have an initial measurement of 2cmx2cmx5cm. Preparations with a diameter of 4mm and a depth of 10mm were made in the resin blocks using the dedicated Diagram® surgical kit to guarantee correct implant insertion. A single dental implant was placed on a 3.5mm preparation to evaluate the effects of under-preparation of the implant site on temperature. The implants used are 4mm in diameter and 10mm long (Diagram®, Schutz-Dental GmbH, Rosbach, Germany).

10.2.2 The protocols

Different screwing protocols with the following characteristics were evaluated:

- Based on the presence of cooling:
    - Cooling with physiological solution (denominated water)

  - Dry

- Based on the instrument used for implant positioning in place:
  - Surgical micromotor (max torque 50ncm)
  - Manual torque ratchet (max torque 100ncm)
- Based on the number of revolutions:
  - 30
  - 50
  - 75
  - 100
  - Manual (non-uniform number of revolutions)

Before the test, for the specimens to remain in place without moving during the test, they were clamped using a bench vice. Two implants were positioned for each protocol, and the average values were considered. The physiological solution is used as a lubricant and not as a coolant, as the purpose is to simulate the presence of blood and saliva in the implant site.

10.2.3 The instrumentation

During each test, the temperature evolution on the screwed surface was monitored by adopting a micro bolometric infrared camera FLIR A40, with a thermal sensitivity of 0.08° C at 30° C, and the image acquisition frequency was set to 50 Hz.

10.3 Results

The results obtained by combining all the different protocols meant that an expert operator positioned, manually or with a surgical micromotor, 24 dental implants, respecting the 12 different protocols obtained by combining the possibilities in the previous section. The data is summarized in Table 10.1. Mean data about the different protocols. and is explained in detail later.

Table 10.1. Mean data about the different protocols.

ID	Speed [rpm]	Ti [°C]	Tf [°C]	DT	Notes
1	Manually	25.2	25.6	0.4	Water
2	Manually	30.1	34.2	4.1	No cooling
3	30	24.7	25.6	0.9	Water
4	30	27.4	28.9	1.5	No cooling
5	50	27.2	28.5	1.3	Water
6	50	26.8	28.9	2.1	No cooling
7	75	27.6	29	1.4	Water
8	75	29.1	31	1.9	No cooling
9	100	25.6	28.5	2.9	Water
10	100	29	32.4	3.17	No cooling
11	30 + manually	29.2	40.2	11	No cooling, smaller preparation (3.5mm)
12	30 + manually	27.4	33.1	5.7	No cooling

Trying to summarize what is in the table, we, therefore, have values defined with ID1, ID2 which involve a dry and non-dry manual positioning of the dental implants. The subsequent ID3 and ID4 provided a 30rpm dry and non-dry protocol until reaching the 100rpm dry and non-dry protocol of ID9 and ID10. The last two protocols (ID11, ID12) carried out to evaluate borderline conditions, which are often proposed in the clinical setting with under-preparation or implant positioning protocols with high torque, were carried out by positioning the implant at 30rpm and completing the preparation with a dynamometric ratchet until reaching values of 100Ncm in the absence of lubricant and a protocol line with under-preparation of the implant site by 0.5mm. Generally, the higher the screwing speed, the higher the maximum temperature reached on the screwed surface.

The presence of water lubrication causes a decrease in the surface temperature of the samples.

Figure 10.1 shows the trend of the specimen's surface temperature over time. The absolute temperature at the hole's edge is expressed on the left vertical axis. In contrast, on the right axis, the temperature is indicated as a difference between the initial and the final time. The temperature increase delta was 0.4 for lubricated sites and 4.1 for dry sites.

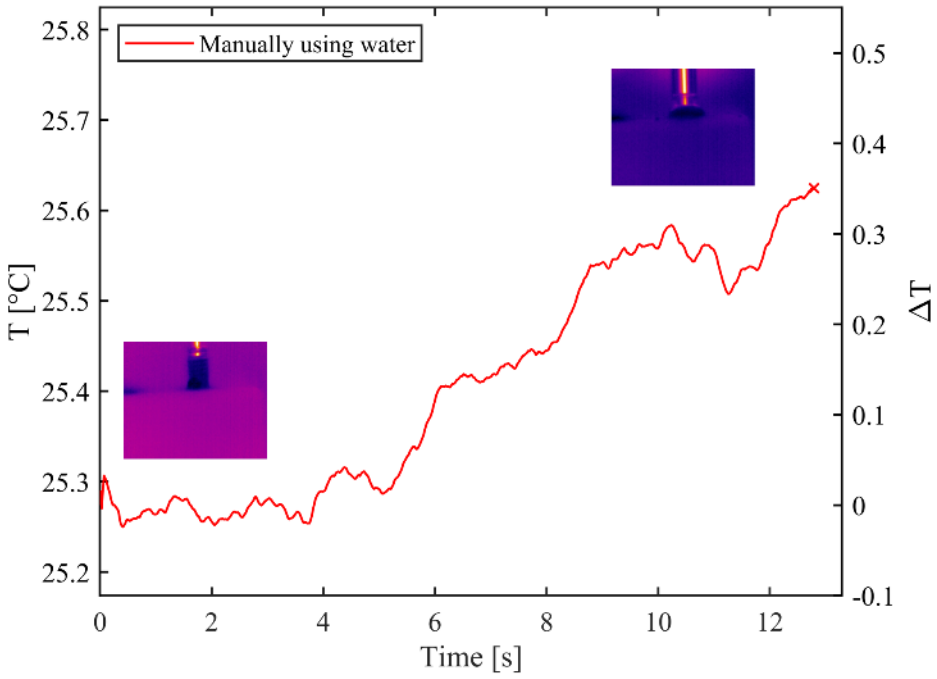

(a)

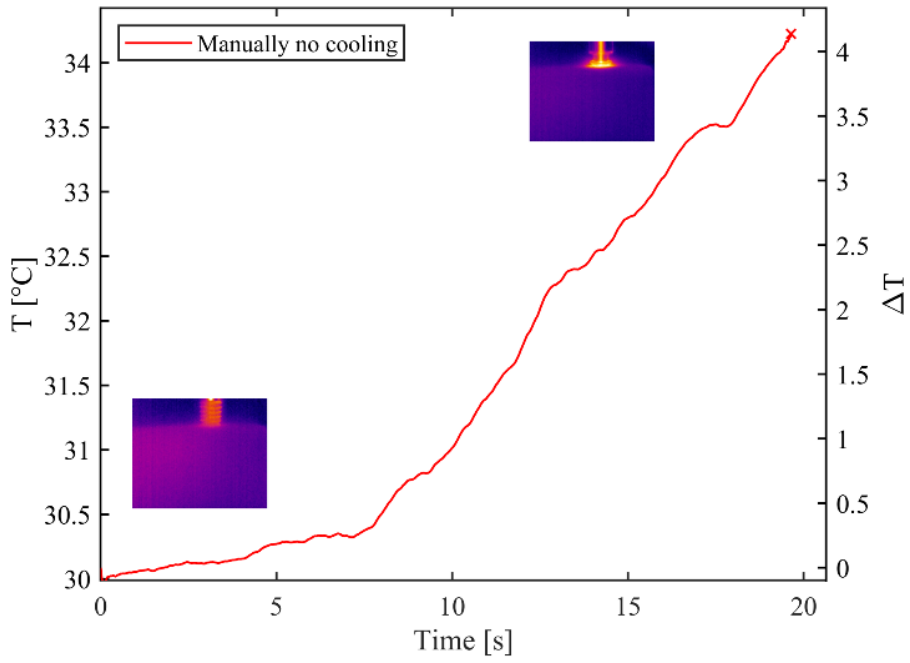

(b)

Figure 10.1:Temperature trend during Manual screwing test ID 01-02: a) with water; b) no cooling

However, during screwing, water accumulates around the hole and makes temperature measurement less accurate (Figure 10.2). Consequently, water on the surface affects the accuracy of temperature measurement and the extent of temperature variation.

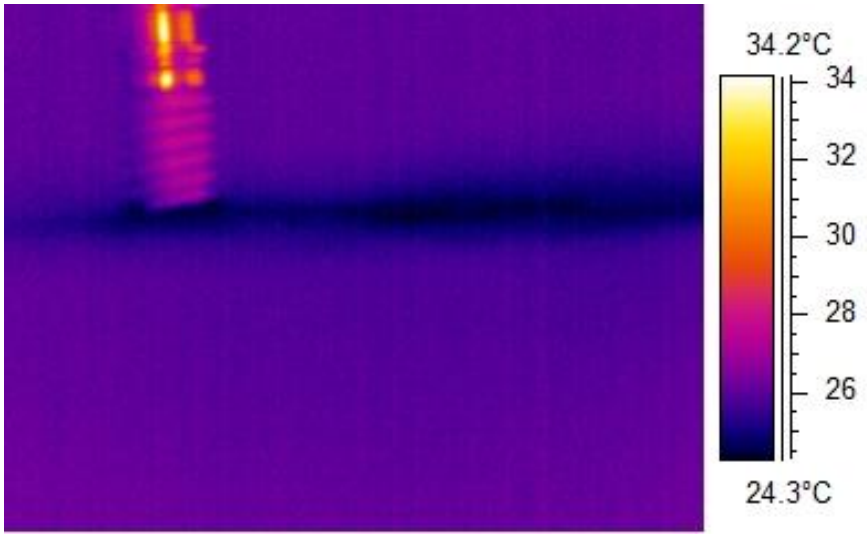

(a)

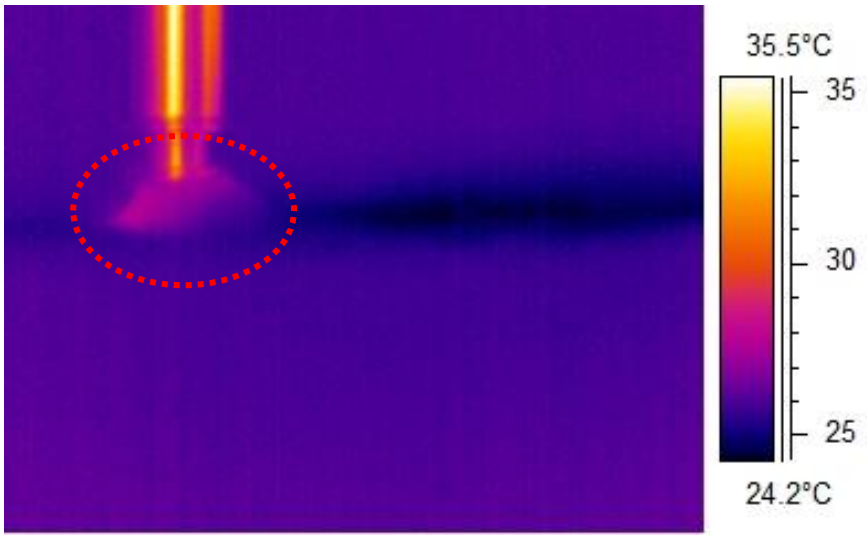

(b)

Figure 10.2: ID screwing test 03 with water lubrification a) before screwing; b) after screwing

A smaller preparation site reaches the test's highest temperature difference value. This could be caused by friction of the titanium implant on the resin base during the screwing process.

The combination of screwing with an electric motor and manual screwing was also tested. The greatest increase in temperature found was associated with manual screwing. Figure 10.3, shows the three phases of the combined screwing process. Figure 10.3a represents the initial stage of the process, a few moments before starting the test. Figure 10.3b shows the temperature distribution at the end of the screwing process with the micromotor and before starting the manual screwing. Finally, Figure 10.3c shows the heat map of the implant at the end of the manual screwing process.

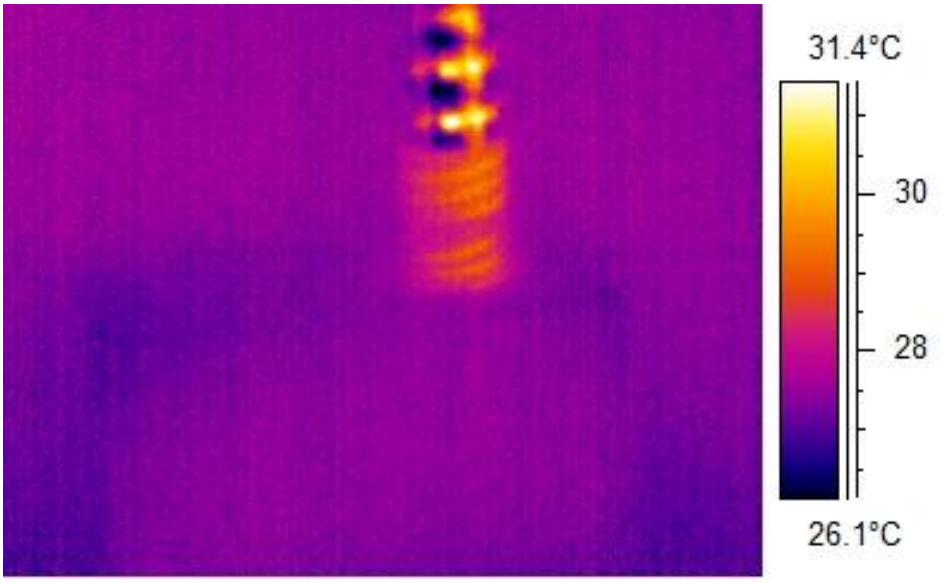

(a)

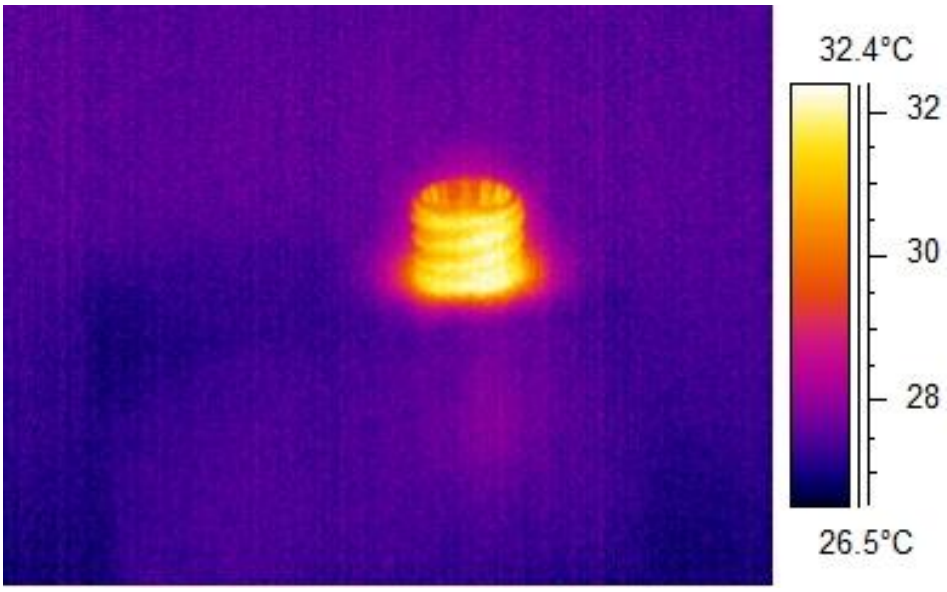

(b)

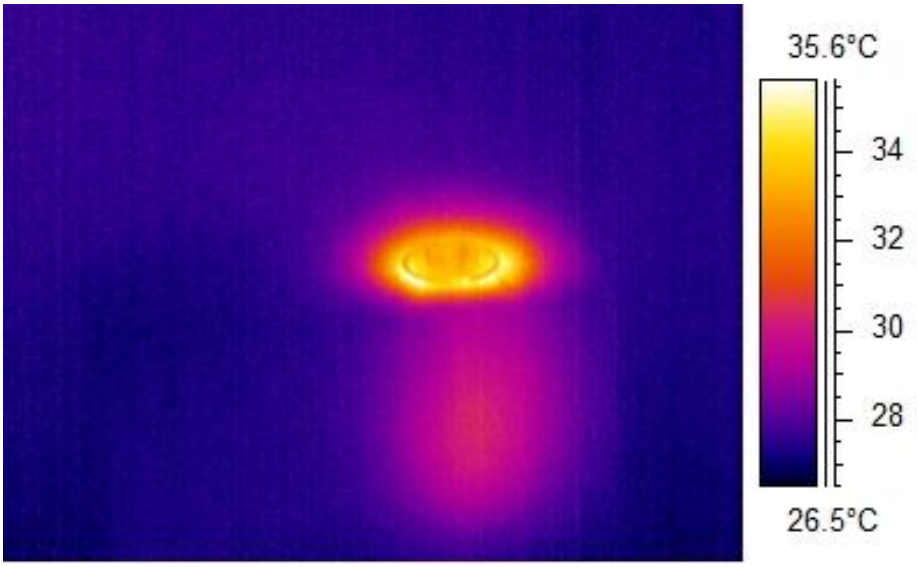

(c)

Figure 10.3: ID screwing test 12 with no cooling a) before screwing; b) after micromotor screwing; c) after manual screwing

Figure 10.4 shows the temperature variation during machine and manual screwing over time. The plateau region in the middle of the curve, where the temperature is approximately constant, represents the moment when the operator changes the screwing method.

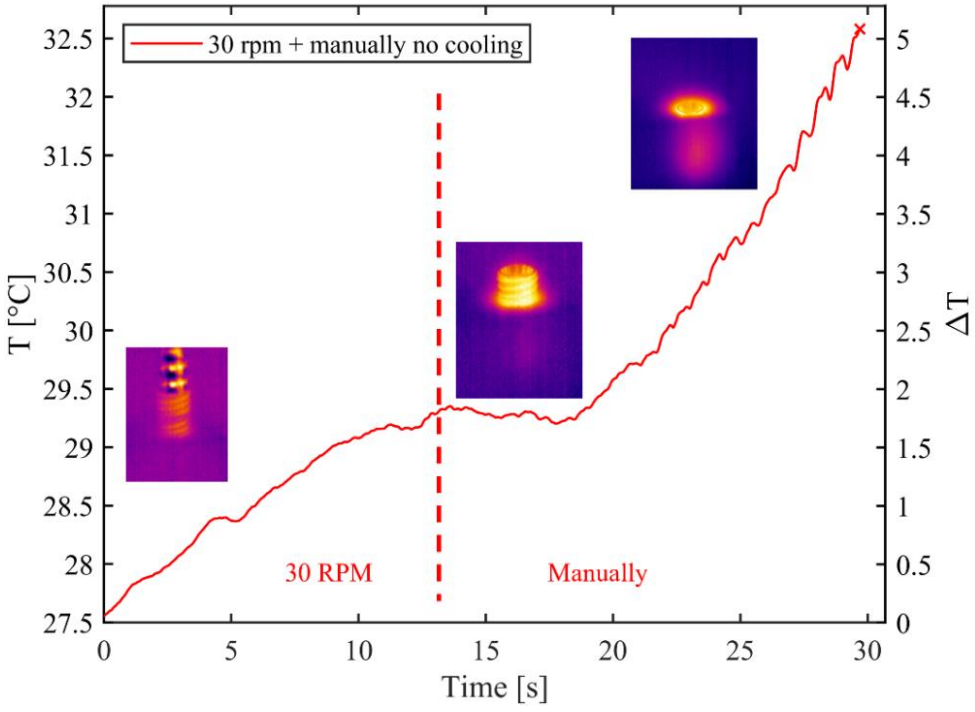

Figure 10.4: Temperature trend during test ID 12, 30rpm+manually.

10.4 Discussion

The limit condition that should never be reached during bone surgery is physical osteonecrosis, in this case, thermal. Osteonecrosis refers to the death of bone tissue due to a lack of blood supply to the affected area. This condition can partially or totally destroy the regenerative capacity of bone tissue and articular cartilage, leading to functional damage to the patient's joint mobility. It can also cause damage to prosthetic implants and may promote infection. Thermal trauma during implant preparation is an essential factor affecting osseointegration and implant survival. Osteonecrosis occurs when the temperature exceeds 47°C for more than a minute; thus, minimizing thermal and mechanical insult to the bone during implant osteotomy is crucial. Studies on implant surgery have long focused on understanding the causes of excessive heat generation during drilling operations. The main goal is to observe heat generation by testing different methodologies and identifying the best solution to the overheating problem. The depth of drilling for dental implants has a significant impact on overheating. Using conventional and piezosurgical drills, it has been demonstrated that the more profound the drilling, the more significant the overheating. For instance, a piezoelectric drill at a depth of 13 mm reached a maximum temperature of 38.10°C. Conventional drills led to less heat development, with a maximum of 33.6°C at the same depth. However, the maximum temperature remained below the critical thermal threshold.

Studies comparing heat generation between guided surgical practice and conventional approaches have shown that guided surgeries pose a higher risk of tissue necrosis due to temperature increase, especially when using larger drill bits (2.2 mm, 3.5 mm, 4.2 mm). The surgical guide impedes water entry used for cooling and increases friction between the drill and the guide handle, leading to significant heat generation. Instead of single drilling, sequential drilling procedures repeatedly overheat the implant site [291].

Variations in irrigation volume and the load applied to the drill were also analyzed. Conventional, sonic, and ultrasonic drills were used on cortical and spongy bone layers. Increasing the irrigation volume resulted in lower temperatures during all tested osteotomies. Conventional rotary instruments caused an increase in temperature of 6.5°C at an irrigation of 20 ml/min, which decreased progressively with higher irrigation volumes. However, no tests reached the critical temperature of 47°C [292].

The material and design of the drill, as well as its usage frequency, also influence bone temperature during site preparation. Steel drill bits generated less heat than ceramic ones at a constant drilling load of 20 kg and a speed of 1,500 rpm. The maximum average temperatures at different depths (3 mm, 6 mm, 9 mm) were noted, with ceramic drills initially causing higher temperatures, possibly due to their lower thermal conductivity than steel. However, the critical temperature of 47°C was never reached in the tests [293]. A review by Dhok et al. [291] comprehensively analyses the thermal dynamics in dental implant procedures, emphasizing the relationship between heat generation and successful osseointegration. It highlights that temperature rise during implant operations can lead to thermal injury of the adjacent bone tissue, potentially causing implant failure. The paper thoroughly examines factors such as drill speed, design, irrigation mode, depth, diameter, and drill material and how they influence osseointegration due to heat generated during drilling—Finite Element Analysis (FEA) studies, including those by Ahmadi et al. [294], have been utilized to assess the impact of drilling parameters on heat generation. These studies reveal that higher feed rates result in lower temperature rises and that water application significantly reduces maximum temperatures. The diameter of the implant is identified as a crucial design parameter, with studies showing that guided osteotomy preparation and sequential drilling protocols can lead to higher temperature deviations compared to conventional methods. Drill speed emerges as a critical aspect of dental implant operations, with findings indicating that higher speeds, such as 2500 RPM, generate less heat and reduce preparation time, while slower speeds result in more frictional heat. However, very low speeds can cause the drill to get stuck, increasing heat generation. The depth of the drill, determined by the bone thickness in which the implant is inserted, also plays a significant role, with deeper drilling associated with higher heat generation. Irrigation is a key component of successful osteotomy, minimising friction, promoting effective drilling, cooling the drill bit and tooth, and preventing infection. The effectiveness of irrigation in controlling rising temperatures has been well-documented, with external irrigation proving more effective than internal irrigation.

Furthermore, the volume of irrigation used during site preparation only sometimes leads to significantly different temperature control compared to a moderate volume. The review concludes by stressing the need for careful consideration of various factors, including drill speed, diameter, depth, and irrigation, to prevent implant failure due to heat generation.

Maintaining the temperature within specific limits is crucial to avoid thermally induced necrosis. The selection of drill parameters and appropriate irrigation methods are vital in controlling rising temperatures during dental implantation. Additionally, the review underscores the need for further research to determine optimal parameters for efficient implant site preparation and post-operation activities. This comprehensive analysis of the factors influencing heat generation during dental implant procedures emphasizes the importance of controlling these factors to ensure the success and safety of the implantation process. Tur et al. [283] conducted a study investigating the thermal performance of metal-based (stainless steel) and ceramic (zirconia) implant drills, mainly focusing on the temperature exposure time during the osteotomy process. The study involved 240 individual preparations, considering factors such as drilling depths (10 and 16 mm), irrigation methods (external and without irrigation), drill materials, and three consecutive drill diameters per material (2.0/2.2, 2.8, and 3.5 mm) with ten identical repetitions for each. Real-time multichannel temperature measurement was conducted during automated drilling procedures in standardized bovine bone specimens. The findings revealed that maximum temperature changes were closely associated with the passive drill withdrawing period, regardless of the drill material, depth, or diameter.

Statistically significant differences in temperature generation between stainless steel and ceramic drills were observed in irrigated testing sites, especially with smaller drill diameters (2.0/2.2 and 2.8 mm). The study concluded a strong association between the highest temperature increase and the passive withdrawing period for both drill materials. The results indicate that high overall temperatures combined with prolonged heat exposure during the surgical procedure could impact the osseointegration process in the future. Other studies have even evaluated the change in temperature of the implant surface following implantoplasty for reasons of peri-implantitis. Sharon et al. [295] explored the efficiency of different dental burs in implantoplasty, a treatment option for peri-implantitis, and the amount of heat generated by each bur. The study evaluated the efficacy of three dental burs (diamond, diamond - Premium Line, carbide) in removing implant substance (titanium) and compared them with a smooth bur (control). Each bur was attached to a high-speed handpiece and applied to a titanium implant for 60 seconds with cooling by water spray. Temperature variations were recorded every 5 seconds, and the amount of implant substance removed (as measured by the reduction in the implant's weight) was evaluated. The results

showed significant differences in the amount of implant substance removed by each bur: the diamond Premium Line bur removed 59.24 mg, carbide 29.39 mg, diamond 11.35 mg, and the smooth bur only 0.19 mg.

Regarding thermal changes, only minimal increases (approximately 1.5 degrees Celsius) were recorded for all four burs. The study concluded that there are considerable differences in the efficiency of various burs when working on titanium. Selecting the appropriate bur can reduce working time. Under proper cooling conditions, implantoplasty does not generate excessive temperature increases that could damage soft tissue or bone surrounding the treated implant.

The deltas in all protocols must be considered to reach tolerable values without lubrication and with the simulated presence of blood and saliva (physiological solution). The only altered values are obtained in experimental protocol ID11 with under-preparation of the implant site. Therefore, considering the temperature of the environments where the studies were carried out as the baseline, the maximum temperature reached was 40.2 degrees, with a delta of 11 degrees C. However, considering the body temperature of 37 degrees C as the starting temperature, and not since there are state transitions of the tested material, therefore considering the linear delta [296], temperatures of 48 degrees could be reached in the case of the ID11 protocol, thus justifying the possibility of creating osteonecrosis in this case. However, going from a temperature of 37 degrees C to 40.17 in the case of the ID10 protocol, which sees the screwing of the implant fixture at 100rpm. Considering the above, it must be ensured that the bone is not overheated or cooled properly after preparing the implant site. It is, therefore, advisable to cool the site once the last drill of the implant surgical kit has been extracted and proceed with implant positioning, maintaining a low number of revolutions and a torque no higher than 50Ncm to avoid incurring osteonecrosis from thermal damage [295,297,298]. A further aspect to consider is that of implant protocols using piezosurgery. Even if the preparation is carried out using these instruments, the implant positioning must necessarily follow a "screwing", and therefore, we always find ourselves faced with the same problem [299]. This problem may be affected by implants that do not have a design with threads and platforms that need to be positioned in the percussion implant preparation. It would always be necessary to evaluate the extent of this osteonecrosis and the ability of the tissue to lead to healing and osteointegration of the implant screw. Still, it would be necessary to carry out biopsies and carry out these studies in vivo. This is one of

the main limitations of this study, in addition to having used a resin with the same consistency as D3 medullary bone.

10.5 Conclusion

The study emphasizes the groundbreaking role of thermal analysis in dental implant procedures. By integrating thermographic cameras for thermal analysis, practitioners can ensure safer and more efficient implant positioning, significantly reducing the risk of complications. This method allows for optimising implant placement, ensuring the best patient outcomes. The use of thermocameras in dental bioengineering is particularly innovative. These devices offer a non-invasive way to monitor and analyze temperature changes during implant insertion. Through detailed thermal imaging, various factors affecting the thermal environment during implant placement, such as material, design, insertion speed, and bone density, can be understood more profoundly.

The future of dental implant procedures is poised for significant advancements in several key areas. Firstly, a deeper understanding of how thermal dynamics affect osteointegration and tissue healing is needed, which can be achieved through more extensive in vivo research, including biopsies. This will offer a more nuanced perspective on how tissues respond to thermal changes during implants.

Continued research into the materials used for drills and implants is critical. Innovations in this area could lead to materials that further minimize thermal impact, focusing on those with optimal thermal properties. Customized drilling and insertion protocols, tailored to individual patient factors like bone density, could significantly enhance the safety and effectiveness of implant procedures. This personalized approach would ensure the best possible outcomes for each patient. Education and training for dental professionals are also vital. As new technologies and methodologies emerge, practitioners must be informed about the latest advancements in thermal analysis and its application in implantology. Finally, with the progression of these technologies, it is essential to address regulatory and ethical considerations to safeguard patient safety and privacy. Ensuring these considerations are met will be crucial in the successful implementation and acceptance of these advanced techniques in dental implantology.

11. TEMPERATURE AND WEIGHT DISTRIBUTION OVER THE KNEE REGION

Crisafulli D., Spataro M., De Marchis C., Risitano G., Milone D. A New Sensorized Approach Based on a DeepLabCut Model and IR Thermography for Characterizing the Thermal Profile in Knees During Exercise. Sensors 2024, 24(23), 7862; https://doi.org/10.3390/s24237862.

Highlights

The temperature of the knee region in 20 participants was monitored during sit-to-stand cycles using an infrared camera. The variations in temperature were analyzed in correlation with weight distribution between the legs during exercise through the use of a Wii Balance Board. An innovative automated methodology for thermal data extraction and post-processing was developed and compared to a conventional semi-automated approach, with the aim of highlighting methodological differences and their implications.

The findings of the proposed protocol demonstrated its potential and suggest it warrants further investigation with a larger cohort of patients. Thermography emerged as a valuable diagnostic tool, offering a more comprehensive assessment of the clinical status of patients when integrated with other diagnostic techniques.

Abstract

The knee is one of the joints most vulnerable to disease and injury, particularly in athletes and older adults. Surface temperature monitoring provides insights into the health of the analysed area, supporting early diagnosis and monitoring of conditions such as osteoarthritis and tendon injuries. This study presents an innovative approach that combines infrared thermography techniques with a Resnet 152 (DeepLabCut based) to detect and monitor temperature variations across specific knee regions during repeated sit-to-stand exercises. Thermal profiles are then analysed in relation to weight distribution data collected using a Wii Balance Board during the exercise. DeepLabCut was used to automate the selection of the region of interest (ROI) for temperature assessments, improving data accuracy compared to traditional time-consuming semi-automatic methods. This integrative approach enables precise and marker-free measurements, offering clinically relevant data that can aid in the diagnosis of knee pathologies, evaluation of the rehabilitation progress, and assessment of

treatment effectiveness. The results emphasize the potential of combining thermography with DeepLabCut-driven data analysis to develop accessible, non-invasive tools for joint health monitoring or preventive diagnostics of pathologies.

11.1 Introduction

The knee, as one of the most complex and vulnerable joints in the human body [300], is prone to various pathological conditions that can affect its surface temperature[301].
Such thermal variations can signify inflammatory processes, injuries, circulatory issues, or other abnormalities. Infrared Thermography (IR) is a non-invasive method used to map body thermal variations, providing valuable diagnostic and monitoring information. Several studies applied IR as a reliable technique to correlate variation in skin temperature to different knee pathologies [302–304]. Early diagnosis is crucial in degenerative knee processes, such as osteoarthritis, to increase the effectiveness of treatment. Carlin et al. [305] clinically evaluated the effectiveness of thermal infrared imaging in the diagnosis and evaluation of knee diseases. According to their results, thermography is a sensitive and reliable method for the diagnosis and monitoring of various knee pathologies, including osteoarthritis, rheumatoid arthritis, ligament and tendon problems.
A recent study [306] analysed thermal normality patterns of the knee joint in professional athletes of different sports. The results showed thermal symmetry in the knee joint, both in the anterior and posterior region, with a contralateral skin temperature difference of less than 0.3°C in elite athletes of judo, basketball, five-a-side football and volleyball with no symptoms of pain or injury. Anterior and posterior knee skin temperatures were similar between men and women. However, sports modalities showed significant differences in knee temperature and anterior-posterior thermal differences. The results highlight the importance of considering differences in motion modalities in the interpretation of thermographic results and in defining strategies to monitor and prevent injuries in athletes. Petrigna et al. [307] conducted a literature review on the use of thermography to assess a thermal attention threshold in people with knee osteoarthritis. Their study proposed a threshold value of 31.3°C, suggesting that knee temperatures at or above this value could indicate the presence of osteoarthritis. However, the values are indicative and related to an analysis of a limited number of case studies. In fact, the conclusion states that there is a need for standardisation of testing protocols and data extrapolation due to the too many differences between studies on this topic, which makes it difficult to propose an unequivocal thermal threshold. In 2019,

Payá et al. [308] explored the reliability of infrared thermography analysis of patellar tendon. The focus has been dedicated to the location of landmarks and region of interest (ROI) that can significantly affect the validity of the collected data.

The study of factors that can influence the accuracy of thermal acquisitions (i.e. [309]) has led over the years to the definition of some protocols for the use of thermography on the human body [310,311]. The definition of the area of interest (ROI) for temperature acquisition is not defined by standard protocols or guidelines, and the position, shape and size of the ROI in the thermogram may vary depending on the operator [312]. The use of external markers to define ROIs is one of the most reliable methods in the analysis of static conditions, whereas in case of analysis of dynamic situations, such as while walking or performing an exercise, the measurement is operator-dependent and often uses data averaged within a control area positioned around the zone of interest [313].

In the recent years, the integration of artificial intelligence algorithms supports the development of new methods to improve diagnostic accuracy, treatment and research processes. In the diagnosis of knee pathologies, AI research has mainly focused on the development of neural networks to perform specific interpretative tasks, such as pathology detection, classification and segmentation [314–319]. Jin et al. [320] proposed an automated approach for the diagnosis of knee osteoarthritis using infrared thermography, dividing the knee area into several zones using the patella as a central reference. As a result, an automated system for thermal screening of the knee was achieved, improving clinical diagnosis.

The thermal behaviour of the knees is closely associated with weight distribution between the legs. Numerous studies have employed the Nintendo™ (Kyoto,Japan) Wii Balance Board™ (WBB) as an effective, low-cost alternative to traditional force plates in biomechanics and rehabilitation research. The WBB is particularly valuable for capturing vertical ground reaction forces and centre of pressure (CoP) data, which are used to evaluate weight bearing asymmetry even during dynamic exercises, such as gait and sit-to-stand cycles [321–325]. This type of data analysis is useful in identifying tendencies such as increased reliance on one leg or shifts in balance, which are critical for clinical assessments of functional ability and fall risk, particularly in aging populations [322,325]. The WBB's efficiency and reliability have been thoroughly validated in the literature, with studies comparing its measurements to those obtained from standard force plates in medical practice [321,323,324,326,327].

In their 2010 study, Clark et al. [327] evaluated the validity and reliability of the WBB as a tool for assessing standing balance. The research involved thirty participants without lower limb pathologies, who performed single-leg and double-leg standing balance tests under eyes-open and eyes-closed conditions on two separate occasions. To determine the WBB's accuracy, its measurements of center of pressure (COP) path length were compared to those obtained using a laboratory-grade force platform (FP), considered the gold standard. Both devices demonstrated strong reliability, with within-device test-retest intraclass correlation coefficients (ICCs) ranging from 0.66 to 0.94 and between-device ICCs ranging from 0.77 to 0.89 across all testing protocols.

These comparisons consistently demonstrate that the WBB provides a robust and accurate measure of postural control and balance parameters, supporting its integration into both research and clinical applications.

This study proposes a new protocol for detecting temperature profiles in various areas of the knee during exercise, aimed at diagnosing potential knee injuries, monitoring disease progression, and evaluating treatment effectiveness. This will be achieved through the combined use of a model trained with DeepLabCut and the infrared thermography technique. The thermal trends were correlated to the weight distribution, evaluated through the WBB acquisition during the sit-to-stand cycles. The differences between the temperature profiles were highlighted by comparing the use of semi-automatic and automatic data extrapolation using a Resnet 152 (DeepLabCut based). This approach combines different methodologies and could find several potential biomedical applications, as it has numerous advantages, including non-invasive operation, does not require the application of external markers to ensure position measurement accuracy, and can be used with a large dataset.

11.2 Materials and Method

A new methodology for detection of the temperature profile on different knee areas during a sit-to-stand exercise is described in this section. Throughout the test, data on weight distribution across the feet were recorded to analyze their correlation with temperature patterns on the knee surface.

Data acquisition of thermal images has been performed at the frequency of 20Hz using the Radiamatic Timage XT infrared camera (IRtech, E instrument Group, Lesmo, Monza Brianza, Italy) equipped with a microbolometer sensor having an optical resolution of 382 x 288 pixels and a thermal sensitivity of 0.04 °C. Thermal images were processed with the

proprietary Timage Connect camera software, Matlab® (The MathWorks Inc., R2024b, Natick, Massachusetts, United States) and deep learning algorithm.

The evaluation of the weight distribution during the exercise have been performed using a Nintendo™ Wii Balance Board™ (WBB) having four load cells, two for each foot. Data on the participant's weight distribution were collected at 20 Hz and transmitted to a computer via Bluetooth. As stated in the introduction, the scientific literature highlights numerous applications utilizing the WBB as an accessible, portable, low-cost tool for assessing balance in patients, demonstrating its reliability in contexts where a high degree of accuracy is not required [328,329]. Rohof et al. [330] assessed the performance of the WBB in a study involving 41 healthy subjects, utilizing the one-leg stance yoga pose "Tree" and the balance game "Table Tilt". Results were compared with two established systems, the MFT-S3 Check and the Posturomed. Their findings indicate that data acquisition with the WBB is comparable to that of laboratory-grade force platforms, confirming its suitability for evaluating postural stability.

No filtering was applied to the data collected from the Wii Balance Board. Conversely, the thermal data were processed using a rlowess filter with a 2% span to suppress outlier spikes and highlight the overall temperature trend. Synchronization between the weight distribution data and knee temperature variations was achieved by aligning them to the test execution timeline.

11.2.1 Cohort

Twenty healthy volunteers participated in this study with no history of knee pain, lower limb surgery or lower limb injuries in the last six months. The sample consists of 14 males and 6 females aged between 22 to 44 years (age = 27.4 ± 5.1 years, body weight = 69.1 ± 14.5 kg, height = 163.0 ± 38 cm). Among the participants 11 showed a BMI in the 18.5-24.9 kg/mm^2 range while the remaining 9 showed a BMI between 25 and 30 kg/mm^2. All subjects provided written informed consent, and all the experiments were carried out according to the principles of the Declaration of Helsinki and declared to had not consumed caffeine or alcohol in the 48 hours prior to the experiment to avoid inducing changes in heart rate and blood pressure [331].

11.2.2 Procedure

Several factors can influence the results of the thermal acquisition during the test. For this reason, to maximize the reliability of this research activity, the previous mentioned

guidelines [310,311] have been followed particularly referring to the room environmental conditions and equipment requirements.

A schematic of the setup configuration is provided in the Figure 11.1, detailing the equipment used and the phases of the sit-to-stand exercise.

The study was carried out in an air-conditioned room with controlled temperature and humidity. During the tests, the average temperature was 27°C with 60% relative humidity. For the test, an infrared camera, fixed on a tripod, was used to acquire thermographic images of the region between the patients' patellar tendon and quadriceps tendon. The camera was positioned at a fixed distance of 0.55 m from the patient, measured at ground level by taking the centre of the WBB and the centre of the tripod as reference. The height of the camera was adjusted according to the anatomical characteristics of each participant to ensure optimal focus on the area of interest. Prior to starting measurements, the patient stood on the WBB, which was calibrated using known weights to ensure accuracy. The participants were asked to wear shorts to ensure the area being analyzed remained exposed. Upon entering the room, participants remained seated at rest for 20 minutes to allow for thermal stabilization, enabling their body temperature to reach equilibrium with the room environment.

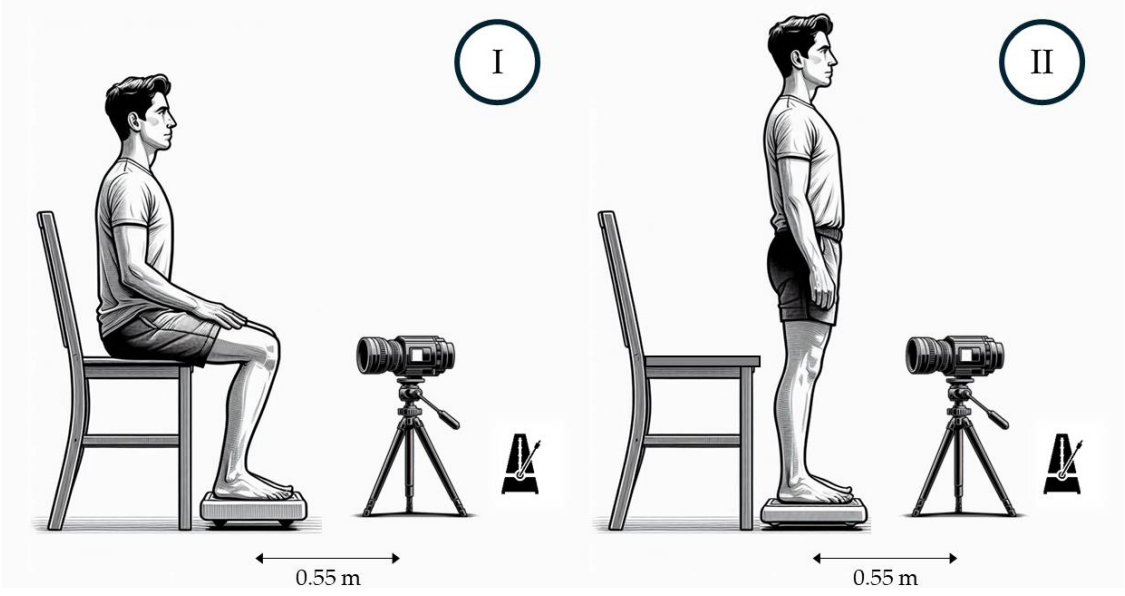

Figure 11.1: Schematic representation of the procedural setup, equipment (WBB, infrared camera and metronome) and sit-to-stand phases: I) sitting phase; II) standing phase.

After this pre-activity phase, participants began the exercise from a sitting position (Figure 11.1 -Phase I), performing repeated cycles of standing up (Figure 11.1 - Phase II) and sitting down for ten minutes. To maintain a consistent exercise pace, a metronome was used, guiding each sit-to-stand cycle (Phase I–Phase II–Phase I) to be completed every 3–4 seconds. To ensure precise identification of the region of interest (ROI) during the analysis phase, metal markers were applied to the subjects' legs, approximately one in the lower end of the quadriceps tendon and the other in the lower end of the patellar tendon (Figure 11.2a). Thermographic images were acquired, ensuring that the area delimited by the markers was fully visible and centered. These markers aid in identifying the region of interest (ROI), enabling comparison across different thermograms during manual data extraction. Previous studies have shown that the use of such markers can improve the accuracy of ROI detection, contributing to greater reproducibility and reliability of results [308].

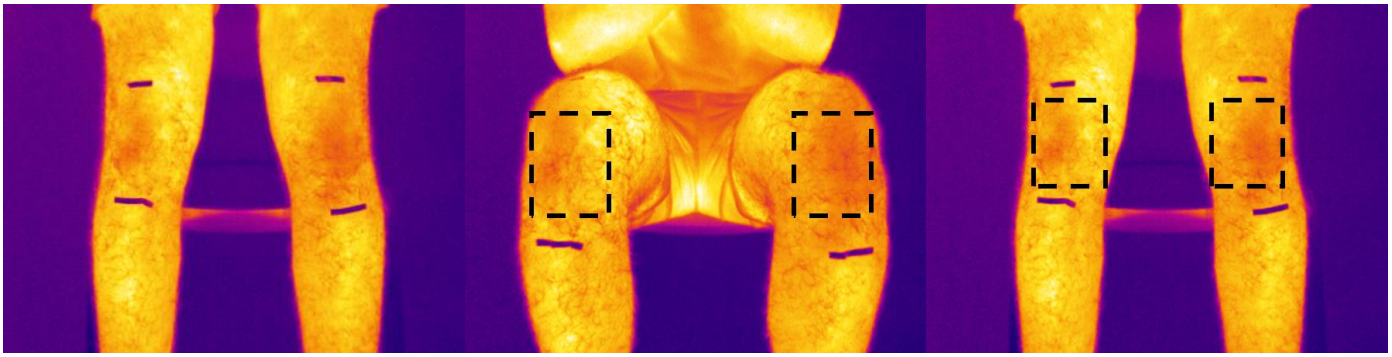

(a) (b) (c)

Figure 11.2: Thermograms during a sit to stand exercise phase: a) Standing position without ROI; b) Sitting position with ROI; c) Standing with ROI.

11.2.3 Semi Automatic Post Processing Methodology

In the semi-automatic post-processing phase, an initial sampling of thermal data acquired via infrared camera has been performed, considering one thermogram every 30 seconds during a 10-minute activity, resulting in a total of 20 frames for each participant. Following this, a rectangular area within the region defined by the metal markers is employed to extract both maximum and minimum temperature values (Figure 11.2b-c). Frame by frame the rectangular box had to be adjusted and redefined according to the current position of the knee regions during the movement from sitting to standing.

11.2.4 Automatic Post Processing Methodology

The automatic post processing pipeline is described in detail in the next chapter. The different zones of interest of the knee have been defined as reported in Figure 11.3, inspired by the photographic knee pain map proposed by Elson et all. [332]. On each knee six zones have been defined; superior lateral (LS), superior medial (SM), Patella (P), lateral and medial joint line areas (LJLA and MJLA), patella tendon (PT). Each acronym is preceded by the letter 'R' or 'L' to designate the right or left leg, respectively.

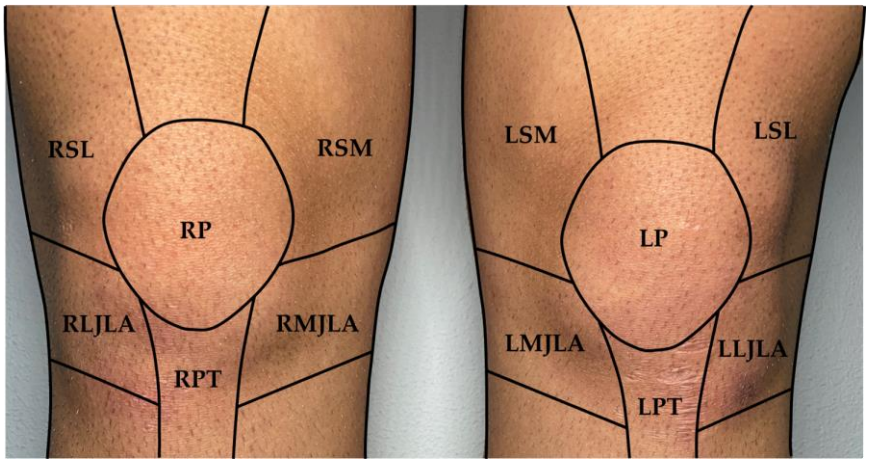

Figure 11.3: Named knee zones and boundaries: SL, superior lateral; SM superior medial; P, patella; LJLA lateral joint line area; MJLA medial joint line area; PT, patella tendon. Initial letters: R, right leg; L, left leg.

11.2.5 Overview of DeepLabCut

DeepLabCut (v2.3.10) is a software toolbox designed for markerless motion capture using deep learning algorithms[333–335]. It provides a framework that allows researchers to track and analyze the movement of animals or humans from video data without the necessity of attaching physical markers to subjects. This is achieved through a process where neural networks are trained to recognize and follow key points on the body, even in complex and varied environments. DeepLabCut's approach is based on transfer learning, meaning it can be trained with relatively few annotated frames and still achieve high accuracy in pose estimation across diverse subjects and settings. Motion capture systems like DeepLabCut are especially useful for studies where traditional marker-based techniques are impractical or intrusive. By using image-based tracking, it captures detailed motion data that is valuable in fields such as neuroscience, ethology, and biomechanics. The flexibility of this system

makes it suitable for both laboratory and naturalistic settings, accommodating a wide range of experimental conditions and movement types[336–339].

The underlying architecture of DeepLabCut often employs deep residual networks (such as ResNet), which are crucial for handling the challenges associated with training deep neural networks. Specifically, the software employs a ResNet-152, which is a deep residual network known for its exceptional performance in neural networks. As outlined in the ResNet architecture, this deeper variant of ResNet utilizes a bottleneck design that incorporates three layers for each residual function 1 × 1, 3 × 3, and another 1 × 1 convolution where the 1 × 1 layers play a vital role in dimension reduction and restoration[340,341]. This advanced configuration addresses issues such as the vanishing gradient problem, making it possible to train deeper networks and improve pose estimation accuracy. By requiring input image dimensions that are multiples of 32 and using a 7 × 7 convolutional layer followed by max pooling, DeepLabCut leverages these structural advancements to efficiently process images at high resolution.

This design allows the software to maintain performance while analyzing high-resolution images, ensuring that critical details in the motion data are not lost. The ability to capture and analyze motion with such precision allows DeepLabCut to be used in other domains, such as thermographic imaging. Here, its capacity to track body regions could be leveraged to estimate thermal data points accurately. By applying this method, researchers could segment and analyze temperature variations over time in a non-invasive way, offering a new approach to studying physiological processes linked to movement and heat distribution.

DeepLabCut model performance

The videos were manually labeled according to the regions described in Figure 11.3. For each video, significant frames were extracted using the k-means algorithm to avoid the issue of labeling the same data twice. Subsequently, 80 % of the dataset was used by DeepLabCut for training purposes while the remaining 20% for validation. The training process, outlined in Table 11.1, involved multiple iterations, each defined by distinct dataset sizes, shuffle parameters, and precision metrics. Data were reported iteratively until the identified parameters no longer showed variation, ensuring that the model had reached a stable state.

Table 11.1: Training Results of DeepLabCut Model

Iter.	Train Iter.	Dataset (%)	Shuffle	Train Error (px)	Test Error (px)	p-cut	Train Err (p-cut)	Test Err (p-cut)
0	25k	80	1	11.6	11.8	0.5	7.3	7.4
1	250k	80	1	10.6	10.5	0.5	6.3	6.5
2	300k	80	1	9.6	9.3	0.5	5.8	5.7

Table 11.1 provides an overview of the key metrics from the training process, demonstrating the stabilization of model performance:

- Train and Test Errors: Both training and testing errors, measured in pixels, showed a steady decrease across iterations before reaching stability. The training error reduced from 11.6 px in the first iteration to 9.6 px in the final iteration, while the test error decreased from 11.8 px to 9.3 px.
- p-cut Adjusted Errors: Errors recalculated using the p-cut threshold (p-cut = 0.5) followed a similar trend, with the train error under p-cut decreasing from 7.3 px to 5.8 px and the test error dropping from 7.4 px to 5.7 px.

These results highlight the refinement of the model's performance, with iterations continuing until the parameters stabilized and no longer exhibited changes. This demonstrates the robustness of the training process, and the reliability of the methodology applied.

11.2.6 Overview of Statistical Analysis

To present the findings and compare the semi-automatic and automatic methods for temperature extraction, a statistical analysis using MATLAB was conducted. Bar charts were generated to evaluate the number of participants showing a correlation between the leg bearing the greater load and the leg with the most significant temperature variation, based on the results from both methodologies. Additionally, the extracted thermal data, averaged over the region of interest (ROI), was compared to data from a specific area of the knee. Specifically, a linear model was employed as correlation analysis between the maximum temperature extracted using the semi-automatic method and the temperature recorded at the medial collateral ligament using the proposed automatic method. A similar analysis was conducted for the minimum temperature, comparing it with the temperature measured at the patella. Classifications were performed based on gender (male-female), body mass index (BMI; normal weight < 18.4, overweight > 18.4), and the presence of weight asymmetry (one leg bearing > 52% of the weight). Finally, the Bland–Altman analysis was conducted

to assess the agreement between two measurement methods across four regions: Right Patella, Left Patella, Right Ligament, and Left Ligament.

11.3 Results

Combined thermographic analysis and Deep learning techniques (Deeplabcut trained model) enabled the assessment of thermal profiles across various knee regions during repeated sit-to-stand exercises. Specifically, evolving knee temperature profiles were captured during 10-min cycles of sit-to-stand exercises. Two post-processing methodologies—semi automatic and automated—were investigated and are detailed in the following sections. The thermal profile trends on participants' knees were additionally correlated with weight distribution assessments between the legs, measured using the WBB.

11.3.1 Temperature Assessment

The physical activity produces a generalized temperature modification on the body, related to a variation on skin blood flow [342]. Figure 11.4 shows a visible variation in the temperature distribution in the legs between the two thermograms of a participant before and after performing the exercise.

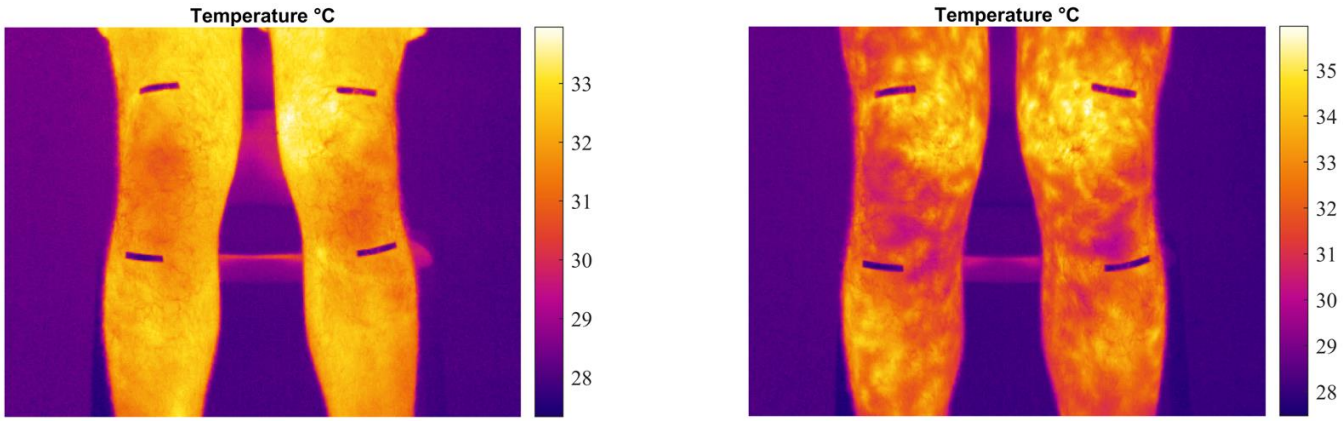

(a) *(b)*

Figure 11.4: Temperature map of the knee region: (a) pre-exercise; (b) post-exercise.

11.3.2 Semi automatic post-processing

The semi-automatic post-processing method for thermal profile extraction consisted of positioning a rectangular ROI frame by frame on the knee region, as shown previously in Figure 11.2. For all participants, maximum and minimum temperature from each frame have

been extracted from the ROI, since the highest temperature consistently appeared in the region of the medial collateral ligament, while the lowest temperature was observed in patella or patellar tendon area. These findings align with the impact of physical exercise on skin microvascular responsiveness, which appears to be greater in the medial collateral ligament region. This heightened responsiveness is reflected in the consistently higher temperatures observed in this area, compared to the lower temperatures recorded in the patellar tendon region [343].

The thermal profile of one participant has been reported in terms of temperature variation over the time (Figure 11.5). In the graph, red markers indicate the right leg, whereas blue markers represent the left leg.

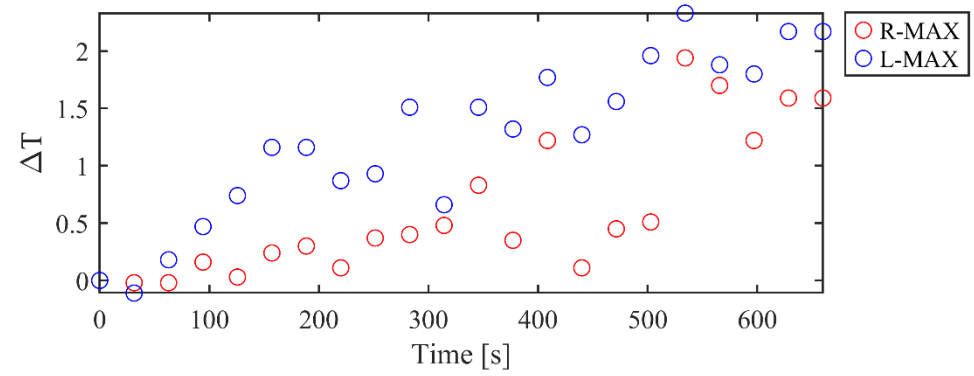

(a)

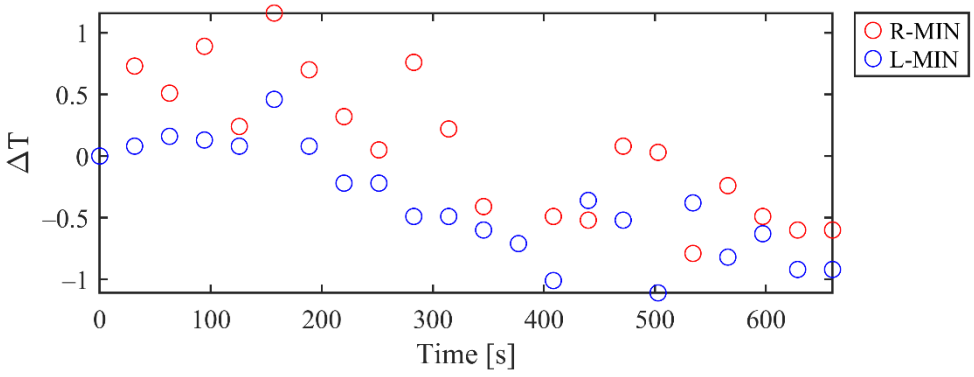

(b)

Figure 11.5: Temperature variation during exercise for the right (red) and left (blue) legs is shown for: (a) maximum temperature trend and (b) minimum temperature trend.

During the test, maximum temperature consistently displayed an increasing trend, while minimum temperature generally exhibited a decreasing trend in most cases, according to the increasing blood flow to the active muscle as stated by Simmons et al. [342].

11.3.3 DeepLabCut Post-Processing

The automation of temperature data extraction for specific knee regions was developed using the thermal dataset acquired as described in Chapter 11.2. Automating the process through DeepLabCut model allows for efficient processing of large datasets to determine a position of a specific target over the time.

In this study, one image per second was provided as input to the Resnet 152 model for each participant over 10 minutes of exercise (approximately 600 images per participant), resulting in output pixel coordinates marking the center of each knee region defined in the Figure 11.3 for every frame. The neural network identified the various knee regions throughout all phases of movement, as shown in the Figure 11.6, with an average likelihood function of 0.99 for all case studies. Temperature values for each knee area were subsequently extracted from these pixel coordinates across the entire exercise duration.

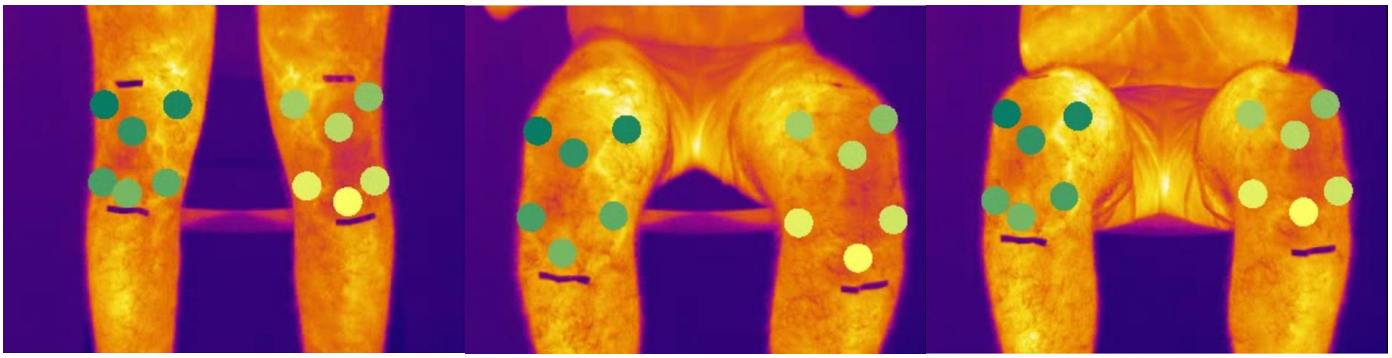

(a) (b) (c)

Figure 11.6: Thermograms during a sitting phase, green circles represent the point detected by the DeepLabCut model on the knee area on the standing phase (a), during sitting phase (b) and sitting (c).

The temperature profiles extracted with the automatic post-processing methodology for each knee zones have been reported in Figure 11.7.

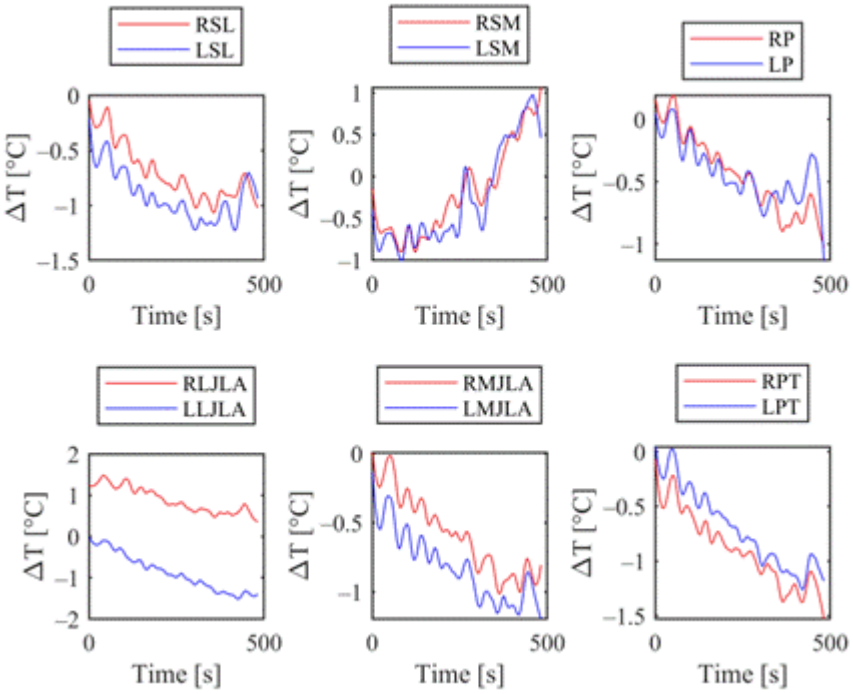

Figure 11.7: Temperature evolution on knee areas showed in Figure 11.3.

As previously observed during the semi-automatic post-processing phase, a notable temperature increase is associated with the region encompassing the medial collateral ligament. This observation is further supported by the temperature trend analysis across different knee areas, which also highlights a significant increase in the medial collateral ligament region (see Figure 11.7, RSM and LSM curves).

The results for the patellar region and patellar tendon (RP and LP, RPT and LPT) showed a decrease in temperature as indicated in the previous paragraph.

No evidence of a correlation patterns emerged from the comparison of the other different temperature trend of the knee areas over the participants.

11.3.4 Weight distribution evaluation

This section presents the results of data acquisition from the WBB. Assessing asymmetries in body weight distribution between the legs could impact the thermal profiles extracted from knee regions, depending on the leg analyzed. Therefore, this study evaluated the distribution of weight between the legs, as well as between the forefoot and rearfoot, and continuously monitored the center of pressure (CoP) position throughout the exercise. By tracking these variables during the sit-to-stand cycles, it is possible to account for potential

influences of weight distribution on knee temperature profiles, thereby enhancing the precision of thermal assessment and its relevance to knee joint health.

Figure 11.8 depicts the progression of data collected from the four load cells throughout the activity. For clarity and readability, the results are displayed over a reduced time interval (from 20 to 36 sec), focusing on a subset of sit-to-stand cycles.

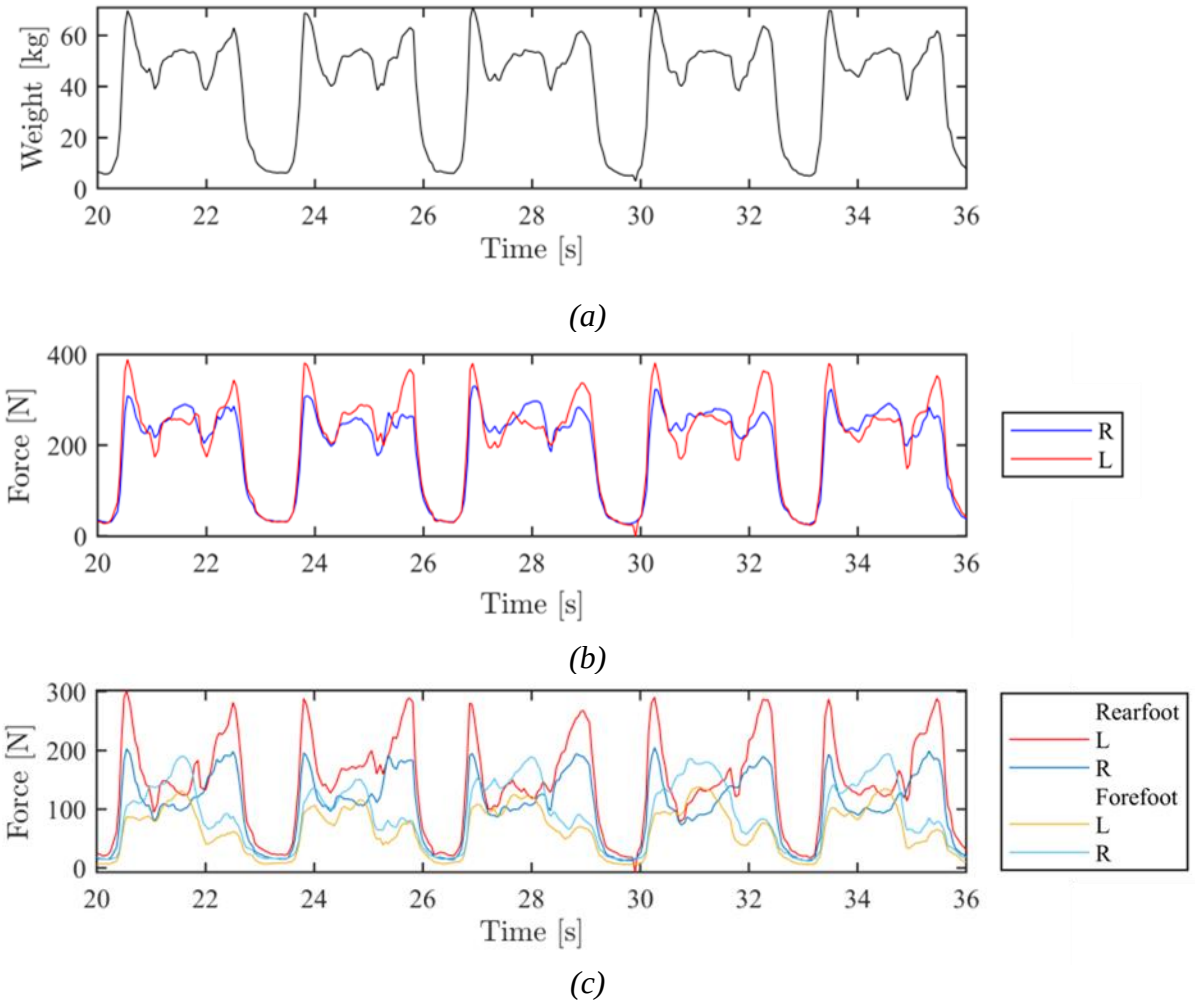

Figure 11.8: Wii Balance board acquisition from 20 to 36 sec of the sit-to stand activity: (a) Weight distribution (kg); (b) Force distribution on right (blue) and left (red) leg; (c) Force distribution on left (red) and right (blue) rearfoot, left (yellow) and right (cyan) forefoot.

Figure 11.8a illustrates the trend in total weight distribution over the selected time interval. When the participant stands, the weight is fully distributed into the feet, resulting in an increase in weight recorded by the WBB. During this phase, the value stabilizes around a level corresponding to the participant's static weight. In the sitting phase, weight is

transferred to the chair, leading to a decrease in the graph curve until reaching a minimum value near zero, indicating that nearly all weight is transferred to the chair.

Figure 11.8b illustrates the distribution of weight force over the selected time interval, divided between the legs. Here, a slight tendency of the participant to exert more force on the left leg while rising is observed. In general, patients did not exhibit an asymmetry in weight distribution between the legs exceeding 54.5% during exercise performance. Specifically, 13 out of 20 participants (65%) demonstrated a weight distribution of at least 52% on one leg during the exercise. Interestingly, this patient group exhibited more pronounced warming of the medial collateral ligament in the leg bearing greater weight compared to the leg with less load. Figure 11.8c shows the distribution of force between the forefoot and rearfoot for both legs over the same time interval. In all participants, it was noted that the rearfoot carries the greatest load when in the standing position.

Data on the position of the center of pressure (CoP) were assessed using the WBB during the exercise (Figure 11.9). The coordinate point (0,0) represents the center of the WBB, with the x-axis indicating medio-lateral direction displacement and the y-axis representing antero-posterior direction movement of the subject. The percentages in each corner quantify body weight distribution across the four load cells. Over time, the trajectory of the CoP position forms an elongated shape aligned with the direction of movement. Additionally, the weight force is predominantly exerted on the rearfoot, with a slight imbalance toward the left side.

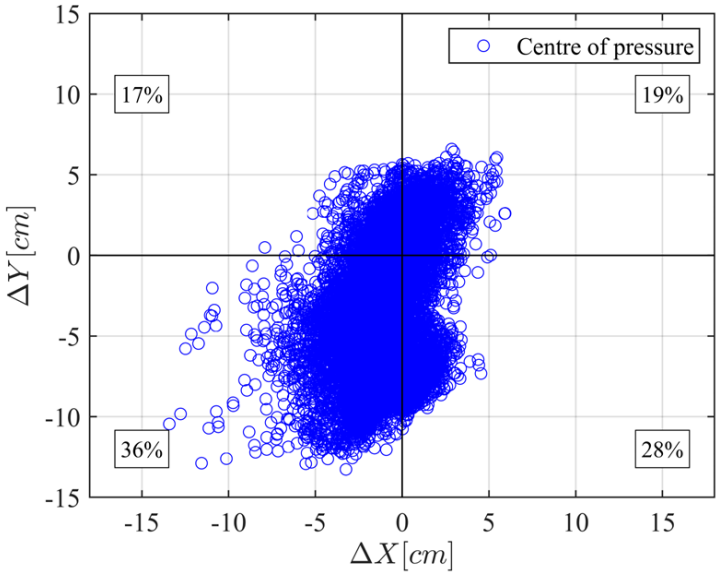

Figure 11.9: Centre of pressure position and body weight distribution on the feet for each of the four loadcell (in %) during the exercise.

11.3.5 Statistical analysis

In this section the results of statistical analysis have been presented. Specifically, the number of participants showing agreement between the leg bearing the greater load and the leg exhibiting the highest increase or decrease in temperature, was examined. This evaluation was carried out by considering both the results of the semi-automatic method and those of the automated method and the results have been displayed in the bar charts of Figure 11.10. In the graphical representation, male participants are indicated in blue and female participants in green. For each gender, the measurements classified as "AGREEMENT" (AG) indicate that both methodologies produced consistent results, demonstrating a correlation between the leg bearing the greater load and the leg exhibiting either increased heating of the medial collateral ligament or increased cooling of the patella.

Measurements classified as "DISAGREEMENT" (NAG) reflect cases where the two methods produced the same non-matching results. For example, for males, one case showed no correlation between the most loaded leg and the leg with the greatest thermal variation, while for females, this discrepancy occurred in three cases (Figure 11.10b).

Conversely, the measurements categorized as "PARTIAL AGREEMENT" (PAG) represent instances where one method identified a correlation between the most loaded leg and the leg with the most significant thermal variation, while the other method did not.

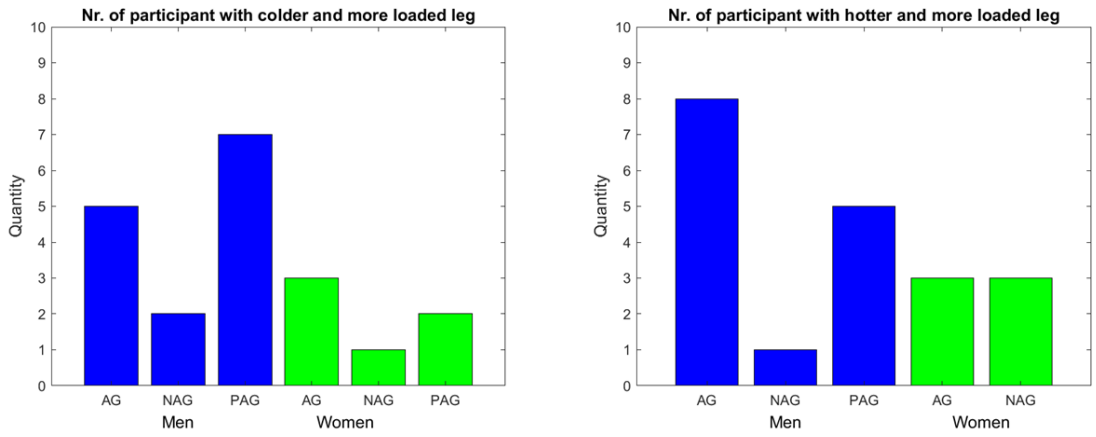

(a) *(b)*

Figure 11.10: Correlation between the leg bearing the greater load and the leg with the most significant thermal variation classified by gender (men=blue, women=green) (AGREE (AG) true for both methods, DISAGREE (DAG) false for both methods, PARTIAL AGREEMENT (PAG) true for one of the two methods): (a) Leg with the greatest cooling; (b) Leg with the greatest heating.

The linear regression model was applied to evaluate the interclass correlation between temperatures obtained using semi-automatic and automatic methods. The results have been further distinguished by gender, BMI and asymmetries in body weight distributions. Since the automatic methods provide continuous, real-time data, while the semi-automatic method captures only 20 discrete measurements, the automatic data was interpolated to match the specific timestamps of the semi-automatic readings. Following this adjustment, the correlation between the methods was analyzed, along with the coefficient of determination (R^2). Across 80 measurements, 67% demonstrated a strong correlation, with an average R^2 of 0.71 ± 0.17, indicating high agreement between the methods (Figure 11.11).

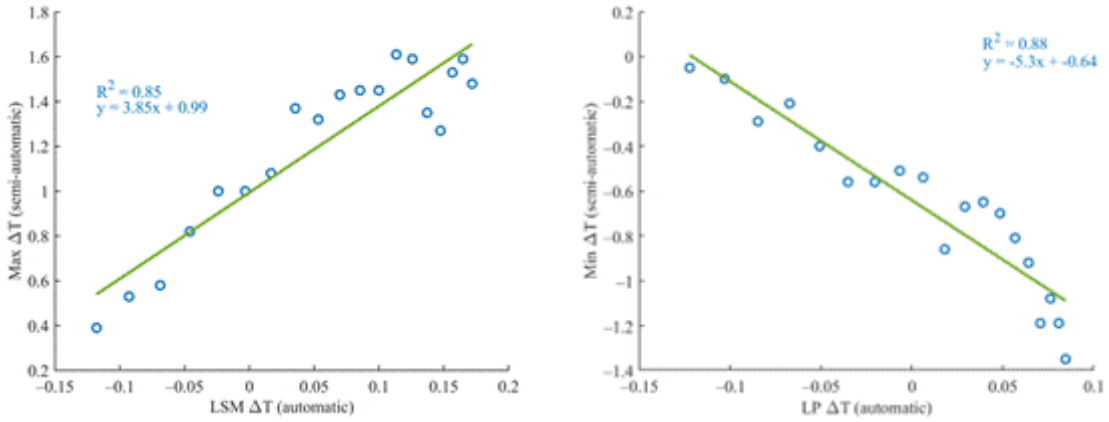

(a) *(b)*

Figure 11.11: Regression analysis between the semi-automatic method and the automatic one. A strong correlation was found for the 67% of the measurements with R^2 of 0.71 ± 0.17, both for the ligament(a) and the patellar zone (b)

As shown in Table 11.2, the results indicate that women, participants with a normal weight, and those with unbalanced conditions exhibited slightly higher correlations compared to other groups. The remaining 33% of the total measurement exhibited a weak correlation, with an average R^2 of 0.12 ± 0.08, suggesting little to no agreement. Among the strongly correlated measurements (67%), a further analysis was performed based on gender and other participant characteristics. Investigating the lack of correlation in these cases, the issue appears to stem from the quality of the thermal data obtained through the semi-automatic acquisition method. This hypothesis is supported by the higher RMSE (root mean square error) values observed in the temperature-time trends of the semi-automatic method

compared to those of the automatic method, indicating greater variability and reduced reliability in the semi-automatic measurements (Figure 11.12).

Table 11.2: Correlation analysis between semiautomated and automated method

		Correlated Cases (67.5%)	**W**	**M**	**BMI >18.4**	**BMI < 18.4**	**Balanced**	**Not Balanced**
R^2	Mean	0.71	0.72	0.68	0.66	0.72	0.69	0.71
	Std	0.17	0.17	0.2	0.21	0.16	0.21	0.16

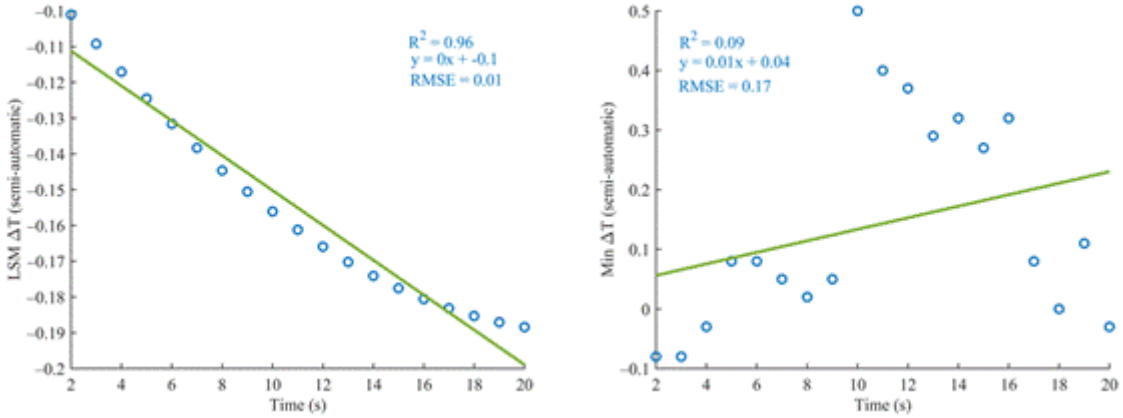

(a) *(b)*

Figure 11.12: Thermal trend in the automatic (a) and semi-automatic (b) methods shows distinct differences. The automatic shows a clear decreasing trend, with an RMSE of 0.01, indicating near-perfect linear trend. In contrast, the semi-automatic method lacks a significant correlation, reflected by a much higher RMSE of 0.15.

The Bland-Altman test was conducted to assess the agreement between the two methodologies across the four regions of Right Patella, Left Patella, Right Ligament, and Left Ligament. The results show notable differences in agreement depending on the anatomical region.

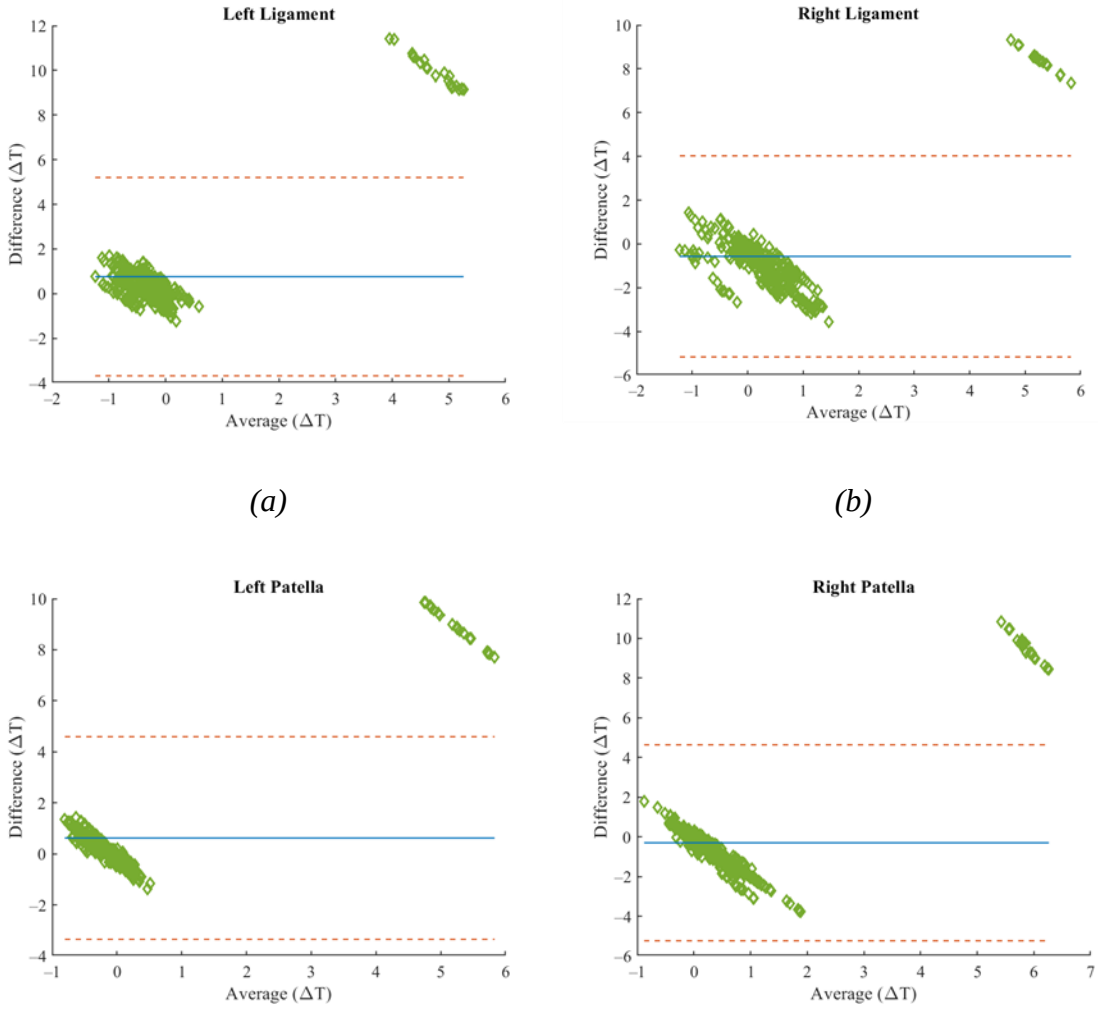

Figure 11.13: Bland–Altman plots of Left and Right Ligament (a,b), Right Patella, and Left Patella (c,d). The green diamonds represent the individual data points, plotting the difference between the two methods on the y-axis against the average of the two measurements on the x-axis. The blue line indicates the mean difference between the two methods. The red dashed lines represent the 95% confidence range, within which most of the data points are expected to fall.

Overall, the ligament regions (Right and Left) exhibited better agreement between the methods, with minimal bias and tighter limits of agreement. In contrast, the patella regions (Right and Left) showed larger variability, wider limits of agreement, and occasional outliers, suggesting less consistent agreement, particularly at higher measurement values.

11.4 Conclusion and discussion

This study introduces a novel methodology for monitoring temperature variations across distinct knee regions during repetitive exercise cycles, alongside tracking weight distribution over time. This dual approach enables the identification of postural imbalances and explores potential correlations between asymmetric weight-bearing and abnormal temperature variations in the legs.

The cyclic execution of the sit-to-stand exercise was observed to result in localized warming of the medial collateral ligament, while the patella and patellar tendon tended to exhibit a cooling effect in most cases. This distinct thermal response pattern may reflect the different mechanical demands placed on different knees during repetitive weight-bearing transitions, highlighting the influence of the exercise on joint thermoregulation. Specific warming of the medial collateral ligament is related to the nature of the exercise; in fact, the squat is often used to assess recovery of the medial collateral ligament following surgical intervention [344].

Additionally, comparison of knee temperature trends with weight distribution data revealed that greater warming of the medial collateral ligament was associated with the leg bearing a higher load. Specifically, in participants who demonstrated an asymmetrical weight distribution, with more than 52% of their body weight on one leg (13 out of 20 participants), the increased thermal response of the medial collateral ligament corresponded to the more heavily loaded leg. This finding suggests a relationship between mechanical load and localized heat generation in knee areas, providing insights into how load-bearing influences knee temperature dynamics during repetitive motion. No clear association was identified between temperature trends in other knee regions and weight distribution patterns. The primary aim of this study was to introduce a novel method for analyzing thermal responses during movement; however, further research is needed to better understand the thermal behavior across various knee areas. When comparing the two methodologies for assessing the match between the leg bearing the greater load and the leg exhibiting the highest increase or decrease in temperature, gender differences were evaluated. Among male participants, the results were more definitive in detecting trends in maximum temperature variations, whereas greater uncertainty was observed in the evaluation of minimum temperature changes. This discrepancy may be attributed to the fact that thermal variations associated with heating are

more pronounced and easier to detect compared to those related to cooling, which tend to be less distinct. For female participants, however, no significant conclusions could be drawn due to the smaller sample size relative to male participants, limiting the statistical power of the analysis. A linear regression model was employed to evaluate the interclass correlation between temperatures obtained using the semi-automatic and automatic methods. The automatic method, which provides continuous real-time data, was compared to the semi-automatic method, which captures 20 discrete measurements. To ensure compatibility, the automatic data was interpolated to align with the specific timestamps of the semi-automatic readings. The correlation between the two methods was then analysed, and the strength of the relationship was quantified using the coefficient of determination (R^2), providing insight into the consistency and reliability of the methods.

The results demonstrate the capabilities of both semi automatically processed and DeepLabCut-driven automated methods, highlighting the advantages and limitations of each. Semi-automatic data processing involves repetitive steps, requiring operators to select and analyse individual frames to export results. While increasing the sampling rate of thermal data (up to the infrared camera's acquisition frequency) can improve accuracy, this approach is time-consuming as operators must manually define regions of interest (ROIs) for each frame. In contrast, the automated system proved to be a reliable tool for identifying knee regions to extract temperature data accurately. Due to its DeepLabCut-driven nature, the system can handle large input datasets without excessive processing time or the risk of operator errors inherent in repetitive tasks. This scalability and reliability underscore its utility for extensive thermal monitoring applications without compromising accuracy or efficiency. Despite the majority of the measurements showed a strong correlation between the two methos ($R^2 = 0.71 \pm 0.17$), a weak correlation was observed in 33% of them. This is addressed to the quality of thermal data obtained via the semi-automatic acquisition method. This hypothesis is supported by higher RMSE values observed in the temperature-time trends of the semi-automatic method, indicating greater variability and reduced reliability compared to the automatic method.

The Bland-Altman analysis revealed variations in agreement between the two methods depending on the anatomical region. The patella regions showed less consistent agreement, with wider limits of agreement, greater variability, and systematic biases, particularly at higher temperatures. In contrast, the ligament regions exhibited stronger agreement, with

near-zero biases, narrower limits of agreement, and minimal variability. These results highlight better reliability of the methods in ligament regions compared to patella regions.

The thermal response in the human body is closely tied to exercise type. For instance, repetitive movements like stepping up and down, treadmill walking, or cycling activate different muscle groups and lead to varying heat emission patterns. Therefore, future research could explore the thermal responses of various body regions under different types of exercises to gain more insights into muscle activation and heat distribution. Moreover, future studies could investigate the influence of dietary habits, hormonal levels and metabolic rate to identify potential correlations with temperature variations and their underlying physiological mechanisms.

Although all participants in the present study reported no known knee issues, future research could focus on individuals with diagnosed knee pathologies. This would enable a comparison of thermal and weight distribution responses between those with knee conditions and healthy participants, potentially uncovering differences in temperature variations and load distribution patterns associated with specific knee disorders. Such findings could significantly enhance rapid diagnostic techniques, injury prevention, and the monitoring of recovery progress post-surgery. Furthermore, these applications could be extended beyond the knee to other commonly injured areas, such as the ankle, elbow, and shoulder, particularly in contexts involving physical activity.

CONCLUDING REMARKS

This thesis represents a collection of some of the research activities that have been carried out during the three years of the PhD course. The knowledge in the field of mechanical engineering and machine design has been deepened and utilized in materials and components that find application in the bioengineering field. The use of innovative methodologies such as infrared thermography and numerical simulations permitted the investigation of factors affecting the fatigue life of materials.

The application of the Risitano Thermographic Method and Static Thermographic Method were applied in the two types of stainless steels AISI 304L and 316L. The last one in particular is the most widely used type of stainless steel in the field of bioengineering.
Analyses were conducted on the fatigue life of the specimens with regard to the influence of component thickness, notching effect, manufacturing technology and the heat treatment used to realize them.
The three-month visiting researcher experience at the Institute of Physics of Materials in Brno, Czech Republic, provided the know-how to further study the materials tested also from the microstructural point of view, opening up new possibilities for national and international research and collaboration.

Numerical simulation methods and the use of machine learning have made it possible to define a new and innovative method for designing the hip prosthesis, optimizing the component from a tribological and mechanical point of view, in a customized manner on the patient.
The use of the Strain Energy Density approach has enabled the study of notches in AISI 304L stainless steel and the influence on fatigue life of geometric imperfections in welded joints. This approach can be applied in a very similar way to the geometric imperfections of components produced by additive manufacturing techniques in the biomedical landscape, with particular reference to the scaffold and lattice structures that are increasingly being used nowadays.
Thermography has also been proposed as a method of diagnosis possible abnormalities on bone during dental implant and on the health of the knee region of patients in relation to their body weight distribution between the legs.

Energy approaches represent fertile ground for scientific research and will increasingly find application in all areas of engineering in the future.

LIST OF PUBLICATIONS

Foti P., **Crisafulli D**., Santonocito D., Risitano G., F. Berto, Effect of misalignments and welding penetration on the fatigue strength of a common welded detail: SED method predictions and comparisons with codes, Int. J. Fatigue. 164 (2022). https://doi.org/10.1016/j.ijfatigue.2022.107135. [JOURNAL–IF:6(2024)]

Milone D., Risitano G., Pistone A., **Crisafulli D.**, Alberti F., A New Approach for the Tribological and Mechanical Characterization of a Hip Prosthesis Through a Numerical Model Based on Artificial Intelligence Algorithms and Humanoid Multibody Model, Lubr. 2022. 10 (2022) 160. https://doi.org/https://doi.org/10.3390/lubricants10070160. [JOURNAL – IF: 3.584 (2024)]

Crisafulli D., Foti P., Santonocito D., An innovative experimental energy-based approach for the life prediction of notched details, IOP Conf. Ser. Mater. Sci. Eng. (2023). https://doi.org/10.1088/1757-99X/1275/1/012018. [PROCEDIA – NATIONAL CONFERENCE]

Crisafulli D., Fintová S., Santonocito D., D'Andrea D., Microstructural characterization and mechanical behaviour of Laser Powder Bed Fusion stainless steel 316L. Theoretical and Applied Fracture Mechanics, 131 (2024). https://doi.org/10.1016/j.tafmec.2024.104343 [JOURNAL–IF: 5.3 (2024)]

Crisafulli D., Spataro M., De Marchis C., Risitano G., Milone D., A New Sensorized Approach Based on a DeepLabCut Model and IR Thermography for Characterizing the Thermal Profile in Knees During Exercise. Sensors 2024, 24(23), 7862; https://doi.org/10.3390/s24237862
[JOURNAL–IF: 3.4 (2024)]

LIST OF TABLES

LIST OF FIGURES

REFERENCES

[1] Campbell FC. Fatigue and Fracture: Understanding the Basics. ASM International; 2012.

[2] Wöhler A. Über die festigkeitsversuche mit eisen und stahl. Ernst & Korn; 1870.

[3] Morgan EF, Unnikrisnan GU, Hussein AI. Annual Review of Biomedical Engineering Bone Mechanical Properties in Healthy and Diseased States 2018. https://doi.org/10.1146/annurev-bioeng-062117.

[4] Thornton GM, Schwab TD, Oxland TR. Fatigue is more damaging than creep in ligament revealed by modulus reduction and residual strength. Ann Biomed Eng 2007;35:1713–21. https://doi.org/10.1007/s10439-007-9349-z.

[5] Wojtys EM, Beaulieu ML, Ashton-Miller JA. New perspectives on ACL injury: On the role of repetitive sub-maximal knee loading in causing ACL fatigue failure. Journal of Orthopaedic Research 2016;34:2059–68. https://doi.org/10.1002/jor.23441.

[6] Chen J, Kim J, Shao W, Schlecht SH, Baek SY, Jones AK, et al. An Anterior Cruciate Ligament Failure Mechanism. American Journal of Sports Medicine 2019;47:2067–76. https://doi.org/10.1177/0363546519854450.

[7] Purevsuren T, Kwon MS, Park WM, Kim K, Jang SH, Lim YT, et al. Fatigue injury risk in anterior cruciate ligament of target side knee during golf swing. J Biomech 2017;53:9–14. https://doi.org/10.1016/j.jbiomech.2016.12.007.

[8] Gratton A, Buford B, Goswami T, Gaddykurten D, Suva L, Buford A, et al. Failure Modes of Biomedical Implants. Journal of the Mechanical Behaviour of Materials 2002.

[9] Teoh SH. Fatigue of biomaterials: a review. vol. 22. 2000.

[10] Hernandez-Rodriguez MAL, Ortega-Saenz JA, Contreras-Hernandez GR. Failure analysis of a total hip prosthesis implanted in active patient. J Mech Behav Biomed Mater 2010;3:619–22. https://doi.org/10.1016/j.jmbbm.2010.06.004.

[11] Shemtov-Yona K, Rittel D. Identification of failure mechanisms in retrieved fractured dental implants. Eng Fail Anal 2014;38:58–65. https://doi.org/10.1016/j.engfailanal.2014.01.002.

[12] Shemtov-Yona K, Rittel D. Fatigue of dental implants: Facts and fallacies. Dent J (Basel) 2016;4. https://doi.org/10.3390/dj4020016.

[13] Niinomi M. Metallic biomaterials. Journal of Artificial Organs 2008;11:105–10. https://doi.org/10.1007/s10047-008-0422-7.

[14] Haqqani HM, Mond HG. The implantable cardioverter-defibrillator lead: Principles, progress, and promises: Principles. PACE - Pacing and Clinical Electrophysiology 2009;32:1336–53. https://doi.org/10.1111/j.1540-8159.2009.02492.x.

[15] Kleemann T, Nonnenmacher F, Strauss M, Kouraki K, Werner N, Fendt A, et al. Long-term performance and lead failure analysis of the Durata defibrillation lead compared to its previous model, the recalled Riata defibrillation lead. J Cardiovasc Electrophysiol 2019;30:2012–9. https://doi.org/10.1111/jce.14087.

[16] Pimenta AR, Tavares SSM, Dias DF, Correa SR, Sobreiro AL, Diniz MG. Failure analysis of a titanium hip prosthesis. Journal of Failure Analysis and Prevention 2021;21:28–35. https://doi.org/10.1007/s11668-020-01041-2.

[17] Bahraminasab M, Hassan MR, Sahari BB, Nasab MB. Metallic biomaterials of knee and hip-A review. Trends Biomater Artif Organs 2010;24:69–82.

[18] Frost HM. Wolff's Law and bone's structural adaptations to mechanical usage: an overview for clinicians. Angle Orthod 1994;64:175–88.

[19] Aherwar A, K Singh A, Patnaik A. Current and future biocompatibility aspects of biomaterials for hip prosthesis. AIMS Bioeng 2015;3:23–43. https://doi.org/10.3934/bioeng.2016.1.23.

[20] Niinomi M. Recent Metallic Materials for Biomedical Applications. Metallurgical and Materials Transactions A 2002;33A:477–86.

[21] Illustration of Typical Knee Replacement, Hardware Components Re – Hip and Knee Handbook of Joint Replacement n.d. https://hipandkneehandbook.com/illustration-of-typical-knee-replacement-hardware-components-re/ (accessed September 9, 2024).

[22] Liu X, Chu PK, Ding C. Surface modification of titanium, titanium alloys, and related materials for biomedical applications. Materials Science and Engineering R: Reports 2004;47:49–121. https://doi.org/10.1016/j.mser.2004.11.001.

[23] Campanelli LC. A review on the recent advances concerning the fatigue performance of titanium alloys for orthopedic applications. J Mater Res 2020. https://doi.org/10.1557/jmr.2020.305.

[24] Iwana D, Nishii T, Miki H, Sugano N, Sakai T, Ohzono K, et al. Proximal bone remodelling differed between two types of titanium long femoral components after cementless revision arthroplasty. Int Orthop 2008;32:431–6. https://doi.org/10.1007/s00264-007-0357-2.

[25] Niinomi M. Mechanical biocompatibilities of titanium alloys for biomedical applications. J Mech Behav Biomed Mater 2008;1:30–42. https://doi.org/10.1016/j.jmbbm.2007.07.001.

[26] Maksimkin A V., Senatov FS, Niaza K, Dayyoub T, Kaloshkin SD. Ultra-high molecular weight polyethylene/titanium-hybrid implant for bone-defect replacement. Materials 2020;13. https://doi.org/10.3390/ma13133010.

[27] Li YH, Shang XY, Li YJ. Fabrication and characterization of TiMoCu/PMMA composite for biomedical application. Mater Lett 2020;270. https://doi.org/10.1016/j.matlet.2020.127744.

[28] Pillar RM. Overview of Surface Variability of Metallic Endosseous Dental Implants: Textured and Porous Surface-Structured Designs. Implant Dent 1998;7:305–14.

[29] Wadood A. Brief overview on nitinol as biomaterial. Advances in Materials Science and Engineering 2016;2016. https://doi.org/10.1155/2016/4173138.

[30] Nouri A, Wen C. Introduction to surface coating and modification for metallic biomaterials. Surface Coating and Modification of Metallic Biomaterials, Elsevier Inc.; 2015, p. 3–60. https://doi.org/10.1016/B978-1-78242-303-4.00001-6.

[31] Davis J. Handbook of materials for medical devices. Metallic materials. ASM international, 2003, p. 22–30.

[32] Bazaka O, Bazaka K, Kingshott P, Crawford RJ, Ivanova EP. Metallic Implants for Biomedical Applications. Inorganic Materials Series: The Chemistry of Inorganic Biomaterials, vol. 7, 2021, p. 1–98.

[33] Ganesh VK, Ramakrishna K, Ghista DN. Biomechanics of bone-fracture fixation by stiffness-graded plates in comparison with stainless-steel plates. Biomed Eng Online 2005;4. https://doi.org/10.1186/1475-925X-4-46.

[34] Bordji G, Jouzeau J-Y, Mainard D, Payan E, Delagoutte+ J-P, Netter P. Evaluation of the effect of three surface treatments on the biocompatibility of 316L stainless steel using human differentiated cells. Biomaterials 1996;17:491–500.

[35] Banerjee P, White IR. Allergic contact dermatitis at the application site of an electrosurgical earthing plate occurring in a windscreen repairer. Contact Dermatitis 2001;44:97–130.

[36] Disegil JA, Eschbachz L. Stainless steel in bone surgery. Injury, Int I Care Injured 2000;31.

[37] Findik F. Recent developments of metallic implants for biomedical applications 2020;8:33–57.

[38] F75 Standard Specification for Cobalt-28 Chromium-6 Molybdenum Alloy Castings and Casting Alloy for Surgical Implants (UNS R30075) n.d. https://www.astm.org/standards/f75 (accessed September 9, 2024).

[39] F1537 Standard Specification for Wrought Cobalt-28Chromium-6Molybdenum Alloys for Surgical Implants (UNS R31537, UNS R31538, and UNS R31539) n.d. https://www.astm.org/f1537-20.html (accessed September 9, 2024).

[40] Marti A. Cobalt-base alloys used in bone surgery. Injury 2000;31 Suppl 4. https://doi.org/10.1016/S0020-1383(00)80018-2.

[41] Al Jabbari YS. Physico-mechanical properties and prosthodontic applications of Co-Cr dental alloys: a review of the literature. J Adv Prosthodont 2014;6:138–45. https://doi.org/10.4047/JAP.2014.6.2.138.

[42] Wang Y, Tan Q, Pu F, Boone D, Zhang M. A Review of the Application of Additive Manufacturing in Prosthetic and Orthotic Clinics from a Biomechanical Perspective. Engineering 2020;6:1258–66. https://doi.org/10.1016/J.ENG.2020.07.019.

[43] Tom T, Sreenilayam SP, Brabazon D, Jose JP, Joseph B, Madanan K, et al. Additive manufacturing in the biomedical field-recent research developments. Results in Engineering 2022;16:100661. https://doi.org/10.1016/J.RINENG.2022.100661.

[44] Jardini AL, Larosa MA, Macedo MF, Bernardes LF, Lambert CS, Zavaglia CAC, et al. Improvement in Cranioplasty: Advanced Prosthesis Biomanufacturing. Procedia CIRP 2016;49:203–8. https://doi.org/10.1016/J.PROCIR.2015.11.017.

[45] Deng L, Zhao X, Wei C, Qu W, Yu L, Zhu S. Application of a three-dimensional printed segmental scapula prosthesis in the treatment of scapula tumors. Journal of International Medical Research 2019;47:5873–82. https://doi.org/10.1177/0300060519875336/ASSET/IMAGES/LARGE/10.1177_0300060519875336-FIG6.JPEG.

[46] Li Y, Shi Y, Lu Y, Li X, Zhou J, Zadpoor AA, et al. Additive manufacturing of vascular stents. Acta Biomater 2023;167:16–37. https://doi.org/10.1016/J.ACTBIO.2023.06.014.

[47] Huang S, Wei H, Li D. Additive manufacturing technologies in the oral implant clinic: A review of current applications and progress. Front Bioeng Biotechnol 2023;11. https://doi.org/10.3389/FBIOE.2023.1100155.

[48] Shuib S, Azemi MA, Binti I, Arrif M, Hamizan NS. Design for Additive Manufacturing and Finite Element Analysis for High Flexion Total Knee Replacement (TKR). Journal of Mechanical Engineering 2021;18:97–110.

[49] Altair – The Implant Boom: It's Now Hip to Replace Your Hip n.d. https://additivemanufacturing.com/2018/08/16/altair-the-implant-boom-its-now-hip-to-replace-your-hip/ (accessed September 10, 2024).

[50] 3D Printing the Future of Surgery - 3DPrint.com | The Voice of 3D Printing / Additive Manufacturing n.d. https://3dprint.com/163831/3d-printing-the-future-of-surgery/ (accessed September 10, 2024).

[51] Jayanth N, Venkata Roshan M, Sakthi Balaji S, Durga Karthik P, Barathwaj A, Rishiyadhav G. Additive manufacturing of biomaterials: A review. Mater Today Proc 2023. https://doi.org/10.1016/J.MATPR.2023.09.190.

[52] Gao W, Zhang Y, Ramanujan D, Ramani K, Chen Y, Williams CB, et al. The status, challenges, and future of additive manufacturing in engineering. Computer-Aided Design 2015;69:65–89. https://doi.org/10.1016/J.CAD.2015.04.001.

[53] Ribeiro I, Matos F, Jacinto C, Salman H, Cardeal G, Carvalho H, et al. Framework for Life Cycle Sustainability Assessment of Additive Manufacturing. Sustainability 2020, Vol 12, Page 929 2020;12:929. https://doi.org/10.3390/SU12030929.

[54] Mirzaali MJ, Moosabeiki V, Rajaai SM, Zhou J, Zadpoor AA. Additive Manufacturing of Biomaterials—Design Principles and Their Implementation. Materials 2022, Vol 15, Page 5457 2022;15:5457. https://doi.org/10.3390/MA15155457.

[55] Türker H, Aksoy B, Özsoy K. Fabrication of Customized dental guide by stereolithography method and evaluation of dimensional accuracy with artificial neural networks. J Mech Behav Biomed Mater 2022;126:105071. https://doi.org/10.1016/J.JMBBM.2021.105071.

[56] Dehurtevent M, Robberecht L, Hornez JC, Thuault A, Deveaux E, Béhin P. Stereolithography: A new method for processing dental ceramics by additive computer-aided manufacturing. Dental Materials 2017;33:477–85. https://doi.org/10.1016/J.DENTAL.2017.01.018.

[57] Arif ZU, Khalid MY, Noroozi R, Hossain M, Shi HTH, Tariq A, et al. Additive manufacturing of sustainable biomaterials for biomedical applications. Asian J Pharm Sci 2023;18:100812. https://doi.org/10.1016/J.AJPS.2023.100812.

[58] Qin Y, Wen P, Guo H, Xia D, Zheng Y, Jauer L, et al. Additive manufacturing of biodegradable metals: Current research status and future perspectives. Acta Biomater 2019;98:3–22. https://doi.org/10.1016/J.ACTBIO.2019.04.046.

[59] Jauer L. Additive Manufacturing of Magnesium Alloys. 9th Symposium on Biodegradable Metals 2017.

[60] Jauer L. Selective Laser Melting of Magnesium Alloys. World PM 2016.

[61] Jauer BJL, Voshage M, Meiners W. Selective laser melting of magnesium alloys. Eur Cell Mater 2015;30.

[62] Yang C, Huan Z, Wang X, Wu C, Chang J. 3D Printed Fe Scaffolds with HA Nanocoating for Bone Regeneration. ACS Biomater Sci Eng 2018;4:608–16.

[63] Li Y, Jahr H, Lietaert K, Pavanram P, Yilmaz A, Fockaert LI, et al. Additively manufactured biodegradable porous iron. Acta Biomater 2018;77:380–93. https://doi.org/10.1016/J.ACTBIO.2018.07.011.

[64] Wen P, Qin Y, Chen Y, Voshage M, Jauer L, Poprawe R, et al. Laser additive manufacturing of Zn porous scaffolds: Shielding gas flow, surface quality and densification. J Mater Sci Technol 2019;35:368–76. https://doi.org/10.1016/J.JMST.2018.09.065.

[65] Dienel KEG, Van Bochove B, Seppälä J V. Additive Manufacturing of Bioactive Poly(trimethylene carbonate)/β-Tricalcium Phosphate Composites for Bone Regeneration. Biomacromolecules 2020;21:366–75. https://doi.org/10.1021/ACS.BIOMAC.9B01272.

[66] Luo JP, Huang YJ, Xu JY, Sun JF, Dargusch MS, Hou CH, et al. Additively manufactured biomedical Ti-Nb-Ta-Zr lattices with tunable Young's modulus: Mechanical property, biocompatibility, and proteomics analysis. Materials Science and Engineering: C 2020;114:110903. https://doi.org/10.1016/J.MSEC.2020.110903.

[67] Wang X, Xu S, Zhou S, Xu W, Leary M, Choong P, et al. Topological design and additive manufacturing of porous metals for bone scaffolds and orthopaedic implants: A review. Biomaterials 2016;83:127–41. https://doi.org/10.1016/J.BIOMATERIALS.2016.01.012.

[68] Izri Z, Bijanzad A, Torabnia S, Lazoglu I. In silico evaluation of lattice designs for additively manufactured total hip implants. Comput Biol Med 2022;144:105353. https://doi.org/10.1016/J.COMPBIOMED.2022.105353.

[69] D'Andrea D, Risitano G, Guglielmino E, Piperopoulos E, Santonocito D. Correlation between mechanical behaviour and microstructural features of AISI 316L produced by SLM. Procedia Structural Integrity 2022;41:199–207. https://doi.org/10.1016/j.prostr.2022.05.022.

[70] Crisafulli D, Fintová S, Santonocito D, D'Andrea D. Microstructural characterization and mechanical behaviour of laser powder Bed Fusion stainless steel 316L. Theoretical and Applied Fracture Mechanics 2024;131. https://doi.org/10.1016/j.tafmec.2024.104343.

[71] Campanelli LC. A review on the recent advances concerning the fatigue performance of titanium alloys for orthopedic applications. J Mater Res 2020. https://doi.org/10.1557/jmr.2020.305.

[72] Czichos H. Handbook of Technical Diagnostics. Springer Berlin Heidelberg; 2013. https://doi.org/10.1007/978-3-642-25850-3.

[73] Turner TA. Diagnostic thermography. Vet Clin North Am Equine Pract 2001;17:95–114. https://doi.org/10.1016/s0749-0739(17)30077-9.

[74] Tattersall GJ. Infrared thermography: A non-invasive window into thermal physiology. Comp Biochem Physiol A Mol Integr Physiol 2016;202:78–98. https://doi.org/10.1016/j.cbpa.2016.02.022.

[75] Cadena V, Andrade D V., Bovo RP, Tattersall GJ. Evaporative respiratory cooling augments pit organ thermal detection in rattlesnakes. J Comp Physiol A Neuroethol Sens Neural Behav Physiol 2013;199:1093–104. https://doi.org/10.1007/s00359-013-0852-4.

[76] Tattersall GJ, Andrade D V., Abe AS. Heat exchange from the toucan bill reveals a controllable vascular thermal radiator. Science (1979) 2009;325:468–70. https://doi.org/10.1126/science.1175553.

[77] Holanda AGA, Cortez DEA, Queiroz GF de, Matera JM. Applicability of thermography for cancer diagnosis in small animals. J Therm Biol 2023;114. https://doi.org/10.1016/j.jtherbio.2023.103561.

[78] Zdero R, Brzozowski P, Schemitsch EH. Biomechanical stress analysis using thermography: A review. J Biomech 2023;160. https://doi.org/10.1016/j.jbiomech.2023.111822.

[79] Bergmann G, Graichen F, Rohlmann A. Hip joint loading during walking and running, measured in two patients. I Biomrchanics 1993;26:969–90.

[80] Vanderby R, Kohles SS. Thermographic stress analysis in cortical bone. J Biomech Eng 1991;113:418–22. https://doi.org/10.1115/1.2895421.

[81] Hyodo K, Tateishi T. Application of Thermoelastic Stress Analysis Method to Joint Biomechanics. Hip Biomechanics, 1993.

[82] Hyodo K, Inomoto M, Ma W, Miyakawa S, Tateishi T. Thermoelastic Femoral Stress Imaging for Experimental Evaluation of Hip Prosthesis Design. JSME International Journal 2001;44:1065–71.

[83] Shah S, Bougherara H, Schemitsch EH, Zdero R. Biomechanical stress maps of an artificial femur obtained using a new infrared thermography technique validated by strain gages. Med Eng Phys 2012;34:1496–502. https://doi.org/10.1016/j.medengphy.2012.02.012.

[84] Zanetti EM, Musso SS, Audenino AL. Thermoelastic stress analysis by means of a standard thermocamera. Exp Tech 2007;31:42–50. https://doi.org/10.1111/j.1747-1567.2007.00147.x.

[85] Kobles SS, Vanderby R. Thermographic strain analysis of the proximal canine femur*. vol. 19. n.d.

[86] Kohles SS, Vanderby R, Phd JR. A Comparison of Strain Gage Analysis to Differential Infrared Thermography in the Proximal Canine Femur. 35th Annual Meeting Orthopaedic Research Society, 1989, p. 490.

[87] Bagheri ZS, El Sawi I, Bougherara H, Zdero R. Biomechanical fatigue analysis of an advanced new carbon fiber/flax/epoxy plate for bone fracture repair using conventional fatigue tests and thermography. J Mech Behav Biomed Mater 2014;35:27–38. https://doi.org/10.1016/j.jmbbm.2014.03.008.

[88] Pavan D, Morello F, Monachino F, Rovere G, Camarda L, Pitarresi G. Similar biomechanical properties of four tripled tendon graft models for ACL reconstruction. Arch Orthop Trauma Surg 2022;142:1155–65. https://doi.org/10.1007/s00402-021-04030-8.

[89] Augustin G, Davila S, Udiljak T, Vedrina DS, Bagatin D. Determination of spatial distribution of increase in bone temperature during drilling by infrared thermography: Preliminary report. Arch Orthop Trauma Surg 2009;129:703–9. https://doi.org/10.1007/s00402-008-0630-x.

[90] Augustin G, Zigman T, Davila S, Udilljak T, Staroveski T, Brezak D, et al. Cortical bone drilling and thermal osteonecrosis. Clinical Biomechanics 2012;27:313–25. https://doi.org/10.1016/j.clinbiomech.2011.10.010.

[91] Marković A, Lazić Z, Mišić T, Šćepanović M, Todorović A, Thakare K, et al. Effect of surgical drill guide and irrigans temperature on thermal bone changes during drilling implant sites – Thermographic analysis on bovine ribs. Vojnosanit Pregl 2016;73:744–50. https://doi.org/10.2298/VSP141208041M.

[92] Kalidindi V. Optimization of drill design and coolant systems during dental implant surgery. University of Kentucky Master's Theses 2004;314.

[93] Di Fiore A, Sivolella S, Stocco E, Favero V, Stellini E. Experimental analysis of temperature differences during implant site preparation: Continuous drilling technique versus intermittent drilling technique. Journal of Oral Implantology 2018;44:46–50. https://doi.org/10.1563/aaid-joi-D-17-00077.

[94] Kley P, Frentzen M, Küpper K, Braun A, Kecsmar S, Jäger A, et al. Thermotransduction and heat stress in dental structures during orthodontic debonding. Journal of Orofacial Orthopedics 2016;77:185–93. https://doi.org/10.1007/s00056-016-0023-7.

[95] DiBenedetto M, Yoshida M, Sharp M, Jones B. Foot Evaluation by Infrared Imaging. Mil Med 2002;167:384–92.

[96] Olaya Mira N, Viloria Barragán C, Plata JA. Evaluation of different Jaipur foot-ankle assemblies using infrared thermography. Prosthet Orthot Int 2021;45:184–8. https://doi.org/10.1177/0309364620958510.

[97] Ravichandran G, Rosakis AJ, Hodowany J, Rosakis P. On the Conversion of Plastic Work into Heat During High-Strain-Rate Deformation, AIP Publishing; 2003, p. 557–62. https://doi.org/10.1063/1.1483600.

[98] Kapoor R, Nemat-Nasser S. Determination of temperature rise during high strain rate deformation. Mechanics of Materials 1998;27:1–12.

[99] Rosa G La, Risitano A. Thermographic methodology for rapid determination of the fatigue limit of materials and mechanical components. Int J Fatigue 2000;22:65–73.

[100] Fargione G, Geraci A, Rosa G La, Risitano A. Rapid determination of the fatigue curve by the thermographic method. J Basic Eng Trans ASME, Ser D 2002;24:37.

[101] Melvin AD, Lucia AC, Solomos GP. THE THERMAL RESPONSE TO DEFORMATION TO FRACTURE OF A CARBON/EPOXY COMPOSITE LAMINATE. Compos Sci Technol 1993;46:345–51.

[102] Beghi MG, Bottani CE, Caglioti G. IRREVERSIBLE THERMODYNAMICS OF METALS UNDER STRESS. Res Mechanica: International Journal of Structural Mechanics and Materials Science 1986;19:365–79. https://doi.org/10.4028/www.scientific.net/ssp.3-4.471.

[103] Plekhov OA, Naimark OB. THEORETICAL AND EXPERIMENTAL STUDY OF ENERGY DISSIPATION IN THE COURSE OF STRAIN LOCALIZATION IN IRON. Journal of Applied Mechanics and Technical Physics 2009;50:127–36.

[104] Risitano A, Risitano G. Determining fatigue limits with thermal analysis of static traction tests. Fatigue Fract Eng Mater Struct 2013;36:631–9. https://doi.org/10.1111/ffe.12030.

[105] Clienti C, Fargione G, La Rosa G, Risitano A, Risitano G. A first approach to the analysis of fatigue parameters by thermal variations in static tests on plastics. Eng Fract Mech 2010;77:2158–67. https://doi.org/10.1016/j.engfracmech.2010.04.028.

[106] Risitano A, Risitano G, Clienti C. Fatigue limit by thermal analysis of specimen surface in mono axial traction test. EPJ Web Conf, vol. 6, EDP Sciences; 2010. https://doi.org/10.1051/epjconf/20100638010.

[107] Lazzarin P, Zambardi R. A finite-volume-energy based approach to predict the static and fatigue behavior of components with sharp V-shaped notches. Int J Fract 2001;112:275–98.

[108] Lazzarin P, Zambardi R. The equivalent strain energy density approach re-formulated and applied to sharp V-shaped notches under localized and generalized plasticity. Fatigue Fract Eng Mater Struct 2002;25:917–28. https://doi.org/10.1046/j.1460-2695.2002.00543.x.

[109] Lazzarin P, Livieri P, Berto F, Zappalorto M. Local strain energy density and fatigue strength of welded joints under uniaxial and multiaxial loading. Eng Fract Mech 2008;75:1875–89. https://doi.org/10.1016/j.engfracmech.2006.10.019.

[110] Foti P, Filippi S, Berto F. Fatigue assessment of welded joints by means of the Strain Energy Density method: Numerical predictions and comparison with Eurocode 3. Frattura Ed Integrità Strutturale 2019;47:104–25. https://doi.org/10.3221/IGF-ESIS.47.09.

[111] Lazzarin P, Sonsino CM, Zambardi R. A notch stress intensity approach to assess the multiaxial fatigue strength of welded tube-to-flange joints subjected to combined loadings. Fatigue Fract Eng Mater Struct 2004;27:127–40. https://doi.org/10.1111/J.1460-2695.2004.00733.X.

[112] Tawancy HM. Failure Analysis of 304 Stainless Steel Components Used in Petrochemical Industry Applications. Metallography, Microstructure, and Analysis 2019;8:705–12. https://doi.org/10.1007/s13632-019-00578-5.

[113] Rossi S, Leso SM, Calovi M. Study of the Corrosion Behavior of Stainless Steel in Food Industry. Materials 2024;17. https://doi.org/10.3390/ma17071617.

[114] Boujelbene M, Kharrat M, Dammak M, Maalej A. Tribological behaviour of the 304L/HDPE contact: application for the knee prostheses. Int J Exp Comput Biomech 2009;1:214–24. https://doi.org/10.1504/IJECB.2009.0292.

[115] Ye Y, Wang Y, Ma X, Zhang D, Wang L, Li X. Tribocorrosion behaviors of multilayer PVD DLC coated 304L stainless steel in seawater. Diam Relat Mater 2017;79:70–8. https://doi.org/10.1016/j.diamond.2017.09.002.

[116] Manwatkar SK, Kuhite KS, Narayana Murty SVS, Ramesh Narayanan P. Metallurgical Analysis of Failed AISI 304L Stainless Steel Tubes Used in Launch Vehicle Applications. Metallography, Microstructure, and Analysis 2015;4:497–507. https://doi.org/10.1007/s13632-015-0247-8.

[117] Berto F, Lazzarin P, Wang CH. Three-dimensional linear elastic distributions of stress and strain energy density ahead of V-shaped notches in plates of arbitrary thickness. Int J Fract 2004;127:265–82. https://doi.org/10.1023/B:FRAC.0000036846.23180.4d.

[118] Kotousov A, Wang CH. Three-dimensional stress constraint in an elastic plate with a notch. Int J Solids Struct 2002;39:4311–26. https://doi.org/10.1016/S0020-7683(02)00340-2.

[119] Fischer C, Fricke W, Rizzo CM. Experiences and recommendations for numerical analyses of notch stress intensity factor and averaged strain energy density. Eng Fract Mech 2016;165:98–113. https://doi.org/10.1016/j.engfracmech.2016.08.012.

[120] Fischer C, Fricke W, Rizzo CM. Experiences and recommendations for numerical analyses of notch stress intensity factor and averaged strain energy density. Eng Fract Mech 2016;165:98–113. https://doi.org/10.1016/j.engfracmech.2016.08.012.

[121] Foti P, Berto F. Some useful expressions and a proof of the validity of the volume free procedure for the SED method application. Eng Fract Mech 2022;274. https://doi.org/10.1016/j.engfracmech.2022.108818.

[122] Foti P, Crisafulli D, Santonocito D, Risitano G, Berto F. Effect of misalignments and welding penetration on the fatigue strength of a common welded detail: SED method predictions and comparisons with codes. Int J Fatigue 2022;164. https://doi.org/10.1016/j.ijfatigue.2022.107135.

[123] Foti P, Santonocito D, Risitano G, Berto F. Fatigue assessment of cruciform joints: Comparison between Strain Energy Density predictions and current standards and recommendations. Eng Struct 2021;230. https://doi.org/10.1016/j.engstruct.2020.111708.

[124] Corigliano P, Cucinotta F, Guglielmino E, Risitano G, Santonocito D. Fatigue assessment of a marine structural steel and comparison with Thermographic Method and Static Thermographic Method. Fatigue Fract Eng Mater Struct 2019;43:734–43. https://doi.org/10.1111/ffe.13158.

[125] Santonocito D. Evaluation of fatigue properties of 3D-printed Polyamide-12 by means of energy approach during tensile tests. Procedia Structural Integrity, vol. 25, Elsevier B.V.; 2020, p. 355–63. https://doi.org/10.1016/j.prostr.2020.04.040.

[126] Meneghetti G, Ricotta M, Atzori B. A synthesis of the push-pull fatigue behaviour of plain and notched stainless steel specimens by using the specific heat loss. Fatigue Fract Eng Mater Struct 2013;36:1306–22. https://doi.org/10.1111/ffe.12071.

[127] Meneghetti G, Ricotta M, Atzori B. Experimental evaluation of fatigue damage in two-stage loading tests based on the energy dissipation. Proc Inst Mech Eng C J Mech Eng Sci 2015;229:1280–91. https://doi.org/10.1177/0954406214559112.

[128] Meneghetti G, Ricotta M. The use of the specific heat loss to analyse the low- and high-cycle fatigue behaviour of plain and notched specimens made of a stainless steel. Eng Fract Mech 2012;81:2–16. https://doi.org/10.1016/j.engfracmech.2011.06.010.

[129] Klusák J, Kozáková K, Fintová S, Seitl S. Fatigue lifetimes of 1.4306 and 1.4307 stainless steels subjected to ultrasonic loading. Procedia Structural Integrity, vol. 42, Elsevier B.V.; 2022, p. 1369–75. https://doi.org/10.1016/j.prostr.2022.12.174.

[130] Cichański A, Cichański A. The influence of mesh morphology on the SCF in 2D FEM analysis of flat bars with opposite V-notch under tension. 2016.

[131] Lazzarin P, Berto F, Zappalorto M. Rapid calculations of notch stress intensity factors based on averaged strain energy density from coarse meshes: Theoretical bases and applications. Int J Fatigue 2010;32:1559–67.

[132] Foti P, Berto F. Some useful expressions and a proof of the validity of the volume free procedure for the SED method application. Eng Fract Mech 2022;274. https://doi.org/10.1016/j.engfracmech.2022.108818.

[133] Foti P, Razavi SMJ, Ayatollahi MR, Marsavina L, Berto F. On the application of the volume free strain energy density method to blunt V-notches under mixed mode condition. Eng Struct 2021;230:111716. https://doi.org/10.1016/j.engstruct.2020.111716.

[134] Risitano A, Risitano G. Determining fatigue limits with thermal analysis of static traction tests. Fatigue Fract Eng Mater Struct 2013;36:631–9. https://doi.org/10.1111/ffe.12030.

[135] Wallin KRW. Statistical uncertainty in the fatigue threshold staircase test method 2010. https://doi.org/10.1016/j.ijfatigue.2010.09.013.

[136] Pollak R, Palazotto A, Nicholas T. A simulation-based investigation of the staircase method for fatigue strength testing n.d. https://doi.org/10.1016/j.mechmat.2005.12.005.

[137] Zhao YX, Zhang Y, He HW. Improved measurement on probabilistic fatigue limits/strengths by test data from staircase test method 2016. https://doi.org/10.1016/j.ijfatigue.2016.09.010.

[138] Thompson T, Liu J, Hu C. A comparative analysis of step loading and staircase testing for fatigue strength estimation of an engine component. Fatigue Fract Eng Mater Struct 2023;46:667–81. https://doi.org/10.1111/FFE.13898.

[139] Milone A, Foti P, Filippi S, Landolfo R, Berto F. Evaluation of the influence of mean stress on the fatigue behavior of notched and smooth medium carbon steel components through an energetic local approach. Fatigue Fract Eng Mater Struct 2023;46:4315–32. https://doi.org/10.1111/ffe.14139.

[140] Radaj D. State-of-the-art review on the local strain energy density concept and its relation to the J-integral and peak stress method. Fatigue Fract Eng Mater Struct 2015;38:2–28. https://doi.org/10.1111/ffe.12231.

[141] Nagaishi N, Ogawa Y, Okazaki S, Matsunaga H. Fatigue limit of circumferentially notched metastable austenitic stainless steel under positive/negative stress ratios: Synergistic effects of notch-root mechanistic singularity and phase transformation. Int J Fatigue 2022;165. https://doi.org/10.1016/j.ijfatigue.2022.107229.

[142] Mayama T, Sasaki K, Kuroda M. Quantitative evaluations for strain amplitude dependent organization of dislocation structures due to cyclic plasticity in austenitic stainless steel 316L. Acta Mater 2008;56:2735–43. https://doi.org/10.1016/j.actamat.2008.02.005.

[143] Šmíd M, Kuběna I, Jambor M, Fintová S. Effect of solution annealing on low cycle fatigue of 304L stainless steel. Materials Science and Engineering: A 2021;824. https://doi.org/10.1016/j.msea.2021.141807.

[144] Jambor M, Vojtek T, Pokorný P, Šmíd M. Effect of solution annealing on fatigue crack propagation in the AISI 304L TRIP steel. Materials 2021;14. https://doi.org/10.3390/ma14061331.

[145] Herzog D, Seyda V, Wycisk E, Emmelmann C. Additive manufacturing of metals. Acta Mater 2016;117:371–92. https://doi.org/10.1016/j.actamat.2016.07.019.

[146] Plocher J, Panesar A. Review on design and structural optimisation in additive manufacturing: Towards next-generation lightweight structures. Mater Des 2019;183:108164.

[147] Diegel O, Schutte J, Ferreira A, Chan YL. Design for additive manufacturing process for a lightweight hydraulic manifold. Addit Manuf 2020;36:101446. https://doi.org/10.1016/j.addma.2020.101446.

[148] Yao D, An X, Fu H, Zhang H, Yang X, Zou Q. Dynamic investigation on the powder spreading during selective laser melting additive manufacturing. Addit Manuf 2021;37:101707. https://doi.org/10.1016/j.addma.2020.101707.

[149] Zhang J, Gao J, Song B, Zhang L, Han C, Cai C. A novel crack-free Ti-modified Al-Cu-Mg alloy designed for selective laser melting. Addit Manuf 2021;38:101829. https://doi.org/10.1016/j.addma.2020.101829.

[150] Dario Santonocito, Stanislava Fintová, Vittorio Di Cocco, Francesco Iacoviello, Giacomo Risitano DD. Comparison on Mechanical Behaviour and Microstructural Features Between Traditional and AM AISI 316L. Fatigue Fract Eng Mater Struct n.d.

[151] Montelione A, Ghods S, Schur R, Wisdom C, Arola D, Ramulu M. Powder Reuse in Electron Beam Melting Additive Manufacturing of Ti6Al4V : Particle Microstructure , Oxygen Content and Mechanical Properties. Addit Manuf 2020;35:101216. https://doi.org/10.1016/j.addma.2020.101216.

[152] Galati M, Snis A, Iuliano L. Powder bed properties modelling and 3D thermo-mechanical simulation of the additive manufacturing Electron Beam Melting process. Addit Manuf 2019;30:100897. https://doi.org/10.1016/j.addma.2019.100897.

[153] Ziaee M, Crane NB. Binder jetting : A review of process , materials , and methods. Addit Manuf 2019;28:781–801. https://doi.org/10.1016/j.addma.2019.05.031.

[154] Miyanaji H, Ma D, Atwater MA, Darling KA, Hammond VH, Williams CB. Binder jetting additive manufacturing of copper foam structures 2020;32. https://doi.org/10.1016/j.addma.2019.100960.

[155] Gonzalez JA, Mireles J, Lin Y, Wicker RB. Characterization of ceramic components fabricated using binder jetting additive manufacturing technology. Ceram Int 2016;42:10559–64. https://doi.org/10.1016/j.ceramint.2016.03.079.

[156] Pierre J, Iervolino F, Farahani RD, Piccirelli N, Martin L, Therriault D. Material extrusion additive manufacturing of multifunctional sandwich panels with load-bearing and acoustic capabilities for aerospace applications 2023;61. https://doi.org/10.1016/j.addma.2022.103344.

[157] Salmi M. Additive Manufacturing Processes in Medical Applications 2021.

[158] Culmone C, Smit G, Breedveld P. Additive manufacturing of medical instruments : A state-of-the-art review. Addit Manuf 2019;27:461–73. https://doi.org/10.1016/j.addma.2019.03.015.

[159] Priarone PC, Catalano AR, Settineri L. Additive manufacturing for the automotive industry : on the life - cycle environmental implications of material substitution and lightweighting through re - design. Progress in Additive Manufacturing 2023. https://doi.org/10.1007/s40964-023-00395-x.

[160] Böckin D, Tillman A-M. Environmental assessment of additive manufacturing in the automotive industry. J Clean Prod 2019;226:977–87.

[161] Bedmar J, Riquelme A, Rodrigo P, Torres B, Rams J. Comparison of different additive manufacturing methods for 316l stainless steel. Materials 2021;14. https://doi.org/10.3390/ma14216504.

[162] Takezawa A, Chen Q, To AC. Optimally variable density lattice to reduce warping thermal distortion of laser powder bed fusion. Addit Manuf 2021;48:102422. https://doi.org/10.1016/j.addma.2021.102422.

[163] Fang Z, Wu Z, Huang C, Wu C. Review on residual stress in selective laser melting additive manufacturing of alloy parts. Opt Laser Technol 2020;129:106283. https://doi.org/10.1016/j.optlastec.2020.106283.

[164] Lavecchia F, Guerra MG, Galantucci LM. Chemical vapor treatment to improve surface finish of 3D printed polylactic acid (PLA) parts realized by fused filament fabrication. Progress in Additive Manufacturing 2022;7:65–75. https://doi.org/10.1007/s40964-021-00213-2.

[165] D'andrea D, Risitano G, Raffaele M, Cucinotta F, Santonocito D. Damage assessment of different FDM-processed materials adopting Infrared Thermography. Frattura Ed Integrita Strutturale 2022;16:75–90. https://doi.org/10.3221/IGF-ESIS.62.06.

[166] D'Andrea D, Risitano G, Guglielmino E, Piperopoulos E, Santonocito D. Correlation between mechanical behaviour and microstructural features of AISI 316L produced by SLM. Procedia Structural Integrity 2022;41:199–207. https://doi.org/10.1016/j.prostr.2022.05.022.

[167] Rane K, Petrò S, Strano M. Evolution of porosity and geometrical quality through the ceramic extrusion additive manufacturing process stages. Addit Manuf 2020;32:101038. https://doi.org/10.1016/j.addma.2020.101038.

[168] Mostafaei A, Zhao C, He Y, Reza Ghiaasiaan S, Shi B, Shao S, et al. Defects and anomalies in powder bed fusion metal additive manufacturing. Curr Opin Solid State Mater Sci 2022;26:100974. https://doi.org/10.1016/j.cossms.2021.100974.

[169] Shrestha R, Simsiriwong J, Shamsaei N. Fatigue behavior of additive manufactured 316L stainless steel parts: Effects of layer orientation and surface roughness. Addit Manuf 2019;28:23–38. https://doi.org/10.1016/j.addma.2019.04.011.

[170] Stern F, Kleinhorst J, Tenkamp J, Walther F. Investigation of the anisotropic cyclic damage behavior of selective laser melted AISI 316L stainless steel. Fatigue Fract Eng Mater Struct 2019;42:2422–30. https://doi.org/10.1111/FFE.13029.

[171] Liang X, Robert C, Hor A, Morel F. Numerical investigation of the surface and microstructure effects on the high cycle fatigue performance of additive manufactured stainless steel 316L. Int J Fatigue 2021;149:106273. https://doi.org/10.1016/j.ijfatigue.2021.106273.

[172] La Rosa G, Risitano A. Thermographic methodology for rapid determination of the fatigue limit of materials and mechanical components. Int J Fatigue 2000;22:65–73. https://doi.org/10.1016/S0142-1123(99)00088-2.

[173] D'Andrea D, Gatto A, Guglielmino E, Risitano G, Santonocito D. A comparison on static and fatigue behaviour between traditional and SLM AISI 316L. Journal of Mechanical Science and Technology 2023;37. https://doi.org/10.1007/s12206-022-2103-5.

[174] Braun M, Mayer E, Kryukov I, Wolf C, Böhm S, Taghipour A, et al. Fatigue strength of PBF-LB/M and wrought 316L stainless steel: effect of post-treatment and cyclic mean stress. Fatigue Fract Eng Mater Struct 2021;44:3077–93. https://doi.org/10.1111/ffe.13552.

[175] Wang Y, Wang W, Susmel L. Constant/variable amplitude multiaxial notch fatigue of additively manufactured AISI 316L. Int J Fatigue 2021;152. https://doi.org/10.1016/j.ijfatigue.2021.106412.

[176] Trahair NS, Bradford MA, Nethercot DA, Gardner L. The behaviour and design of steel structures to EC3. CRC Press; 2017.

[177] Lotsberg I. Assessment of design criteria for fatigue cracking from weld toes subjected to proportional loading. Ships and Offshore Structures 2009;4:175–87. https://doi.org/10.1080/17445300902733998.

[178] British Standards Institution. BSI Standards Publication Guide to fatigue design and assessment of steel products 2014.

[179] 1993-1-9 EN. Eurocode 3: Design of steel structures-Part 1-9: Fatigue. European Committee for Standardization: Brussels, Belgium 2005.

[180] Jonsson B, Dobmann G, Hobbacher A, Kassner M, Marquis G. IIW guidelines on weld quality in relationship to fatigue strength 2016:124.

[181] DNV GL AS. DNVGL-RP-C203: Fatigue design of offshore steel structures The. DNV GL - Recommended Practice 2016:176.

[182] Hobbacher A. Recommendations for fatigue design of welded joints and components. vol. 47. Springer; 2016. https://doi.org/10.1007/978-3-319-23757-2.

[183] Atzori B, Lazzarin P, Meneghetti G. Fatigue strength assessment of welded joints: From the integration of Paris' law to a synthesis based on the notch stress intensity factors of the uncracked geometries. Eng Fract Mech 2008;75:364–78.

[184] Lazzarin P, Tovo R. A notch intensity factor approach to the stress analysis of welds. Fatigue Fract Eng Mater Struct 1998;21:1089–103.

[185] Radaj D. Review of fatigue strength assessment of nonwelded and welded structures based on local parameters. Int J Fatigue 1996;18:153–70.

[186] Lazzarin P, Berto F, Gomez FJ, Zappalorto M. Some advantages derived from the use of the strain energy density over a control volume in fatigue strength assessments of welded joints. Int J Fatigue 2008;30:1345–57.

[187] Lazzarin P, Berto F, Zappalorto M. Rapid calculations of notch stress intensity factors based on averaged strain energy density from coarse meshes: Theoretical bases and applications. Int J Fatigue 2010;32:1559–67. https://doi.org/10.1016/j.ijfatigue.2010.02.017.

[188] Berto F, Campagnolo A, Chebat F, Cincera M, Santini M. Fatigue strength of steel rollers with failure occurring at the weld root based on the local strain energy values: modelling and fatigue assessment. Int J Fatigue 2016;82:643–57.

[189] Foti P, Berto F. Fatigue assessment of high strength welded joints through the strain energy density method. Fatigue Fract Eng Mater Struct 2020;43:2694–702. https://doi.org/10.1111/ffe.13336.

[190] Foti P, Berto F. Evaluation of the effect of the TIG-dressing technique on welded joints through the strain energy density method. Procedia Structural Integrity 2020;25:201–8. https://doi.org/10.1016/j.prostr.2020.04.024.

[191] Meneghetti G. The peak stress method applied to fatigue assessments of steel and aluminium fillet-welded joints subjected to mode I loading. Fatigue Fract Eng Mater Struct 2008;31:346–69.

[192] Meneghetti G, De Marchi A, Campagnolo A. Assessment of root failures in tube-to-flange steel welded joints under torsional loading according to the Peak Stress Method. Theoretical and Applied Fracture Mechanics 2016;83:19–30.

[193] Meneghetti G, Campagnolo A, Avalle M, Castagnetti D, Colussi M, Corigliano P, et al. Rapid evaluation of notch stress intensity factors using the peak stress method: Comparison of commercial finite element codes for a range of mesh patterns. Fatigue Fract Eng Mater Struct 2018;41:1044–63.

[194] Nykänen T, Li X, Björk T, Marquis G. A parametric fracture mechanics study of welded joints with toe cracks and lack of penetration. Eng Fract Mech 2005;72:1580–609.

[195] Liu G, Liu Y, Huang Y. A novel structural stress approach for multiaxial fatigue strength assessment of welded joints. Int J Fatigue 2014;63:171–82.

[196] Hobbacher A. Recommendations for Fatigue Design of Welded Joints and Components. 2016. https://doi.org/10.1007/978-3-319-23757-2.

[197] Lazzarin P, Zambardi R. A finite-volume-energy based approach to predict the static and fatigue behavior of components with sharp V-shaped notches. Int J Fract 2001;112:275–98. https://doi.org/10.1023/A:1013595930617.

[198] Lazzarin P, Zambardi R. The equivalent strain energy density approach re-formulated and applied to sharp V-shaped notches under localized and generalized plasticity. Fatigue Fract Eng Mater Struct 2002;25:917–28. https://doi.org/10.1046/j.1460-2695.2002.00543.x.

[199] Lazzarin P, Livieri P, Berto F, Zappalorto M. Local strain energy density and fatigue strength of welded joints under uniaxial and multiaxial loading. Eng Fract Mech 2008;75:1875–89. https://doi.org/10.1016/J.ENGFRACMECH.2006.10.019.

[200] Neuber H. Theory of notch stresses: principles for exact calculation of strength with reference to structural form and material. vol. 4547. USAEC Office of Technical Information; 1961.

[201] Lazzarin P, Zambardi R. A finite-volume-energy based approach to predict the static and fatigue behavior of components with sharp V-shaped notches. Int J Fract 2001;112:275–98. https://doi.org/10.1023/A:1013595930617.

[202] Berto F, Lazzarin P. Recent developments in brittle and quasi-brittle failure assessment of engineering materials by means of local approaches. Materials Science and Engineering R: Reports 2014;75:1–48. https://doi.org/10.1016/j.mser.2013.11.001.

[203] Radaj D, Vormwald M. Advanced methods of fatigue assessment. vol. 9783642307. 2013. https://doi.org/10.1007/978-3-642-30740-9.

[204] Lazzarin P, Lassen T, Livieri P. A notch stress intensity approach applied to fatigue life predictions of welded joints with different local toe geometry. Fatigue Fract Eng Mater Struct 2003;26:49–58. https://doi.org/10.1046/j.1460-2695.2003.00586.x.

[205] Livieri P, Lazzarin P. Fatigue strength of steel and aluminium welded joints based on generalised stress intensity factors and local strain energy values. Int J Fract 2005;133:247–76. https://doi.org/10.1007/s10704-005-4043-3.

[206] Atzori B, Berto F, Lazzarin P, Quaresimin M. Multi-axial fatigue behaviour of a severely notched carbon steel. Int J Fatigue 2006;28:485–93. https://doi.org/10.1016/j.ijfatigue.2005.05.010.

[207] Berto F, Lazzarin P. Fatigue strength of structural components under multi-axial loading in terms of local energy density averaged on a control volume. Int J Fatigue 2011;33:1055–65. https://doi.org/10.1016/j.ijfatigue.2010.11.019.

[208] Lazzarin P, Zambardi R. A finite-volume-energy based approach to predict the static and fatigue behavior of components with sharp V-shaped notches. Int J Fract 2001;112:275–98. https://doi.org/10.1023/A:1013595930617.

[209] Berto F, Lazzarin P. A review of the volume-based strain energy density approach applied to V-notches and welded structures. Theoretical and Applied Fracture Mechanics 2009;52:183–94. https://doi.org/10.1016/j.tafmec.2009.10.001.

[210] Foti P, Santonocito D, Risitano G, Berto F. Fatigue assessment of cruciform joints: Comparison between Strain Energy Density predictions and current standards and recommendations. Eng Struct 2021;230:111708. https://doi.org/10.1016/j.engstruct.2020.111708.

[211] Foti P, Berto F. Strain energy density evaluation with free coarse mesh model. Material Design & Processing Communications 2019:1–4. https://doi.org/10.1002/mdp2.116.

[212] Foti P, Ayatollahi MRMR, Berto F. Rapid strain energy density evaluation for V-notches under mode I loading conditions. Eng Fail Anal 2020;110:104361. https://doi.org/10.1016/j.engfailanal.2019.104361.

[213] Campagnolo A, Zuin S, Meneghetti G. Averaged strain energy density estimated rapidly from nodal displacements by coarse FE analyses: Cracks under mixed mode loadings. Fatigue Fract Eng Mater Struct 2020;43:1658–85. https://doi.org/10.1111/ffe.13187.

[214] Foti P, Razavi SMJ, Ayatollahi MR, Marsavina L, Berto F. On the application of the volume free strain energy density method to blunt V-notches under mixed mode condition. Eng Struct 2021;230:111716. https://doi.org/10.1016/j.engstruct.2020.111716.

[215] Foti P, Razavi SMJ, Berto F. Fracture assessment of U-notched PMMA under mixed mode I/II loading conditions by means of local approaches. Procedia Structural Integrity 2021;33:482–90. https://doi.org/10.1016/j.prostr.2021.10.055.

[216] Berto F, Lazzarin P. Recent developments in brittle and quasi-brittle failure assessment of engineering materials by means of local approaches. Materials Science and Engineering R: Reports 2014;75:1–48. https://doi.org/10.1016/j.mser.2013.11.001.

[217] 1993-1-3:2009 BE. Eurocode 3: Design of steel structures - Part 1-9: Fatigue. Eurocode 3: Design of steel structures - Part 1-9: Fatigue, vol. 7, 2011.

[218] Der Norske Veritas. DNVGL-RP-C203. Fatigue Design of Offshore Steel Structures. Recommended Practice 2016:176.

[219] Maddox SJ. Fitness-for-purpose assessment of misalignment in transverse butt welds subject to fatigue loading. Welding Institute; 1985.

[220] Berge S, Myhre H. Fatigue strength of misaligned cruciform and butt joints. Norwegian Maritime Research 1977;5.

[221] Institution BS. Guide on methods for assessing the acceptability of flaws in metallic structures. British Standards Institution; 1999.

[222] Cucinotta F, Guglielmino E, Longo G, Risitano G, Santonocito D, Sfravara F. Topology Optimization Additive Manufacturing-Oriented for a Biomedical Application. Advances on Mechanics, Design Engineering and Manufacturing II, Springer International Publishing; 2019, p. 184–93. https://doi.org/10.1007/978-3-030-12346-8_18.

[223] Epasto G, Palomba G, D'Andrea D, Guglielmino E, Di Bella S, Traina F. Ti-6Al-4V ELI microlattice structures manufactured by electron beam melting: Effect of unit cell dimensions and morphology on mechanical behaviour. Materials Science and Engineering: A 2019;753:31–41. https://doi.org/10.1016/j.msea.2019.03.014.

[224] Epasto G, Palomba G, D'andrea D, Di Bella S, Mineo R, Guglielmino E, et al. Experimental Investigation of Rhombic Dodecahedron Micro-Lattice Structures Manufactured by Electron Beam Melting. MaterialsTodayProceedings 2019;7:578–85.

[225] Fellah M, Labaïz M, Assala O, Dekhil L, Zerniz N, Iost A. Tribological behavior of biomaterial for total hip prosthesis. Matériaux & Techniques 2014;102:601. https://doi.org/10.1051/mattech/2014027.

[226] Banchet V, Fridrici V, Abry JC, Kapsa Ph. Wear and friction characterization of materials for hip prosthesis. Wear 2007;263:1066–71. https://doi.org/10.1016/j.wear.2007.01.085.

[227] Unsworth A, Hall RM, Burgess IC, Wroblewski BM, Streicher RM, Semlitsch M. Frictional resistance of new and explanted artificial hip joints. Wear 1995;190:226–31. https://doi.org/10.1016/0043-1648(95)06653-5.

[228] Saikko VO. A Three-Axis Hip Joint Simulator for Wear and Friction Studies on Total Hip Prostheses. Proc Inst Mech Eng H 1996;210:175–85. https://doi.org/10.1243/pime_proc_1996_210_410_02.

[229] Shankar S, Nithyaprakash R, Abbas G, Naveen Kumar R, Pramanik A, Kumar Basak A, et al. Tribological behavior of zirconia-toughened alumina (ZTA) against Ti6Al4V under different bio-lubricants in hip prosthesis using experimental and finite element concepts. Mater Lett 2022;307:131107. https://doi.org/10.1016/j.matlet.2021.131107.

[230] Mattei L, Di Puccio F, Ciulli E, Pauschitz A. Experimental Investigation on Wear Map Evolution of Ceramic-on-UHMWPE Hip Prosthesis. Tribol Int 2020;143.

[231] Kourra N, Warnett JM, Attridge A, Dibling G, McLoughlin J, Muirhead-Allwood S, et al. Computed tomography metrological examination of additive manufactured acetabular hip prosthesis cups. Addit Manuf 2018;22:146–52. https://doi.org/10.1016/j.addma.2018.04.033.

[232] Murr LE. Additive manufacturing of biomedical devices: an overview. Materials Technology 2017;33:57–70. https://doi.org/10.1080/10667857.2017.1389052.

[233] Cortis G, Mileti I, Nalli F, Palermo E, Cortese L. Additive manufacturing structural redesign of hip prostheses for stress-shielding reduction and improved functionality and safety. Mechanics of Materials 2022;165:104173. https://doi.org/10.1016/j.mechmat.2021.104173.

[234] Kashyap V, Ramkumar P. Comprehensive analysis of geometrical parameters of crosshatched texture for enhanced tribological performance under biological environment. Proceedings of the Institution of Mechanical Engineers, Part J: Journal of Engineering Tribology 2020;235:434–52. https://doi.org/10.1177/1350650120915136.

[235] Allen Q, Raeymaekers B. The Effect of Texture Floor Profile on the Lubricant Film Thickness in a Textured Hard-On-Soft Bearing With Relevance to Prosthetic Hip Implants. J Tribol 2020;143. https://doi.org/10.1115/1.4047753.

[236] Kashyap V, Ramkumar P. DLC coating over pre-oxidized and textured Ti6Al4V for superior adhesion and tribo-performance of hip implant. Surf Coat Technol 2022;440:128492. https://doi.org/10.1016/j.surfcoat.2022.128492.

[237] Malkiya Rasalin Prince R, Selvakumar N, Arulkirubakaran D, Christopher Ezhil Singh S, Chrispin Das M, Bannaravuri PK, et al. ZrC-Impregnated Titanium-Based Coating as an Effective Lubricating Barrier for Artificial Hip Prosthesis. Mater Perform Charact 2021;10:189–205. https://doi.org/10.1520/mpc20200075.

[238] Senatore A, Risitano G, Scappaticci L, D'Andrea D. Investigation of the Tribological Properties of Different Textured Lead Bronze Coatings under Severe Load Conditions. Lubricants 2021;9:34. https://doi.org/10.3390/lubricants9040034.

[239] Khaskhoussi A, Risitano G, Calabrese L, D'Andrea D. Investigation of the Wettability Properties of Different Textured Lead/Lead-Free Bronze Coatings. Lubricants 2022;10:82. https://doi.org/10.3390/lubricants10050082.

[240] D'Andrea D, Pistone A, Risitano G, Santonocito D, Scappaticci L, Alberti F. Tribological characterization of a hip prosthesis in Si3N4-TiN ceramic composite made with Electrical Discharge

Machining (EDM). Procedia Structural Integrity 2021;33:469–81. https://doi.org/10.1016/j.prostr.2021.10.054.

[241] Ploof G, Alqahtani B, Alghamdi F, Flynn G, Yang CX. Center of Mass Estimation Using Motion Capture System. 2017 IEEE 15th Intl Conf on Dependable, Autonomic and Secure Computing, 15th Intl Conf on Pervasive Intelligence and Computing, 3rd Intl Conf on Big Data Intelligence and Computing and Cyber Science and Technology Congress(DASC/PiCom/DataCom/CyberSciTech), IEEE; 2017. https://doi.org/10.1109/dasc-picom-datacom-cyberscitec.2017.61.

[242] Tanaka R, Takimoto H, Yamasaki T, Higashi A. Validity of time series kinematical data as measured by a markerless motion capture system on a flatland for gait assessment. J Biomech 2018;71:281–5. https://doi.org/10.1016/j.jbiomech.2018.01.035.

[243] D'Andrea D, Cucinotta F, Farroni F, Risitano G, Santonocito D, Scappaticci L. Development of Machine Learning Algorithms for the Determination of the Centre of Mass. Symmetry (Basel) 2021;13:1–16.

[244] Fadela A, Habib L, Abderrahmane B. Finite Element analysis of stress state in the cement of total hip prosthesis with elastomeric stress barrier. Frattura Ed Integrità Strutturale 2021;15:281–90. https://doi.org/10.3221/igf-esis.57.20.

[245] Bhawe AK, Shah KM, Somani S, Shenoy B S, Bhat N S, Zuber M, et al. Static structural analysis of the effect of change in femoral head sizes used in Total Hip Arthroplasty using finite element method. Cogent Eng 2022;9. https://doi.org/10.1080/23311916.2022.2027080.

[246] D'Andrea D, Risitano G, Desiderio E, Quintarelli A, Milone D, Alberti F. Artificial Neural Network Prediction of the Optimal Setup Parameters of a Seven Degrees of Freedom Mathematical Model of a Race Car: IndyCar Case Study. Vehicles 2021, Vol 3, Pages 300-329 2021;3:300–29. https://doi.org/10.3390/VEHICLES3020019.

[247] Mahyudin F, Hermawan H. Biomaterials and Medical Devices. vol. 58. Adv. Struct. Mater.; 2016. https://doi.org/10.1007/978-3-319-14845-8.

[248] Ammarullah MI, Afif IY, Maula MI, Winarni TI, Tauviqirrahman M, Akbar I, et al. Tresca Stress Simulation of Metal-on-Metal Total Hip Arthroplasty during Normal Walking Activity. Materials 2021;14:7554. https://doi.org/10.3390/ma14247554.

[249] Uddin MS, Zhang LC. Predicting the wear of hard-on-hard hip joint prostheses. Wear 2013;301:192–200. https://doi.org/10.1016/j.wear.2013.01.009.

[250] Hegadekatte V, Huber N, Kraft O. Finite element based simulation of dry sliding wear. Model Simul Mat Sci Eng 2004;13:57–75. https://doi.org/10.1088/0965-0393/13/1/005.

[251] Stanković M, Marinković A, Grbović A, Mišković Ž, Rosić B, Mitrović R. Determination of Archard's wear coefficient and wear simulation of sliding bearings. Industrial Lubrication and Tribology 2019;71:119–25. https://doi.org/10.1108/ilt-08-2018-0302.

[252] Ruggiero A, Sicilia A. Lubrication modeling and wear calculation in artificial hip joint during the gait. Tribol Int 2020;142:105993. https://doi.org/10.1016/j.triboint.2019.105993.

[253] Sharma D, Kamran M, Paraye NK, Anant R. Insights into the wear behaviour of electron beam melted Ti–6Al–4V alloy in the as-built and the heat-treated conditions. J Manuf Process 2021;71:669–78. https://doi.org/10.1016/j.jmapro.2021.09.060.

[254] Barber H, Kelly CN, Abar B, Allen N, Adams SB, Gall K. Rotational Wear and Friction of Ti-6Al-4V and CoCrMo against Polyethylene and Polycarbonate Urethane. Biotribology 2021;26:100167. https://doi.org/10.1016/j.biotri.2021.100167.

[255] Wang L, Isaac G, Wilcox R, Jones A, Thompson J. Finite element analysis of polyethylene wear in total hip replacement: A literature review. Proc Inst Mech Eng H 2019;233:1067–88. https://doi.org/10.1177/0954411919872630.

[256] Ackland DC, Moskaljuk A, Hart C, Vee Sin Lee P, Dimitroulis G. Prosthesis Loading After Temporomandibular Joint Replacement Surgery: A Musculoskeletal Modeling Study. J Biomech Eng 2015;137. https://doi.org/10.1115/1.4029503.

[257] Paschold HW, Sergeev A V. Whole-body vibration knowledge survey of U.S. occupational safety and health professionals. J Safety Res 2009;40:171–6. https://doi.org/10.1016/j.jsr.2009.02.008.

[258] Young SN, VanWye WR, Wallmann HW. Sport simulation as a form of implicit motor training in a geriatric athlete after stroke: a case report. Physiother Theory Pract 2018;36:524–32. https://doi.org/10.1080/09593985.2018.1488322.

[259] Cameron PW, Soltero NC, Byers J. Effects of a 60 Minute on Ice Game Simulation on the Balance Error Scoring System. Int J Exerc Sci 2018;11:462–7.

[260] Chung H-J. Optimization Based Dynamic Human Motion Prediction with Modular Exoskeleton Robots as Interactive Forces: The Case of Weight Lifting Motion. Collaborative and Humanoid Robots [Working Title], IntechOpen; 2021. https://doi.org/10.5772/intechopen.98391.

[261] Cheng H, Obergefell L, Rizer A. The development of the GEBOD program. Proceedings of the 1996 Fifteenth Southern Biomedical Engineering Conference, IEEE; n.d. https://doi.org/10.1109/sbec.1996.493162.

[262] Wu Y, Liu J. Research on college gymnastics teaching model based on multimedia image and image texture feature analysis. Discover Internet of Things 2021;1. https://doi.org/10.1007/s43926-021-00015-6.

[263] Erdmann WS, Kowalczyk R. Basic inertial quantities including multi-segment trunk of fit, young males obtained based on personalized data. J Biomech 2020;106:109794. https://doi.org/10.1016/j.jbiomech.2020.109794.

[264] de Leva P. Adjustments to Zatsiorsky-Seluyanov's segment inertia parameters. J Biomech 1996;29:1223–30. https://doi.org/10.1016/0021-9290(95)00178-6.

[265] Cao Z, Hidalgo G, Simon T, Wei S-E, Sheikh Y. OpenPose: Realtime Multi-Person 2D Pose Estimation Using Part Affinity Fields. IEEE Trans Pattern Anal Mach Intell 2021;43:172–86. https://doi.org/10.1109/tpami.2019.2929257.

[266] Feng B, Powell D, Doblas A. Marker-less motion capture system using OpenPose. In: Alam MS, Asari VK, editors. Pattern Recognition and Tracking XXXIII, SPIE; 2022. https://doi.org/10.1117/12.2619059.

[267] Simon T, Joo H, Matthews I, Sheikh Y. Hand Keypoint Detection in Single Images Using Multiview Bootstrapping. 2017 IEEE Conference on Computer Vision and Pattern Recognition (CVPR), IEEE; 2017. https://doi.org/10.1109/cvpr.2017.494.

[268] Wei S-E, Ramakrishna V, Kanade T, Sheikh Y. Convolutional Pose Machines. 2016 IEEE Conference on Computer Vision and Pattern Recognition (CVPR), IEEE; 2016. https://doi.org/10.1109/cvpr.2016.511.

[269] Pagnon D, Domalain M, Reveret L. Pose2Sim: An End-to-End Workflow for 3D Markerless Sports Kinematics—Part 1: Robustness. Sensors 2021;21:6530. https://doi.org/10.3390/s21196530.

[270] Martinez GH, Raaj Y, Idrees H, Xiang D, Joo H, Simon T, et al. Single-Network Whole-Body Pose Estimation. 2019 IEEE/CVF International Conference on Computer Vision (ICCV), IEEE; 2019. https://doi.org/10.1109/iccv.2019.00708.

[271] Riley PO, Schenkman ML, Mann RW, Hodge WA. Mechanics of a constrained chair-rise. J Biomech 1991;24:77–85. https://doi.org/10.1016/0021-9290(91)90328-k.

[272] Jones CJ, Rikli RE, Beam WC. A 30-s Chair-Stand Test as a Measure of Lower Body Strength in Community-Residing Older Adults. Res Q Exerc Sport 1999;70:113–9. https://doi.org/10.1080/02701367.1999.10608028.

[273] Kerr KM, White JA, Barr DA, Mollan RAB. Analysis of the sit-stand-sit movement cycle: development of a measurement system. Gait & Posture 1994;2:173–81. https://doi.org/10.1016/0966-6362(94)90005-1.

[274] Kerr K, White J, Barr D, Mollan R. Standardization and definitions of the sit-stand-sit movement cycle. Gait Posture 1994;2:182–90. https://doi.org/10.1016/0966-6362(94)90006-X.

[275] Tveter AT, Dagfinrud H, Moseng T, Holm I. Health-Related Physical Fitness Measures: Reference Values and Reference Equations for Use in Clinical Practice. Arch Phys Med Rehabil 2014;95:1366–73. https://doi.org/10.1016/j.apmr.2014.02.016.

[276] Viswakumar A, Rajagopalan V, Ray T, Parimi C. Human Gait Analysis Using OpenPose. 2019 Fifth International Conference on Image Information Processing (ICIIP), IEEE; 2019. https://doi.org/10.1109/iciip47207.2019.8985781.

[277] Jamari J, Ammarullah MI, Santoso G, Sugiharto S, Supriyono T, Prakoso AT, et al. Computational Contact Pressure Prediction of CoCrMo, SS 316L and Ti6Al4V Femoral Head against UHMWPE Acetabular Cup under Gait Cycle. J Funct Biomater 2022;13:64. https://doi.org/10.3390/jfb13020064.

[278] Murphy CB. Thermal Analysis. Science (1979) 1966;151:111–2. https://doi.org/10.1126/science.151.3706.111.

[279] Zhao R, Xie R, Ren N, Li Z, Zhang S, Liu Y, et al. Correlation between intraosseous thermal change and drilling impulse data during osteotomy within autonomous dental implant robotic system: An in vitro study. Clin Oral Implants Res 2023;35:258–67. https://doi.org/10.1111/clr.14222.

[280] Raj R, Manju V, Kumar-Gopal V, Eswar M. Analysis of factors determining thermal changes at osteotomy site in dental implant placement - An in-vitro study. J Clin Exp Dent 2021;13:e234–9. https://doi.org/10.4317/jced.57346.

[281] Gungormus M, Erbasar GNH. Transient Heat Transfer in Dental Implants for Thermal Necrosis-Aided Implant Removal: A 3D Finite Element Analysis. Journal of Oral Implantology 2019;45:196–201. https://doi.org/10.1563/aaid-joi-d-18-00210.

[282] Hochscheidt CJ, Shimizu RH, Andrighetto AR, Moura LM, Golin AL, Hochscheidt RC. Thermal Variation During Osteotomy With Different Dental Implant Drills. Implant Dent 2017;26:73–9. https://doi.org/10.1097/id.0000000000000535.

[283] Tur D, Giannis K, Unger E, Mittlböck M, Rausch-Fan X, Strbac GD. Drilling- and withdrawing-related thermal effects of implant site preparation for ceramic and stainless steel twist drills in standardized bovine bone. Clin Implant Dent Relat Res 2022;25:152–65. https://doi.org/10.1111/cid.13151.

[284] Handley A, Hessefort YZ. Improved Skin Health in a One-Year Prospective Bioengineering Analysis of Healthcare Workers' Hands in Long Term?Care. Am J Infect Control 2019;47:S27. https://doi.org/10.1016/j.ajic.2019.04.053.

[285] Matos JDM de, Queiroz DA, Nakano LJN, Andrade VC, Ribeiro N de CR, Borges ALS, et al. Bioengineering Tools Applied to Dentistry: Validation Methods for In Vitro and In Silico Analysis. Dent J (Basel) 2022;10:145. https://doi.org/10.3390/dj10080145.

[286] Zhao Y, Han Y, Chen C, Seo H. Crack Detection in Frozen Soils Using Infrared Thermographic Camera. Sensors (Basel) 2022;22:885. https://doi.org/10.3390/s22030885.

[287] Demirbas AE, Ekici R, Karakaya M, Alkan A. Bone stress and damage distributions during dental implant insertion: a novel dynamic FEM analysis. Comput Methods Biomech Biomed Engin 2021;25:1381–92. https://doi.org/10.1080/10255842.2021.2012765.

[288] Yang B, Irastorza-Landa A, Heuberger P, Ploeg H-L. Analytical model for dental implant insertion torque. J Mech Behav Biomed Mater 2022;131:105223. https://doi.org/10.1016/j.jmbbm.2022.105223.

[289] Klär V, Karl M, Grobecker-Karl T. Bone Damage during Dental Implant Insertion: A Pilot Study Combining Strain Gauge and Histologic Analysis. Applied Sciences 2021;12:291. https://doi.org/10.3390/app12010291.

[290] Varghai K, Eppell SJ, Wang R. Effect of Drilling Speed on Dental Implant Insertion Torque. Journal of Oral Implantology 2020;46:467–74. https://doi.org/10.1563/aaid-joi-d-18-00250.

[291] Dhok K, Adhikari M, Palange A, Dhatrak P. Heat generation during implant site preparation and its effects on osseointegration: A review. Mater Today Proc 2023;72:1035–40. https://doi.org/10.1016/j.matpr.2022.09.157.

[292] Limmeechokchai S, Kan JY, Rungcharassaeng K, Goodacre CJ, Lozada J, Oyoyo U. Heat and Sound Generation During Implant Osteotomy When Using Different Types of Drills in Artificial and Bovine Bone Blocks. Journal of Oral Implantology 2021;48:187–93. https://doi.org/10.1563/aaid-joi-d-20-00361.

[293] Kuster M, Mukaddam K, Zitzmann N, Filippi A, Kühl S. Influence of a Novel Drill Design on Heat Generation During Conventional and Guided Implant Osteotomy. The International Journal of Oral & Maxillofacial Implants 2021;36:e31–41. https://doi.org/10.11607/jomi.8583.

[294] Ahmadi F, Mohammadi R. FEM investigation of drilling conditions on heat generation during teeth implantation. Journal of Computational and Applied Research in Mechanical Engineering 2019;10:25–35.

[295] Sharon E, Shapira L, Wilensky A, Abu-hatoum R, Smidt A. Efficiency and Thermal Changes during Implantoplasty in Relation to Bur Type. Clin Implant Dent Relat Res 2011;15:292–6. https://doi.org/10.1111/j.1708-8208.2011.00366.x.

[296] Ibáñez M, Dieball C, Lasanta A, Godec A, Rica RA. Heating and cooling are fundamentally asymmetric and evolve along distinct pathways. Nat Phys 2024;20:135–41. https://doi.org/10.1038/s41567-023-02269-z.

[297] Bashutski JD, D'Silva NJ, Wang H. Implant Compression Necrosis: Current Understanding and Case Report. J Periodontol 2009;80:700–4. https://doi.org/10.1902/jop.2009.080581.

[298] Jo K-H, Yoon K-H, Park K-S, Bae J-H, You K-H, Han J-H, et al. Thermally induced bone necrosis during implant surgery: 3 case reports. J Korean Assoc Oral Maxillofac Surg 2011;37:406. https://doi.org/10.5125/jkaoms.2011.37.5.406.

[299] Cicciù M, Stacchi C, Fiorillo L, Cervino G, Troiano G, Vercellotti T, et al. Piezoelectric bone surgery for impacted lower third molar extraction compared with conventional rotary instruments: a systematic review, meta-analysis, and trial sequential analysis. Int J Oral Maxillofac Surg 2021;50:121–31. https://doi.org/10.1016/j.ijom.2020.03.008.

[300] Hua X, Shu L. Musculoskeletal modeling and biomechanics of the knee joint. Cartilage Tissue and Knee Joint Biomechanics: Fundamentals, Characterization and Modelling 2024:313–34. https://doi.org/10.1016/B978-0-323-90597-8.00034-7.

[301] Menezes P, Rhea MR, Herdy C, Simão R. Effects of Strength Training Program and Infrared Thermography in Soccer Athletes Injuries. Sports 2018, Vol 6, Page 148 2018;6:148. https://doi.org/10.3390/SPORTS6040148.

[302] Fokam D, Lehmann C. Clinical assessment of arthritic knee pain by infrared thermography. J Basic Clin Physiol Pharmacol 2018;30. https://doi.org/10.1515/JBCPP-2017-0218.

[303] Denoble AE, Hall N, Pieper CF, Kraus VB. Patellar skin surface temperature by thermography reflects knee osteoarthritis severity. Clin Med Insights Arthritis Musculoskelet Disord 2010;3:69–75. https://doi.org/10.4137/CMAMD.S5916/ASSET/IMAGES/LARGE/10.4137_CMAMD.S5916-FIG2.JPEG.

[304] Zeng Y, Feng W, Qi X, Li J, Chen J, Lu L, et al. Differential knee skin temperature following total knee arthroplasty and its relationship with serum indices and outcome: A prospective study. J Int Med Res 2016;44:1023. https://doi.org/10.1177/0300060516655237.

[305] Calin MA, Mologhianu G, Savastru R, Calin MR, Brailescu CM. A review of the effectiveness of thermal infrared imaging in the diagnosis and monitoring of knee diseases. Infrared Phys Technol 2015;69:19–25. https://doi.org/10.1016/j.infrared.2015.01.013.

[306] de Rezende CM, da Silva AG, Sillero-Quintana M, Marins JCB. Patterns of thermal normality of the knee joint in professional athletes of different sports. J Therm Biol 2024;125:103991. https://doi.org/10.1016/J.JTHERBIO.2024.103991.

[307] Petrigna L, Amato A, Roggio F, Trovato B, Musumeci G. Thermal threshold for knee osteoarthritis people evaluated with infrared thermography: A scoping review. J Therm Biol 2024;123. https://doi.org/10.1016/j.jtherbio.2024.103932.

[308] Molina-Payá J, Ríos-Díaz J, Martínez-Payá J. Inter and intraexaminer reliability of a new method of infrared thermography analysis of patellar tendon. Quant Infrared Thermogr J 2021;18:127–39. https://doi.org/10.1080/17686733.2019.1700697.

[309] Fernández-Cuevas I, Bouzas Marins JC, Arnáiz Lastras J, Gómez Carmona PM, Piñonosa Cano S, García-Concepción MÁ, et al. Classification of factors influencing the use of infrared thermography in humans: A review. Infrared Phys Technol 2015;71:28–55. https://doi.org/10.1016/J.INFRARED.2015.02.007.

[310] Ammer K. The Glamorgan Protocol for recording and evaluation of thermal images of the human body. Thermology International 2008;18:125–9.

[311] Thermography Guidelines. IACT Standards and Protocols in Clinical Thermographic Imaging 2002.

[312] Choi E, Lee P-B, Nahm FS. Interexaminer reliability of infrared thermography for the diagnosis of complex regional pain syndrome 2013. https://doi.org/10.1111/srt.12032.

[313] Ludwig N, Formenti D, Gargano M, Alberti G. Skin temperature evaluation by infrared thermography: Comparison of image analysis methods. Infrared Phys Technol 2014;62:1–6. https://doi.org/10.1016/J.INFRARED.2013.09.011.

[314] Garwood ER, Tai R, Joshi G, Watts GJ, Gyftopolous S, Subhas N. The Use of Artificial Intelligence in the Evaluation of Knee Pathology 2020. https://doi.org/10.1055/s-0039-3400264.

[315] Astuto B, Flament I, Namiri NK, Shah R, Bharadwaj U, Link TM, et al. Automatic Deep Learning–assisted Detection and Grading of Abnormalities in Knee MRI Studies (Radiology: Artificial Intelligence 2021, 3, 3, (10.1148/ryai.2021219001)). Radiol Artif Intell 2021;3. https://doi.org/10.1148/RYAI.2021200165/ASSET/IMAGES/LARGE/RYAI.2021200165.FIG6.JPEG.

[316] Touahema S, Zaimi I, Zrira N, Ngote MN. How Can Artificial Intelligence Identify Knee Osteoarthritis from Radiographic Images with Satisfactory Accuracy?: A Literature Review for 2018–2024. Applied Sciences 2024, Vol 14, Page 6333 2024;14:6333. https://doi.org/10.3390/APP14146333.

[317] Abedin J, Antony J, McGuinness K, Moran K, O'Connor NE, Rebholz-Schuhmann D, et al. Predicting knee osteoarthritis severity: comparative modeling based on patient's data and plain X-ray images. Scientific Reports 2019 9:1 2019;9:1–11. https://doi.org/10.1038/s41598-019-42215-9.

[318] Ma B, Chen J, Yan X, Cheng Z, Qian N, Wu C, et al. Objectively assessing visual analogue scale of knee osteoarthritis pain using thermal imaging. Displays 2024;84:102770. https://doi.org/10.1016/J.DISPLA.2024.102770.

[319] Trejo-Chavez O, Amezquita-Sanchez JP, Huerta-Rosales JR, Morales-Hernandez LA, Cruz-Albarran IA, Valtierra-Rodriguez M. Automatic Knee Injury Identification through Thermal Image Processing and Convolutional Neural Networks. Electronics 2022, Vol 11, Page 3987 2022;11:3987. https://doi.org/10.3390/ELECTRONICS11233987.

[320] Jin C, Yang Y, Xue ZJ, Liu KM, Liu J. Automated analysis method for screening knee osteoarthritis using medical infrared thermography. J Med Biol Eng 2013;33:471–7. https://doi.org/10.5405/JMBE.1054.

[321] Abujaber S, Gillispie G, Marmon A, Zeni J. Validity of the Nintendo Wii Balance Board to assess weight bearing asymmetry during sit-to-stand and return-to-sit task. Gait Posture 2015;41:676–82. https://doi.org/10.1016/J.GAITPOST.2015.01.023.

[322] Yamako G, Punchihewa NG, Arakawa H, Tajima T, Chosa E. Evaluation of Sit-to-Stand Movement in Older Adults with Locomotive Syndrome Using the Nintendo Wii Balance Board. Sensors 2023, Vol 23, Page 3368 2023;23:3368. https://doi.org/10.3390/S23073368.

[323] Jeong Y-J, Park D-S. Validity of Ground Reaction Forces during Gait and Sit-to-Stand using the Nintendo Wii Balance Board in Healthy Subjects. Journal of the Korean Society of Physical Medicine 2016;11:85–92. https://doi.org/10.13066/KSPM.2016.11.4.85.

[324] Yang S, Oh Y, Jeon Y, Park D. Test-retest Reliability of Sit-to-Stand and Gait Assessment Using the Wii Balance Board. Physical Therapy Korea 2016;23:40–7. https://doi.org/10.12674/PTK.2016.23.3.040.

[325] Yamako G, Chosa E, Totoribe K, Fukao Y, Deng G. Quantification of the sit-to-stand movement for monitoring age-related motor deterioration using the Nintendo Wii Balance Board. PLoS One 2017;12:e0188165. https://doi.org/10.1371/JOURNAL.PONE.0188165.

[326] D'andrea D, Cucinotta F, Farroni F, Risitano G, Santonocito D, Scappaticci L. Development of Machine Learning Algorithms for the Determination of the Centre of Mass. Symmetry 2021, Vol 13, Page 401 2021;13:401. https://doi.org/10.3390/SYM13030401.

[327] Clark RA, Bryant AL, Pua Y, McCrory P, Bennell K, Hunt M. Validity and reliability of the Nintendo Wii Balance Board for assessment of standing balance. Gait Posture 2010;31:307–10. https://doi.org/10.1016/J.GAITPOST.2009.11.012.

[328] Leach JM, Mancini M, Peterka RJ, Hayes TL, Horak FB. Validating and Calibrating the Nintendo Wii Balance Board to Derive Reliable Center of Pressure Measures. Sensors 2014, Vol 14, Pages 18244-18267 2014;14:18244–67. https://doi.org/10.3390/S141018244.

[329] Bartlett HL, Ting LH, Bingham JT. Accuracy of force and center of pressure measures of the Wii Balance Board. Gait Posture 2014;39:224–8. https://doi.org/10.1016/J.GAITPOST.2013.07.010.

[330] Rohof B, Betsch M, Rath B, Tingart M, Quack V. The Nintendo® Wii Fit Balance Board can be used as a portable and low-cost posturography system with good agreement compared to established systems. Eur J Med Res 2020;25:44. https://doi.org/10.1186/S40001-020-00445-Y.

[331] Vinader-Caerols C, Monleón S, Carrasco C, Parra A. Effects of Alcohol, Coffee, and Tobacco, Alone or in Combination, on Physiological Parameters and Anxiety in a Young Population. J Caffeine Res 2012;2:70. https://doi.org/10.1089/JCR.2012.0018.

[332] Elson DW, Jones S, Caplan N, Stewart S, St Clair Gibson A, Kader DF. The photographic knee pain map: locating knee pain with an instrument developed for diagnostic, communication and research purposes. Knee 2011;18:417–23. https://doi.org/10.1016/J.KNEE.2010.08.012.

[333] Mathis A, Mamidanna P, Cury KM, Abe T, Murthy VN, Mathis MW, et al. DeepLabCut: markerless pose estimation of user-defined body parts with deep learning. Nat Neurosci 2018;21:1281–9. https://doi.org/10.1038/s41593-018-0209-y.

[334] Nath T, Mathis A, Chen AC, Patel A, Bethge M, Mathis MW. Using DeepLabCut for 3D markerless pose estimation across species and behaviors. Nat Protoc 2019;14:2152–76. https://doi.org/10.1038/s41596-019-0176-0.

[335] Lauer J, Zhou M, Ye S, Menegas W, Schneider S, Nath T, et al. Multi-animal pose estimation, identification and tracking with DeepLabCut. Nat Methods 2022;19:496–504. https://doi.org/10.1038/s41592-022-01443-0.

[336] Milone D, Longo F, Merlino G, De Marchis C, Risitano G, D'Agati L. MocapMe: DeepLabCut-Enhanced Neural Network for Enhanced Markerless Stability in Sit-to-Stand Motion Capture. Sensors 2024;24:3022. https://doi.org/10.3390/s24103022.

[337] Milone D, D'Andrea D, Santonocito D. Smart Design of Hip Replacement Prostheses Using Additive Manufacturing and Machine Learning Techniques. Prosthesis 2024;6:24–40. https://doi.org/10.3390/prosthesis6010002.

[338] Currò E, Bombaci L, Quattrocchi A, De Marchis C, Milone D, Gugliandolo G, et al. A Machine Vision and Electromyographic-Based Approach for Hand Gesture Recognition. 2024 IEEE International Symposium on Medical Measurements and Applications, MeMeA 2024 - Proceedings n.d.:Eindhoven. https://doi.org/10.1109/MeMeA60663.2024.10596876.

[339] Milone D, Risitano G, Pistone A, Crisafulli D, Alberti F. A New Approach for the Tribological and Mechanical Characterization of a Hip Prosthesis Trough a Numerical Model Based on Artificial Intelligence Algorithms and Humanoid Multibody Model. Lubricants 2022;10:160. https://doi.org/10.3390/lubricants10070160.

[340] Insafutdinov E, Pishchulin L, Andres B, Andriluka M, Schiele B. DeeperCut: A Deeper, Stronger, and Faster Multi-Person Pose Estimation Model. Lecture Notes in Computer Science (Including Subseries Lecture Notes in Artificial Intelligence and Lecture Notes in Bioinformatics) 2016;9910 LNCS:34–50. https://doi.org/10.48550/arxiv.1605.03170.

[341] Toshev A, Szegedy C. DeepPose: Human Pose Estimation via Deep Neural Networks. Proceedings of the IEEE Computer Society Conference on Computer Vision and Pattern Recognition 2013:1653–60. https://doi.org/10.1109/CVPR.2014.214.

[342] Simmons GH, Wong BJ, Holowatz LA, Kenney WL. Changes in the control of skin blood flow with exercise training: where do cutaneous vascular adaptations fit in? Exp Physiol 2011;96:822–8. https://doi.org/10.1113/EXPPHYSIOL.2010.056176.

[343] Lanting SM, Johnson NA, Baker MK, Caterson ID, Chuter VH. The effect of exercise training on cutaneous microvascular reactivity: A systematic review and meta-analysis. J Sci Med Sport 2017;20:170–7. https://doi.org/10.1016/j.jsams.2016.04.002.

[344] Ni M, Sun J, Fu J, Du Y, Shen J, Yang X-X, et al. Management of Medial Collateral Ligament Insufficiency During Total Knee Arthroplasty with a Screw and Rectangular Spiked Washer: A Case Series of 14 Patients. Orthop Surg 2020;12:1784–91. https://doi.org/10.1111/os.12818.